Savva, Jill (2023) *A study of the effects of low intensity pulsed ultrasound on bone cells using controlled in vitro exposure methods.* PhD thesis.

http://theses.gla.ac.uk/83709/

A Study of the Effects of Low Intensity Pulsed Ultrasound on Bone Cells Using Controlled *in vitro* Exposure Methods

Jill Savva

BEng (Hons), MSc

Submitted in fulfilment of the requirements for the

Degree of Doctor of Philosophy (PhD)

School of Engineering

College of Science and Engineering

University of Glasgow

June 2023

© J Savva

Abstract

Low Intensity Pulsed Ultrasound (LIPUS) is a type of therapeutic ultrasound approved for treatment of non-union fractures since it was found to accelerate healing in a number of *in vivo* and clinical studies in the 1990's. However, recent independent clinical trials found no significant healing effects, leading to questions over the effectiveness of the treatment. Many *in vitro* experiments have not succeeded in finding a clear and consistent mechanism, partly due to the difficulty in designing apparatus to provide adequate control over the LIPUS field applied to cells. This study developed and used controlled *in vitro* LIPUS exposure methods to investigate the effects of LIPUS fields on bone cells.

The field characteristics of LIPUS transducers with operating frequencies of 45 kHz and 1 MHz were investigated by examining manufacturer's data, measuring the ultrasonic output of a commercial LIPUS transducer and designing and building a new LIPUS transducer based on one of the most common commercial devices.

A custom cell culture vessel (the biocell) was developed to allow a cell layer to be grown on a 6 µm-thick membrane and exposed to LIPUS without changing the LIPUS field. The biocell was immersed in a tank of water at a predetermined separation from a LIPUS transducer. Alignment of the transducer and cell layer was controlled via a custom-built positioning system. LIPUS fields experienced by the cell layers were derived from pressure field mapping in a scanning tank, corrected for any transmission loss through the biocell membrane. An acoustic tile placed behind the cell layer minimised reflections. Temperature measurements on the cell growth surface of a biocell mock-up confirmed no significant temperature rise during LIPUS exposures.

As the extra-cellular matrix stiffness and topology has a significant effect on cellular responses, a 3D exposure method was also developed by seeding cells on 3D-printed scaffolds. The 3D exposure technique showed promise as a potential method of investigating LIPUS effects on cells in a controlled but more *in vivo*-like physical environment.

The murine preosteoblast cell line MC3T3-E1 was chosen as a suitable bone cell model. Markers were chosen from key studies in the LIPUS literature to assess if the reported cellular responses could be replicated with a controlled exposure system. Cell proliferation

was assessed by comparing viable cell counts before and after LIPUS exposure, across the entire growth surface and in pressure bins to assess the effect of pressure amplitude. The expression of protein and genetic markers implicated in mechanotransduction pathways associated with bone growth and mineralisation were also investigated.

Initial studies comparing cellular responses to LIPUS at 1 MHz and 45 kHz over a range of pressure amplitudes indicated 45 kHz LIPUS had the least effect on cell counts and PGE2 expression. This led to the hypothesis that the fast rise time of the 1 MHz pressure pulse produced a rapid switch-on of cyclic radiation force, which stimulated cellular mechanotransduction pathways. The fast rise time hypothesis was tested in the Rise Time Study, which compared the effects of exposure to 1 MHz LIPUS with fast and slow rise times.

Results of the controlled 2D studies suggested that LIPUS exposure had no significant effect on proliferation and markers associated with mechanotransduction pathways. Effects on mineralisation markers were mixed and likely due to the short-term nature of the study compared with the time period of mineralisation of the MC3T3-E1 cell line. The early mineralisation regulator Runx2 was up-regulated significantly six days post-exposure to fast rise time LIPUS. Runx2 is a key transcription factor whose up-regulation stimulates osteogenic differentiation of Mesenchymal Stem Cells (MSCs) and preosteoblasts, eventually leading to increased mineralisation and hence a healing effect. The result suggests runx2 may be sensitive to ultrasound stimulus alone and, therefore, may be a key marker to explain healing effects of LIPUS. Further study is recommended to repeat and verify the findings.

Table of Contents

List of Tables

List of Figures

Author's declaration

I declare that this thesis has been written by myself and is a record of research performed by myself with the exception of the following experiments. Olivia Ngo, visiting PhD candidate from Drexel University, assisted with the 3D scaffold preliminary study. Dr Vineetha Jayawarna provided the 3D-printed scaffolds and advised on gap size. RT-PCR tests and initial analysis of reference genes were performed by Dr Helen Wright of the University of Birmingham. Any contributions from others are clearly referenced and reproduced with permission. This work has not been submitted previously for any other degree at the University of Glasgow or any other institution, and was supervised by Dr Helen Mulvana, Senior Lecturer of the Department of Biomedical Engineering at the University of Strathclyde and Professor Margaret Lucas, Director of the Centre for Medical and Industrial Ultrasonics (C-MIU) at the University of Glasgow.

Acknowledgements

This PhD would not have been completed without the support and encouragement of many people. My heartfelt thanks go to the following people. Firstly, my fabulous PhD peers. The laughs and karaoke kept me sane through the roller coaster ride of the PhD and the pandemic. The equally excellent researchers of C-MIU, in particular Rachael, Rebecca and Xuan, who were so generous with their help and advice whenever asked. Olivia Ngo of Drexel University for being my LIPUS partner for a few months. We had a unique research bond which I will always cherish. Professor Manuel Salmeron-Sanchez and Professor Nikolaj Gadegaard for allowing me the use of the biomedical engineering facilities at the University of Glasgow, especially during the COVID restrictions. Dr Vineetha Jayawarna for providing and advising on the use of the 3D scaffolds. Dr Marie Cutiongco for fabulous training and advice in cell culture and automated microscope scans. Lab managers Julie, Anne and Rachel for all your advice and assistance. Brian Robb and the logistics team (Ian, Ken and Bobby) for your assistance and many trips up and down the stairs to the lab with equipment and materials. Ewan Russell the 3D-printing guru. Professor Sandy Cochran for flinging a bit of money my way when I needed it the most.

Thank you to my incredibly supportive supervisors for providing a combination of expertise, sympathy, patience and hard-nosed pragmatism throughout the project. Dr Helen Mulvana you could always see the clinching bit of detail and come up with just the right

turn of phrase to describe it. And Margaret for seeing the bigger picture when I was drowning in the detail.

And thanks be to my fabulous, ever-suffering family: my kids for surviving almost six years of a not-quite-there mum. My mum for upping sticks from her life-long home to live in my village, pick my youngest up from school and ferry him to his after-school clubs, all the while keeping the laundry juggernaut at bay.

My amazing, caring, loving and long-suffering husband Nick who stuck by me through thick and thin, boasted about my exploits to anyone who would listen, solved my IT issues and was just generally there for the entire journey. Nick has been planning the PhD party for some time now (including margherita van). You deserve this as much as me love.

Finally, I dedicate this PhD to my dad, David Barrie. A lot of colour and laughter went out of my life when you left, but I'm trying my best to pass on your light-hearted, generous and kind outlook to other folks. I know you would have been proud but also know it wouldn't really matter to you as long as I'm happy.

I'll finish with some quotes that got me through:

"Results! Why, man, I have gotten a lot of results! I know several thousand things that won't work" Thomas Edison

"My powers are ordinary. Only my application brings me success" Isaac Newton

"Don't ask for the amount you think you need. Ask for the highest amount you think you can get away with." Prof. Sandy Cochran

"The most effective way to do it, is to do it" Amelia Earhart (and Margaret Lucas)

Covid-19 Impact Statement

As with many studies around this time, the course of this PhD was interrupted by the COVID-19 pandemic. When the first UK lockdown started in March 2020, Trial (A) of the Rise Time Study had just been completed. Though the enforced home working had the positive effect of allowing more time to scrutinise methods, read more *in vitro* papers and learn much more about bone physiology, it also involved juggling the home schooling of three children and their wellbeing during a difficult time.

The rest of the Rise Time Study was carried out from September to November 2020. Running experiments during this period was challenging due to the significant reduction in access to facilities, people and support services, especially in the biomedical engineering laboratories. Impacts are hard to quantify, but some direct adverse effects are listed below.

Growth media samples from the Rise Time Study with base media were stored for 9 months at -20 °C and, as a consequence, suffered degradation in PGE2 concentration. It was assumed for the purpose of analysis that all samples were subject to the same rate of degradation over time, but accuracy of results may have been affected.

The Rise Time Study RT-PCR was originally to be conducted at the University of Birmingham School of Dentistry by myself, with the assistance of a fellow researcher familiar with the work. Due to the Covid lockdown I was not able to travel to Birmingham, and I extracted the RNA samples in Glasgow with no formal training. The RNA extraction was carefully planned and implemented with advice from experts but corruption of samples was still possible due to my inexperience. The RT-PCR was conducted by a University of Birmingham researcher who was not directly involved with the LIPUS study. This, coupled with my limited involvement in the RT-PCR, resulted in the choice of a sub-optimal integrin (Integrin β5) to investigate the mechanotransduction pathways of interest.

The 3D scaffold LIPUS Exposure Study was affected by the unavailability of the original cutting tip used in the preliminary study, which was conducted in February 2020. The only cutting tip available had a flat, unsharpened tip which likely contributed to cavitation, along with the use of a higher power drive, due to the limited access to advice from fellow researchers who were more familiar with the equipment.

Published Work

<u>Abstracts</u>

Savva, J., M. Lucas, and H. Mulvana. A Controlled Study of Pre-osteoblast Proliferation and PGE2 Up-regulation after Exposure to Low Intensity Pulsed Ultrasound., Anglo-French Physical Acoustics Conference (AFPAC) 2020, Institute of Physics, 2020. (Presentation)

<u>Posters</u>

Savva, J., M. Lucas, and H. Mulvana. Low Intensity Pulsed Ultrasound for bone regeneration therapy: a controlled *in vitro* study method., Ultrasound 2018, British Medical Ultrasound Society, 2018.

<u>Conference Papers</u>

Savva, J., M. Lucas, and H. Mulvana. A controlled in vitro study of optimal low intensity pulsed ultrasound fields for stimulation of proliferation in murine osteoblasts., 2019 IEEE International Ultrasonics Symposium (IUS). 2019. (Poster).

<u>Journal Articles</u>

Gupta, D., Savva, J., Li, X., Chandler, J. H., Shelton, R. M., Scheven, B. A., Mulvana, H., Valdasrti, P., Lucas, M., Walmsley, A.D. *Traditional Multiwell Plates and Petri Dishes Limit the Evaluation of the Effects of Ultrasound on Cells In Vitro.* Ultrasound in Medicine & Biology, 2022. **48**(9): p. 1745-1761.

Symbols and Abbreviations

Throughout the work, cellular markers are given in upper case when referring to protein expression (e.g., COX2) and in lower case when referring to RNA expression (e.g., cox2).

Symbol / Abbreviation	Definition	Description
$\varnothing$	Diameter	Transducer diameter (normally in millimetres)
n	Number of samples	Number of samples in a data set
σ	Standard Deviation	Statistical measure of the variance of a data set compared to its mean. The sample standard deviation is used throughout this document: $$\sigma = \sqrt{\frac{\sum(x-\mu)^2}{n-1}}$$
AA	Ascorbic Acid	Vitamin C: added to base media in concentration 50 µg/ml to encourage osteogenic differentiation in the MC3T3-E1 cell line
ArA	Arachidonic Acid	Fatty acid converted to prostaglandins by COX-1 and COX-2.
ACAN	Aggrecan	proteoglycan essential for collagen ECM formation
ACTB	Beta Actin	Housekeeping gene for qRT-PCR
A_{ER}	Effective radiating area	The area of a therapeutic ultrasound head that produces 95% of the ultrasonic energy, usually measured at 3 mm from the front face.
ALP	Alkaline phosphatase	Secreted by osteoblasts. Up-regulates mineralisation by breaking down pyrophosphate, which inhibits calcium crystallisation throughout the body.
BGP	Beta-glycerophosphate	Also, β-Glycerophosphate or Glycerol-2-phosphate. Added to growth media to drive osteogenic differentiation of preosteoblasts and MSCs *in vitro*.
BMP	Bone Morphogenetic Protein	A group of growth factors (or cytokines) involved in bone formation and repair

Symbol / Abbreviation	Definition	Description
BSC	Biological Safety Cabinet	Biological Safety Cabinet
C-JUN	C-JUN protein	Protein encoded by the jun gene. Forms AP-1 early response transcription factor with c-Fos. Required for cell proliferation.
COL I (or 1)	Collagen Type 1	Collagen which makes up the organic component of bone
COL II	Collagen Type 2	Collagen laid down by chondrocytes to form cartilage (e.g., in soft callus)
COL X	Collagen Type X	short chain collagen expressed by hypertrophic chondrocytes during endochondral ossification
COX1/2	Cyclooxygenase 1/2	Enzymes involved in synthesis of prostaglandins
CP	Crossing Point	The number of cycles of PCR for the reaction curve for a specific gene to reach a chosen threshold.
c-myc	c-myc transcription factor	Transcription factor associated with cell proliferation.
CW	Continuous Wave	Continuously repeating ultrasound wave (i.e., NOT pulsed)
DC	Duty cycle	Describes ratio of time a pulse is ON – equal to pw x prr and usually referred to as a ratio (0-1) or percentage (0%-100%)
ECM	Extra-cellular matrix	A 3D network of collagen or mineralised molecules that form the structure of tissue on which cells can grow.
egr-1	Early Growth Response Protein 1	Transcription factor associated with cell differentiation and mitosis (proliferation).
ERK	Extracellular signal-related kinase	Also referred to as mitogen-activated protein kinase (MAPK), although it is now generally referred to as a subset of that family. Part of the MAPK/ERK pathway which is known to activate many transcription factors. Can be activated by mechanotransduction.
ETOH	Ethanol	Used for sterilisation in cell culture, usually mixed to 70 % concentration

Symbol / Abbreviation	Definition	Description
f	Frequency	Frequency in Hz
Fgfr	Fibroblast growth factor / receptor (2,3)	Growth factors (or their receptors) involved in regulation of preosteoblast proliferation. Up-regulated by Runx2.
FN	Fibronectin	Extra-cellular matrix protein
HA	Hydroxyapatite, $Ca_{10}(PO_4)_6(OH)_2$	Crystal making up 50% of mineralised bone by volume, 70% by weight.
HSP	Heat Shock Protein	Protein expressed by MSCs and osteoblasts in response to heat stress. Promotes osteogenic differentiation and mineralisation.
IL-1	Interleukin-1	Cytokine secreted by macrophages – up-regulates COX1and COX2.
IL-6	Interleukin-6	Cytokine secreted by macrophages and osteoblasts – regulates inflammation.
IL-8	Interleukin-8	Cytokine secreted by macrophages, osteoblasts and endothelial cells. Promotes migration of endothelial cells and angiogenesis
I_{SATA}	Spatial-averaged, temporal-averaged Intensity	Defined as the transmitted power of an ultrasound transducer, divided by the effective radiating area.
I_{SATP}	Spatial-averaged, temporal-peak Intensity	Peak intensity of the spatial-averaged pulse of a transducer.
MMP-13	Matrix metallopeptidase 13 (or Collagenase 3)	This enzyme cleaves collagen and is expressed in hypertrophic chondrocytes and mature osteoblasts. Likely to have a role in converting the soft callus to hard, mineralised callus.
MSC	Mesenchymal Stem Cell	Stem cells that can differentiate into chondrogenic or osteogenic lineage
mTOR	Mechanistic target of Rapamycin	Protein kinase related to PI3K. Integrates inputs from upstream pathways and plays central role in regulation of metabolism and physiology.
NES	nestin	Intermediate filament protein. Involved in formation of ECM during tooth formation and mineralisation.

Symbol / Abbreviation	Definition	Description
NF-κB1	Nuclear Factor Kappa-light-chain-enhancer of activated B cells	Protein found in almost all animal cell types – involved in cellular responses to stimuli including stress and cytokines. Controls transcription of DNA, cytokine production and cell survival.
NO	Nitric Oxide	Intercellular signalling compound, expressed by osteocytes in response to mechanical stimulus.
OCN	Osteocalcin	Secreted by mineralising osteoblasts. Bonds with hydroxyapatite and binds to collagen via the matrix protein osteopontin (OPN).
OMD	Osteomodulin / osteoadherin	Protein expressed in mineralised tissues, involved in binding ECM to hydroxyapatite.
ON	Osteonectin	Also known as SPARC. Glycoprotein that plays a key role in mineralisation: binds strongly to Type 1 Collagen and hydroxyapatite.
OPG	Osteoprotegerin	Down-regulates osteoclast activation by competitively binding with RANKL.
OPN	Osteopontin	Secreted by mineralising osteoblasts. Bonds with collagen matrix and hydroxyapatite via osteocalcin.
OSX	Osterix	Transcription factor that plays major role in regulating differentiation of MSCs to osteoblasts
$\hat{p}_-$	Maximum peak-negative pressure	
p38	p38 MAPK	A class of Mitogen-activated protein kinases (MAPK) responsive to stress stimuli such as cytokines and heat shock.
PGE2	Prostaglandin E2	Protein expressed by osteocytes and osteoblasts in response to mechanical stimulus. Thought to play a role in regulation of inflammation and osteogenic differentiation
PI	Propidium Iodide	Dye used to assess cell viability. The dye only stains nuclei of dead cells with compromised membranes.
PTH-R1	Parathyroid hormone-related protein R1	Hormone regulating endochondral bone development.

Symbol / Abbreviation	Definition	Description
prr	pulse repetition rate	Also known as pulse repetition frequency. Number of LIPUS pulses in 1 second (Hz)
pw	pulse width	Duration of a LIPUS pulse in seconds
RANKL	Receptor activator of nuclear factor κB (NFκB) Ligand	Binds to RANK receptors on osteoclast precursor cells, enhancing activation, survival and maturation. Secreted by osteoblasts, osteoclasts and regulated by macrophages.
R_{BN}	Beam non-uniformity ratio	Measure of non-uniformity of transducer beam. Equal to the maximum square-pressure divided by the average square-pressure across the beam.
ROS	Reactive oxygen species	Highly reactive chemicals such as peroxide, formed as a natural biproduct of aerobic metabolism. Play important roles in cell signalling and homeostasis. Can increase dramatically during environmental stress (such as heating)
RT	Rise Time	The time taken (in seconds) for a signal amplitude to increase from 10 % to 90 % of its 'steady-state' amplitude.
RT-PCR	Real Time	Real Time Polymerase Chain Reaction. DNA analysis method
RUNX2	Runt-related transcription factor 2	Key transcription factor required for osteogenic differentiation of MSCs. Also known as core-binding factor subunit alpha-1 (CBFα1).
SAFHS	Sonic Accelerated Fracture Healing System	LIPUS device by Smith & Nephew / Bioventus (US). More recently called the Exogen device. Also sometimes refers to specialist direct coupling in vitro exposure system typically consisting of 6 SAFHS transducers in array designed to directly couple to the base of each well of a standard 6-well culture plate.
SEM	Standard Error of the Mean	A statistical measure describing the extent to which a sample mean is likely to differ from the true population mean. Equal to the standard deviation (σ) divided by the square root of the number of samples (n).
SMAD	Amalgam of SMA ('small worm	Main transducers of signals (within a cell) from receptors of the TGF-β superfamily.

Symbol / Abbreviation	Definition	Description
	phenotype) and MAD genes	
SP7	see OSX	An alias of osterix
SPARC	Secreted protein, acid and rich in cysteine	Another name for osteonectin (see ON).
TGF-β#	Transforming growth factor	Group of signalling cytokines produced by white blood cells and macrophages. Play a role in activation of cellular pathways associated with differentiation and proliferation.
TSC-22	Transforming Growth Factor- beta stimulated clone-22	Early response gene associated with cell proliferation. Induced by TGF-β1.
VEGF	Vascular Endothelial Growth Factor	Growth factor promoting angiogenesis by migration and proliferation of endothelial cells.

CHAPTER 1
INTRODUCTION

Low intensity pulsed ultrasound (LIPUS) is a type of therapeutic ultrasound used in the treatment of fractured bone. It was first approved for clinical use in 1995 by the US United States Food and Drug Administration [1] after *in vivo* and clinical studies suggested that treatment with LIPUS accelerated fracture healing [2, 3]. It was subsequently approved for the treatment of non-union fractures (fractures that have not healed after 9 months) by the National Institute for Health and Care Excellence (NICE) in 2010 [4]. LIPUS is seen as a non-invasive, cheaper alternative to surgery, with an estimated cost saving of £2,407 per non-union fracture [4].

As well as fractures, LIPUS is used clinically for soft tissue wounds, ulcers and sports injuries [5]. It is also the subject of research for dental and maxillofacial bone healing [6, 7], improving the fusion of bone grafts to surrounding tissue [8], accelerating cell proliferation and mineralisation in artificial implants seeded with cells [9] and stimulating proliferation and differentiation of stem cells [10]. This thesis focusses on LIPUS as a treatment to accelerate healing of fractured bone.

Despite being available for clinical use for over 25 years, the mechanisms by which LIPUS promotes fracture healing are still not fully understood. This uncertainty, coupled with some independent clinical trials finding no healing effects [11], have led to recent questions over the efficacy and value of LIPUS treatment [12]. The lack of understanding of the mechanisms is partly due to the inherent complexity of the bone healing process and partly due to the difficulty in designing *in vitro* experiments to isolate those mechanisms while providing adequate control of the ultrasound exposure. Failure to control the ultrasound field and any secondary effects, such as reflections within the culture well, plate vibrations and thermal effects, can result in varying conditions unique to each apparatus. I hypothesised these effects have resulted in conflicting findings in the LIPUS literature, making it difficult to draw accurate conclusions regarding the healing mechanisms involved. This thesis contributes to the field by proposing a controlled exposure method to isolate the ultrasound exposure from secondary effects introduced by the apparatus, which might not occur to the same extent *in vivo*, such as reflections, plate vibrations and thermal

effects. The method was used to investigate cellular responses to direct LIPUS stimulus and compare the outcomes with findings in the literature, to assess if the exposure apparatus influenced results. 3D printed culture systems were also investigated for their potential to create a cell growth environment as a better model for physiological bone tissue, with the future aim of mimicking the thermal, reflection and fluid flow effects induced by the propagation of the LIPUS field through bone structure.

This chapter sets the scene by first examining the design and operation of commercial LIPUS systems (1.1). The bone healing process and clinical benefits attributed to LIPUS are described in 1.2. The main methods of *in vitro* LIPUS exposure used in the literature to date are reviewed in 1.3. Finally, 1.4 outlines the scope of this thesis and its contribution to LIPUS research.

1.1 LIPUS Systems

LIPUS systems typically consist of a drive unit and ultrasound transducer. The transducer is coupled to the skin in the vicinity of the fracture site via coupling gel. Treatment typically consists of several weeks of daily 20-minute exposures and some devices, for example the Exogen Bone Healing System (Bioventus, US), allow treatment to be carried out by the patient at home. Table 1.1 gives published details of transducers and manufacturers' data for a selection of commercial LIPUS devices designed specifically for fracture healing and used in studies in the LIPUS literature described in Chapter 2.

The manufacturers' data normally consists of parameters required by the IEC and British Standards for ultrasonic physiotherapy devices [13, 14], which are concerned primarily with device safety rather than dosage or clinical efficacy [15]. These parameters are described in more detail in Chapter 3, but briefly, they require that the device has an effective intensity, defined as the maximum rated output power in Watts divided by the effective radiating area (A_{ER}) in cm^2, of no more than 3 W/cm^2, and a beam non-uniformity ratio (R_{BN}), which is the ratio of the maximum mean-square pressure in the field divided by the mean-square pressure averaged over the effective radiating area, of no more than 8. These limits are designed to ensure the device does not induce any harmful thermal or mechanical effects in tissue, by limiting both the overall delivered energy and any local maxima. The effective intensity is equivalent to the spatial-average, temporal-average intensity (I_{SATA}), which is often used to define LIPUS fields in the literature.

Device	Transducer(s)	Ultrasound Parameters
Exogen (Bioventus, US) [16]	f = 1.5 MHz $\varnothing$ = 22 mm A_{ER} = 3.88 cm^2 R_{BN} < 4	I_{SATA} = 30 mW/cm^2 pw = 200 µs prr = 1 kHz DC = 0.2
Therasonic 1032 (EMS, UK) [17]	f = 1.1 MHz or 3 MHz. Large treatment head: A_{ER} = 4.4 / 3.9 cm^2 $R_{BN} \leq 6$ Small treatment head: A_{ER} = 0.7 / 0.6 cm^2 $R_{BN} \leq 5$	I_{SATA} = up to 2.54 W/cm^2 pw = 2 ms or CW prr = 166 Hz, 100 Hz, 50 Hz, CW DC = 0.33, 0.25, 0.1, CW
Primo Therasonic 360/460 (EMS, UK) [18]	f = 1.1 MHz or 3.4 MHz. Large treatment head: A_{ER} = 4 cm^2 R_{BN} < 5 Small treatment head: A_{ER} = 0.6 cm^2 R_{BN} < 5	I_{SATA} = up to 1.5 W/cm^2 pw = 2 ms or CW prr = 250 Hz, 167 Hz, 125 Hz, 100 Hz, 50 Hz, CW DC = 0.5, 0.33, 0.25, 0.2, 0.1, CW
Phys-assist (Orthosonics, UK) [19]	'Longwave' device, hemispherical treatment head f = 45 kHz A_{ER} = 12.8 cm^2 R_{BN} not specified	I_{SATA} = max 940 mW/cm^2 CW only
Sonopuls 492 (Enraf, NL) [20]	Large / small dual frequency heads f = 1 MHz / 3 MHz A_{ER} 5.0 / 0.8 cm^2 $R_{BN} \leq 6$	I_{SATP} = max 300 mW/cm^2 pw = 2 ms prr = 16 Hz, 48 Hz, 100 Hz, CW DC = 0.032, 0.096, 0.20, CW
Osteotron (Ito Co. Ltd, JP) [21]	Two probes: f = 1.5 MHz / 750 kHz $\varnothing$ = 32 mm $R_{BN} \leq 3.5 / \leq 3.0$ A_{ER} 3.9 cm^2 / 3.5 cm^2	I_{SATA} = 30, 45, 60 mW/cm^2 prr = 100 Hz, 1 kHz pw = 2.0 ms, 200 µs DC = 0.20

Table 1.1 Some LIPUS Devices with manufacturers' published data
f: frequency; $\varnothing$: transducer diameter; R_{BN}: Beam Non-uniformity Ratio; A_{ER}: Effective Radiating Area; I_{SATA}: spatial-average, temporal-average intensity; I_{SATP}: spatial-averaged, temporal-peak intensity; pw: pulse width; prr: pulse repetition rate; CW: continuous wave; DC: duty cycle, which is equal to pw $\times$ prr. Images of devices used with kind permission from manufacturers (details in references).

The standard also limits self-heating of the devices to $\leq 10\ °C$ when coupled via coupling gel to a tissue mimic in simulated clinical use (defined as the maximum power setting for 30 minutes, at ambient temperature 23 °C) and $\leq 27\ °C$ in air with no coupling gel.

Table 1.1 shows that the Exogen device has a fixed set of output parameters with a low intensity of 30 mW/cm^2. This is probably because the device is designed only for bone healing and for use by the patient at home, with fixed settings and exposure times to control dose. The other devices are intended for use by clinicians to treat a wide range of injuries including fractures, soft tissue wounds and sports injuries such as tendonitis. Manufacturers usually provide a number of combinations of frequency, pulse and amplitude settings and it is down to the clinician to choose the treatment regime.

Operating frequencies of LIPUS devices range from 0.75 MHz to 3 MHz. A handful of devices also operate at 45 kHz, such as the Phys-assist longwave system (Orthonics, UK). LIPUS at this lower frequency is thought to travel further into tissue due to the longer wavelength and lower tissue absorption. Wider beam widths at lower frequencies also mean the ultrasound is spread over a larger area [19]. Low frequency LIPUS studies in the literature are discussed in Chapter 2. Controlled methods for assessing 45 kHz LIPUS and comparing cellular responses to LIPUS with low and high frequencies are developed in Chapter 3, and a controlled comparison is conducted in the Frequency Study described in Chapters 4 and 5.

Comparing LIPUS effective radiating areas (A_{ER}), these range from 3.5 cm^2 to 5 cm^2 at frequencies of 0.75 to 1.5 MHz. 3 MHz devices have smaller A_{ER} of 0.6 cm^2 to 0.8 cm^2. Whereas the longwave device has A_{ER} 12.8 cm^2. Pulse widths are either 200 µs or 2 ms and pulse repetition rates range from 16 Hz up to 1 kHz. Many devices also offer a non-pulsed, continuous wave option.

Both *in vivo* and *in vitro* LIPUS studies have compared the effects of varying LIPUS field parameters on apparent healing effects. These are discussed in detail in Chapter 2. But before discussing the effects of LIPUS on fracture healing, it is first necessary to have some understanding of bone physiology, growth and healing after fracture: topics covered in the next section.

1.2 Bone Physiology, Growth and Healing

1.2.1 Bone Physiology

Far from being an inert support for the mammalian body, bone is a complex and living tissue that responds and adapts to its environment. As well as providing overall structure, support and mobility, bones store minerals and provide protection for organs. There are two types of bone tissue: cortical (or compact) and trabecular (also known as cancellous or spongy bone). Cortical bone is hard and dense and provides compressive strength. Trabecular bone is porous and resembles a fluid-soaked sponge. Its structure allows it to deform in response to impact loads. The configuration and concentrations of these materials differs depending on the type of bone and its function.

The bone type most prone to non-union fractures is the long bone. Figure 1.1 shows the basic long bone structure and locations of long bones in the human skeleton.
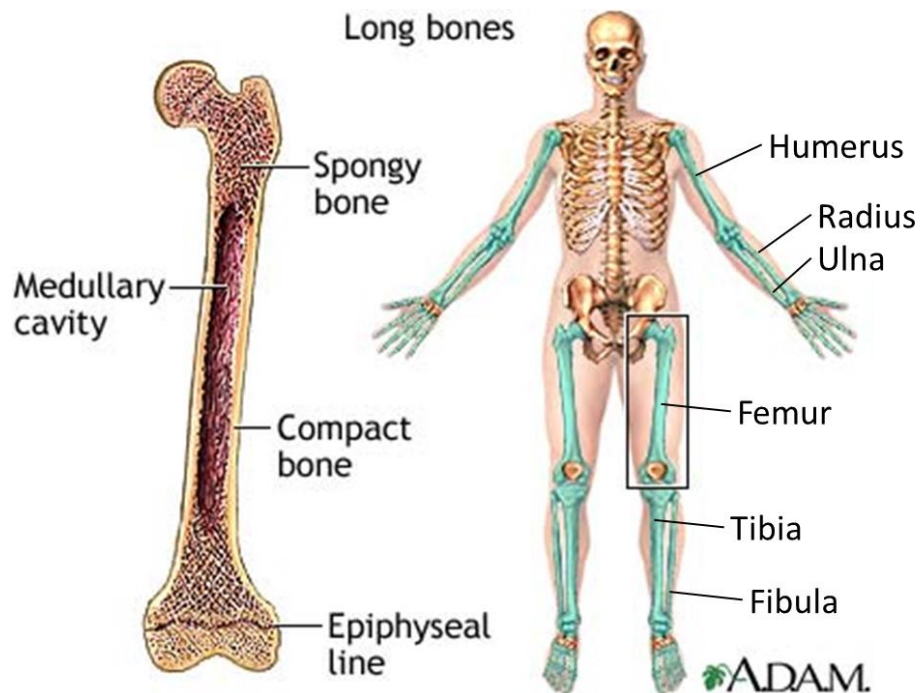
Figure 1.1: Long bones and their structure, from [22].
A long bone is a bone whose length is greater than its width. Left: the structure of a long bone, labelled with the main components. The central diaphysis consists of compact (cortical) bone wrapped around the medullary cavity, containing the bone marrow. The epiphyses on the ends are largely made up of trabecular or spongy bone and include the epiphyseal line, the main origin of primary bone growth in infants. Right: Skeleton with indication of largest long bones in the human body.

The long bone structure is made up of the long diaphysis in the centre with proximal and distal epiphyses at either end. The diaphysis consists almost entirely of cortical bone, wrapped around the central medullary cavity containing the bone marrow, with a thin layer of trabecular bone between. The epiphyses have larger cross-sectional areas consisting mainly of trabecular bone and a thin outer layer of cortical bone. The epiphyseal line is a plate of cartilage in the epiphyses, which is responsible for lengthening the bone during childhood.

Figure 1.2 shows the structure of the long bone in more detail. Figure 1.2A shows the overall long bone structure with bone marrow and blood vessels in the centre. Cortical (or compact) bone consists of a series of mineralised layers called lamellae, which wrap around the bone and form tube-like structures (osteons) around blood vessels travelling longitudinally via Haversian canals. Blood vessels also traverse laterally through the bone to the medullary cavity via Volkmann's canals (Figure 1.2B & C). Lining the outer surface of the cortical bone is the periosteum (Figure 1.2B), which has an outer fibrous membrane and an inner layer of lining cells from the osteoblast lineage - the main cells responsible for laying down mineralised bone [23].
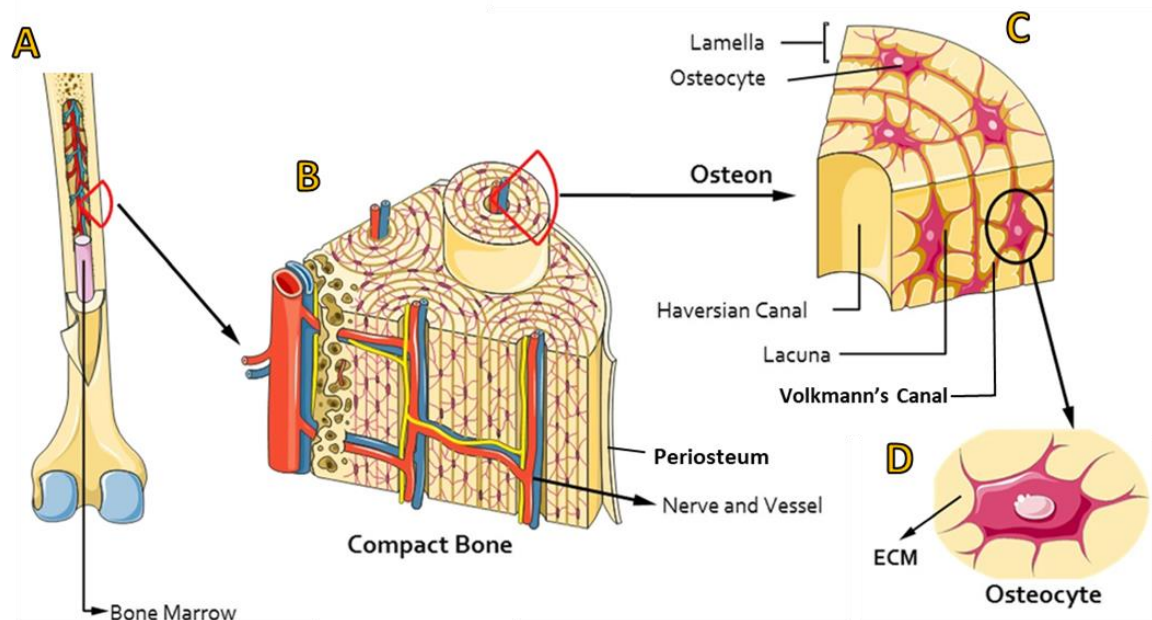
Figure 1.2: Bone tissue configuration in a long bone, from [24].
A: long bone structure. B: The compact bone of the diaphysis is made up of a series of mineralised layers called lamellae, which wrap around a central cavity containing blood vessels and extracellular fluids. C: The resulting tube-like structures are called osteons. The central canal is the Haversian canal, and Volkmann's canals penetrate laterally through the lamellae. D: The canals deliver nutrients to osteocytes, bone cells embedded in the mineralised extra-cellular matrix (ECM).

Within the lamellar structure are osteocytes (Figure 1.2C & D), the only living cells contained within mature mineralised cortical bone. The membranes of these cells form long dendritic processes that extend through tiny fluid-filled passages (canaliculae), which link to the bone marrow, the haversian and Volkmann's canals, lining cells and other osteocytes. Extra-cellular fluid flows through the canaliculae, carrying nutrients and removing waste products through constant low-level flow induced by blood flow and body movement [25].

1.2.2 Primary Bone Growth and Healing

The healing process in fractured bone depends on a number of factors including where the fracture has occurred, the degree of mobility and stability of the fracture site, the extent of damage and the gap size between bone fragments [26]. In fracture sites with good mechanical stability and small gaps, the bone can heal by directly laying down the lamellar or trabecular structure. This process, illustrated in Figure 1.3, is known as primary healing and is the same process involved in bone growth in the foetus and young children.
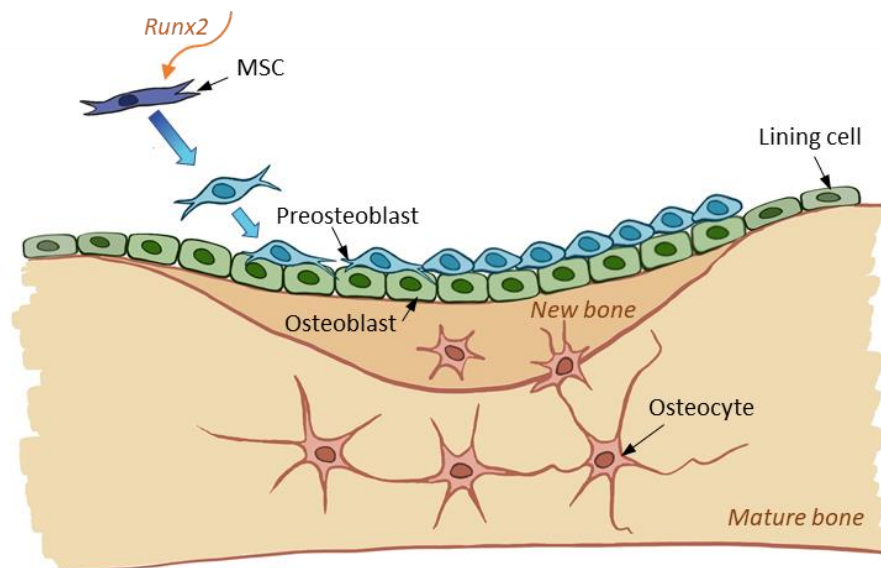
Figure 1.3: Primary bone healing schematic.
Mesenchymal stem cells differentiate into preosteoblasts in presence of osteogenic cytokines and transcription factors such as Runt-related transcription factor 2 (Runx2). Preosteoblasts adhere to the new bone surface and proliferate. Once confluent they mature into osteoblasts with cuboidal morphology and begin laying down mineralised matrix. Once fully mineralised, some become dormant lining cells, some osteocytes embedded in the mature bone and the remainder undergo programmed cell death (apoptosis). Based on various figures in the literature [27, 28].

Mesenchymal stem cells differentiate to the osteogenic lineage in the presence of various growth factors such as Runt-related transcription factor 2 (Runx2). Preosteoblasts migrate to the surface and proliferate. Once confluent they mature into osteoblasts with cuboidal morphology and lay down mineralised matrix. Some become flat, dormant lining cells and some become embedded in the new bone, where they differentiate into osteocytes. The remainder undergo programmed cell death (apoptosis).

1.2.3 Secondary Healing

In fractures with poor mechanical stability, secondary healing is more likely to occur. This form of healing is of foremost interest in LIPUS research because non-union fractures are more likely to heal by this process. Secondary healing is more complex than primary healing with many parallel processes but can be split into four main stages. Figure 1.4 summarises these stages at the tissue level and cellular level.

The first stage is inflammatory (Figure 1.4A), where fibroblasts and blood cells very quickly lay down a fibrous blood clot (hematoma) and release small signalling proteins called cytokines. The cytokines recruit mesenchymal stem cells and inflammatory cells, including macrophages and neutrophils, which debride damaged soft tissue [29]. Osteoclasts are also recruited to absorb damaged bone [26].

Macrophages regulate inflammation by secreting Interleukin-1 (IL-1). This cytokine up-regulates cyclooxygenase 1 and 2 (COX1 and COX2) - enzymes that synthesise pro-inflammatory prostaglandins. At some point, the macrophages switch from pro-inflammatory to anti-inflammatory phenotypes that promote tissue repair and angiogenesis (the making of new blood vessels) [26, 29]. Mesenchymal stem cells (MSCs) are recruited, mainly from the periosteum and bone marrow [29] and differentiate to chondrocytes. The chondrocytes lay down cartilage to form the soft callus, which provides some initial mechanical stability to the fracture site (Figure 1.4B).

Preosteoblasts migrate from the periosteum and are also recruited via osteogenic differentiation of MSCs. The preosteoblasts proliferate and infiltrate the soft callus, then differentiate to mature osteoblasts, which lay down the minerals to form the hard callus. Some chondrocytes also differentiate into osteoblasts and contribute to ossification [30].
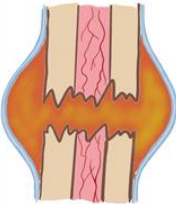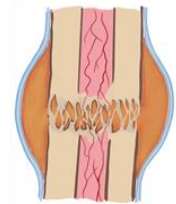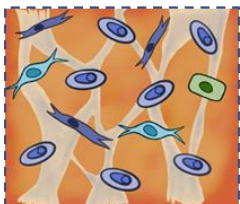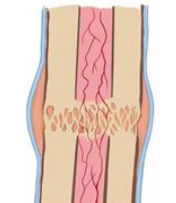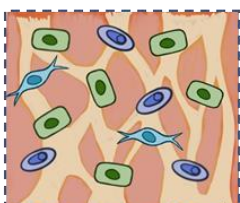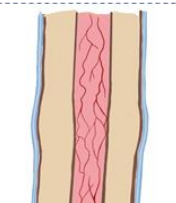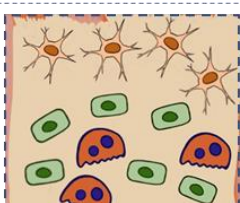
Figure 1.4: Secondary healing process after a long bone fracture.
Based on diagrams and timescales for human fracture healing from multiple sources [26, 29, 31]. A: 0 to 7 days post fracture, macrophages regulate inflammation and debride damaged tissue. Fibroblasts and platelets lay down a fibrous hematoma. Osteoclasts remove damaged bone. MSCs are recruited and differentiate to chondrocytes. B: 5 to 14 days post fracture, chondrocytes lay down cartilage to form soft callus. MSCs differentiate to preosteoblasts and proliferate. C: 12 to 21 days post fracture, preosteoblasts and some chondrocytes differentiate to mature osteoblasts and replace soft callus with hard mineralised callus. D: Osteoblasts lay down lamellar structure and osteoclasts remove surplus woven bone. Some osteoblasts mature into osteocytes embedded in the bone structure. This remodelling stage can take many months to complete.

The hard callus tissue is referred to as woven bone due to its random structure (Figure 1.4C). The final stage (Figure 1.4D) involves the reshaping and remodelling of woven bone into the final lamellar structure. Chondroclasts absorb cartilage and osteoclasts absorb the woven bone while osteoblasts lay the lamellar layers. The first three stages: inflammation, soft callus and hard callus, take place relatively quickly, within 3 to 6 weeks [32]. The remodelling stage is much longer, taking up to 2 years. In mice, which are often used as models for *in vivo* and *in vitro* studies, the process is quicker. The first three stages take around 2 to 3 weeks and the remodelling stage 3 to 5 weeks after initial fracture [32].

The mineralisation process involves osteoblasts first secreting collagen molecules and proteoglycans. The collagen polymerises to form collagen fibres [33] and the proteoglycans, also present in the extra-cellular fluid, regulate crystallisation of calcium salts. Osteoblasts also secrete alkaline phosphatase (ALP), an enzyme that enables crystallisation of calcium salts by breaking down pyrophosphate, which inhibits the crystallisation process throughout the rest of the body. Within a few days the calcium salts precipitate on the surfaces of the collagen fibres to form hydroxyapatite crystals. Mature cortical bone contains approximately 30 % organic collagen matrix and 70 % hydroxyapatite by weight [33], though newly formed bone may have a higher proportion of organic components. The high tensile strength of the Collagen fibres and high compressional strength of hydroxyapatite crystals combine to give bone its high mechanical strength. As an indication, human femoral cortical bone has a longitudinal tensile yield stress of 135 MPa, similar to that of cast iron, and compressive yield stress of 115 MPa, approaching that of granite [34].

Worthy of note is the increasing interest in the role of osteocytes in bone healing. Although it has long been accepted that osteocytes are the main mechanosensory cell in mature bone, they were not thought to play a significant part in bone healing. However, in recent years studies have indicated that osteocytes play an active role in bone homeostasis: regulating osteoblast and osteoclast functions in healthy tissue, and sending chemical signals to initiate the bone healing process after damage [25, 28].

1.2.4 Non-union Fractures and LIPUS Mechanisms

Non-union fractures most often occur when mechanical instability is too great to allow the bone to heal by either primary or secondary healing. Often surgical intervention is required to introduce more stability and allow the natural healing process to take place. Note that mechanical stability does not equal no movement: in fact healing is inhibited when the fracture site is fixed too rigidly [26]. Small axial movements of less than 1 mm are recommended for optimal secondary fracture healing [35]

Other known and suspected causes of non-unions are due to age and lifestyle-related conditions such as osteoporosis, smoking, obesity and diabetes. These conditions result in vascular defects that inhibit angiogenesis [29]; prolonged inflammation (where macrophages fail to switch from their pro-inflammatory to anti-inflammatory states [26]);

and failure to mineralise (i.e. to differentiate and proliferate adequate numbers of mature osteoblasts) [36, 37].

As previously mentioned, LIPUS improved healing rates of non-union fractures in clinical trials [3]. Past *in vitro* studies have suggested that LIPUS can improve chances of healing by promoting the factors inhibited in non-unions. In brief, LIPUS has been shown to:

- Promote angiogenesis (formation of new blood vessels) by up-regulating interleukin-8 (IL-8) and vascular endothelial growth factor (VEGF) in osteoblasts. These signalling proteins promote the recruitment and proliferation of endothelial cells that line blood vessels [38]. Restoration of blood supply to the wound promotes healing by allowing nutrients in the blood to reach the fracture site.

- Stimulate release of Prostaglandin E2 (PGE2) and Nitric oxide (NO) in osteocytes [39], osteoblasts [40] and preosteoblasts [41], which in turn promotes switching of macrophages to their anti-inflammatory state [42] and regulates differentiation of MSCs to the osteoblastic lineage [43].

- Enhances osteogenic differentiation of MSCs (by a number of factors including direct up-regulation of RUNX2 [44]); stimulates migration [45], proliferation [46] and differentiation and mineralisation of preosteoblasts and osteoblasts [47, 48].

Exactly how LIPUS stimulates the various cell types is still not known, but the mechanism under the most scrutiny is mechanotransduction, i.e., the ability of bone cells to respond to mechanical stimuli. Mechanical stresses and strains resulting from movement and exercise induce the bone to strengthen itself, through the healing of microfractures and strengthening of the bone structure. This complex process is still an area of active research, but it is well known that osteocytes and osteoblasts play a key role [25]. Figure 1.5 illustrates the mechanosensors and mechanotransduction pathways involved in osteogenesis, showing the complex interplay of the pathways and the processes that result.
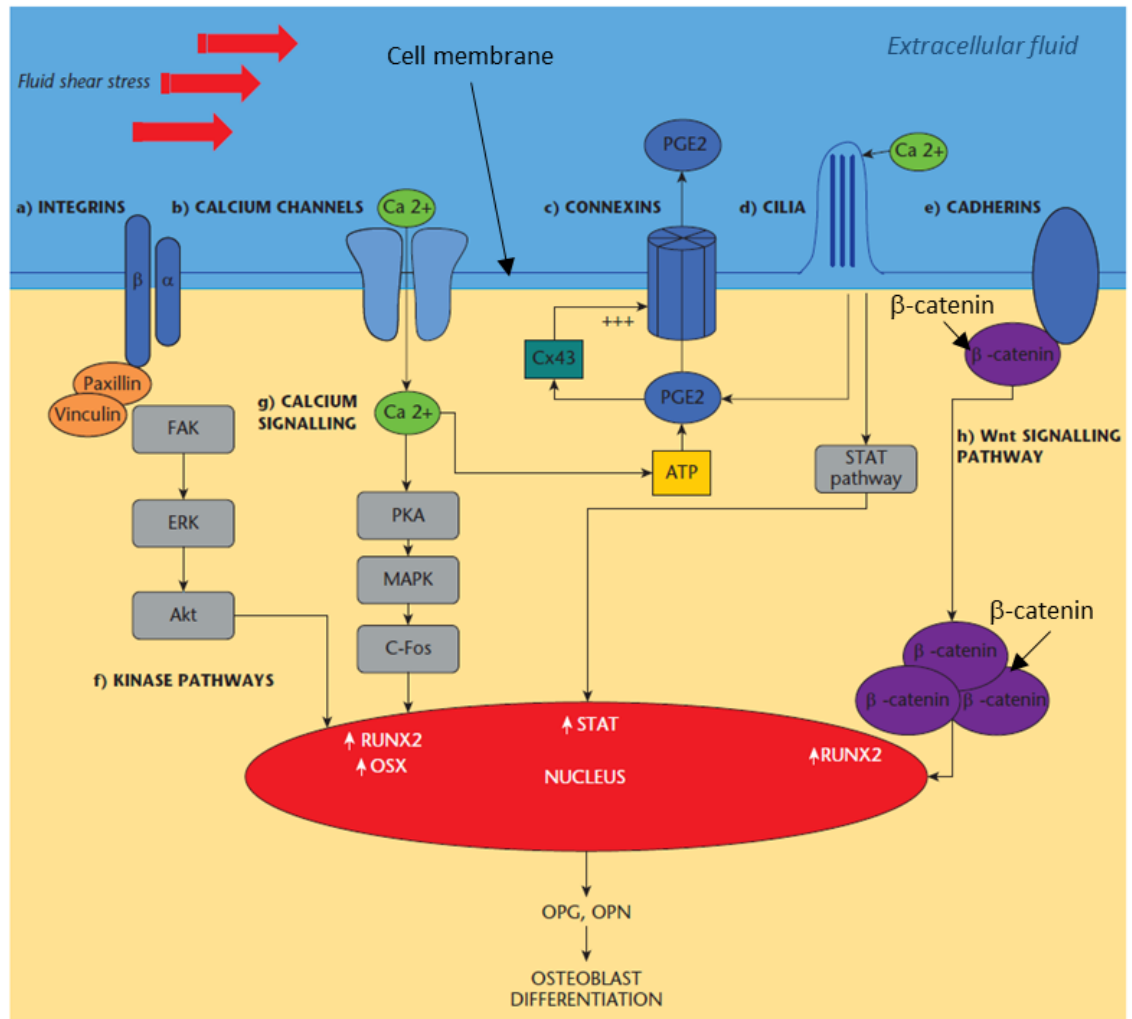
Figure 1.5: Mechanotransduction pathways involved in osteogenesis, from [49]. Movement induces stresses and strains in the extracellular fluid, which act on cell membrane mechanosensors. (a) Integrins adhere to the surrounding ECM and react to fluid shear stress by up-regulating osteogenic factors runx2 and osx via (f) kinase pathways; (b) calcium ion channels stimulate flow of calcium in and out of the cell and up-regulate runx2 and osx via (g) the calcium signalling pathway; (c) connexins release PGE2 and are up-regulated by PGE2 via Cx43; (d) calcium influx to cilia up-regulate the STAT pathway and PGE2 release; (e) cadherins disassociate with β-catenin, which in turn up-regulates runx2 via (h) the Wnt signalling pathway.

The major cellular mechanotransduction components thought to respond to LIPUS are integrins and ion channels [25]. Integrins bind to the surrounding extracellular matrix (ECM) and respond to mechanical stresses induced by body movements or via interstitial fluid flow. Ion channels respond to strain and can also respond to voltage changes and shear forces from fluid flow. Of particular interest when studying bone are the calcium ion channels in osteoblasts and osteocytes, which trigger release of calcium stored in the cell [28]. These mechanotransduction pathways are discussed further in Chapter 2.

A study by Tang et al. [41] linked LIPUS stimulus to a mechanotransduction pathway in MC3T3-E1 preosteoblasts and the up-regulation of Cyclo-oxygenase 2 (COX-2) and Prostaglandin-E2 (PGE2). This same mechanotransduction pathway has been shown to be triggered in osteoblasts by fluid shear stress [50]. Tang's work is cited on the website of the Exogen Bone Healing System (Bioventus, US) as evidence that the mechanism of LIPUS stimulus is mechanotransduction. The study employs a systematic approach to confirming the pathway by disabling individual components and confirming a reduction in downstream markers. However, upon examination of the physical acoustics of the exposure setup, there appears to be very little control over the ultrasonic field applied to the cells. The LIPUS transducer was simply dipped in the petri dish in which the cells were growing, on the benchtop. There is no reported assessment of the acoustic field *in situ*: only the manufacturer's data was quoted. And there is no reported assessment of temperature during exposure, therefore no assessment or discussion of potential heating arising from driving the transducer in air or from standing wave effects in the petri dish.

The need for controlled exposure conditions *in vitro* was also highlighted by ter Haar et al. in their guidelines for reporting exposure conditions when assessing bioeffects of ultrasound [51]. They recommended that any study attempting to correlate biological effects with exposure to ultrasound must ideally measure or predict the ultrasound fields *in situ*, and that the maxima and spatial distribution of pressure and intensity be reported. Thermal effects must also be considered even if not thought to be a possible mechanism, as heat can be produced not only by the direct ultrasound stimulus but also by self-heating of the transducer, reflections and standing waves in the apparatus and by vibration of solid structures in the path of the ultrasound beam.

Even small thermal changes can affect cellular responses. A study of bone marrow stromal cells and osteoblast-like MG63 cells found that a temperature of 39 °C, only 2 °C above incubator and body temperature, induced proliferation and mineralisation [52]. Early studies of diathermy (the deliberate heating of tissue to promote healing) found that temperature differences of 1.5 to 3 °C promoted the growth of femur and tibia in rats and dogs [53, 54].

The *in vitro* exposure conditions of LIPUS studies in the literature show that experimental apparatus for exposures vary greatly in their level of definition and control of the LIPUS

fields applied to cell layers. This makes comparison between studies difficult, leads to conflicting results (as discussed in more detail in Chapter 2) and is a major hindrance in deducing the most likely mechanisms involved in LIPUS stimulation of fracture healing. The next section assesses the most common exposure methods adopted by previous LIPUS *in vitro* studies to find the most controlled and repeatable methods.

1.3 Common *in vitro* LIPUS Exposure Methods

This section reviews the main methods and apparatus of *in vitro* LIPUS exposures used in past studies in the literature. All the *in vitro* LIPUS studies considered are summarised in Appendix A. Each method is illustrated and given a descriptive name for ease of reference throughout this thesis. The extent of control of the acoustic field is assessed along with the potential to induce secondary effects. The most controlled method is then chosen as the exposure method for the *in vitro* studies described in this thesis.

1.3.1 Benchtop Dip Method

The simplest LIPUS exposure method is the benchtop dip method (Figure 1.6) used by Tang et al. in their mechanotransduction pathway study already described [41]. Two other studies were found to use this method: Whitney et al. [55] investigated integrin-mediated mechanotransduction pathways of chondrocytes, while Suzuki et al. [56] assessed LIPUS effects on osteoblast mineralisation. In the benchtop dip method, the transducer is dipped directly into a standard culture well on the benchtop.
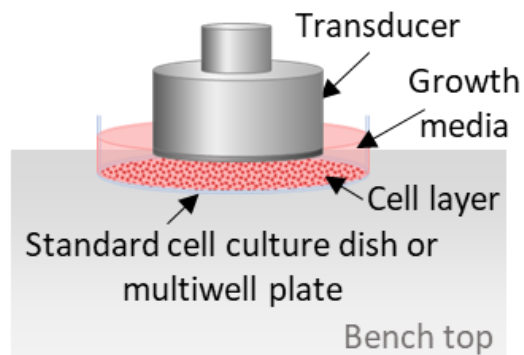
Figure 1.6 Benchtop dip method.
The LIPUS transducer is dipped directly into the growth media of a standard culture dish or multiwell plate on the bench top.

The benchtop dip method is likely to induce multiple reflections in the culture dish. When sound energy travelling through one material meets the boundary of a new material, a proportion of the sound is reflected. The ratio of the reflected intensity (I_r) to the incident intensity (I_i), known as the reflection coefficient, R (Figure 1.7).

$$I_r = R \times I_i$$
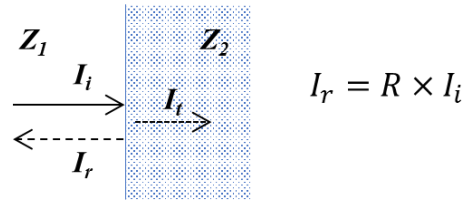
Figure 1.7: Reflection of sound at a boundary of two materials
Z_1 and Z_2 = specific acoustic impedances of materials 1 and 2; I_i = Intensity of incident field; I_t = intensity of field transmitted through new material; I_r = intensity of reflected field; R = reflection coefficient.

The proportion of sound reflected is dependent on the specific acoustic impedance of the materials, defined as:

$$Z = \rho c \tag{1.1}$$

Where Z is the specific acoustic impedance in kg/m^2/s (or Rayls), ρ is the density of the medium in kg/m^3 and c the speed of sound in m/s. For illustration, the simple case of a plane wave at normal incidence to a boundary between two materials, where the material thickness is much greater than one wavelength, the reflection coefficient is [57]:

$$R = \left(\frac{Z_2 - Z_1}{Z_2 + Z_1}\right)^2 \tag{1.2}$$

Table 1.2: summarises the approximate reflection coefficients predicted for the material boundaries in the benchtop dip method, calculated via equation 1.2. The first boundary is media to polystyrene (PS) at the base of the well. With an R of 0.054, the majority of the sound passes through. It will then meet a PS to air boundary, as there will be a small layer of air between the petri dish base and the benchtop. This boundary has a reflection coefficient of 0.999, meaning almost 100% of the incident intensity will be reflected back. The reflected sound will travel back and meet either a media-air boundary (R = 0.999) or a media-transducer boundary.

Boundary	Z_1 (kg/m^2/s)	Z_2 (kg/m^2/s)	R
Growth media / PS	1.5 x 10^6 [57]	2.4 x 10^6 [58]	0.054
PS / air	2.4 x 10^6	415 [57]	0.999
Growth media / air	1.5 x 10^6	415	0.999
Growth media / PZT4	1.5 x 10^6	35 x 10^6 [59]	0.842

Table 1.2: Approximate reflection coefficients of boundaries in the benchtop dip method. Specific Acoustic Impedances are from the literature [57, 60]. PS = Polystyrene; PZT4 = lead zirconate titanate type 4, a 'hard' piezoelectric material used as the active elements of an ultrasound transducer. Growth media is assumed to have the same impedance as water.

The active element of the transducer is likely to be a piezoelectric material: here lead zirconate titanate type 4 (PZT4) is assumed. At this boundary 84.2% of the incident intensity will be reflected back to the cells. Note the actual reflection coefficient is likely to be lower as many transducers have a layer on top of the active element with an impedance closer to that of water to minimise internal reflections. Even with a matching layer, a significant proportion of the energy will be reflected back into the dish, leading to multiple reflections that will interfere with the direct field.

If the distance between transducer and well base is a multiple of a half -wavelength, $\lambda/2$, a standing wave pattern might be induced which has the potential of exposing cells to a static pressure. The build-up of reflected energy within the well could lead to heating of the cells and growth media, and the cells on the base are likely to experience higher pressures and possible heating due to increased energy deposition at the boundary. The possible presence of these local pressure and temperature effects are the reason ter Haar et al. [51] recommended *in situ* measurement or prediction of temperature and pressure fields in ultrasound *in vitro* exposure methods.

While conditions within the well might be replicated by careful and repeatable positioning of the transducer and culture dish, the method is difficult to repeat without using precisely the same transducer, dish size, media depth and transducer front face depth and angle. This makes the method prone to variation when replicated in other laboratories.

Examining the level of control or measurement of *in situ* LIPUS fields in previous *in vitro* LIPUS exposure studies employing the bench top dip method, Tang et al. [41] did not

describe any control measures. Suzuki et al. [56] limited the separation between the LIPUS transducer front face and well bottom between 3 mm and 4 mm, but this equates to a difference equal to one wavelength of ultrasound at the frequency tested (1.5 MHz), meaning differences in pressure fields within the well likely due varying interference of reflected and incident waves. Whitney et al [55] adopted a modelling approach and set the separation between transducer and well base to 6 mm. No mention was made of how the distance was controlled. No trials reported *in situ* temperature so there is no way of knowing if cellular responses were influenced by thermal effects.

1.3.2   Direct Coupling Method

The direct coupling method is another benchtop method involving direct coupling of the transducer or transducers to the base of a standard culture well, usually via a coupling layer of ultrasound gel or water (Figure 1.8). This is a very common method, used by half of all the LIPUS *in vitro* studies summarised in Appendix A. Its popularity is partly due to the LIPUS device manufacturer, Bioventus, designing a customised system allowing the direct coupling and simultaneous driving of six Exogen LIPUS transducers to the base of a 6-well culture plate.
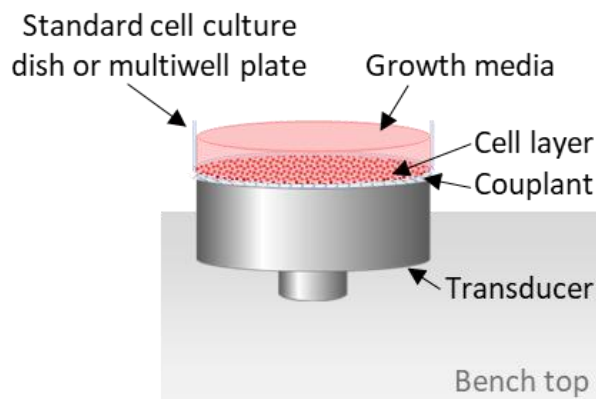
Figure 1.8 Direct coupling method.
A culture vessel sits on top of the transducer with a coupling layer, such as ultrasound gel, between the base and the transducer front face.

This method is prone to thermal effects, especially when the transducer front face is directly coupled just below the cell layer. A study by Leskinen and Hynynen [58] measured temperature rises up to 2.7 °C at the base of a standard culture plate after 20 minutes LIPUS exposure with the transducer coupled directly to the base via ultrasound

gel. When the gel was replaced with a similar thickness of water path, with the transducer immersed in a tank of water, the measured temperature rise was only 0.3 °C. They concluded the smaller increase was due to the more efficient heat transfer of the water compared to the gel in air. A study by Miyasaki et al. [61] compared LIPUS stimulation of primary mouse calvarial osteoblasts with direct heat shock stimulation, via the direct coupling method. LIPUS treatment was 15 minutes at the frequency 3 MHz and I_{SATA} 30 mW/cm^2. Heat shock treatment was delivered by placing the samples in an incubator at 42 °C for 20 minutes. They found both treatments promoted the expression of heat shock proteins (HSPs) as compared to untreated controls, along with increased mineralisation in both sample sets. HSP promotes osteogenic differentiation of mesenchymal stem cells through the Extracellular signal-related kinase (ERK) signalling pathway: one of the pathways upon which LIPUS is thought to act [62]. The paper assumed LIPUS stimulus was purely mechanical in nature and no temperature measurements were reported, but it is a strong possibility that the samples were responding to heat induced by the apparatus rather than direct LIPUS stimulus alone.

This method is also more prone to reflection effects and standing waves than the benchtop dip method because the highly reflective growth media-to-air interface is no longer broken up by the less reflective transducer front face. A number of studies, e.g., Unsworth et al. [47] and Fung [39], attempted to reduce the effect of standing waves in a culture well with media-air interface by ensuring the depth of culture media is not a multiple of a half wavelength at the LIPUS frequency. Both studies assumed that the speed of sound in the media was 1500 m/s, making one wavelength at 1.5 MHz approximately 1 mm. Both trials then set the depth of their media to just over 2 mm (2.078 in Unsworth and 2.1 mm in Fung) to avoid standing waves. In fact, the speed of sound in water varies with temperature, and at 37 °C, the temperature at which most *in vitro* studies are conducted, the speed of sound is 1524 m/s (via Lubbers and Graaf's equation [63]). Additional proteins and nutrients in the growth media are likely to increase density and therefore the speed of sound. A more appropriate speed might therefore be the speed of sound in blood, which is approximately 1575 m/s [64]. At this sound speed, one wavelength in media could be as much as 1.05 mm, which means the depth of media in Unsworth and Fung et al.'s papers could coincide with two wavelengths and induce the very standing waves they were attempting to avoid. Thus, the potentially healing cellular responses reported by the studies (enhanced mineralisation of preosteoblasts in the case of Unsworth et al. [47] and up-

regulation of mechanotransduction markers in osteocytes in Fung et al. [39]) may have been due to stimulation by reflections or standing wave fields introduced by the apparatus and changing the pressure and intensity amplitudes experienced by the cells, rather than the direct LIPUS stimulus. Again, the unknown conditions make it difficult to replicate the results of the study.

It should be noted that some *in vitro* effects are valid depending on the end goal of the study. For example, LIPUS is used in stem cell research to increase proliferation [65] and differentiation towards the osteogenic phenotype [66], where the direct coupling technique is the most common and produces repeatable results, regardless of the physical mechanism inducing the response. The issue here is the inference that cellular responses observed in the *in vitro* laboratory conditions will also occur *in vivo*.

1.3.3 Tank Dip Method and Inverted Tank Dip Method

The tank dip method (Figure 1.9A), like the benchtop dip method, involves the transducer being dipped into the media of the culture dish, except that here the dish or multiwell plate is part-immersed in a heated water tank. The inverted tank dip method (Figure 1.9B) is a variant, which is less controlled due to the large reflective area of the media-air interface at the media surface in the culture plate, as already discussed in the previous section.
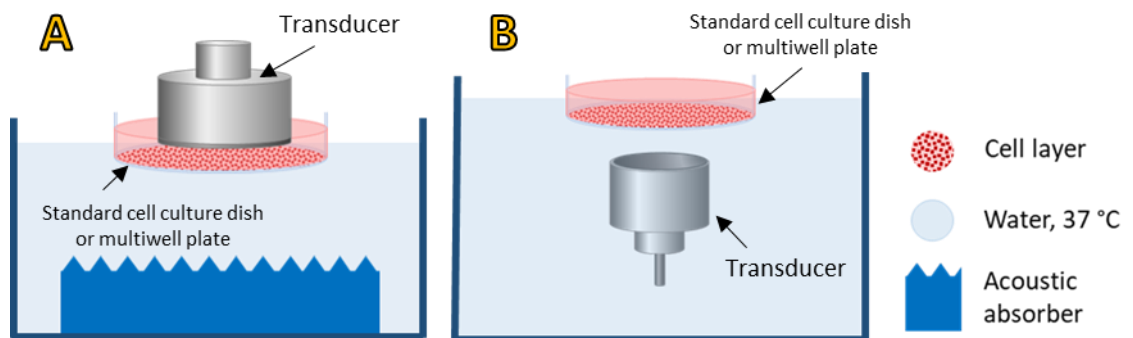
Figure 1.9: A: Tank dip method and B: inverted tank dip method.
The culture dish sits in a water bath, usually held at 37 °C. A: The transducer is immersed in the well and an acoustic absorber in the tank controls reflections. B: The transducer is immersed and facing up towards the base of the culture well, with water path between.

These setups offer some improvements over the benchtop dip method in terms of reflections off the base and walls of the culture dish, as the acoustic impedance of polystyrene is closer to water, with a reflection coefficient R of approximately 0.05. A study by Secomski et al. [67] provided a detailed evaluation of the tank dip method and

concluded it had minimal effect on the ultrasound field. However, Secomski assumed the reflections off the plate base were insignificant due to the low reflection coefficient calculated via Equation (1.2). Leskinen and Hynynen [58] measured the reflection coefficient of a standard Greiner plate using two transducers driven with a broadband pulser-receiver to cover the frequency range 0.65 MHz to 10 MHz and found it was frequency-dependent: following that predicted by Brekhovskikh in 1960 [68] for a thin plate with the same media on both sides, (Figure 1.10 and Equation 1.3).
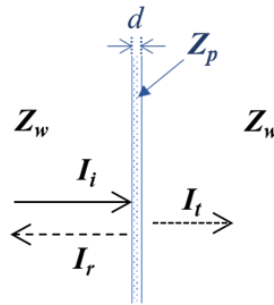
Figure 1.10: Propagation of Sound through a thin plate
Figure shows example of a thin plate of thickness d and acoustic impedance Z_p surrounded with water (Z_w). I_i, I_t and I_r are as defined in Figure 1.7.

$$R = \frac{Z_p^2 - Z_w^2}{Z_w^2 + Z_p^2 + 2j \cot(\alpha_p d)} \qquad (1.3)$$

Where Z_p and Z_w are the specific acoustic impedance of the plate material and water, j the imaginary unit, α_p the wave number in the plate at the frequency of interest (ω/c_p, where c_p is the speed of sound in the plate material) and d the plate thickness. This results in a frequency-dependent reflection coefficient ranging from almost zero up to 0.44, with minima and maxima spaced approximately 940 kHz apart. Figure 1.11 shows the reflection coefficients predicted via Equation 1.3 for three plate thicknesses, including the particular case of $d = 1.22$ mm determined by Leskinen and Hynynen [58].
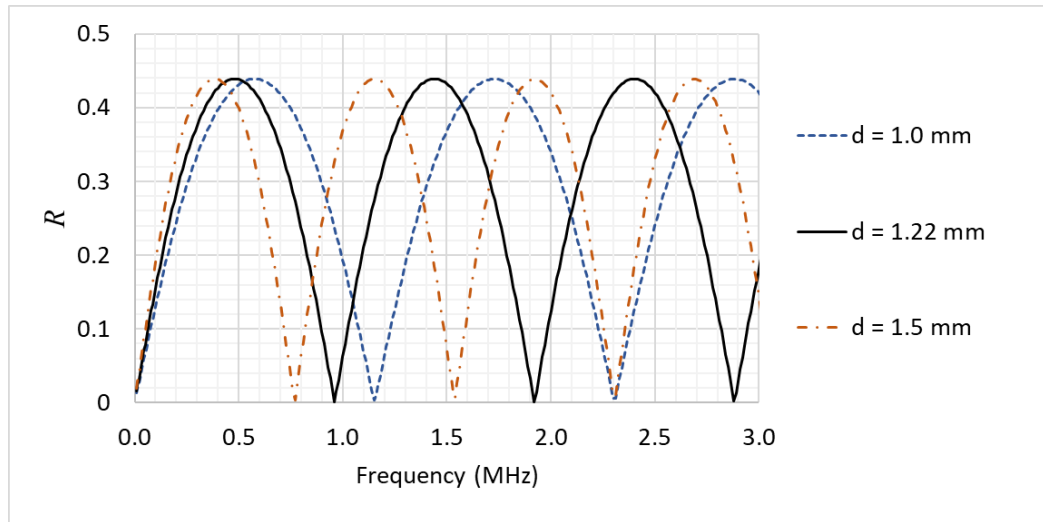
*Figure 1.11: Calculated reflection coefficient (R) of well plate base
via the Brekhovskikh equation (1.3) with speed of sound (c_p) and specific acoustic
impedance (Z_p) of the culture plate material taken from Leskinen & Hynynen [58]: i.e.,
c_p = 2305 m/s, Z_p = 2.4 kg.$m^{-2}s^{-1}$, Z_w = 1.5 kg.$m^{-2}s^{-1}$. The reflection coefficients are plotted
against frequency for plate thicknesses (d) of 1.22 mm (as in [58]), 1.0 mm and 1.5 mm. ,
to illustrate the potential significant effects of plate thickness tolerance on reflection
characteristics across the LIPUS frequency range.*

The points at which R drops to zero correspond to the plate thickness resonances. The
resonance at 940 kHz corresponds to the first mode, where the half-wavelength in the plate
is equal to the plate thickness of 1.22 mm. This dip in reflection coefficient was confirmed
by Leskinen and Hynynen by direct measurement. This plate mode introduces direct
mechanical vibration effects but could also induce heating of the plate and therefore the
cell layer. Figure 1.11 also illustrates that plate modes could occur at typical LIPUS
frequencies, depending on the plate thickness: e.g. plate thickness 1.5mm corresponds with
a plate thickness mode at just above 1.5 MHz. These plate modes, and the varying
reflection coefficient with frequency, are likely to affect cellular responses by varying
direct vibration, heating and ultrasound intensities that cells experience. These effects
could contribute to the variation in results between studies because they are peculiar to the
exposure apparatus.

The same study used non-invasive laser doppler vibrometer measurements and Schlieren
imaging (an acousto-optic technique using laser light to map changes in refraction caused
by a sound pressure wave) to image the base of the well plate during sonication. The
results indicated shear waves and Lamb waves were generated in the plate (Figure 1.12). It
was noted that these vibrations were likely to propagate to surrounding wells in a multiwell
plate. Such vibrations could also induce local heating effects.
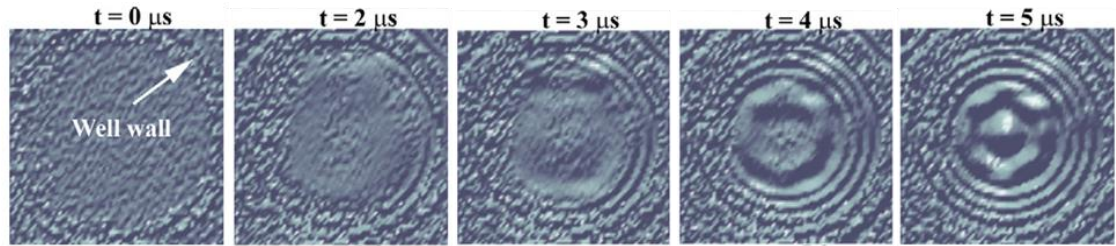
Figure 1.12: Laser Doppler Vibrometer scans of well base during ultrasonic stimulus. adapted from [58]. Frequency was 1.035 MHz and the transducer was immersed in a water tank with the front face positioned 7 mm below the culture well. The images clearly show the plate vibrations induced by LIPUS exposure.

Leskinen and Hynynen's investigation of plate modes and thermal effects arose from a previous study where they employed the inverted tank method to expose MG63 osteoblast-like cells to LIPUS [69] and found the WNT / β-catenin signalling pathway (a pathway associated with cell proliferation and migration, and partly activated by PGE2) was stimulated by both ultrasound and direct heating. They concluded the stimulation of the pathway could have been due to the direct plate vibrations and heating induced by the exposure apparatus.

Another study employing the inverted tank dip method, by Zhang et al. [70], reported the temperature of the growth media increased from 37 °C to 40 °C during a 30-minute LIPUS exposure. A significant up-regulation of heat shock proteins (HSPs) were observed in the exposed stem cells (as mentioned previously, HSPs are upregulated in MSCs and osteoblasts in response to heat stress, and can promote osteogenic differentiation [62]).

It can be concluded, from the above two studies, that the inverted tank dip method is prone to significant secondary effects of plate vibrations and heating, induced by the ultrasound exposure apparatus and should not be used for controlled *in vitro* LIPUS exposures. The tank dip method is likely to be less prone to these secondary effects, but will likely induce similar plate vibrations and reflection effects and for that reason the tank dip methods were not chosen as the method for this study.

1.3.4 Absorption Tube Method

The absorption tube method (Figure 1.13) is a more controlled form of the inverted tank dip method. The transducer is positioned in a water tank underneath the culture well so the ultrasound is directed up through the cell layer.
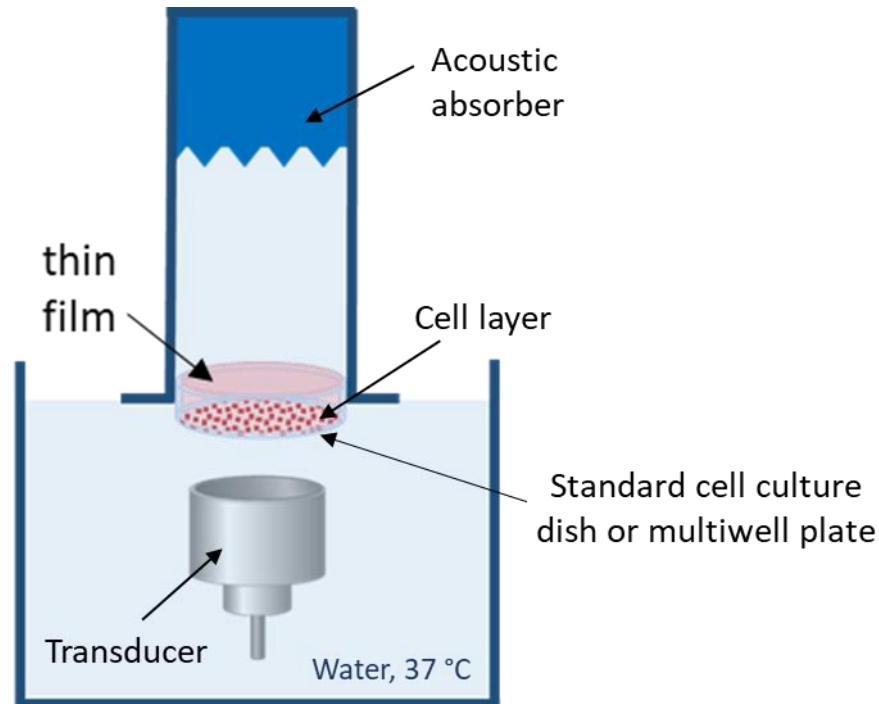
Figure 1.13: Absorption tube method.
The transducer is positioned in a water tank with front face directed towards the base of the culture dish and an absorption tube, consisting of either acoustic absorber only or a water-filled tube coupled to the media via a thin film, with acoustic absorber at the top of the tube. In each case the acoustic absorber absorbs the direct sound and minimises reflections.

To reduce reflections from the media-air boundary a water-filled absorption tube is positioned above with a thin membrane (film) coupled to the media in the culture dish. An acoustic absorber at the top end of the tube absorbs the remaining sound energy. Other forms of this method use only an absorber and do not use the water-filled tube. The absorber reduces the standing wave effects of the media-air interface, but will still be subject to plate resonances and vibrations. With the transducer immersed in the water, heating effects should be reduced to a minimum. This was demonstrated by Leskinen and Hynynen [58], who measured a rise of only 0.7 °C in an absorption tube setup compared to 2.7 °C when the transducer was coupled via ultrasound gel only.

Four *in vitro* studies out of the forty-two summarised in Appendix A used this method, with varying degrees of controls. It has the advantage of still allowing the use of standard culture ware. The most controlled example was a study by Bandow et al. [71], who also made *in situ* measurements of the LIPUS field and verified reflections were not present. This study exposed MC3T3-E1 murine preosteoblasts to 1.5 MHz LIPUS (200 µs, 1 kHz, 30 mW/cm^2 I_{SATA}) and found no effect on mineralisation markers, contrary to many other

studies using the direct coupling method. This supports the theory, already proposed in 1.3.2, that cells are exposed to heat in the direct coupling method, which would result in an up-regulation of HSP, which is known to promote proliferation and differentiation [62]. In the absence of heating in Bandow's method, no effect was observed.

1.3.5 Custom Tank Method

The custom tank method (Figure 1.14) is the final method considered in this review. A custom sample holder (or in one case, a culture flask) containing the cells under test and filled with growth media is immersed in a water tank in the beam of the LIPUS transducer. Any self-heating of the transducer is dissipated in the surrounding water. The custom sample holder is designed to minimise the effect on the acoustic field, though any effects should still be quantified.
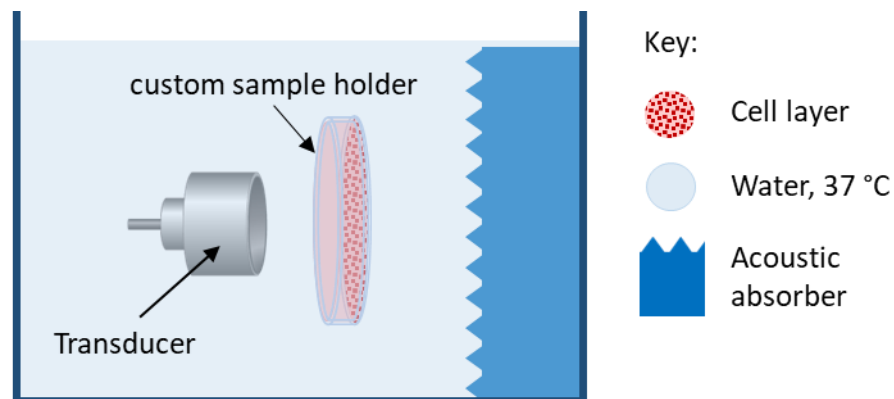
Figure 1.14: Custom tank method
A custom sample holder (or a filled culture flask) containing the cells is immersed in a water tank at a controlled separation from the LIPUS transducer. An acoustic absorber behind the sample holder minimises reflections within the tank.

Only two of the LIPUS studies summarised in Appendix A used the custom tank method. The first was also one of the earliest *in vitro* studies, run by Webster et al. in 1978 [72]. Fibroblasts were held in suspension between two 130 µm-thick Melinex windows (Melinex is a form of Biaxial oriented polyester, or BoPET, film). The LIPUS field (3 MHz, 2 ms, 100 Hz, temporal peak intensity 500 mW/cm^2) induced cavitation in the sample and resulted in membrane changes and increased protein synthesis. In the second, the MG63 osteoblast-like cell line was exposed to 3 MHz continuous wave ultrasound at I_{SATA} 140 mW/cm^2 to 990 mW/cm^2. This study found reduced expression of mineralisation

markers post-exposure, again contrary to the findings of those studies employing the direct coupling method.

As demonstrated by its use in the 1978 study, the custom tank method is not new. But it is not a common exposure method in LIPUS studies. This is likely because *in vitro* methods and protocols are normally designed for standard culture ware, with multiple treatments of small samples to produce a large number of replicates to overcome the inherently variable biological cell responses. The method also requires a tank large enough to accommodate the transducer, sample holder, absorber and mounting apparatus, which ideally should all fit into the limited space of a Biological Safety Cabinet (BSC) to reduce the risk of contamination. Despite its complexity, this method offers the maximum control over the LIPUS field and, if carefully designed, removes the issues of plate vibrations and unwanted thermal effects. This exposure method was therefore chosen for the studies described in this thesis.

As already mentioned, reflections, vibrations and thermal effects are likely to be present to some degree *in vivo*. Although the custom tank exposure method was adopted with the aim of establishing a method for exposure of cells to repeatable, controlled LIPUS fields, The exposure experienced *in vivo* would be influenced by the structure of the bone and soft tissues surrounding the cells. For this reason, exposure methods involving 3D cell growth environments were also investigated.

1.3.6   3D *in vitro* Exposure Methods

A number of 3D methods were found while reviewing past *in vitro* LIPUS trials, involving cells grown in hydrogels and 3D-printed matrices. These methods have the advantage of providing a growth environment for the cells more like that of *in vivo* conditions. Cell growth and behaviour changes in response to the surrounding environment and the ultrasound field is changed *in vivo* by scattering, absorption and reflection effects in tissue and bone. The 3D structure of bone is also thought to enhance fluid flow, a significant stimulus for mechanotransduction of bone cells (discussed in more detail in 2.3.2). Recent advances in 3D printing allow the printing of materials that are able to sustain cell growth into many possible shapes, making it more and more possible to produce mimics of complex *in vivo* environments. This thesis includes an investigation of the feasibility of growing bone cells in 3D-printed growth environments, to assess their potential to mimic

the structure of bone tissue *in vivo*. These methods could then be used as tissue mimics to investigate cellular responses to LIPUS in a controlled environment designed to produce secondary effects of a similar magnitude to bone tissue.

1.4 Chapter Summary and Thesis Outline

This chapter introduced the concept and applications of Low Intensity Pulse Ultrasound for bone healing. LIPUS has been available for clinical use to treat non-union fractures for over 25 years after promising results in early *in vivo* and clinical trials. But the mechanisms by which it promotes healing are still not fully understood due to the inherent complexity of the bone healing process and the difficulty in designing *in vitro* experiments to isolate the mechanisms while providing adequate control of LIPUS exposure.

Section 1.1 presented a number of commercial LIPUS systems and examined typical operating frequencies, intensities and pulse settings from available manufacturers' data. These tended to be limited to those required by International and British Standards for physiotherapy devices, which are mainly concerned with safety rather than dosage or efficacy. Section 1.2 described bone physiology, focussing on long bones, which are the most likely bone shape to suffer from non-union fractures. In simple terms, bone healing can occur by two possible processes: either primary bone growth, where the bone is laid down systematically in a manner that builds the structure as it goes, and secondary healing, which is more likely in non-unions and involves formation of a soft callus to provide some stability, which mineralises to form woven bone that is remodelled over a period of up to 2 years into the long bone structure with its circular osteons, lamellar layers and canalicular system. The clinical causes of non-union fractures were also discussed and some of the healing effects attributed to LIPUS introduced. These were increased rates of blood vessel formation to allow nutrients to flow into the site and waste to flow out; stimulation of intracellular signalling proteins such as PGE2 and NO, which promote switching of macrophages to an anti-inflammatory state and osteogenic differentiation of MSCs; and up-regulation of osteogenic transcription factors such as RUNX2.

Some of these healing effects were found via *in vitro* LIPUS studies, where cells involved in the bone healing process were exposed to LIPUS in a laboratory and cellular responses with potentially healing effects were assessed. Section 1.3 examined the LIPUS exposure methods used in past LIPUS studies from the literature and found five main exposure

methods with varying degrees of control over the LIPUS fields. Some methods had apparatus with the potential to influence the ultrasonic field by introducing reflections and/or standing waves within the culture wells, direct vibration by excitation of plate modes and thermal effects. While these secondary effects could occur to some degree *in vivo*, especially at the interface between tissue and bone and within the bone structure itself, it is unlikely that the magnitude of these effects would be recreated in laboratory apparatus. Therefore, the approach adopted in this study was to minimise these 'secondary' effects and isolate the direct ultrasound exposure, in order to assess the effect of this one aspect of LIPUS treatment on cellular responses in a controlled apparatus. With that aim in mind, the custom tank method was chosen as the method that offered the most control. By assessing cellular responses to the direct ultrasound only, we can verify (or rule out) whether this is the physical stimulus that induces the potentially healing responses, or if the cells are responding to increased sound pressures, heating or plate vibrations that may be unique to the apparatus.

The next chapter of this thesis describes a comprehensive review of the LIPUS literature, which covers first discoveries of LIPUS healing effects through *in vivo* studies, describes the clinical trials that led to the adoption of LIPUS as a treatment for fractures, and finally details the *in vitro* studies that attempted to isolate the mechanisms. The mechanisms are further explored in Section 2.3.2. Section 2.3.3 discusses 3D *in vitro* study methods and their potential for assessing cellular responses in growth environments more analogous to *in vivo* conditions. Section 2.4 summarises the chapter and describes the main aims and objectives of this study.

Chapter 3 describes the cell culture methods and ultrasonic devices used in the *in vitro* studies. Section 3.1 discusses the choice of cell line and the dyes and protocols adopted for assessment of cellular protein and RNA markers. The ultrasonic fields of LIPUS transducers were investigated by characterising a commercial LIPUS transducer and characterising a custom-built LIPUS device based on the dimensions of the commercial Exogen device (Bioventus, US). The field characteristics of these transducers informed the pressure amplitudes used in the LIPUS exposure studies, which were carried out with two transducers providing comparable LIPUS fields at 1 MHz and 45 kHz.

Chapter 4 describes the design and development of the custom tank LIPUS exposure method and exposure protocols adopted for the *in vitro* studies undertaken. A new cell culture vessel (the biocell) was developed to allow the growth of a cell layer and controlled exposure of that cell layer when immersed in a tank of water in the far field of a LIPUS transducer. Sections 4.3 to 4.5 describe a series of LIPUS exposure studies using the custom tank and cell culture vessel. Section 4.6 describes a feasibility study investigating the use of 3D-printed scaffolds as cell growth surface and potential to provide a growth and LIPUS exposure environment more like that of *in vivo* conditions.

Chapter 5 presents the results of the in vitro studies and these results are discussed in detail in Chapter 6. Finally, Chapter 7 presents the conclusions of this thesis and the future work that could be undertaken to continue pursuing the research.

CHAPTER 2

LITERATURE REVIEW: LOW INTENSITY PULSED ULTRASOUND

This literature review starts with the first discoveries of the potential for ultrasound to produce healing effects in bone through *in vivo* animal studies (2.1), followed by a review of the clinical trials that led to the recommendation of LIPUS as an available treatment for non-union fractures (2.2). The possible mechanisms of LIPUS and *in vitro* studies exploring those mechanisms are described in Section 2.3. Section 2.4 concludes the chapter by describing the context of this work in relation to LIPUS research to date, and its contributions to the field.

2.1 First Discoveries and *in vivo* Studies

The acceleration of bone healing as a result of exposure to ultrasound was first reported by Buchtala et al. in 1950 [73] after observing healing effects in dogs. In the same year, Maintz [74] treated radial fractures in rabbits with ultrasound intensities of 500 mW/cm^2 to 2500 mW/cm^2 and found this slowed healing rates overall but noticed that osteogenesis (new bone growth) occurred in healthy bone some distance from the treatment area. In 1952 De Nunno [75] found osteogenesis was stimulated in femoral fractures in rabbits, and Murolo and Claudio [76] reported accelerated healing of fractures in guinea pigs when exposed to pulsed ultrasound. The following year, Corradi and Cozzolino [77] reported accelerated callus formation and healing in fresh radial fractures of rabbits compared to controls when exposed to ultrasound at 500 mW/cm^2, and also in humans following a limited clinical study.

Bender et al. [78] and Ardan et al. [79] hypothesised that the mechanism of LIPUS-induced healing was heating of the tissue. Ardan made uniform cuts in the upper femurs of dogs and used the opposite femurs as controls, then exposed them to ultrasound with powers 5 W to 25 W to deliberately induce temperature rises of 7 °C or more. Both studies found that extent of heating brought about cell necrosis (i.e., death) and delayed healing.

In 1970 Dyson et al. [80] studied the effects of ultrasound stimulation on tissue regeneration in the outer ear, or pinna, of rabbits. Although pinnae consist of cartilage rather than bone, the study produced some informative results on the possible mechanisms involved. Pulsed ultrasound fields with frequency 3.5 MHz and pulse intensity amplitudes of 0.1 W/cm^2 to 8 W/cm^2 were employed. The pulse width (*pw*) and repetition rate (*prr*) were adjusted to bring about similar temperature rises of 1.3 to 1.5 °C in the tissue (effectively maintaining the same temporal average intensity), ranging from continuous wave at 0.1 W/cm^2 to *pw* = 1 ms and *prr* = 55 Hz at 8 W/cm^2. The optimum amplitude intensities for wound healing were found to be 0.5 W/cm^2 (with pw = 2 ms and prr = 100 Hz) or lower, with over 25% greater wound closure compared to controls. Healing was inhibited at 8 W/cm^2. Having kept temperature rise constant, thermal effects could be ruled out and Dyson et al. postulated that the healing was due to mechanical effects, suggesting that acoustic streaming within the tissue was acting on the cell membranes and stimulating enzyme activity. Later in 1989 Dyson and Young [81] also found that angiogenesis (formation of new blood vessels) was accelerated in skin lesions of adult rats when treated with 0.1W/cm^2 I_{SATA} ultrasound with frequency 750 kHz and 3 MHz.

In 1983, Duarte [82] used ultrasound fields at 4.9 MHz and 1.65 MHz at intensities of 57 mW/cm^2 and 49.6 mW/cm^2 respectively to treat rabbit femurs and fibulae. Pulse width was 5 µs and repetition rate 1 kHz. The frequency of ultrasound did not make any apparent difference to healing rates, and both ultrasound-treated groups showed accelerated healing (measured by radiography and callus area) compared with controls. In the absence of any measurable heating or cavitation effects, Duarte hypothesised that the healing effects were due to voltages induced by the piezoelectricity of bone – the induction of an electric field in response to vibration. In 1986 Klug et al. [83] exposed lower leg fractures in rabbits to continuous wave ultrasound with intensity 0.2 W/cm^2, for 3 minutes every 2 days, and found time to healing was five weeks earlier as compared to controls (measured by scintigraphy, i.e., the absorption of radioactive substances taken up most in areas of new bone growth).

In 1985, Duarte and Xavier [82, 84] reported the results of *in vivo* trials on rabbits and human clinical trials on non-union fractures using lower intensity pulsed ultrasound (1.5 MHz, 30 mW/cm^2, 20 minutes per day) where they had found beneficial effects.

Duarte patented the ultrasonic device used and this patent [85] was later taken on by Exogen in the US and Ortosonic in South America.

In 2001 Azuma et al. [86] used the Exogen device (1.5 MHz, *pw* 200 µs, *prr* 1 kHz, I_{SATA} 30 mW/cm^2) to attempt to pinpoint the stage of bone growth where therapeutic ultrasound had the optimal effect. They used rats as a model and assessed healing 25 days after a surgically-induced femoral fracture. One group of rats was given daily LIPUS treatment over the full 24 days, a second group was treated on days 1 to 8, the third on days 9 to 16 and the last group on days 17 to 24. The aim was to identify if healing effects were dependent on the stage of fracture growth, assuming the three 8-day periods corresponded to the first three stages of secondary healing as described in Section 1.2.3. Opposite femurs were used as controls. Those treated for 8 days only showed similar increases in mechanical strength on day 25 post-fracture, regardless of when the LIPUS treatment took place. Those treated continuously for 24 days exhibited the most healing, suggesting LIPUS accelerates healing regardless of the stage of fracture healing at which it is applied.

In 2003 Greenleaf et al. [87] measured the movement induced by LIPUS treatment (1.5 MHz, *pw* 200 µs, *prr* 1 kHz, $I_{SATA} = 30$ mW/cm^2) on a cadaveric human radius with a simulated fracture. Laser interferometer measurements demonstrated that the ultrasound induced small cyclic movements of the bone ends, with a velocity of 1 to 2 µm/s at the same frequency as the pulse repetition rate (i.e., 1 kHz). They hypothesised that the motion was induced by the cyclic radiation force, and that this was the physical mechanism that induced the healing response, by simulating the effects of physical activity.

Recent work by Hsu et al. [88] examined the use of LIPUS for promoting the integration of titanium dental implants. They seeded the implants with MG62 osteoblast-like cells and inserted them into the metaphysis of rabbit tibia (the region between the long section of a long bone and the epiphysis). They found increased blood flow and higher prevalence of mature type 1 collagen fibres around the LIPUS-treated implants as compared to controls (3 mins per day, 1 MHz, I_{SATP} 50, 150 & 300 mW/cm^2, CW and *pw* 2 ms, *prr* 100 Hz).

Kumugai et al. [89, 90] used a novel and rather gruesome approach of conjoining a genetically-altered green-fluorescent protein (GFP+) mouse with a wild-type (WT) mouse, creating a fracture on the fibula of the WT mouse and treating with LIPUS. LIPUS

treatment consisted of 20 minutes per day with the Sonic Accelerated Fracture Healing System (SAFHS, Smith & Nephew, US) at 1.5 MHz, *pw* 200 μs, *prr* 1 kHz and I_{SATA} 30 mW/cm^2). The GFP+ mouse has an enhanced fluorescent protein present in almost every cell, allowing the migration of cells from one mouse to the other to be monitored under fluorescent microscope. The team hypothesised LIPUS would stimulate the migration of circulating osteoprogenitor cells to the fracture site, and this was confirmed when significantly more GFP cells were seen in LIPUS-treated subjects as compared to controls. This recruitment was limited to the first two weeks after fracture, as the number of GFP cells observed at 4 weeks was only slightly larger than the control group. This is an interesting mechanism, as the number of osteoprogenitor cells is limited at the fracture site, so recruiting more from elsewhere in the body would be beneficial to healing, especially in the initial stages. The team hypothesised this was due to up-regulation of the SDF-1 chemokene and its receptor CXCR4, which were up-regulated in LIPUS-treated subjects. These molecules are known to regulate the homing of progenitor cells, and SDF-1 is known to be induced in the periosteum of injured bone to increase recruitment of mesenchymal stem cells to the injury site [91]. A similar study involved injecting MC3T3-E1 preosteoblasts into the heart of mouse subjects with induced bone defects, which also found increased levels of SDF-1 and recruitment of the cell line to the defect area, with an associated enhancement of bone mineral density [92].

Fung et al. 2012 [93] tested the effects of LIPUS (1.5 MHz, *pw* 200 μs, *prr* 1 kHz, I_{SATA} 30 mW/cm^2 and 150 mW/cm^2) on induced femoral fractures in 54 rats. The 30 mW/cm^2 After 6 weeks, subjects treated with the 30 mW/cm^2 LIPUS were found to have significantly higher bone volume fraction and woven bone percentage measured by microCT and histological measurements, and significantly higher failure torque, than those treated with 150 mW/cm^2 LIPUS. They observed that lower intensity LIPUS induced healing effects whereas higher intensities could have a detrimental effect on healing. Bronoosh et al. 2015 [94] also saw no significant evidence of healing in mandibular bone defects in rabbits when treated with higher intensity LIPUS at I_{SATA} 500 mW/cm^2, at frequencies 1 MHz and 3 MHz (pulse characteristics not specified).

An interesting study from Jung et al. [95] tested an unusual focussed LIPUS device intended for neuromodulation on fractured rat calvaria (the upper parts of the skull). The focussed LIPUS device consisted of a bowl-shaped element with diameter 6 cm and radius

of curvature 7 cm producing an acoustic focus of width 3.5 mm and length 6.2 mm. The operating frequency was 650 kHz and it was driven in pulsed mode (*pw* 1 ms, *prr* 100 Hz, 100 mW/cm^2 I_{SPTA}) at 4 points, for 5 minutes per point, daily for a period of 8 weeks. The team monitored healing via CT imaging every two weeks and found local enhanced bone regeneration at the treatment sites, and immunofluorescent staining revealed the cells present were proliferating more than those in sham-treated controls. The LIPUS treatment group also had a 1.5-fold higher cell count than the sham-treated group, further indicating that LIPUS had stimulated proliferation *in vivo*, which would promote healing by increasing the numbers of mineralising cells.

In 2014 Fung et al. [96] conducted a study on closed femoral fractures of rats, comparing effects of LIPUS (1.5 MHz, I_{SATA} 30 mW/cm^2, *pw* 200 µs, *prr* 1 kHz) at three axial treatment distances (0, 60 and 130 mm) from the front face of the Exogen device (Bioventus, US). They hypothesised that during clinical LIPUS treatment the cells *in vivo* would be in the near field of the LIPUS transducer, where the pressure field has not resolved to a smooth shape and is prone to fluctuate. To test this, they varied the separation between cells and transducer between 0 mm and 130 mm (which was at the focus and as such corresponded to a pressure peak along the beam axis). Rubber gel blocks were used to set the separations and the devices were calibrated to produce the same intensity, taking into account the attenuation of the gel blocks. Fractures treated in the far field exhibited enhanced tissue mineral density (TMD) and peak mechanical torque compared with controls at 4 weeks post-fracture. The TMD was 13% greater than controls and peak torque 70 % above controls (0.17 Nm compared to 0.10 Nm in controls). Fung et al. hypothesised that the enhanced mechanical properties were the result of far field LIPUS enhancing total bone volume and mineralisation. They went on to use their setup to test the effects of LIPUS in near and far fields on osteocytes and their ability to affect subsequent downstream effects on osteoblasts *in vitro*, discussed later in Section 2.3.1.

To summarise, the evidence from *in vivo* animal studies supports the theory that LIPUS accelerates fracture healing. The next section describes clinical human trials and the adoption of LIPUS as an approved treatment.

2.2 Clinical Trials and Adoption

As mentioned in Section 2.1, Duarte and Xavier patented a bone healing ultrasonic device which was developed by Ortosonics in South America and Smith and Nephew (later Bioventus) in the US. In 1994 the Smith and Nephew device (the Exogen) was used in a multi-institutional, randomised, double-blinded and placebo-controlled clinical trial by Heckman et al. [3]. 67 subjects with tibial fractures were treated with the Exogen device (1.5 MHz; I_{SATA} 30 mW/cm^2; pw 200 µs; prr 1 kHz; 20 minutes per day). Treatment began within 7 days of the initial fracture. Time to weight bearing was found to improve by 25%, and radiographically-assessed healing by 38%, in the LIPUS-treated group compared with the placebo-treated control group. Heckman calculated that this improvement in healing could represent a saving of around $15,000 per patient [97]. The device was quickly approved for clinical use by the United States Food and Drug Administration [1].

In 1997 Kristiansen et al. [98] conducted an almost identical trial to Heckman on 60 patients with radial fractures. This trial also found a 38 % improvement in days to radiographic healing, with an average of 61 days for the treated group and 98 days for those treated with sham devices. Later Nolte et al. [99] treated a set of subjects with non-union fractures, with an average time of 61 weeks since initial fracture, and reported that 86% of fractures had achieved clinical and radiographic healing within 22 weeks of beginning LIPUS treatment.

Other clinical trials demonstrated improved healing rates for smokers [100], infected non-unions [101], atrophic (no callus formed) and hypertrophic (callus formed but not joined) non unions [102]. In 2000 the US Food and Drug Administration (FDA) approved the Exogen device for treatment of non-unions [103] and the same device was approved for clinical use in the NHS by the National Institute for Health and Care Excellence (NICE) in 2010 [104]. Since then, many studies have attempted to find the underlying healing mechanisms induced by LIPUS stimulation, with the majority exposing bone cells *in vitro* to the Exogen LIPUS field (1.5 MHz, pw 200 µs, prr 1 kHz, I_{SATA} 30 mW/cm^2).

Despite the body of evidence supporting the healing effects of LIPUS there is still ongoing debate over its effectiveness. Some trials found no significant difference in healing rates compared with controls. Rue et al [105] studied the effects of LIPUS treatment on military personnel with fresh tibial stress fractures brought about by rigorous training. They found

no evidence of accelerated healing (radiographic, clinical or return to duty) with LIPUS compared to sham-treated subjects. It is possible that these stress fractures, which generally involve many micro-fractures within the bone with much smaller gaps between bone surfaces, would more likely heal by the primary healing process. Perhaps this result indicates that LIPUS is more effective in the case of secondary healing of more serious fractures with larger gap sizes between bone ends.

The most recent and largest clinical trial was conducted by Busse et al. [11] and reported in 2016. The study consisted of a randomised clinical trial covering 43 North American trauma centres and including 501 patients with tibial fractures of various causes after surgical treatment with intramedullary nailing procedures. Tibial fractures were chosen because they are at high risk of non-union and are the most common fracture where LIPUS is employed. The authors found no significant difference between LIPUS-treated groups and placebo-treated control groups. In 2017 Busse co-authored a systematic review of clinical evidence for LIPUS (Schandelmaier et al. [106]). This review noted that when clinical trials with low risk of bias were given highest credence in analysis (i.e., not directly funded or conducted by LIPUS device manufacturers) there was no evidence of LIPUS accelerating clinical or radiographic healing. This led to the publishing of a linked clinical practice guidance article in the BMJ (Poolman et al. [12]) recommending to halt the use of LIPUS for treatment of fresh fractures, osteotomies and non-unions.

Despite these recommendations, NICE in the UK still approves the treatment for non-unions [4] and research continues, with interest from the world of dentistry for synthetic bone and dental implants [6, 7]. The next section examines the attempts to date to discover the physical and biological mechanisms by which LIPUS might act at the cellular level, by conducting *in vitro* testing.

2.3 LIPUS Mechanisms and *in* vitro Studies

Many *in vitro* studies have attempted to explain the physical and biological mechanisms responsible for the observed healing effects of low intensity pulsed ultrasound. As discussed in Chapter 1, the findings of these studies could be influenced to varying degrees by the exposure apparatus adopted and this leads to some studies having conflicting conclusions regarding cellular mechanisms. Therefore, for clarity, the discussion of *in vitro* papers in Section 2.3.1 focusses on general cellular responses grouped as far as possible

into the stages of secondary fracture healing. Section 2.3.2 then examines the cellular mechanisms which are the focus of many LIPUS studies. Finally, more specialised 3D *in vitro* trials are reviewed and considered in Section 2.3.3.

2.3.1 General findings of *in vitro* LIPUS studies

The following sections are a description of *in vitro* LIPUS studies found in the literature. The focus here is on the findings and any further considerations for *in vitro* exposure apparatus, rather than a full critique of the methods, which were discussed in detail in Section 1.3. The studies are split up into the approximate stage of secondary fracture healing described in Section 1.2.3 and ordered according to cell type. A summary table (Table A.2) of all the studies considered is provided in Appendix A, including brief descriptions of LIPUS devices, exposure parameters and methods, and findings. Some dental studies are included where relevant as odontoblasts mineralise in a similar manner to osteoblasts in bone.

2.3.1.1 Stage 1: Inflammation and immune response. Haematoma formation by fibroblasts and angiogenesis.

Stage 1 of secondary fracture repair involves inflammation regulated by macrophages and cytokines, haematoma formation by fibroblasts and the formation of blood vessels (angiogenesis) by endothelial cells. Webster and Dyson et al. [72] were early adopters of *in vitro* techniques for investigating effects of ultrasound on cells, following on from Dyson's earlier *in vivo* work [80]. In 1978 They used a custom tank method to expose human fibroblasts to continuous 3 MHz ultrasound with intensities of 0.5 to 2.0 W/cm^2 and found significant increase in protein synthesis, accompanying increased permeability of cell membranes. Further studies by the same group found that the effects observed were caused by the likely presence of inertial cavitation during ultrasound exposures [72, 107].

Ultrasound-induced cavitation describes the formation of bubbles in a medium when exposed to ultrasound. Cavitation can occur if the pressure exceeds a threshold for enough time, and if there are gas nuclei present (i.e., tiny pockets of undissolved gas) (Figure 2.1). The threshold at which this occurs depends on ultrasound frequency, amplitude, and the concentration of gas nuclei in the medium. If the pressure amplitudes are relatively low the bubbles oscillate in a stable manner (stable cavitation, Figure 2.1(a)). If the pressure

amplitudes are high, oscillations become unstable and can result in violent collapse of the bubbles when the fluid momentum overcomes the internal pressure of the bubble (inertial cavitation, Figure 2.1(b)) [108]. This collapse causes a shock wave, which can also be accompanied by localised high temperatures and pressures and sometimes high-speed jetting, i.e., localised high speed displacement of the medium. All these effects can damage cell membranes.
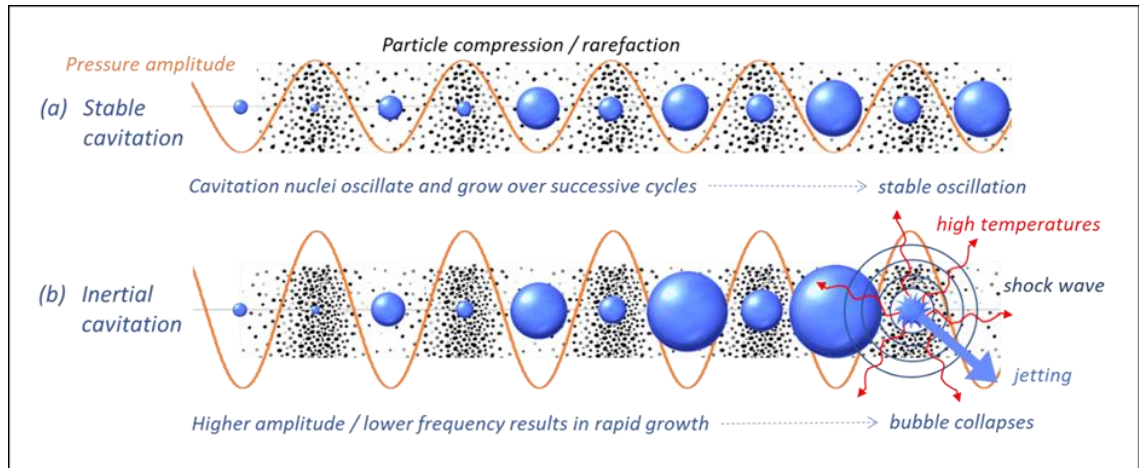
Figure 2.1: Ultrasound-induced cavitation (own illustration).
Occurs when the maximum rarefactional (negative) sound pressure exceeds a threshold, dependent on the static pressure in the medium and the presence of undissolved gas nuclei. In stable cavitation (a) the pressure amplitudes are low enough that stable oscillating bubbles are produced. High rarefactional pressure amplitudes can result in inertial cavitation (b), resulting in unstable bubble oscillations that lead to bubble collapse, which can result in shock waves, transient high temperatures and pressures, and jetting.

Cavitation is very unlikely *in vivo* at LIPUS intensities, and due to the lack of available undissolved gas nuclei in most tissues (with some exceptions, the most notable being lung tissue) [109]. However, constructive interference of reflections within an *in vitro* apparatus could increase the pressure amplitude enough to induce inertial cavitation. Another reason to avoid the influence of reflections in *in vitro* studies.

In 1999 Doan, Reher et al. [19, 38] used the tank dip method to expose three cell types to LIPUS. The cell types were human primary gingival fibroblasts, human mandibular osteoblasts and human monocytes: a type of white blood cell that can differentiate to the macrophage phenotype. The cells were exposed to two LIPUS conditions: 1 MHz with *pw* 2 ms; *prr* 100 Hz and spatial-average, pulse-average intensity I_{SAPA} 0.1 to 1.0 W/cm^2; and continuous wave (CW) 45 kHz with I_{SATA} 5 to 50 mW/cm^2. Note the effective radiating area (A_{ER}) of the LIPUS devices were very different: 2 cm^2 at 1 MHz and 12.8 cm^2 at

45 kHz. LIPUS at both frequencies up-regulated proliferation and collagen production of the fibroblasts and osteoblasts compared with controls. All cell types expressed significantly higher levels of Vascular Endothelial Growth Factor (VEGF), a cytokine that promotes angiogenesis by stimulating the migration and proliferation of endothelial cells.

Zhou et al. [110] found increased proliferation of primary human skin fibroblasts in a study conducted using the direct coupling method: the most common method of the *in vitro* LIPUS studies reported. The Sonic Accelerated Fracture Healing System (SAFHS, Exogen, US) consisted of a set of six transducers directly coupled to the base of each well of a 6-well culture plate via coupling gel. LIPUS settings consisted of 1.5 MHz; *pw* 200 μs; *prr* 1 kHz; I_{SATA} 30 mW/cm^2. The study also found evidence that a mechanotransduction pathway was activated by the LIPUS treatment via stimulus of Integrin β1. Integrins connect the cell membrane to the surrounding ECM and are well known to play a part in transducing mechanical stimuli. These pathways, discussed in more detail in Section 2.3.2.4, are the subject of many LIPUS studies as they are considered the most likely mechanism by which LIPUS stimulation acts on cells.

Iwanabe et al. [111] exposed the gingival epithelial cell line GE1 to 3 MHz LIPUS (temporal-average intensity I_{TA} 160 and 240 mW/cm^2; 25% duty cycle, 15 mins daily) and found increased proliferation, migration and expression of integrins α6 and β4. Another study by Su et al. [112] exposed human umbilical vein endothelial cells (HUVECs) and human microvascular endothelial cells (HMECs) to 0.5 MHz LIPUS ('mean' intensity 210 mW/cm^2, peak pressure 0.5 MPa) and found increased apoptosis and reduced cell viability. The relatively low frequency and high peak pressure indicates a risk of cavitation, which may have contributed to cell death, and highlights the need for low intensities, especially for *in vitro* testing.

To summarise the potentially healing effects of LIPUS in Stage 1 of the bone healing process, we can say from these studies that LIPUS exposure may:

- Increase proliferation of fibroblasts, which begin to lay down the initial collagenous ECM of the haematoma to allow healing to begin.

- Up-regulate Vascular Endothelial Growth Factor (VEGF), a cytokine that promotes angiogenesis, i.e., the formation of blood vessels, which can bring valuable nutrients and aid recruitment of healing cells to the fracture site.

- Activate mechanotransduction pathways via Integrins, which trigger multiple cellular processes such as proliferation, migration and differentiation to healing phenotypes.

Another conclusion from the early studies is that care should be taken to ensure cavitation is not present in the *in vitro* apparatus by keeping the intensity and pressure amplitudes low and minimising the occurrence of bubbles, which may provide the seed for cavitation to occur.

2.3.1.2 Stage 2: Soft Callus. MSCs migrate to site, proliferate and differentiate into chondrocytes or preosteoblasts. Chondrocytes lay down collagen (Type II) to form the soft callus ECM.

Stage 2 of fracture healing involves the migration of MSCs to the fracture site, where they proliferate and differentiate to chondrocytes or preosteoblasts. Chondrocytes lay down the collagenous soft callus and preosteoblasts begin to proliferate in preparation for the hard callus formation in Stage 3. Sena and Angle et al. [113, 114] employed the SAFHS to apply LIPUS to rat bone marrow-derived stem cells. They treated the cells for 20 minutes and found up-regulation of early response genetic markers associated with cell mitosis and proliferation, and the osteogenic markers osteonectin (on) and osteopontin (opn), indicating the MSCs were differentiating towards the osteogenic lineage. Angle et al. varied intensity (I_{SATA} 2, 15 & 30 mW/cm^2) and number of daily treatments (3, 5 & 7 days) and found stimulation of mechanotransduction pathways with maximum stimulation at 15 to 30 mW/cm^2. Alkaline phosphatase (ALP), a marker for preosteoblast differentiation, up-regulated by up to 209% after 5 days treatment with I_{SATA} 30 mW/cm^2.

Marvel et al. [115] cultured adipose-derived mesenchymal stem cells on the BioFlex (Flexcell International Corporation, US), a specialist culture plate with a thin (0.5 mm) silicone rubber base that has low transmission loss (0.6 dB as measured in the study). Proliferation reduced and calcium secretion increased in LIPUS-treated samples. Marvel speculated the reduced proliferation might be due to the cells differentiating to the osteogenic lineage. Marvel also noted the low stiffness of the Bioflex plates, which was

around 1.6 MPa compared with the 1 GPa of standard polystyrene culture plates, may also have an effect on cell behaviour. Stiffer substrates are known to encourage osteogenic differentiation of stem cells [116]. Calcium increase might indicate the mechanical stimulation of calcium ion channels in the cell membranes, but this coupled with the drop in proliferation might also indicate cell apoptosis due to prolonged mechanical stress [117].

The direct coupling method was used again by Lim et al. [118] to expose human alveolar MSCs (alveolar is the bony ridge forming the sockets of the upper teeth). The cells were grown in 35 mm petri dishes and exposed to 1 MHz LIPUS (50 mW/cm^2, 10% and 20% duty cycles, 10 minutes per day). Cell migration and proliferation were up-regulated, with optimum duty cycle of 20 %. Xie et al [65] exposed human bone marrow MSCs to LIPUS (1.5 MHz; 20% duty cycle; *prr* 1 kHz, I_{SATA} 30 to 89 mW/cm^2, durations 5, 10 and 20 mins per day for up to 4 days), using a direct coupling device similar to the SAFHS, but coupled to 6-well or 96-well plates. They found proliferation increased when the cells were exposed to 5 minutes of I_{SATA} 50-60 mW/cm^2, and proposed this was via activation of the PI3K / Akt mechanotransduction pathway. Proliferation reduced for daily exposures of 10 minutes or more, again suggesting cell viability suffered with prolonged LIPUS exposure and indicating the cells were under stress. As the direct coupling method is prone to heating, this may have been mechanical or thermal stress. The exact nature of the stress is unknown because *in situ* vibration and temperatures were not predicted or measured.

Gao et al. [119] used the tank dip method, dipping their transducer (Duoson, SRA Developments, UK) directly into 6-well plates suspended in a water-filled absorbent silicone rubber chamber. They exposed dental pulp stem cells (DPSCs) to 5-minute LIPUS treatment (1 MHz, *pw* 3.2 ms, *prr* 63 Hz). The DPSCs were exposed to I_{SATA} 250 mW/cm^2 and their proliferation increased, as well as their expression of piezo 1&2 proteins and stimulation of the ERK 1/2 mechanotransduction pathways. The expression of piezo 1&2 proteins indicates activation of piezo ion channels: stretch or voltage-activated channels that allow calcium ions to be released from within the cell membrane, another candidate for the mechanism of LIPUS-induced healing, as increased release of calcium could encourage mineralisation at Stage 3.

A more controlled *in vitro* investigation was conducted by Lai et al. [44], who adopted the absorption tube method to investigate the differentiation of primary human mesenchymal

stem cells from bone marrow to the chondrogenic or osteogenic phenotypes. They treated the cells with LIPUS consisting of 1 MHz, *pw* 2 ms, *prr* 100 Hz, I_{SATP} 200 mW/cm^2, 20 minutes daily over 1-4 weeks, with the device held 30 mm from the base of the well. The *in situ* intensity was derived by direct measurement of the field corrected for transmission loss through the well base. The transducer was positioned on a rotating plate to reduce the risk of standing waves and heating of the cell layer. LIPUS-treated cells exhibited increased osteogenic differentiation and up-regulation of Runt-related transcription factor 2 (runx2), an essential transcription factor that encourages osteogenic differentiation of MSCs and preosteoblasts [49].

Following on from Greenleaf's *in vivo* study showing 1 kHz cyclic movements in bone induced by the cyclic radiation force of LIPUS [87], Argadine and Greenleaf et al. [120] hypothesised it was the cyclic radiation force that induced the healing stimulus. To test this, the ATDC5 chondrocytes were exposed to LIPUS via the SAFHS direct coupling system and exposed to the Exogen pulse (1.5 MHz, *pw* 200 µs, *prr* 1 kHz, I_{SATA} 30 mW/cm^2). Another direct coupling system was set up with 6 moving coil transducers driven with a 1 kHz square wave and 20% duty cycle and calibrated to produce the same displacement amplitude in the base of the well as the Exogen devices (4 nm), measured via scanning laser vibrometer. Thus, the vibration induced by the cyclic radiation force was the main stimulus in the 1 kHz case. The chondrocytes were treated for 20 minutes per day for 6 to 12 days. The number and total area of collagen nodules were quantified by Alcian blue staining. When treatments were initiated early (day 3 to day 5) both the 1.5 MHz LIPUS and the 1 kHz vibration increased the total area of collagen nodules. When treatment was initiated later (7+ days), the 1 kHz square wave treatment resulted in significantly more stimulus of nodules than the 1.5 MHz, *prr* 1 kHz LIPUS treatment. The results agree with other studies applying direct 1 kHz mechanical vibration to cells, which show that displacements of the order of 10 to 30 nm stimulate osteogenesis in mesenchymal stem cells [121, 122].

Another study of chondrocytes by Whitney et al [55] used the benchtop dip technique, immersing a 5 MHz transducer (V300, Panametrics, US) with 12.7 mm diameter, producing spatial average pressure of 14 kPa (unclear if this is peak or rms) for 3 minutes continuous wave (CW). They found mechanotransduction pathways were activated by via integrins. Another study by Xia et al. [123] on primary rabbit articular cartilage

chondrocytes found stimulation of mechanotransduction pathways via Integrin β1, and up-regulation of collagen type II, the collagen type produced by chondrocytes to form the soft callus ECM.

Mukai et al [124] tested aggregated primary rat chondrocytes to LIPUS. Aggregated culture systems involve growing cells in suspension, which encourages them to form 3D morphology and behaviour. The chondrocyte aggregate was suspended in a culture tube that was immersed in a water tank and exposed to LIPUS with a system based on the Exogen SAFHS (1.5 MHz; A_{ER} 3.88 cm^2; *pw* 200 µs; *prr* 1 kHz; I_{SATA} 30 mW/cm^2). The transducer was held in the tank 3 cm from the cells. *In situ* hydrophone measurements estimated the LIPUS exposed amplitude was around 70% of the quoted LIPUS amplitude. The study found increased proliferation, and up-regulation of collagen type II. A temporary up-regulation of the cytokine Transforming Growth Factor Beta 1 (TGF-β1) was also observed, and it was hypothesised that this growth factor was mediating the downstream effects on proliferation and differentiation.

Parvizi et al. [125, 126] exposed primary rat chondrocytes to LIPUS (1 MHz, *pw* 200 µs, *prr* 1 kHz, I_{SATA} 50 mW/cm^2 / 230 kPa peak pressure and I_{SATA} 120 mW/cm^2 / 360 kPa peak pressure). Proliferation did not change with respect to controls but LIPUS stimulated the release of intracellular calcium, indicating possible activation of calcium ion channels, further discussed in Section 2.3.2.

To summarise, the findings of *in vitro* LIPUS studies concerned with process in Stage 2 of secondary fracture healing, indicated LIPUS may:

- Up-regulate the cytokine TGF-β1, a growth factor known to influence cell proliferation and differentiation, in chondrocytes. This would help speed up soft callus formation by increasing the number of chondrocytes, which lay down the collagen of the soft callus ECM.
- Up-regulate the production of collagen in chondrocytes, which will speed up the formation of soft callus.
- Up-regulate migration and proliferation of MSCs and their differentiation to the osteogenic lineage, perhaps by the stimulation of the osteogenic transcription

RUNX2. This up-regulation would potentially speed up the rate of formation of the hard callus and mineralisation at Stage 3 of fracture healing.

- Stimulate the release of calcium in MSCs via calcium ion channels, thus potentially providing the calcium supply for mineralisation to occur at Stage 3 of fracture healing.

In addition, Argadine et al. found that exposing cells to 1 kHz displacements similar to those induced by the LIPUS SAFHS direct coupling system resulted in similar up-regulation of collagen nodule formation as the 1.5 MHz LIPUS-exposed samples, indicating it could be the cyclic radiation force that provides the main physical stimulus of the cells in LIPUS treatment.

2.3.1.3 Stage 3: Hard callus. Osteoprogenitors proliferate, mature to osteoblasts and mineralise

Stage 3 of fracture healing is the formation of the mineralised hard callus. Preosteoblasts migrate to the fracture site and proliferate, then mature into osteoblasts, which lay down the mineralised matrix of bone, consisting of fibrous Collagen Type I and calcium-based hydroxyapatite crystals. From the studies described in previous sections, Doan, Reher et al. [19, 38] found up-regulation of proliferation and collagen production in osteoblasts. Sena, Angle et al. [113, 114] found exposure of rat bone marrow-derived stem cells to daily 20-minute exposures to 1.5 MHz LIPUS at I_{SATA} 2 mW/cm^2 resulted in a significant increase (up to 225 % as compared to controls) in mineralisation after 24 days of treatment. And two studies found increased calcium release or up-regulation of markers associated with calcium ion channels [115, 119].

Many *in vitro* LIPUS studies have focussed on osteoblasts as the main producers of mineralised bone. A common cell line used for studying osteoblasts is the MC3T3-E1 murine preosteoblast cell line, derived from mouse calvaria. This cell line is discussed in more detail in Section 3.1.1 because it is the cell line chosen for the studies in this thesis. Briefly, the MC3T3-E1 cell line behaves much like primary mouse (and human) preosteoblasts *in vivo*: proliferating until confluent then differentiating into mature osteoblasts, mineralising, and eventually taking the form of osteocytes. They are also known to express the same osteogenic markers as primary cells [127].

Studies using this cell line include the study by Tang et al. [41], already discussed in Chapter 1, who adopted the benchtop dip method with an Exogen device (1.5 MHz; *pw* 200 µs; *prr* 1 kHz; I_{SATA} 30 mW/cm^2). They found increased expression of COX-2 protein and mRNA, PGE2 and activation of integrins and the FAK/PI3K/Akt & ERK mechanotransduction pathways (see Figure 1.6 for illustration of these pathways). A previous study by Kokubu et al. [128] used the more controlled absorption tube method and their results supported the Tang study: observing PGE2 levels three times that of the controls 60 minutes after exposure with the same LIPUS settings. They also found up-regulation of cox-2 and levels of PGE2 were suppressed by a COX-2 inhibitor, indicating COX-2 expression led to PGE2 production.

Another benchtop dip study by Katiyar et al. [129] explored the effects of LIPUS (*pw* 200 µs; *prr* 1 kHz) with varying frequency (0.5 MHz to 5 MHz) and intensity (I_{SATA} from 1 to 500 mW/cm^2) and exposure times (5, 10, 30, 30 mins per day for two days) on proliferation of MC3T3-E1 cells. They found increased proliferation with optimal frequency 1.5 MHz, I_{SATA} 74.3 mW/cm^2, 30 mins exposure (+50% wrt controls). I_{SATA} of 464 mW/cm^2 or more resulted in decreased proliferation and cell death (possibly due to cavitation). Note the depth of medium in the wells was 4 mm, which was an integer multiple of wavelengths at the optimal frequency of 1.5 MHz (4λ, compared to $4/3\lambda$ at 0.5 MHz and 13.33λ at 5 MHz), so the optimum result may correspond to a standing wave in the apparatus.

Tassinary et al. [46, 130] used direct coupling of a single LIPUS transducer (Sonic Compact, HTM, BR; 1 MHz, 20% duty cycle, I_{SATA} 200 mW/cm^2, 30 minutes exposure time) and found proliferation of MC3T3-E1 cells increased, along with activation of cellular pathways regulating cell metabolism, DNA transcription and cell survival in response to stimuli including cytokines and mechanical stress. They also found increased mineralisation and hypothesised this was due to increased calcium and phosphate uptake, as concentrations dropped in the media.

Another study by Kaur et al. [131] exposed the MC3T3-E1 cell line to LIPUS with a directly coupled custom device (Smile Sonica, Canada: 1.5 MHz, *pw* 200 µs, *prr* 1 kHz and I_{SATA} 30 mW/cm^2). The LIPUS exposures resulted in increased cell viability downstream up-regulation of mineralisation markers runx2, ocn and opn. Kaur proposed

that LIPUS exposure had increased levels of reactive oxygen species (ROS), which in turn activated the MAPK and ERK1/2 pathways, which regulate many cellular processes including cell viability and proliferation. However, the MAPK/ERK pathways can also be up-regulated by heat stress [62]: a factor that cannot be ruled out because temperature was not monitored during this study.

Another two studies exposing MC3T3-E1 preosteoblasts to LIPUS with the Exogen SAFHS system or equivalent via direct coupling methods were Unsworth et al. [47] and Tabuchi et al. [132]. The first study found increased mineralisation coupled with increased ALP and mmp-13 (an enzyme that breaks down collagen). The study concluded that LIPUS stimulates the conversion of the soft callus to the hard mineralised callus. The second study found no difference in ALP expression and no significant effects on proliferation but did find levels of ocn (or bglap) increased significantly with respect to controls after 24 hours. A high-density oligonucleotide microarray analysis, which analysed thousands of genes simultaneously, found up-regulation of genes associated with skeletal and muscular development and cellular movement: e.g., mmp-13 which was also found by Unsworth et al. and fibrillin, a glycoprotein involved with formation of elastic fibres of connective tissue. Down-regulated genes were associated with gene expression, the cell cycle, cellular development, growth and proliferation. E.g., tgf-β1 was down-regulated. These results suggested LIPUS was stimulating differentiation and mineralisation over proliferation.

Man et al. [45] used a scratch assay technique and found MC3T3-E1 cells exposed to LIPUS exhibited increased migration: a phenomenon which had also been observed *in vivo* [89, 90]. The effects were similar for 1 MHz and 45 kHz LIPUS fields (1 MHz: *pw* 3.2 ms, *prr* 63 Hz, I_{SATA} 250 mW/cm^2. 45 kHz: CW, I_{SATA} 25 mW/cm^2). In a later trial, Man et al. [6] exposed the Mouse Dental Papilla Cell-23 (MDPC-23) odontoblast-like cell line to the 45 kHz LIPUS field and assessed cell viability and proliferation. Cell viability remained constant, and proliferation increased when cells were treated either with 2 x 15-minute or 1 x 30-minute exposures. LIPUS treatment significantly increased mineralisation with 3 x 10-minute and 1 x 30-minute treatments. PCR analysis found mineralisation and differentiation markers alkaline phosphatase (alp), collagen Type 1 (col1a1), nestin (nes) and osteomodulin (omd) were significantly up-regulated after a single 30-minute treatment.

Another microarray analysis was carried out by Lu et al. [133] on the SAOS-2 cell line: a human osteosarcoma cell line that can readily form a mineralised extra-cellular matrix. They used the Exogen SAFHS system with six transducers directly coupled to a six-well plate via coupling gel (temperature not monitored). They found increased expression of integrins and cytoskeletal genes, tgf-β1 and 2 (contrary to Tabuchi et al. [132] who found reduced tgf-β1), igf2 (agreed with Tabuchi et al.) and bp6, mapk. The study also saw up-regulation of apoptosis-related genes: note these are genes which regulate apoptosis and do not necessarily indicate programmed cell death – they could just indicate the cell has experienced mechanical or thermal stress. Some genes reduced apoptosis (e.g., the appropriately named survivin) and some increased the likelihood (e.g., Tumour necrosis factor superfamily, member 7).

Miyasaka et al. [61] exposed primary mouse calvarial osteoblasts to 3 MHz LIPUS (30 mW/cm^2, pulse characteristics not reported) for 15 minutes and compared resulting heat shock protein up-regulation with heating of samples in a 42°C incubator. They did not monitor the temperature of the media or cell layer during LIPUS exposure, claiming LIPUS induced the heat shock protein by mechanical stimulation alone (as the assumption was made from previous LIPUS studies that the LIPUS exposure did not induce thermal effects). They also found increased mineralisation and phosphorylation of Smad 1 & 5, which is normally activated by Bone Morphogenetic Protein (BMP), a cytokine involved in bone formation and repair, but was still activated with LIPUS even when a BMP signal blocker (Noggin) was used. This again highlights the main concern around the direct coupling method – that of unwanted thermal effects.

Liu et al [134] used the direct coupling method (system based on the SAFHS: 1.5 MHz; *pw* 200 µs; *prr* 1 kHz) to expose primary murine periosteum-derived cells to LIPUS at a range of I_{SATA} from 10 to 90 mW/cm^2, with 30 minutes to 2 hours exposure times. They found reduced inflammation by inhibition of Interleukin-6 and Interleukin-8 via the NF-κβ pathway at 2 hours exposure. 30 minutes exposure resulted in increased mineralisation and associated mRNA markers runx2, osx, opn and ocn. Maung et al. 2020 [135] also used the direct coupling method to expose the same cell type to 3 MHz LIPUS (30 mW/cm^2; *pw* 1 kHz). They found no effect on proliferation but increased expression of alp and protein levels at day 7, and increased expression of bmp-2 and its protein BMP-2, osterix and phosphorylated-smad, with increased mineralisation after 21 days.

Suzuki et al. [56] exposed the rat osteosarcoma (ROS) cell line to LIPUS (1.5 MHz; pw 200 µs; prr 1 kHz; I_{SATA} 30 mW/cm^2) using the benchtop dip method and found increased mineralisation, ALP, runx2, msx2, dlx5, osx, bsp and bmp-2 mineralisation markers.

A well-controlled study by Li et al. [136] used the absorption tube method with a Sonopuls 490 (Delft, NL) to deliver LIPUS (1 MHz; pw 2 ms; prr 100 Hz; I_{SPTA} 200 mW/cm^2) for 15 minutes to primary rat osteoblasts. The exposure conditions and spatial characteristics of the LIPUS field were fully reported. The device was held in the far field and temperature of the medium was monitored (although temperature effects at the cell layer can still not be discounted). They found increased PGE2 expression and cell density, with an optimal I_{SPTA} of 600 mW/cm^2. This agreed with the studies of Reher et al. [38, 40], who found increased proliferation and PGE2 (via COX-2), as well as collagen expression and nitric oxide (NO) in primary human mandibular osteoblasts. NO, like PGE2, is associated with regulatory intercellular signalling from osteocytes in response to mechanical stress [28]. Reher et al. found PGE2 and NO were stimulated at two very different LIPUS frequencies: 1 MHz (A_{ER} 2 cm^2; pw 2 ms; prr 100 Hz; I_{SAPA} 0.1 to 1.0 W/cm^2) and 45 kHz (A_{ER} 12.8 cm^2; CW; I_{SATA} 5 to 50 mW/cm^2). They also found proliferation of primary human mandibular osteoblasts increased at 1 MHz (+52% at 1 W/cm^2 I_{SAPA}). Collagen production showed a marked increase at lower intensities, with +55 % with respect to controls at 1 MHz, I_{SAPA} 0.1 W/cm^2, and +112 % at 45 kHz, I_{SATA} 30 mW/cm^2.

Another study investigating low frequency LIPUS at 45 kHz was that by Man et al [6], who exposed the MDPC-23 odontoblast-like cell line to continuous wave 45 kHz LIPUS, I_{SATA} 25 mW/cm^2 using the tank dip method. While viability remained constant, proliferation, differentiation and mineralisation all increased, along with mineralisation markers col1, alp, omd and nes.

Two studies, by Imai et al. [137] and Huang et al. [138] used primary human mandibular fracture haematoma-derived cells and directly coupled six transducers to the bases of a 6-well plate via a thin water layer and exposed to LIPUS (1.5 MHz, pw 200 µs, prr 1 kHz, I_{SATA} 30mW/cm^2, 20 minutes daily for up to 20 days). The studies found no change in proliferation, but increased mineralisation. The first study found increased expression of osteogenic markers alp, ocn, runx2, osx, opn, pth-r1 mRNA. The latter study found

increased levels of BMP 2, 4 & 7, although the levels were significantly different on different days after LIPUS exposure.

A study by Olkku et al. [69] highlighted the thermal effects of the inverted tank dip method. They exposed MG63 osteoblasts to 10-minute exposures of 1 MHz LIPUS, 1 kHz, 200μs, ISATA 41 to 407 mW/cm^2. The transducer was held 7.7 mm under the base of a 24-well plate. Temperatures up to 48°C were reported at the highest intensity. The study found activation of the wnt/β-catenin pathway via PI3K / Akt and mTOR cascades, but these were very likely due to the thermal effects induced mainly by the setup.

By contrast another two studies by Harle et al. [139, 140] involving the MG63 osteoblast cell line were well controlled. The custom tank method was employed and while a standard culture flask was used, the LIPUS field was measured *in situ* using a hydrophone (3 MHz; CW; I_{SATA} 140 to 990 mW/cm^2). The temperature was also measured *in situ* and a check on cavitation was carried out (significant temperature rises and cavitation detected at intensities greater than 500 mW/cm^2). At lower intensities the protein expression of fibronectin, and ECM protein, was increased. The study found no change in proliferation or collagen type 1 compared with controls, and decreased expression of mineralisation markers osteonectin (ON), osteopontin (OPN) and bone sialoprotein (BSP). TGF-β1 and TGF-β3 expression increased. They performed the same study on human periodontal ligament cells and found decreased levels of FN and COL1, and increased levels of ON and OPN. OPN only increased at 990 mW/cm^2, indicating cavitation or thermal effects influenced the result.

Bandow et al. [71] exposed MC3T3-E1 cells, which had been grown to mature osteoblasts for 3 weeks to 20 minutes of 1.5 MHz LIPUS (*pw* 200 μs; *prr* 1 kHz; I_{SATA} 30 mW/cm^2). This study used a controlled absorption tube method, with six transducers held 130 mm below a six-well plate in a heated water tank, with a silicon absorption chamber placed on top to eliminate reflections. They saw no difference in osteogenic markers runx2 and ocn (perhaps due to the maturity of the cells, as runx2 is an early regulator of osteogenesis [49]). The also observed a high RANKL/OPG ratio. These two proteins regulate the production of osteoclasts, and a high RANKL/OPG ratio encourages MSCs to differentiate towards the osteogenic lineage.

Finally, an intriguing study by Fung et al. [39] exposed the MLO-Y4 osteocyte cell line to LIPUS in six well plates using a modified direct coupling method where the distance from the LIPUS transducer was varied between 0 mm, 60 mm and 130 mm using rubber cylinders. The LIPUS transducers were by Exogen (Smith and Nephew, US) and were modified by the manufacturer to produce the same LIPUS characteristics at each distance (1.5 MHz; *pw* 200 µs; *prr* 1 kHz; I_{SATA} 30 mW/cm^2). The expression of β-catenin in the osteocytes (part of the Wnt - β-catenin mechanotransduction pathway) was increased at the distances 60 mm and 130 mm compared with controls. The media from the osteocytes, which should contain any intercellular signalling molecules (e.g., NO and PGE2) were then used to culture MC3T3-E1 cells, which showed reduced proliferation, increased migration (via scratch assay) and mineralisation (Alizarin red staining). The study suggested that osteocytes do indeed regulate osteoblast behaviour by chemical signalling induced by LIPUS stimulus.

Following this review of papers considering effects of LIPUS on cellular processes in Stage 3 of fracture healing, LIPUS exposure may:

- Up-regulate proliferation, migration, collagen production and mineralisation of osteoblasts.
- Activate calcium ion channels to release calcium and further promote mineralisation.
- Stimulate the FAK and ERK mechanotransduction pathways via Integrins
- Up-regulate the expression of PGE2 via the enzyme COX2 and the above mechanotransduction pathway.
- Up-regulate nitric oxide (NO), another intercellular signalling protein which is expressed by osteocytes in response to mechanical stress.
- Increased mineralisation correlated with increased expression of various osteogenic markers, such as runx2, ocn, alp, opn and osx.

2.3.1.4 Summary of in vitro findings

To attempt to draw some conclusions from the overall findings of *in vitro* LIPUS studies, we must look to those studies with most control and definition of the LIPUS field applied

to the cells, and where secondary effects such as cavitation and temperature rise have been directly discounted or are unlikely.

The majority of the studies described used the direct coupling technique, which we have established are prone to thermal effects. Therefore, these studies can only be considered if the temperature is monitored. The benchtop dip technique is also prone to reflections and thermal effects and so cannot be seen as reliable. In fact, the number of controlled LIPUS studies to draw results from is very limited. From the results of the most controlled studies, we can conclude that there is evidence to support the following statements:

- LIPUS may increase proliferation and collagen expression of fibroblasts [19].
- LIPUS may increase expression of VEGF by fibroblasts, osteoblasts and monocytes [38].
- LIPUS may up-regulate migration and proliferation of MSCs and their differentiation to the osteogenic lineage, perhaps by the stimulation of a key osteogenic transcription factor RUNX2. [44].
- LIPUS may stimulate expression of aggrecan and release of intercellular calcium ions (Ca^2+) and promotes endochondral ossification of chondrocytes [124-126].
- LIPUS may increase PGE2 expression of osteoblasts via COX-2, which may be up-regulated via the integrin-mediated FAK and ERK mechanotransduction pathways [40, 128], [136].
- LIPUS may stimulate the Wnt-β-catenin pathway in osteocytes, which in turn regulate osteoblast migration and mineralisation [39].

The optimal physical properties of LIPUS fields found to induce potentially healing effects in clinical, *in vivo* and *in vitro* studies are:

- I_{SATA} from 15 mW/cm^2 to 140 mW/cm^2
- Pulse repetition rates of 100 Hz or 1 kHz.

The ultrasound frequency does not appear to affect cellular responses to a great extent, with effects reported at 45 kHz [19, 38, 40], 1 MHz [19, 38, 40, 125] and 1.5 MHz [124] in the most controlled studies. The *in vivo* and *in vitro* work by Argadine and Greenleaf, who compared the effects of 1 MHz LIPUS at the pulse repetition rate of 1 kHz with an

equivalent continuous wave field at the same frequency, strongly supports their hypothesis that it is the cyclic radiation force of LIPUS that provides the physical stimulus promoting healing effects [87, 120]. This is further supported by studies applying direct 1 kHz vibration to MSCs [121]. Effects were also reported at pulse repetition rates of 100 Hz, suggesting a range of possible pulse repetition frequencies, though there is limited evidence for other repetition rates. The next two sections discuss the biological mechanisms that are the main focus of research into LIPUS stimulation.

2.3.2   LIPUS Mechanisms

2.3.2.1   Thermal Effects

Thermal effects have largely been discounted as a LIPUS mechanism based on animal studies, the low intensities involved, and the small changes in temperature ($<1°C$) noted in early trials [113, 141]. It has already been established that some *in vitro* setups induce large changes in temperature due to either transducer self-heating, standing waves or vibration modes induced in plates. Therefore, temperature should always be monitored during *in vitro* trials to rule out thermal effects in the cellular responses. However, small changes in temperature due to LIPUS exposure are still likely, there will always be some heating due to the ultrasound energy travelling through and being absorbed by the tissue [109]. This is especially true at the soft tissue / bone boundary where a portion of the ultrasound will be reflected and might result in a higher amplitude of vibration, which would likely induce more heating [108]. As already discussed, it is well established that heating causes cellular effects and even healing in bone tissue [52, 53].

2.3.2.2   Piezoelectricity

In 1983 Duarte proposed the healing effects of LIPUS were due to the vibration inducing a piezoelectric effect in bone following his *in vivo* studies on rabbit femurs and fibulae [82]. The piezoelectric properties of bone were first reported by Fukada and Yasuda in 1957 [142], who found that a shearing force applied to dried, *ex vivo* bone induced an electric field when the direction of the force caused the crystalline structure aligned to the collagen fibres to rub against each other. Later in 1981, Behari and Singh [143] detected an electrical signal of 64 µV within *in vivo* bone in response to ultrasound at the low intensity of 3.8 mW/cm^2.

Recent work has shown that electrical potentials can be induced in cortical bone in the MHz range. Okino et al. [144] were able to fabricate an ultrasound transducer using bovine cortical bone, inducing a voltage of 120 µV pk-pk from a 10 kPa pk-pk excitation signal in the frequency range 0.7 to 2.5 MHz. The voltages induced by LIPUS may be large enough to open voltage-gated calcium ion channels in the cell membrane, which require voltages in the order of a few tens of millivolts to activate directly [145]. Taking the measurements from the Okino paper as a guide, the pk-pk pressure of the LIPUS field would have to be around 1700 kPa to induce voltages over 20 mV. It will be shown in Chapter 3 that LIPUS fields are likely to involve pressures much less than this. Though the potentials induced by vibration may contribute to healing effects, in more subtle ways, I consider it unlikely to be the main mechanism of LIPUS healing.

2.3.2.3 Direct stimulus of vibration modes of cellular structures

Another possible mechanism could be direct mechanical stimulus of structures in the cells. Louw et al. [146] argued that cell nuclei could be directly affected by ultrasonic fields, bypassing the integrin or ion channel pathways and directly affecting nuclear processes. They modelled a bovine chondrocyte and predicted that cytoplasmic and nuclear stress was maximised at a frequency of 5.2 MHz. *In vitro* exposures of bovine chondrocytes at 2, 5 and 8 MHz showed enhanced expressions of early response genes c-fos, c-fun and c-myc, which regulate proliferation and differentiation, were maximised at 5 MHz, with no corresponding phosphorylation of ERK, the principal pathway for those genes. This is an intriguing result but as the required frequency is significantly higher than the typical LIPUS frequency, it was not considered further in this study.

2.3.2.4 Mechanotransduction

It is well established that bone reshapes and remodels itself in response to mechanical stimuli. The concept was first suggested in the 19th century by the German anatomist Culmann [147], who observed that the patterns of mineralised structures in trabecular bone aligned with the principal stress directions formed by functional loading. Later Julius Wolff proposed a simple mathematical model relating the shape of bone to mechanical stress, which became known as Wolff's law of bone transformation [25]. Over the years the theory has evolved and become more complex, but the basic concept is that bone tissue is sensitive to, and adapts to, its mechanical environment.

The main mechanical stimulus experienced by bone is due to muscle activity during movement or exercise. The tensile forces from muscles, combined with compressional forces from movement and gravity, induce bending moments along the long bones of the limbs [148]. This induces a number of phenomena known to stimulate mechanotransduction pathways in bone cells (see Figure 2.2).

First, there is a direct deformation (strain) of the osteocytes embedded in the calcified matrix and the osteoblast-like lining cells. Bending also induces interstitial fluid flow in the lacuna-canalicular network, resulting in shear stresses along the processes and membranes of the embedded osteocytes (Figure 2.2). This fluid flow also creates a streaming potential between the two sides of the bone, resulting in electrical stimulation that may encourage mineralisation by opening voltage-operated calcium ion channels in cell membranes [25].
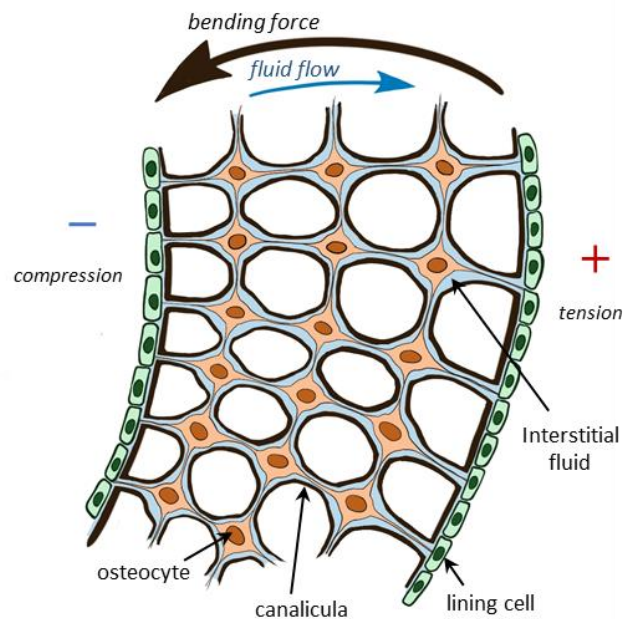
Figure 2.2 Sketch of stimulating phenomena induced in bending bone.
Own illustration based on figures from two sources [25, 149]. The bending force induces a direct strain in the embedded osteocytes. The compression and tension differential induces interstitial fluid flow through the canaliculae, applying shear stress to the osteocyte processes. Flow of charged ions within the interstitial fluid also induces electrical streaming potentials.

LIPUS has already been shown to induce movement of bone ends and surrounding tissues by Greenleaf et al. [87], where bone ends moved at the same frequency as the LIPUS pulse repetition rate (1 kHz), likely caused by the cyclic radiation force of the LIPUS pulse. The

bone ends moved at a velocity of 1 to 2 µm/s at the 1 kHz rate, suggesting the overall amplitude of movement was 10 to 20 nanometres. A seemingly small movement but at the cellular level, with human osteoblast and osteocyte diameters being 20-50 µm and 5-20 µm respectively, such a displacement would represent a strain ($\Delta L/L$) of around 1000 microstrains ($\mu\varepsilon$). This is within the range of strain amplitudes of 500-2000 $\mu\varepsilon$ measured *in vivo* during moderate to vigorous exercise by Burr et al. [150]. The frequency of bone end movement induced by LIPUS is higher than those induced by exercise. The strains observed by Burr were governed by step rate, at around 1-2 Hz, although shorter pulses of around 10 Hz were also present. A recent study by researchers at the University of Glasgow demonstrated up-regulation of MSC osteogenic differentiation when stimulated with direct 1 kHz vibration with vertical displacements of 22 nm [122].

A finite element study by Wang et al. [151] found the structure of the lacuna-canalicular network and embedded osteocytes, with long cell processes running through tiny fluid-filled cavities, amplified strain under cyclic loading. This amplification increased with frequency, reaching a peak gain of 3.4 at 100 Hz (the pulse repetition rate of some LIPUS systems). This would result in strain amplitudes significantly higher than those measured by Burr et al. Therefore, it is feasible that LIPUS induces the levels of strain required to excite the mechanotransduction pathways of embedded osteocytes.

Fluid flow induced by LIPUS in the lacunae canalicular structure was predicted in a computational study by Baron et al [152] using a finite element model. They found shear stresses of up to 1.5 Pa were induced by a LIPUS field at the walls of the lacuna-canalicular system. This result was reproduced by Weinbaum et al. [153]. These levels of shear stress have been shown to trigger mechanotransduction pathways in osteocytes and osteoblasts [154]. Osteocytes are known to produce signalling molecules such as PGE2 and NO in response, which are thought to up-regulate the osteogenic differentiation of MSCs [48, 155, 156]. In the case of a fracture, osteocytes in the neighbouring bone tissue are also thought to regulate the fracture healing by recruiting MSCs to the site [28].

Mechanotransduction pathways are complex and still the subject of ongoing research. In general, these pathways consist of chains of proteins that form a link between receptors on the cell membrane to the cell nucleus, transducing environmental signals from outside the cell membrane to the cell nucleus. One such pathway associated with LIPUS is the

pathway involving MAPK (Mitogen-Activated Protein Kinases) and ERK (Extracellular signal-Related Kinase). The receptor is switched 'on' when a signalling molecule binds to it, or in the case of integrins or certain calcium ion channels, in response to mechanical strain. The receptor and proteins in the chain communicate by adding phosphate groups to neighbouring proteins, resulting in a signalling cascade along the chain to the cell nucleus. When this chemical signal reaches the nucleus it can trigger a change in the cell, such as expression of certain genes, production of RNA to build certain proteins, and/or cellular responses such as mitosis (division), apoptosis (death) or differentiation. Figure 1.6 in Chapter 1 illustrates the mechanotransduction pathways involved in osteogenesis. Figure 2.3 shows the mechanotransduction pathways of an osteocyte. From the available evidence there appears to be much cross-talk and interplay between pathways and as such it is difficult to isolate a single path to gene expression.

All the above pathways have been implicated in various LIPUS studies. The Wnt pathway was stimulated in osteocytes in the osteocyte / osteoblast study by Fung et al [39]. The FAK and Akt (including PI3K) pathways were stimulated in [41], [55] and [65]. The ERK [41, 110, 114, 119, 131] and P38 [46, 114, 119, 123, 130] pathways were also implicated, along with the related MAPK pathway [55], [123]. Integrin expression is often implicated [111]. Hu et al. [157] used the direct coupling method to treat human periodontal ligament cells with LIPUS (1.5 MHz, pw 200 µs, prr 1 kHz, I_{SATA} 30, 60 & 90 mW/cm^2) and found maximum effect with treatment times of 20 minutes per day at 90 mW/cm^2, with stimulation of ALP, runx2, integrin β1, osteocalcin and an increase in mineralisation. All effects were inhibited by Integrin β1 inhibitor, strongly suggesting a mechanotransduction pathway was involved.
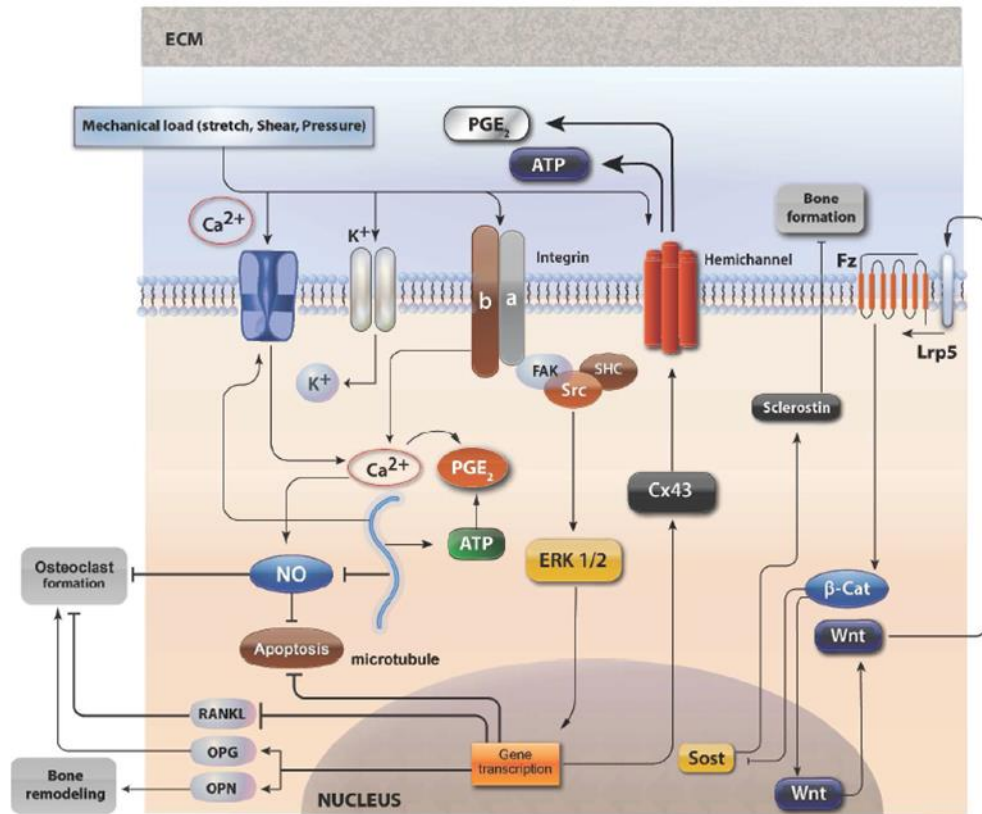
Figure 2.3: Mechanotransduction pathways of the osteocyte, reproduced from [158]. The diagram illustrates the regulatory role of the osteocyte in bone formation or resorption, by expression of signalling compounds to decrease or increase osteoclast formation. Mechanical loads, such as fluid shear stresses, activate calcium channels in the membrane and trigger an influx of calcium ions (Ca^{2+}). Ca^{2+} promotes PGE2 synthesis and inhibits NO generation. Integrins on the cell membrane also respond to mechanical stress and are linked to ERK1/2 stimulation, which induces transcription of Cx43 to enable release of PGE2 and ATP via connexin hemichannels. PGE2 and NO are thought to act as intercellular messengers to stimulate bone formation. Bone formation is further stimulated by β-catenin and the associated Wnt pathway via mechanical stimulus of primary cilia. Wnt is suppressed by expression of sclerostin, a negative regulator of bone formation.

Another pathway implicated in LIPUS studies [115], [119], [125, 126] are calcium ion channels, shown in Figures 1.6 and 2.4, and also referred to as piezo channels when activated by voltage or cation channels which are activated by stretching of the membrane. Calcium ions are a major intercellular signalling mechanism used throughout the body for fast responses to stimuli, including bone remodelling in response to movement [159]. LIPUS is thought to act directly on the stretch-activated channels, but these channels can also indirectly encourage activation of the piezo channels [119], [159]. Figures 1.6 and 2.4 illustrate that these channels not only control the release and intake of calcium ions to the cell, which is important for inter and intra-cellular homeostasis, but are also linked to the expression of PGE2.

The available evidence leads to the hypothesis that the most likely physical mechanism of LIPUS is the movement of bone induced by the cyclic radiation force. This movement stimulates the mechanotransduction pathways of osteocytes and osteoblasts by either direct vibration or the increased fluid flow in the lacuna-canalicular system, inducing a variety of healing responses through intercellular signalling, including differentiation of MSCs to the osteogenic lineage, proliferation of preosteoblasts and differentiation and mineralisation of osteoblasts. To reproduce these complex processes would require the structures of bone to be present in any study. In order to begin to do this *in vitro* there is a need to grow the cells in a 3D environment as close to bone tissue as possible. A number of 3D LIPUS studies have already been conducted, and these are examined in the next section.

2.3.3   3D *in vitro* LIPUS studies

The final consideration for this review are 3D *in vitro* LIPUS studies. As established in the previous section, the 3D *in vivo* environment affects not only the physical phenomena induced by LIPUS (e.g., fluid flow in the canalicular network) but also the morphology, behaviour of cells, and even the ability to study intercellular interactions in co-cultures. In 2007, Noriega et al. [160] cultured primary human chondrocytes in 3D scaffolds, noting that the 3D environment encouraged the chondrocytes to maintain their phenotype. Cultured in a monolayer, the cells were prone to reverting to a fibroblastic phenotype. Once seeded in the scaffolds (made up of a porous membrane of chitosan polymer) the cells were exposed to continuous ultrasound twice in one day, consisting of 1.5 MHz for 161 seconds, 5 MHz for 51 seconds or 8.5 MHz for 24 seconds. The benchtop dip method was used but multiple exposures were highly likely as more than one scaffold was present in each culture dish. The exposure intensity was estimated to be less than 30 mW/cm^2 in each case (no further details of LIPUS field given). They found that LIPUS treatment increased cell viability, Type II collagen and expression of aggrecan mRNA compared to controls. Although the LIPUS exposure method was crude, this study highlights that it is possible to grow cells in a more *in vivo*-like 3D environment and shows the potential of 3D cultures to more realistically mimic the biological and physical conditions *in vivo*.

More recently, Veronick et al [161, 162] cultured MC3T3-E1 preosteoblast cells in collagen hydrogels and exposed these to LIPUS (20 minutes, 1 MHz, *prr* 1 kHz, *pw* 200 μs, I_{SATA} 30 mW/cm^2 and 150 mW/cm^2). Cells were also seeded on 2D culture ware and exposed to the same LIPUS field (exposure method not reported). Both PGE2 and

COX-2 mRNA expression were up-regulated significantly in the 3D cultures as compared to 2D controls, and those exposed to LIPUS were up-regulated further, with optimum intensity 30 mW/cm^2.

In 2014, Vazquez et al [163] came up with an intriguing method of investigating mechanical loading on bone (note this was not a LIPUS trial). This study involved a 3D co-culture system, where MLO-Y4 osteocytes were embedded in Collagen hydrogel and MG63 osteoblast cells were layered on the top surface, thus mimicking to some extent the layer of osteogenic cells in the periosteum of bone. The co-culture was mechanically loaded by cyclic compression of the gel with $4000 - 4500$ µε. PGE2 was up-regulated in the osteocytes in response to the loading, and Type 1 pro-collagen was also increased.

Finally, more recent research has used 3D-printing techniques to print and seed collagen gels, and even to print with polymers doped with hydroxyapatite crystals to more closely mimic the 3D structure of bone [164]. So far only simple lattice-patterned matrices have been printed, but it could be possible in future to 3D print more complex shapes and perhaps even reproduce something like the lamellar structures of cortical bone or the random structure of woven bone. This could pave the way for mimics of bone tissue structures, to attempt to recreate the LIPUS fields and fluid flows that may result in a healing stimulus.

2.4 Chapter Summary and Study Aims

2.4.1 Chapter Summary

Chapter 2 presented a comprehensive literature review of LIPUS research, from first discoveries through *in vivo* studies and clinical trials, to *in vitro* studies that have attempted to find the physical and cellular mechanisms for LIPUS healing. Early *in vivo* and clinical studies showed promising results and led to the approval of the Exogen LIPUS device (1.5 MHz, 200 µs, 1 kHz, I_{SATA} 30 mW/cm^2) as a treatment for non-union fractures. However, a more recent review of clinical trials questioned the benefits of LIPUS, citing a recent independent, controlled clinical trial that showed no significant improvements in healing rates. This was not helped by a failure of the many *in vitro* trials to find a healing mechanism, with the use of different apparatus between trials with varying controls over the LIPUS field, as discussed in Section 1.3. Section 2.3.1 reported the general findings of

in vitro LIPUS studies, and the studies considered are summarised in Appendix A. Drawing conclusions from these studies is a difficult task due to the myriad of observations and pathways considered and, in some cases, conflicting findings between studies.

Comparing results of the most controlled studies in Section 2.3.1.4, it can be concluded that LIPUS may:

- Increase proliferation and collagen expression of fibroblasts [19].
- Increase expression of VEGF by fibroblasts, osteoblasts and monocytes [38].
- Stimulate osteogenic differentiation of MSC's [44].
- Stimulate expression of aggrecan and release of intercellular calcium ions (Ca^2+), and promotes endochondral ossification of chondrocytes [124-126].
- Increase PGE2 expression of osteoblasts via COX-2 [40, 128], [136].
- Stimulate the Wnt-β-catenin pathway in osteocytes, which in turn regulate osteoblast migration and mineralisation [39].

From the review of possible LIPUS mechanisms in 2.3.2, the most promising physical mechanism is the cyclic movement of bone in sympathy with the cyclic radiation force of the LIPUS pulse, as demonstrated by Argadine, Greenleaf *et al.* in their *in vivo* studies [87, 120]. This movement is of a similar magnitude to mechanical strains resulting from physical exercise, which are known to stimulate the mechanotransduction pathways of osteocytes and osteoblasts by either direct vibration or the increased fluid flow in the lacuna-canalicular system. These mechanotransduction pathways stimulate intercellular signalling (mainly by osteocytes), which in turn triggers up-regulation of a variety of healing responses, such as osteogenic differentiation of MSCs, proliferation of preosteoblasts and differentiation and mineralisation of osteoblasts. More recent studies have also confirmed that osteogenic differentiation of MSCs is up-regulated by direct vibration of the same frequency and magnitude observed by Argadine and Greenleaf [121, 122]

This hypothesis suggests that the healing mechanisms are reliant upon the interaction of the LIPUS field with tissue and bone *in vivo*. However, *in vitro* studies have observed significant cellular responses to LIPUS exposures in standard culture ware, which is a very different environment. The review of exposure methods in Section 1.3 established that the

apparatus in many of these studies could induce reflections, vibrations and thermal effects that may not occur to the same degree *in vivo*. This thesis also explores the feasibility of using 3D methods to investigate cellular responses to LIPUS in 3D growth environments more like physiological bone.

2.4.2 Study Aims

Following on from the examination of the bone healing process, the possible physical and healing mechanisms of LIPUS stimulation, examination of exposure apparatus and the results from LIPUS studies in the literature, the aims and objectives of this study are listed briefly below and then discussed in more detail in the paragraphs that follow.

- Design and build a controlled *in vitro* LIPUS exposure system to minimise the effect of the apparatus on the LIPUS field, plate vibrations and thermal effects.
- Investigate the characteristics of LIPUS fields and select suitable devices to reproduce the required fields in conjunction with the controlled exposure system.
- Use the controlled exposure system to investigate cellular responses to direct LIPUS stimulus.
- Choose a suitable cell model to attempt to replicate results in the literature and to demonstrate behaviour close to those of bone cells *in vivo*.
- Choose a mix of cellular markers that are suspected to be affected by reflections, vibration and thermal effects induced by the apparatus of previous studies, and those that were consistently observed regardless of the exposure method.
- Choose other cellular markers and exposure conditions to investigate the most likely mechanisms (e.g., the physical mechanism of cyclic radiation force with fast/slow rise time; markers associated with mechanotransduction and mineralisation)
- Analyse the results to determine which markers were likely affected by apparatus (i.e., no significant change observed in samples exposed to LIPUS compared to controls), and if any were sensitive to the direct LIPUS stimulus alone (i.e., significant change in LIPUS-treated samples compared to controls).
- Assess the results to determine the LIPUS exposure conditions (if any) that produced the most significant cellular responses.

- Investigate the feasibility of using 3D-printed growth surfaces for LIPUS study, with the eventual aim of investigating cellular effects of LIPUS in environments more like the physiological structure of bone.

The design and development of the LIPUS exposure system is described in Chapter 4. The system is designed to minimise secondary effects such as reflections, plate vibrations and heating being introduced by the apparatus. It is recognised that reflections, vibration and heating do occur *in vivo*. For instance, mineralised bone is known to reflect ultrasound and reflections at the tissue-bone interface are known to produce localised pressure peaks and localised heating [108]. However, the magnitudes of these effects are likely to differ significantly between *in vivo* conditions and lab conditions. By isolating this one part of the stimulus we can rule in or out the direct stimulus as being one of the physical mechanisms that produces healing effects in real fractures, make the ultrasound field applied to the cells more repeatable and make results more likely to be replicated in other laboratories. Designing such an exposure system also allows the pressure fields of LIPUS transducers to be characterised in free-field conditions in a standard scanning tank using a needle hydrophone and removes the need for making in-situ measurements. If using off-the-shelf commercial LIPUS devices without any characterisation, such a system would also mean the cells were exposed to intensities close to the effective intensity provided in the manufacturer's data.

The MC3T3-E1 murine preosteoblast cell line was chosen as an appropriate cell model because it exhibits many of the behaviours of preosteoblasts *in vivo*, differentiates to mature osteoblasts and mineralises. This cell line was also used in many of the *in vitro* studies discussed in the literature review. The choice of cell line is discussed in more detail in Chapter 3, along with the cell culture and immunocytochemistry methods used to test for cellular markers of healing. Chapter 3 also describes the investigations undertaken of LIPUS fields and the final selection of devices to use in the LIPUS exposure studies.

Cellular markers were chosen from the healing markers associated with osteoblasts in the LIPUS studies described in Chapter 2. These markers and reasons for selection are described in the following paragraphs.

Proliferation

Preosteoblasts proliferate until the available growth area is exhausted, at which point they tend to start differentiating and laying down the mineralised matrix. Therefore, early up-regulation of proliferation in preosteoblasts at a fracture site can stimulate faster healing by populating the site with preosteoblasts faster and therefore ultimately speeding up mineralisation, which is the ultimate goal.

Some studies in the literature found LIPUS exposure up-regulated proliferation of preosteoblasts [46, 129], while others found no effect [132, 135]. These mixed outcomes suggested proliferation might be stimulated by secondary effects of the exposure apparatus rather than the ultrasound itself.

Prostaglandin E2 (PGE2)

The expression of PGE2 is up-regulated in bone cells in response to mechanical stress and is an important intercellular signalling protein in bone healing. Tang et al. [41] and Reher et al. [40] found PGE2 expression in primary murine osteoblasts and MC3T3-E1 preosteoblasts were up-regulated at 24 hours post-exposure, and that this was induced by COX-2 via the integrin-mediated mechanotransduction FAK / PI3K / Akt and ERK pathway. The Tang paper used the benchtop dip method, which was likely to be subject to secondary effects described in Chapter 1. Reher also found it increased using the tank dip method. Indeed, PGE2 was consistently up-regulated by every LIPUS study that investigated it as a marker. This means PGE2 is a candidate for a marker that might be affected by direct LIPUS exposure.

Genetic mechanotransduction markers – Integrin β5 (itgb5) and Cyclo-oxygenase-2 (cox2)

Integrin β5 (itgb5) and Cyclo-oxygenase-2 (cox2) RNA expression was investigated, to assess more markers of Integrin mediated FAK/AkT/ERK mechanotransduction pathway associated with COX-2 and PGE2 protein expression by Tang et al. [41]. Like PGE2, COX-2 and its associated mRNA marker were consistently up-regulated in all studies where it was assessed.

Itgb5 was not the optimal integrin for this study (see the covid-19 impact statement). Integrin β5 is associated with exercise-induced mechanotransduction in bone [165] but it is more present in the surrounding muscles, which are stimulated to up-regulate irisin and this hormone stimulates the strengthening of bone tissue. It is not thought to be associated with the osteoblast or osteocyte mechanotransduction pathways. The Future Work section (7.4) describes the integrins that should be the focus of any investigation of mechanotransduction in the future.

Genetic markers for mineralisation were chosen to investigate if the ultrasound stimulus of LIPUS alone could up-regulate osteoblast mineralisation. All of these markers, described in the following paragraphs, were observed to have mixed responses to LIPUS exposure in the *in vitro* studies discussed in the literature review.

Collagen Type 1 (col1)

Col1 makes up the majority of the hard collagenous matrix laid down by mineralising osteoblasts. This mineralisation marker was not assessed in many LIPUS studies but was reported as being up-regulated in response to 45 kHz LIPUS [6] and exhibited no change in two more controlled LIPUS studies using the absorption tube method [71] and custom tank method [140].

Osteocalcin (ocn) and Osteopontin (opn)

OCN and OPN are matrix proteins that form part of bone and are also secreted by mineralising osteoblasts, in smaller quantities compared to COL1. Both proteins are necessary for binding and aligning the collagen ECM to hydroxyapatite crystals. OCN is used as an indicator of osteoblast activity because it is only produced by osteoblasts when they are synthesising the organic matrix [166]. OCN, or its genetic marker ocn, was generally found to be up-regulated in LIPUS *in vitro* studies [131, 132, 135] but no change was found in a study with more controlled exposure condition (using the absorption tube method) [71]. OPN is also laid down by osteoblasts during mineralisation and has multiple functions, including providing a site for binding of osteoclasts during bone remodelling. OPN (or opn) was also observed to have mixed responses to LIPUS in the literature, with a number of studies finding up-regulation after LIPUS exposure [56, 131, 134] and one more controlled study (custom tank method) finding opn levels reduced [140].

Runt-related Transcription Factor (runx2)

Runx2 was chosen as a marker because it is an early regulator of osteoblast differentiation. The up-regulation of runx2, an early regulator of mineralisation, was observed in a number of LIPUS trials in MSCs, preosteoblasts, osteoblasts and odontoblasts (dental cells similar to osteoblasts) [44, 56, 70, 131, 134, 137, 157]. Runx2 was up-regulated in all studies except one [71].

All the studies where the mineralisation markers runx2, col1, opn and ocn, were up-regulated used the direct coupling method, whereas more controlled methods such as [71] resulted in no change or a reduction in the markers. This suggests the mineralisation of osteoblasts may be sensitive to one or more of the secondary effects induced by the direct coupling method (i.e., reflections, direct vibration and/or heating). Therefore, direct LIPUS stimulus alone might not have an effect on these markers.

Table 2.1 summarises the *in vitro* LIPUS exposure studies conducted using the LIPUS exposure system, with the overall purpose and cellular markers assessed. PGE2 was assessed throughout all the studies because this was consistently up-regulated in all *in vitro* LIPUS studies where it was considered in the available literature.

Study	Purpose	Cellular markers assessed
Pressure Amplitude Study (4.3)	Assess exposure method and establish the LIPUS pressure amplitudes required to illicit the optimal cellular response	Proliferation, PGE2
Frequency Study (4.4)	Compare cellular responses to 1 MHz LIPUS and 45 kHz LIPUS	Proliferation, PGE2
Rise Time Study (4.5)	Investigate cellular responses to LIPUS with fast and slow switch-on of cyclic radiation force.	Proliferation, PGE2, genetic markers cox-2, itgb5, col1, ocn, opn & runx2

Table 2.1: Summary of in vitro LIPUS exposure studies conducted in this work. Method sections are given for each study, along with the study purpose and cellular markers assessed.

Finally, another aim is to assess the feasibility of growing cells on 3D-printed scaffolds in an attempt to introduce a growth environment closer to *in vivo* conditions. Bone cells such

as preosteoblasts, osteoblasts and osteocytes display differences in morphology and cellular behaviours in 3D environments compared to standard two-dimensional culture vessels. 3D-printed scaffolds are used by researchers to investigate their efficacy as bone graft material [164]. Some LIPUS researchers have used hydrogels to create 3D culture environments to test the effects of LIPUS and vibration in a growth environment more like *in vivo* [162, 167]. In this work the use of stiffer scaffolds, to mimic the stiffness of mineralised bone, was investigated. The scaffolds were simple lattice structures but other structures could also be printed. The simple scaffolds were used to test the feasibility of the method.

In summary, the body of work in this thesis provides controlled LIPUS exposure methods, investigates cellular responses of preosteoblasts to the ultrasound stimulus of LIPUS with minimal secondary effects from the apparatus, and proposes feasible 3D methods with the end goal of growing bone cells on 3D structures that mimic the *in vivo* structures of bone. The methods adopted are described in detail in the next two chapters.

CHAPTER 3
CELL CULTURE METHODS AND ULTRASONIC DEVICES

This chapter details the cell culture methods and ultrasonic devices used in the *in vitro* LIPUS exposure studies. The chosen cell line is described along with cell culture methods, staining of live and fixed cells for counting cells in proliferation trials, the quantification of Prostaglandin E2 in growth media by enzyme-linked immunosorbent assay (ELISA), and the identification and quantification of RNA markers associated with mineralisation and the mechanotransduction pathway resulting in up-regulation of PGE2. The ultrasonic devices used to produce LIPUS fields are also described, along with the results and analysis of pressure field measurements of devices used in the LIPUS exposure trials.

3.1 Cell Culture and Immunocytochemistry

3.1.1   Cell line and culture methods

3.1.1.1 MC3T3-E1 cell line

Cell experiments were performed using the murine preosteoblast cell line MC3T3-E1 [168]. This cell line was chosen as the optimum animal model for the preosteoblast phenotype, as it has been shown to mineralise to extracellular matrix with similar structure as observed *in vivo*, and expresses high levels of mRNA of mineralisation markers such as bone sialoprotein (BSP) and osteocalcin [169]. It was also used in past *in vitro* trials studying LIPUS mechanisms, most notably the study by Tang et al. [41] linking LIPUS with COX-2 and PGE2 up-regulation via the Integrin / FAK / PI3K / Akt / ERK mechanotransduction pathway, and the study by Man et al. [45] comparing 1 MHz and 45 kHz LIPUS effects on osteoblast migration. The following sections describe procedures for cell culture, staining and immunocytochemistry followed throughout *in vitro* trials. All cell work was conducted in a Class II Biological Safety Cabinet (Thermo Scientific MSC Advantage 1.2 m). Volumes above 1 ml were transferred via sterile disposable serological pipettes and pipettor. Volumes below 1 ml were transferred via standard micropipettes (Gilson) with sterile disposable tips.

The MC3T3-E1 cell line (Subclone unknown, ATCC, US) is a preosteoblast cell line derived from primary mouse calvarial cells, i.e., from the top of the skull. It is used for preosteoblast and osteoblast *in vitro* testing because it has been shown to proliferate, differentiate to osteoblasts and osteocytes, and mature and mineralise in a similar manner to preosteoblasts *in vivo*. When cultured in αMEM growth media with no ascorbic acid, consisting of 89 % MEM-α (Gibco A1049001), 10 % Fetal Bovine Serum (Gibco 10270106) and 1 % Penicillin-Streptomycin (Gibco 15140122), the MC3T3-E1 cell line proliferates but does not mineralise. When this base media is supplemented with ascorbic acid (AA) and β-glycerol phosphate (BGP) [127] the cell line differentiates, matures and mineralises. Media supplemented with these nutrients, usually in the concentrations of 50 µg/ml AA and 10 mM BGP, is known as osteogenic media as it is used to induce osteogenic differentiation of stem cells [170] and osteoblast-like cell models, including MC3T3-E1 [169]. AA (or vitamin C) plays a vital role in mineralisation by enabling the correct folding of collagen into stable triple helix molecules [171]. A lack of vitamin C is known to cause the bone-deforming disease scurvy, illustrating the vital role it plays. β-glycerol phosphate is added to provide phosphate ions needed for the production of hydroxyapatite crystal formation during mineralisation [170].

A study by Franceschi et al. [172] compared the expression of osteogenic markers of the MC3T3-E1 cell line grown in base media and in osteogenic media. With base media alone, levels of osteogenic genetic markers remained low and no mineralisation took place. The addition of ascorbic acid and β-glycerol phosphate to the growth media enabled mineralisation and significantly up-regulated the mineralisation markers alkaline phosphatase (ALP), osteopontin (OPN) and osteocalcin (OCN).

A later study by Wang et al. [173] established that this ability to mineralise was limited to subclones 4, 14 and 24 of MC3T3-E1. The exact subclone of MC3T3-E1 cells used in this study are unknown, but their ability to mineralise was verified by biomedical engineering researchers at the University of Glasgow in previous studies [174].

Another consideration when using the MC3T3-E1 cell line is the potential loss of the preosteoblast phenotype with continuous passaging (or subculturing). This is an essential process for obtaining the cell population sizes required for *in vitro* testing and involves growing cells to confluence (usually in culture flasks), detaching them and dividing the

detached cells between new culture flasks to increase cell numbers. A study by Yan et al [175] revealed the cell line loses its preosteoblast phenotype and ability to mineralise after 30 passages. Thus, the passage number was closely monitored in this study. A stock population of cells were established and cryogenically frozen in vials each containing 500,000 cells at passage 16. These vials were then defrosted and grown on to seed biocells and undergo LIPUS exposure at passage 19. Exposing cells at the same passage number to LIPUS minimised the differences in behaviour and phenotype that might have occurred between cell generations.

As described in the previous chapter, the effect of LIPUS exposure on the expression of genetic markers for mineralisation by the MC3T3-E1 cell line was investigated as part of this study. The genetic markers were Collagen Type I, runx2, ocn and opn. Table 3.1 summarises the timeline and magnitude of expressions of these markers at different stages of differentiation of the MC3T3-E1 cell line after introduction of osteogenic media.

Phenotype ->	Preosteoblast	Intermediate	Mature Osteoblast
MC3T3-E1 timescales	1 to 6 days	4 to 12 days	9+ days
Runx2	++	+	-
Collagen Type I	++	++	+
Osteocalcin	-	+	++
Osteopontin	++	+	+++

Table 3.1: Differentiation of MC3T3-E1 cell line
from preosteoblast to mature osteoblast phenotype with approximate expected timescales and mineralisation marker levels based on available literature [127, 172, 176, 177]. Runx2 expression is an early marker of osteogenic differentiation. Expression is high in preosteoblasts and reduces as osteoblasts mature. Collagen Type 1 expression is high until the osteoblasts are mature. Osteocalcin expression increases with osteoblast maturity. Osteopontin has a mixed reported expression throughout osteogenic maturation but is at its highest in mature, mineralising osteoblasts.

Runx2 is an early regulator of mineralisation and is up-regulated significantly in the cell line in the first 6 days, then gradually reduces as the cell matures. Collagen Type I is also significantly expressed up to 12 days after introduction of osteogenic media, and then drops off at 9+ days. Osteocalcin is a late indicator of mineralisation, which is up-regulated from 4 to 12 days then significantly so from 9 days plus. Osteopontin is more variable throughout the mineralisation process, being at high levels of expression from 1 to 6 days then dropping off in the intermediate (4 to 12 days) period and then significantly increasing at 9+ days.

3.1.1.2 Cell culture methods

The process of culturing the MC3T3-E1 was as follows. A 25 cm^2 culture flask of MC3T3-E1 cells at passage 14 was obtained and the cells cultured in tissue culture flasks at seeding densities of 10,000 cells/cm^2 in base growth media. Cells were incubated at 37 °C in a humidified atmosphere of 95 % air and 5 % CO_2. The media was changed every 2-3 days. Once the cells reached 80 – 90 % confluency they were sub-cultured (or passaged) using the following procedure. After washing with modified Dulbecco's Phosphate Buffered Saline (DPBS, Sigma D8537, US), the cells were detached with Trypsin-EDTA 0.25 % (TE, T4049, Sigma, US). Once detached, media was added to neutralise the TE and the solution was well-mixed by gentle pipetting. A 10 µl sample was mixed with 10 µl Trypan Blue dye (0.4 %, 15250-061, Gibco, US) to enable viable cell counts in a hemocytometer. The cell mix was centrifuged (DM0412, Camlab, UK) at 100 g for 8 minutes and the liquid poured off to leave the cell ball. 1 ml warm growth media was added, and the cell-media solution mixed by gentle pipetting. The appropriate volume of cell-media solution was then added to the next set of culture flasks to achieve a seeding concentration of 10,000 cells/cm^2.

3.1.1.3 Freezing, storage and defrosting cell stock

The cells were grown on in 75 cm^2 culture flasks to obtain a large stock of passage 16 cells, which were frozen in cryo-vials (CryoTubes[TM], Nunc[TM], US) in batches of 500,000 cells to 1 ml of freezing media, consisting of 95 % base growth media and 5 % DMSO (D4120, Fisher, US). Once frozen, vials were stored in a liquid nitrogen cryo-chamber until required.

To defrost, each cryo-vial was placed in a 37 °C water bath for 2 minutes, then the contents mixed into 9 ml media pre-warmed to 37 °C in a 15 ml centrifuge tube and centrifuged at 100 g for 8 minutes. The media mixture was removed to leave the cell ball, then 1 ml warm (37 °C) media was added and mixed by gentle pipetting. This was then added to a 25 cm^2 culture flask with 5 ml media that had been incubated for at least one hour prior to seeding to warm to 37 °C and take up CO_2. This provided the optimum conditions for the cells after being subjected to the stress of freezing and defrosting.

3.1.2 Cell staining and immunocytochemistry

3.1.2.1 Cell viability staining – live cells

Cell proliferation of live cells was quantified by comparing viable cell counts before and after ultrasound exposure. Viable cells were identified by fluorescent staining. Staining of live cells in low frequency trial #1 was achieved with the ReadyProbes cell viability kit Blue/Red (Invitrogen R37610), containing two fluorescent dyes: (1) Hoechst 33342 (Ex 360 nm/ Em 460 nm), which stained the nuclei of all cells, live or dead; and (2) Propidium Iodide (Ex 535 nm / Em 617 nm) which stained the nuclei of dead cells with compromised membranes. 3 drops of Hoechst (approximately 125 µl) and 3.5 drops of Propidium Iodide (approximately 145 µl) were added per 2 ml of media to make a dye mix, which was added to each sample after removal of the original media. The samples were incubated for 15 minutes at 37 °C before imaging. After imaging the dye mix was removed and the sample washed with DPBS before either refreshing the growth media (pre-LIPUS exposure) or detaching the cells for a hemocytometer cell count (post-LIPUS exposure).

3.1.2.2 Cell viability staining – fixed cells

Staining of fixed cell samples were carried out using the Hoechst dye of the ReadyProbes kit mentioned in Section 3.1.2.1 and a live/dead fixable staining kit: either Green (Invitrogen L34969, Ex 495/ Em 520) or Far red (Invitrogen L34973, Ex 650 / Em 665). The dye in this staining kit reacts with cellular amines. Dead cells with compromised membranes allow the dye to stain amines within the cell and its nucleus, resulting in intense fluorescent staining, whereas only surface and free amines of live cells are stained at much lower intensities.

The live/dead fixable stains were activated according to manufacturer's protocol by adding 50 µl DMSO to the vial of reactive dye and mixing well. 2 µl of dye was then added to 2 ml DPBS and mixed well. Growth media was removed from each sample, followed by DPBS wash, then the 2 ml live/dead dye added. The sample was wrapped in foil to protect it from light and moisture as much as possible from this point on. After 30 minutes incubation at room temperature the dye was removed, and the sample washed three times with 8 ml DPBS. 3 ml of 4 % paraformaldehyde (PFA) was then added to fix the cells. After 15 minutes incubation, PFA was removed, and the sample washed with 10 ml DPBS. Hoechst dye mix (3 drops Hoechst in 2 ml DPBS) was added, and the sample incubated for a further 60 minutes at room temperature. The Hoechst was then removed, and the sample washed with 8 ml DPBS, then 8 ml DPBS + 1 % BSA (Bovine Serum Albumin Fraction V, Roche). Finally, 3 ml DPBS + 1 % BSA was added, and the samples stored at 4 °C wrapped in foil until ready for imaging.

3.1.2.3 Fluorescent Microscope Imaging

Images were captured using fluorescent microscopes with filter cubes capable of imaging the wavelengths corresponding to each fluorescent stain used, and integral cameras to capture the images for image processing. The microscopes used were the Olympus IX73 (pilot study and low frequency trial #1), the Leica DMi8 and the Invitrogen EVOS FL Auto 2 (all other *in vitro* trials). The cell counts were conducted using ImageJ processing software [178, 179]. Specific detail on image capture, processing and cell counting techniques are provided in Chapter 4.

3.1.2.4 Prostaglandin E2 ELISA

The concentration of Prostaglandin E2 (PGE2) in the growth media of samples was determined by Enzyme-linked Immunosorbent Assay (ab133021, Abcam, UK) according to the ELISA protocol [180]. Briefly, all reagents and samples were brought to room temperature and 1x wash buffer prepared by mixing 38 ml of sterilised deionised water with 2 ml of 20x wash buffer. Next a set of PGE2 standards were prepared by mixing PGE2 stock standard (concentration 50,000 pg/ml) in appropriate quantities with growth media to achieve seven standards (Std #1 to Std #7) with PGE2 concentrations of 2500 pg/ml, 1250 pg/ml, 635 pg/ml, 313 pg/ml, 156 pg/ml. 78.1 pg/ml and 39.1 pg/ml

respectively. 100 µl of samples under test and ELISA standards were added to each well of the supplied ELISA plate, in the layout illustrated in Table 3.2.

	1	2	3	4	…	12
A	Bs	Std #1	Std #5	Sample #3	…	Sample #67
B	Bs	Std #1	Std #5	Sample #4	…	Sample #68
C	TA	Std #2	Std #6	Sample #5	…	Sample #69
D	TA	Std #2	Std #6	Sample #6	…	Sample #70
E	NSB	Std #3	Std #7	Sample #7	…	Sample #71
F	NSB	Std #3	Std #7	Sample #8	…	Sample #72
G	B0	Std #4	Sample #1	Sample #9	…	Sample #73
H	B0	Std #4	Sample #2	Sample #10	…	Sample #74

Table 3.2: ELISA Microplate layout.
Bs = Blank: substrate only; TA = Total activity: conjugate + substrate; NSB = Non-specific binding: media + assay buffer + conjugate + substrate; B_0 = 0 pg/ml standard: media + conjugate + antibody + substrate. Std #1 to #7: standard PGE2 concentrations. All other 74 wells are test samples: sample + conjugate + antibody + substrate.

50 µl PGE2 alkaline phosphatase conjugate (PGE2-APC) was added to all wells containing PGE2 standards #1 to #7 and all samples, followed by 50 µl PGE2 antibody. The PGE2 antibodies bind with PGE2 or the PGE2-APC and are captured by the mouse IgG antibodies in each well of the pre-coated ELISA plate. The higher the concentration of PGE2, the less the PGE2 antibodies bind with the PGE2-APC.

100 µl media, 50 µl assay buffer and 50 µl PGE2-APC were added to the non-specific binding (NSB) wells to provide a measure of the absorbance in the absence of PGE2 antibodies. The B_0 wells are the 0 pg/ml standard well, to which is added 100 µl media, 50 µl PGE2-APC and 50 µl PGE2 antibody. At this point the plate is incubated for 2 hours at room temperature on a plate shaker running at 250 rpm to enable the binding process to take place. The contents of the wells were aspirated, and all wells washed with 3×400 µl of 1× wash buffer, tapping the plate firmly on lint-free paper towel to remove any remaining buffer. 200 µl p-Nitrophenyl phosphate (pNpp) substrate was added to all wells. The pNpp reacts with any APC remaining in the well (i.e., the APC that has not bound to PGE2

antibodies) to produce a yellow hue of wavelength 405 nm. Thus, the higher the concentration of PGE2 in the sample, the lower the intensity of the yellow colour. 5 µl of PGE2-APC was also added to the TA wells to indicate absorbance with full binding of pNpp to APC. The plate was incubated at room temperature for 45 minutes to allow this reaction to take place.

After the final incubation, 50 µl stop solution (trisodium phosphate) was added to all wells to halt the reaction, and the absorbance at 405 nm was read with a standard microplate reader (Infinite 200 Pro, Tecan), with a correction for the plate absorbance at 580 nm. To analyse the data, the optical densities of all wells were blanked by subtracting the optical density of the Bs well. Then the net optical density of all standard and sample wells was calculated by subtracting the average optical density of the NSB wells from the average optical density of each. The net optical densities of the standard wells were plotted and regressions performed to find the best fit to the standard curve. The best fits to the data were found by either a 4-parameter logistic regression or a log-log power regression conducted within Excel. The PGE2 concentrations of all samples were then calculated using the regression formula. Further details of the analysis of each PGE2 ELISA, along with the best fit formulae found, are given in Chapter 4.

3.1.3 Genetic markers

Testing for expression of genetic mineralisation markers, Integrins and COX-2 were carried out in these in vitro LIPUS studies (in the Rise Time Study, Trial C, Section 4.5.4.3). Expression was assessed by real-time Polymerase Chain Reaction (RT-PCR).

RNA was extracted with the RNEasy Plus Mini kit (Qiagen, DE) following the kit protocol. All surfaces and pipettes were regularly cleaned and sprayed with RNaseZap (Thermo Fisher, UK) to remove Rnase, which can break down RNA in samples. Full PPE was worn (face mask, gloves, lab coat) throughout and each step conducted in the BSC to avoid contamination.

After extracting media and storing 1 ml for the PGE2 ELISA, the top membrane of the biocell was removed and the growth surface washed with 10ml DPBS. The cells were detached with 2ml Trypsin-EDTA and the T-E, which was then neutralised with 3ml media, mixed well by gentle pipetting and then the mixed cells were stained with Trypan

Blue dye and viable cells counted via Hemocytometer. The cell mix was centrifuged for 8 minutes at 100g, then the supernatant was completely aspirated.

The RNA extraction then involved adding Buffer RLT Plus to the cell pellet (350 µl for < 5×10^6 cells; 600 µl for 5×10^6 to 1×10^7 cells) followed by the same volume of Rnase-free 70% ethanol, then mixed well by pipetting. The sample was then transferred to a RNEasy spin column in a RNEasy collection tube and centrifuged for 15 seconds at >8,000g. DNA was removed from the samples by first adding 350 µl Buffer RW1 and again centrifuging for 15 seconds at >8,000g, then adding 10 µl Dnase I stock solution to 70 µl Buffer RDD. The solution was gently mixed by inverting the tube and centrifuged briefly to collect residual liquid from the sides of the tube. 80 µl Dnase I incubation mix was added directly to the spin column membrane and incubated on the benchtop for 15 minutes, allowing any DNA to be fully digested.

350 µl Buffer RW1 was then added to the RNEasy spin column, and the mixture centrifuged at >8,000g for 15 seconds. Flow-through was discarded then 500 µl Buffer RPE added and the sample centrifuged again for 15 seconds at >8,000g. Flow-through was discarded and 500 µl Buffer RPE again added, then centrifuged for 2 minutes at >8,000g. The spin column was then placed in a new collection tube and centrifuged at 15,000g for 1 minute to remove any remaining RPE. 50 µl RNase-free water was then added directly to the membrane and the sample centrifuged at >8000g for 1 minute to elute the RNA. The eluate was then pipetted back in to the sample and centrifuged again to increase concentration of collected RNA. The final RNA sample was stored in the collection tube at -20°C, then transported to a -80 °C freezer until all samples were ready for PCR analysis.

3.1.3.1 RT-PCR

Due to COVID-19 restrictions, the real-time Polymerase Chain Reaction (RT-PCR) analysis could not be conducted in person and was instead conducted by a researcher at the University of Birmingham Dental School (see acknowledgements and covid impact statement for details). The RNA samples were couriered to site and stored at -80 °C until the analysis could take place. The following protocol is reproduced from their lab report.

cDNA synthesis from the samples were pre-formed with the Bioline Tetro cDNA synthesis kit following manufacturer's guidelines. Reference and target genes were chosen from the literature and cDNA-specific primers (Table 3.3) purchased from Merck.

Gene	Sequences	Efficiency
Housekeeping		
Gapdh	F: tgcaccaccaactgcttag – R: ggatgcagggatgatgttc	1.76
B2M	F: acccccactgaaaaagatga - R: atcttcaaacctccatgatg	2.04
ACTB	F: aacagtccgcctagaagcac – R: cgttgacatccgtaaagacc	1.8
HPRT1	F: gattagcgatgatgaacca – R: tccagcaggtcagcaaaga	1.8
YWHAZ	F: gttgtaggagcccgtaggt - R: gccaagtaacggtagtagtca	1.8
Target		
COL1	F: tagcaaaattgaggccaagg - R: ggacttgtggatcctggcta	1.76
COX2	F: gtctacaaccgcacacgt - R: aattccttactggctgtgc	1.958
ITGB5 (integrin β5)	F: gcactttcctctgtctggt - R: ttcaggaagtcacgcaccac	1.86
OCN	F: gcagagtgtgacatcattgacatcc - R: gaccgcaccttctcctccag	1.77
OPN	F: ctccagtgcaccttcatc - R: ccatgttccaccacttga	1.84
RUNX2	F: ctccagtgcaccttcatc - R: ccatgttccaccacttga	1.9

Table 3.3: Primers used in the qPCR with RNA sequences.
The process was run with five candidate housekeeping genes and the most stable candidate was used to analyse the RNA results of the target markers.

Real-time PCR reactions were performed using the Roche LightCycler480 system in a 96 well microtiter plate format with a final volume of 10 µl using 1 µl of cDNA, 5 µl Roche SYBR green I Master PCR mix, Primers at 0.5 µM, and RNase/DNase free water. Cycling conditions were: 95°C for 5 minutes (preincubation); amplification cycle 95°C for 20 seconds, 62 °C for 30 seconds and 72 °C for 30 seconds. Quantification occurs during the 72°C step of the amplification cycle. Amplification was followed by a melt curve. All samples were amplified in duplicate and two non-template controls per primer pair were included in every run.

Expression levels are obtained as crossing point (CP) values for each sample (the number of cycles required for the reaction curve to reach a chosen threshold.) by employing the second derivative max method as computed by the Lightcycler 480 software version 1.5 (Roche Diagnostics) with standard settings and following vendor instructions. PCR efficiency for each primer pair was determined using dilutions of sample cDNA (1:1 – 1:1000) and the light cycler 480 software determined plots and efficiency.

Analysis of the gene expression data was conducted with the statistical algorithm BestKeeper [181]. BestKeeper was used to assess the stability of the housekeeping genes and find the most appropriate reference. The BestKeeper program index is created using the geometric mean of the CP values of each of the candidate genes. The variation of the gene, based on CP values, is displayed along with the standard deviation and coefficient of variance. Genes with standard deviation greater than one are considered inconsistent, whilst the lowest standard deviation is considered the most stable [182, 183].

PCR efficiencies were calculated (Table 3.3). The BestKeeper expression (Table 3.4) indicated that ACTB had the lowest standard deviation and was therefore the most stable reference gene. Fold change against ACTB was then calculated using the lightcycler 480 software. Data was normalised to sham controls at 24 hours post-exposure.

	ACTB	B2M	GAPDH	HPRT1	YWHAZ
n	27	27	27	27	27
geo Mean [CP]	14.37	22.48	15.47	21.23	18.97
ar Mean [CP]	14.39	22.59	15.54	21.26	19.01
min [CP]	12.88	19.78	13.22	19.66	17.44
max [CP]	16.26	30.34	18.91	24.97	21.90
std dev [± CP]	**0.55**	1.69	1.23	1.06	1.05
CV [% CP]	3.82	7.49	7.89	4.96	5.54
std dev [± x-fold]	1.38	2.70	2.06	1.86	1.86

Table 3.4: Expression stability of housekeeper genes evaluated by BestKeeper
ACTB was found to be the most stable candidate, with the lowest standard deviation in the
Crossover Point (CP).

3.1.4 Statistical Analysis of Cellular Markers

Statistical analysis of viable cell counts, PGE2 and cellular markers consisted of computing the numerical average (mean) for each condition under test. The errors in cell count results were represented by Standard Error of the Mean (SEM):

$$SEM = \frac{\sigma}{\sqrt{n}}$$ (2.1)

Where σ is the standard deviation and n the sample size (or number of replicates). SEM describes the extent to which a sample mean is likely to differ from the true population mean.

Where the SEM of a ratio or a percentage difference was required, the SEM was calculated from the quadrature combination of the standard deviations of the two sample sets being compared as follows:

$$\sigma_T = \frac{\mu_2}{\mu_1}\sqrt{\left(\frac{\sigma_1}{\mu_1}\right)^2 + \left(\frac{\sigma_2}{\mu_2}\right)^2}$$ (2.2)

where σT, combined (total) standard deviation of the ratio, σ1 and σ2 are the standard deviations of samples sets 1 and 2, and μ1 and μ2 are the means of sample sets 1 and 2.

Statistical significance of the mean values of cellular markers compared to controls or other LIPUS conditions was assessed by one-tailed Student's t-test, assuming all samples had equal variance and a normal distribution, with a minimum confidence level of 95% (p = 0.05), unless stated otherwise.

3.2 Ultrasonic Devices: Design and Acoustic Characterisation

Commercial LIPUS systems have been available for clinical use since the mid-1990's. All devices currently available were discussed in Chapter 1. Although commercial devices have been used in many LIPUS trials, often the definition of the acoustic field is limited to data the manufacturers are required to publish, according to the International Electrotechnical Commission (IEC) and British Standard [14]. The standard is focussed on safety in clinical practice and does not attempt to measure clinical dose or efficacy. As a

consequence, the acoustic field parameters specified, detailed in Section 3.2.1.2, are concerned only with potential heating of tissue. I propose a series of new parameters, designed to describe the LIPUS dose experienced by cells *in vitro*, in 3.2.1.3.

A study of the ultrasound pressure fields of real therapeutic LIPUS devices was conducted with a scanning system developed for the purpose (3.2.1). The first device was the Duo Son (SRA Developments, UK), a dual frequency LIPUS system used in previous *in vitro* trials by researchers at the University of Birmingham, where the migration of osteoblasts and proliferation of odontoblasts exposed to 1 MHz and 45 kHz LIPUS fields were compared [6, 45]. The second device was a purpose-designed LIPUS transducer based on the transducer of the Exogen 4000 (Bioventus, NL): a system used in many LIPUS trials and recommended for clinical use by the FDA and NICE. Their performances were compared with manufacturer's data and their suitability for controlled *in vitro* LIPUS exposures assessed. Finally, in 3.2.4, two transducers were selected for use in controlled *in vitro* LIPUS exposures and fully characterised to deliver the exposure conditions required.

3.2.1 Ultrasound Pressure field mapping

Two scanning systems were developed to measure the ultrasound pressure fields of ultrasonic transducers. The high frequency (HF) system was designed and implemented first, but was limited to frequencies greater than 500kHz due to the fixed sample rate and finite buffer size of the digitiser. The low frequency (LF) system was capable of measuring fields of any frequency, but designed primarily for 500 kHz or less.

Both systems were controlled from a PC running LabVIEW software. The HF software was written in collaboration with a fellow PhD student from the University of Strathclyde by modifying the existing code of a high-speed continuous B-mode scanning system. The system was designed to run raster scans in a manner compliant with the British Standards for medical ultrasound fields [184].

Figure 3.1 illustrates the equipment configurations of both systems. In both, the software controlled a positioning system consisting of X, Y, Z and rotational motors with resolutions 0.625 µm in translation and 0.1° in rotation. The positioning system was installed above a water tank with dimensions W60 x H90 x D90 cm. The tank was filled

with deionised water that was outgassed via a high-speed pump to reduce the risk of cavitation during measurements.
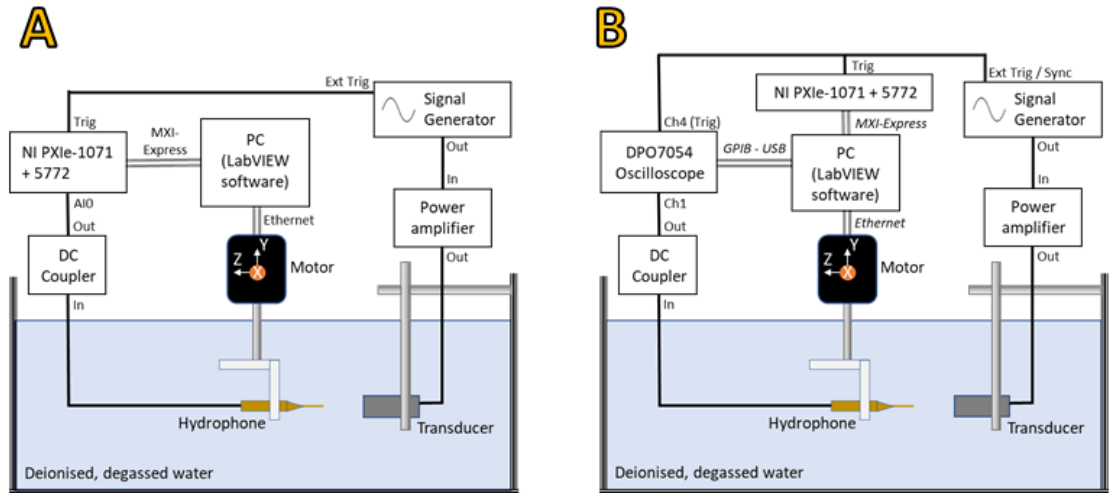
Figure 3.1: Equipment configurations of the pressure field scanning systems.
*A: the high frequency (HF) system; **B**: the low frequency (LF) system. The two systems have similar set-ups except each system has a different method of data capture. The HF system uses a NI PXie-1071 + 5772 digitiser and the LF system uses the digital output of the DPO7054 oscilloscope.*

The LabVIEW software controlled the PXie-1071 box with 5772 digitiser (National Instruments, US), which triggered the transducer drive system (usually a signal generator and power amplifier). The transducer was driven in burst mode where possible to enable isolation of the direct sound from any reflections within the tank. The resulting pressure field was measured with a needle hydrophone mounted under the positioning system, allowing full control of its position in the field.

Table 3.5 describes the reference needle hydrophones used to measure pressure at each frequency of interest. All were manufactured by Precision Acoustics (UK). All calibrations and measurements were conducted with the same preamplifier (PA17122), DC coupler (DCPS635) and optional booster amplifier (HA195), into a 50 Ω load.

Digitisation of the hydrophone voltage output was achieved with the 5772 digitiser in the HF system, where the hydrophone output signal was monitored in the LabVIEW software and on an oscilloscope (DPO7054, Tektronix, UK). In the LF system, the same oscilloscope was used to monitor and digitise the signal, which was transferred to the software via a GPIB-USB interface.

Frequency	Serial number	Diameter (mm)	Sensitivity (mV/MPa)	Uncertainty	Source
45 kHz	2716	2.0	1639	10.8%	Linear interpolation of NPL calibration at 40 kHz and 50 kHz, corrected for gain of in-line attenuator A222[1]
1 MHz	2714	0.5	297	No booster: 14% With booster: 14.1%	Manufacturer's calibration
1.5 MHz	2704	0.2	54.5	No booster: 19.8% With booster: 20%	Interpolation of manufacturer's calibration at 1MHz and 2MHz

Table 3.5: Needle hydrophones used for scanning tank measurements. Including frequency of interest, serial number, diameter, sensitivity, uncertainty and source of uncertainty.

Both systems consisted of an Alignment program and a Stepped Scan program. The Alignment program allowed free movement of the motors controlling the hydrophone position, and continuously monitored the voltage output of the hydrophone during any movement in X, Y or Z. After each movement the beam shape and position of the maximum mean-square voltage was displayed to allow the user to move the motor to that position.

Alignment of the hydrophone to the transducer beam axis was achieved by a near-far method where possible, especially when scans involved movements in the Z-plane (where axial alignment was critical). First the transducer and hydrophone were mounted in the tank and aligned by eye in translation, rotation and tilt. The separation was set to a 'near' distance in the far field of the transducer (usually the last axial maximum, Z_0) and the hydrophone voltage output was maximised by adjusting the translational alignment in XY. The separation was then set to a far distance ($\geq 2Z_0$) and the hydrophone output maximised

---

[1] The measured sensitivity was corrected for the attenuator's average attenuation over the bandwidth, derived from Precision Acoustics sensitivity data with and without the attenuator (21.6 dB ±0.5 dB).

by adjusting the tilt and rotation of the transducer. Alignment was achieved when minimal change was observed between the near and far maximum positions.

Once alignment was achieved, the Alignment program was closed and the Stepped Scan program started. The Stepped Scan program ran a stepped raster scan according to the user-defined scan parameters: the X/Y/Z spans and step sizes. During a stepped scan, the digitised output voltage waveform of the hydrophone was captured at each scan point. The capture could be repeated a number of times and averaged to reduce effects of background noise. The captured waveforms were saved to position-stamped delimited text files for further analysis. The LF system also output a readme file with scan settings and user notes to aid identification and post-processing.

Voltage measurements of both systems were validated by comparing peak-to-peak voltages with a recently calibrated oscilloscope (MD03014, Tektronix, US). Peak-to-peak voltages matched to within ±0.03 mV. The HF system was found to have a stable DC offset of 4 mV. In the LF system the oscilloscope was observed to have a DC offset of 0.5 ±0.1 mV. DC offsets were checked prior to every scan and removed from the hydrophone voltage waveform during post-processing.

3.2.1.1 Initial post-processing

Initial post-processing of scanning tank data was carried out in MATLAB (MathWorks, UK). A MATLAB script was written to import the tab-delimited text files, order data and remove DC offsets. The hydrophone voltage waveforms at each scan point were converted to root-mean-square (rms) and minimum voltages over an integer number of cycles of the frequency of interest. The rms and minimum voltages were converted to rms and peak-negative pressures by:

$$p = \frac{v}{M}$$
(3.1)

Where M is the voltage sensitivity of the hydrophone in Volts/Pascal, v is the voltage in Volts and p is the pressure in Pascals. If a booster amplifier was used the voltage was also divided by amplifier gain.

The rms and peak-negative pressures could be plotted as line scans in the X or Y directions to illustrate the beam shape, or as colourmaps showing a 2D cross-section of the beam. The MATLAB script was modified for each analysis with specific scan parameters, water temperatures, DC offsets and reference hydrophone sensitivities. The unique MATLAB script for each set of scan results was saved in the results folder with the scan data to allow repeat analyses if necessary. An example MATLAB script used to process an XY scan, *Analyse_XY_Scan_SACellArea.m*, is provided in Appendix B, Section B.1.1.

3.2.1.2 Post-processing 1: British Standard BS EN 61689:2013

British Standard BS EN 61689:2013 [14] defines ultrasound field characteristics to which physiotherapy devices must comply. The measurements and derived characteristics are designed for safety, i.e., to avoid heating of the tissue, rather than clinical dose or effectiveness. The standard requires manufacturers to make field measurements with the reference hydrophone positioned very close (3mm) to the front face, probably because most LIPUS devices are directly coupled to the patient's skin via ultrasound gel. These measures are described in the following paragraphs, along with the methods used to calculate them in the case of the Duo Son and LIPUS devices.

The rated output power (P) is defined in the standard as the maximum output power of the device. The power can be measured using a radiation force balance, but can also be estimated by integrating the mean square pressures of a raster scan encompassing the entire beam by:

$$P = \frac{prr.pw}{\rho c} \sum_{k=1}^{N} p_k^2 . a_k \tag{3.2}$$

where *prr* is the pulse repetition rate in Hz; *pw* the pulse width in seconds; ρ the density of the medium in kg/m^3; *c* the speed of sound in water in m/s; *k* the scan point index; *N* the number of scan points; p_k the rms pressure measured at the scan point *k* in Pascals; a_k the area of the beam over which the rms pressure applies in m^2. For raster scans, the area a_k is equal to s^2, where s is the scan step size.

It was not possible to perform a raster scan of the Duo Son device due to the fact that bubbles form on the front face during measurements. Instead, all parameters were

estimated from line scans. For a line scan in a single plane, the area contribution of each pressure value was calculated according to the contributing areas illustrated in Figure 3.2.
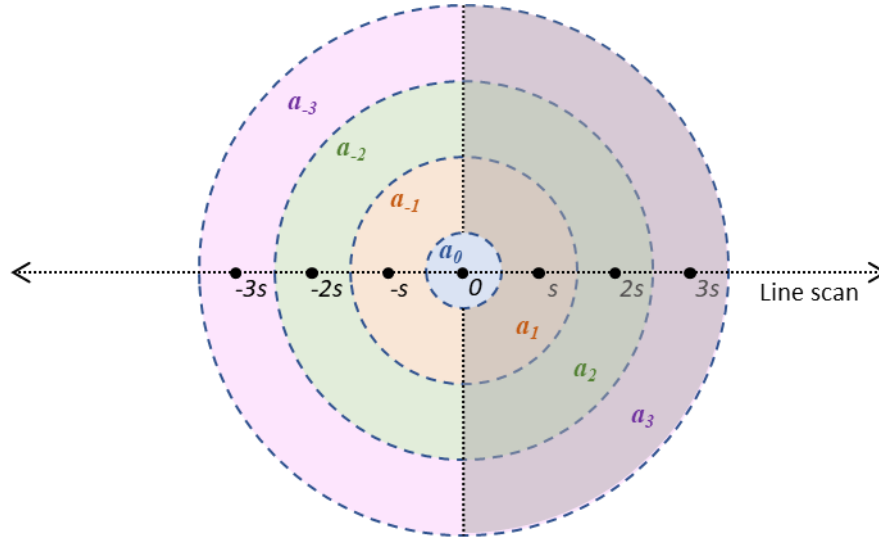
Figure 3.2: Areas of contribution for each scan point in a line scan to the total mean-square acoustic pressure, where s is the step size. E.g., area a_0 (blue) corresponds to the centre scan point '0'; area a_{-1} (peach) to scan point '-s'; area a_1 (greyed peach) to scan point 's', area a_{-2} (green) to scan point '-2s' and so on. Each area is assumed to have the same sound pressure as measured at the associated scan point.

The centre point, a_0, of the scan therefore contributed the area given by:

$$a_0 = \frac{\pi s^2}{4} \tag{3.3}$$

All other scan points contributed the areas given by:

$$a_k = \frac{\pi}{2}\left[\left(|x_k| + \frac{s}{2}\right)^2 - \left(|x_k| - \frac{s}{2}\right)^2\right] \qquad |x_k| > 0 \tag{3.4}$$

where x_k is the position of scan point k in m (where $k = 0$ is the beam centre). The effective radiating area (A_{ER}) is defined in the standard as "the area close to the treatment head which contains 100 % of the total mean square acoustic pressure", and is derived from the raster scan. First the total mean-square acoustic pressure, p_t^2, is found by:

$$p_t^2 = \sum_{k=1}^{N} p_k^2 \tag{3.5}$$

Each value of p_k^2 is sorted into descending order, and a summation conducted from the largest value to the smallest, until the cumulative sum is less than or equal to 75 % of p_t^2. The total number of scan points in the cumulative sum is then multiplied by the unit area of the scan (s^2 for raster scans, a_0 for line scans) to find the beam cross-sectional area, A_{BCS}. The A_{BCS} is then multiplied by a conversion factor (1.333) to convert the A_{BCS}, containing 75 % of the total power, to A_{ER}, the area containing 100 % of the total power.

To estimate A_{ER} from line scans, the same sorting of the mean square pressures can be conducted by repeating each mean square pressure value m times, where m is its contributing area a_k divided by the central unit area a_0. A_{BCS} and A_{ER} are then found in the same way as above. The effective intensity (I_e in the standard but referred to in this report as $I_{SATA,AER}$ for consistency of notation), is the spatial-average, temporal-average intensity over the effective radiating area A_{ER} and is calculated by:

$$I_{SATA,A_{ER}} = \frac{P}{A_{ER}} \tag{3.6}$$

where P is the acoustic power, normally measured with a radiation force balance. It can also be estimated from raster or line scans by:

$$I_{SATA,A_{ER}} = \frac{prr.pw}{A_{ER}\rho c} \sum_{k=1}^{N} p_k^2 . a_k \tag{3.7}$$

The beam non-uniformity ratio (R_{BN}) is a unitless ratio of the maximum intensity in the field with the total intensity over the A_{ER}. The parameter is designed to identify 'hot-spots' in the transducer response, where tissue heating might be significantly higher than the spatial-average intensity would suggest. For an instrument to be cleared for clinical use the R_{BN} must be less than or equal to 8. In practise this can be found from the squared rms acoustic pressures by:

$$R_{BN} = \frac{p_{max}^2 A_{ER}}{p_t^2 a_0} \tag{3.8}$$

where p_t^2 is the sum total of all the rms pressures in the field and p_{max}^2 the maximum mean-square pressure in the field. For raster scans, $a_o = s^2$. For line scans, a_0 is the central unit area (Equation 3.3).

The calculations of R_{BN} in this report are estimates because the maximum mean-square pressure was not determined over the entire field. Similarly, the A_{ER} of the purpose-built LIPUS transducer was determined at 100 mm and not 3 mm as stipulated in the standard. But as each device was evaluated at the same separation as *in vitro* testing conditions, the estimates provide a reasonable description of the field incident on the cells.

3.2.1.3 Post processing 2: LIPUS dose parameters

Apart from varied control over the ultrasound field, another difficulty in comparing results between different *in vitro* LIPUS trials is the lack of a standard method of quantifying the field applied to the cell layer. Spatial-average intensities are the most common measure but give limited information about the beam shape. As discussed earlier in Chapter 1, in 2011 ter Haar et al. [51] published guidance on reporting ultrasound exposure conditions for bio-effect studies, and recommended the ultrasound field be characterised *in situ*, and ideally spatial distribution of pressure and intensity should be reported. In addition, to relate ultrasound field characteristics to biological mechanisms we must take into account how these mechanisms are measured. Cellular responses are measured either globally over the entire cell population of a culture vessel, e.g. by measuring the concentration of substances in the growth media (such as PGE2 in 3.1.2.4 or PCR in 3.1.3); or staining and imaging, where local effects can be assessed.

Global measures of biological mechanisms require global measures of the LIPUS field. It is therefore proposed to quantify the LIPUS dose by determining the spatial-average pressures and intensities over the area of the cell layer. Maximum pressures and intensities should also be given as an indication of the spread of amplitudes. Where staining allows local effects to be assessed, a raster scan of the ultrasound beam can be translated into pressure bins, and each area within those bins analysed separately to produce results mapped to a range of pressures.

LIPUS stimulus is thought to be mechanical in nature. In medical ultrasonics mechanical effects are normally equated with pressure, and more specifically peak-negative pressure, as the rarefactional amplitude is the main cause of cavitation. I therefore propose to use peak-negative pressure as the main descriptor of the LIPUS field. Intensity is still quoted to indicate energy dose over time and to compare with past trials.

When comparing LIPUS dose between frequencies, the frequency dependency of mechanical effects should also be taken into account. The longer wavelengths of lower frequencies make cavitation more likely to occur (due to the longer time period of rarefactional pressure). For this reason, I propose to use the Mechanical Index (*MI*) as a guide to compare the potential effects of 45 kHz and 1 MHz, the two frequencies used in the Frequency Study detailed in Chapter 4. *MI* is a unitless measure for prediction of the onset of inertial cavitation used as an indicator of diagnostic ultrasound safety. The standard equation for *MI* is:

$$MI = \frac{\hat{p}_-}{\sqrt{f}}$$
(3.9)

where $\hat{p}_-$ is the maximum peak-negative pressure in MPa and f the frequency in MHz. The *MI* was derived for water, so it is arguably a more relevant measure for *in vitro* tests than for tissue, as these are mainly conducted in water and water-like growth media. However, the *MI* is not a good predictor of cavitation onset at frequencies below 500 kHz. The above equation is based on a model of cavitation threshold which approaches zero at very low frequencies, and as such the *MI* over-estimates the mechanical effects at frequencies below 500 kHz. Ahmadi et al. proposed a more valid prediction of low frequency MI in their review of bio-effects of low frequency ultrasound [185], mainly:

$$MI_{LF} = \frac{\hat{p}_- - P_0}{\sqrt{f(MHz)}}$$
(3.10)

where P_0 is one standard atmospheric pressure (0.101325 MPa)[2]. Using both *MI* equations: (3.9) for frequencies greater than 500 kHz and (3.10) for frequencies less than or equal to 500 kHz, provides a potential method of comparing mechanical effects between low and high frequency.

The proposed LIPUS dose parameters are summarised in Table 3.6. All can be derived from an XY raster scan of the acoustic field with the hydrophone positioned at a distance equal to the separation between transducer and cell layer. Only the scan points (k) lying within the area of the cell layer, A_c, are included in the calculations.

---

[2] Note that subtracting P_0 from the peak negative pressure results in negative MI_{LF} values at low peak-negative pressures. In these cases it is proposed to round the MI_{LF} to zero.

	Symbol	Description	Formula	Units
Maxima	$\hat{p}_-$	Maximum peak-negative pressure across the cell layer	$max(p_{-,k})$	Pa
	$\widehat{MI}$	Maximum MI across the cell layer	> 500 kHz: Eqn. 3.9 ≥ 500 kHz: Eqn. 3.10	-
	$\hat{I}_{PA}$	Maximum pulse-average intensity across the cell layer	$\dfrac{\hat{p}^2}{\rho c}$	W/cm²
	$\hat{I}_{TA}$ ISPTA	Maximum temporal-average intensity across the cell layer	$\hat{I}_{PA} \times prr \times pw$	W/cm²
Spatial-average	p_{-,SA,A_c}	Spatial-average peak-negative pressure across the cell layer	$\dfrac{1}{A_c}\displaystyle\sum_{A_c} p_{-,k} a_k$	Pa
	MI_{SA,A_c}	Spatial-average MI across the cell layer	$\dfrac{1}{A_c}\displaystyle\sum_{A_c} MI_k a_k$	-
	I_{SAPA,A_c}	Spatial-average, pulse-average intensity across the cell layer	$\dfrac{1}{\rho c A_c}\displaystyle\sum_{A_c} p_k^2 a_k$	W/cm²
	I_{SATA,A_c}	Spatial-average, temporal-average intensity across the cell layer	$I_{SAPA,A_c} \times prr \times pw$	W/cm²

Table 3.6: Summary of proposed LIPUS dose parameters.
The top set are maxima or peak parameters and are the maximum values of pressure / MI, intensity in the beam. The bottom four parameters are spatial-averaged over the cell layer (which may not be the full extent of the LIPUS beam)

Any effects of the culture vessel on the LIPUS field must be taken into account by prediction or measurement. For pressure bins, the range and centres of the pressure bins should be defined. The spatial-average parameters described above can also be computed for each pressure bin.

When comparing LIPUS fields of different frequency it is likely that separate devices would be used (as in the studies reported in this thesis). If this is the case the pressure beam shape should also be reported, with an indication of beam width (e.g., the half-pressure or -6 dB beam width).

3.2.2 LIPUS field study #1: Duoson device

Researchers from the School of Dentistry at the University of Birmingham kindly loaned their dual-frequency LIPUS device, which they had used in a number of previous *in vitro* LIPUS studies [6, 45], for characterisation. The results reported here were also included in a co-authored paper currently in review for publication in Ultrasound in Medicine and Biology (see Publications list at the front of this thesis).

The Duoson consists of two transducers arranged concentrically within one housing. The outer transducer (Figure 3.3(A)) operates at 45 kHz and is a Langevin design with back mass, piezoelectric rings, electrodes and front mass pre-stressed by a central bolt. The second transducer (Figure 3.3 (B)) is located in the central nib of the front face and operates at 1 MHz.
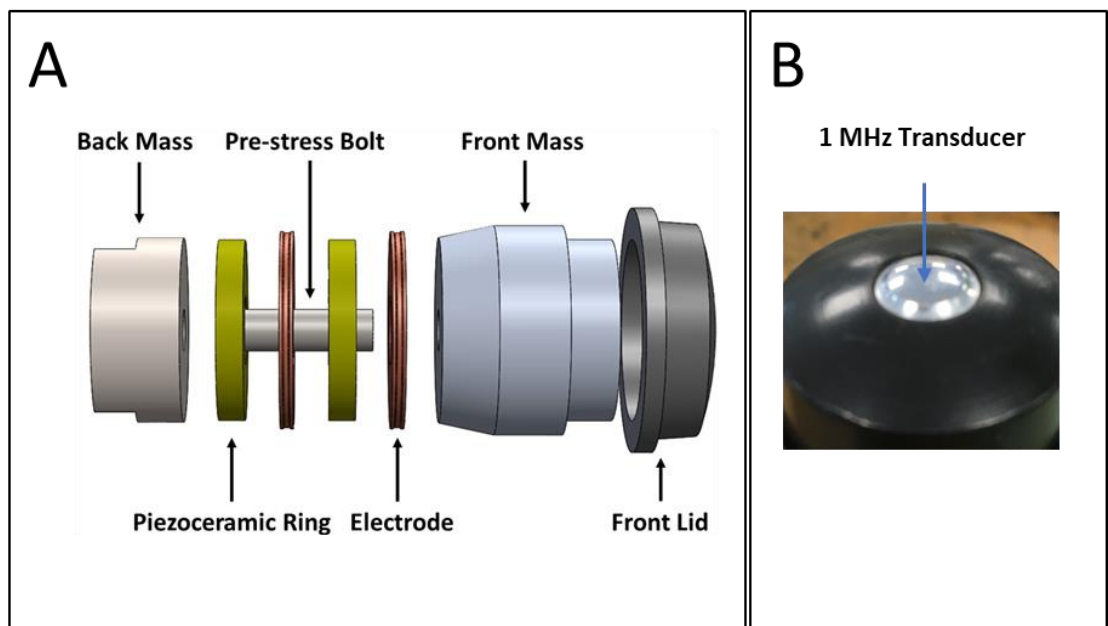
Figure 3.3: Construction of the Duo Son dual-frequency transducer.
A: CAD schematic showing Langevin design of 45 kHz transducer, reproduced from [186].
B: photograph of the Duo Son front face showing the 1 MHz transducer in the centre.

The detailed design of the 1 MHz transducer is not known, but is either a piezoelectric disc or dome operating in the thickness mode. The manual reports that the 1 MHz sound field is divergent so the curved shape may have the purpose of defocussing the beam. The manual also states the plastic front lid provides acoustic impedance matching with tissue [187].

The Duoson was designed to be a combined ultrasonic diathermy and LIPUS device, with the purpose of inducing thermal and mechanical effects in tissue. As such, the output power and intensity settings of the commercial device were higher than conventional LIPUS devices. The University of Birmingham version was customised by the manufacturer (at the request of the Birmingham researchers) to produce lower intensities for a series of LIPUS studies [6, 45, 119, 188]. The University of Birmingham device has eight modes of operation, with three being dual frequency modes, where the 1 MHz and 45 kHz transducers are driven simultaneously. Only the single frequency Modes, 1, 2, 3, 4 and 6 were considered for this study, and the details of these modes are given in Table 3.7.

Mode	Frequency	Power, mW	Intensity, mW/cm^2	Pulse characteristics
1	1 MHz	14 mW	191 (I_{SAPA}) 38 (I_{SATA})	$pw = 3.2$ ms $prr = 63$ Hz Duty cycle $= 0.2$
2	1 MHz	58 mW	763 (I_{SAPA}) 153 (I_{SATA})	
3	45 kHz	159 mW	10	CW
4	45 kHz	406 mW	25	CW
6	45 kHz	1217 mW	75	CW

Table 3.7: Modes of the custom Duoson device
with frequency, power, intensity and pulse settings calibrated by the manufacturer.
Characterisation of the pressure field of the device was performed in Modes 1, 2 and 3.

3.2.2.1 Acoustic characterisation of the Duoson device

The acoustic pressure fields produced by the Duoson in Modes 1, 2 and 3 were measured at separations of 3 mm and 5 mm from the front face, which were the most likely maximum and minimum separation distances between front face and cell layer during the LIPUS studies conducted by the University of Birmingham.

The Duoson was characterised with a modified version of the LF scanning system, with the set-up illustrated in Figure 3.4. The transducer was not designed to be immersed in water so it was positioned with only the front face immersed, approximately 8 mm below the surface. The device was levelled with the aid of a miniature spirit level. The system had no

external trigger, so was switched on for the duration of measurement and the oscilloscope set to trigger off the amplitude of the hydrophone output voltage.
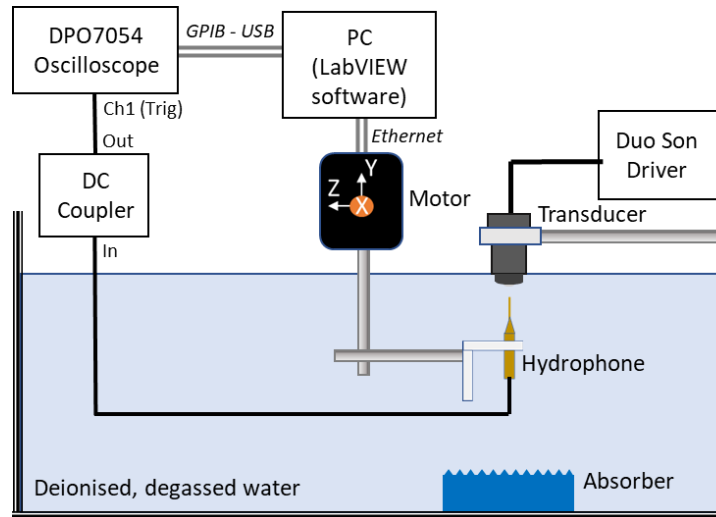
Figure 3.4: Duo Son pressure field measurement setup.
Pressure measurements used the LF scanning system, with the Duoson aligned so its front face was facing down towards the bottom of the tank. An absorber was placed underneath to limit reflections.

The hydrophone was first aligned by eye to the centre of the front face. Further alignment was achieved in Modes 1 and 2 (the 1 MHz modes) by adjusting the hydrophone position to find the point of maximum pressure, ensuring the hydrophone was in the far field. Further alignment was not possible in Mode 3 because of the continual formation of bubbles on the front face. The bubbles appeared only while the device was being driven at 45 kHz and were observed to coalesce around the outside of the central metal nib, shown in Figure 3.5.
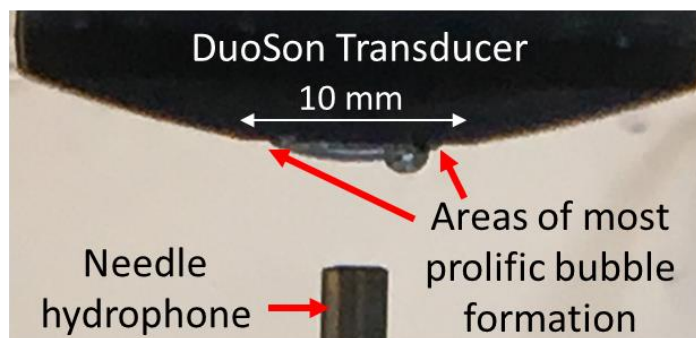
Figure 3.5: Bubble formation on the Duoson front face.
The bubbles formed on the metallic nib of the transducer front face and are thought to be due to and electrochemical reaction (galvanic corrosion) in proximity with the differing metals of the needle hydrophone and clamps.

If not removed, the bubbles would enlarge and eventually seed inertial cavitation, which was evident when the characteristic 'whoosh' of broadband emissions was clearly audible. The onset of cavitation was almost immediate in Modes 4 and 6, therefore the Duoson pressure field was not measured in these modes. The bubbles were initially thought to be caused by the displacement of air trapped between the metal body and plastic cover of the device. However, bubbles still formed after very long periods (>4 hours) of soaking and driving, when all the air within the cavity should have been expelled.

A more likely explanation is that the front face of the central transducer, which appeared to be aluminium, was effectively the anode to the more noble gold layer of the needle hydrophone active element, the proximity of which was inducing a galvanic corrosion current. The bubble formation improved when the tank was refilled with freshly deionised water and freshly degassed, but bubbles still formed, albeit at a slower rate. It is therefore likely that either the water was not fully degassed by the degassing pump or the shallow depth at which the Duoson front face was held meant it was in water that had re-absorbed some oxygen.

In addition to bubble formation, the continuous wave drive of Mode 3 made it impossible to isolate the direct sound from tank reflections. Placing an acoustic absorber on the base of the tank mitigated but did not eliminate the effects. Instead, a number of repeats were made and the measurements least affected by bubbles were averaged. As a result, standard deviations were high, averaging 15 % across the main beam at 5 mm separation and 35 % at 3 mm separation.

Once aligned, line scans were conducted in the X and Z planes (of the tank scanning system) in Mode 3 and in the X-axis for Modes 1 and 2. Initial measurements were conducted at 35 °C to approximate temperature conditions during *in vitro* exposures and some measurements were conducted at 27 °C. Comparisons of beam shape and amplitude showed no significant differences between measurements at the two temperatures. Table 3.8 summarises the test conditions for each mode.

Mode	Frequency	Intensity	Separation	Number of Scans	Temperature
1	1 MHz	191 mW/cm^2	3 mm	$1 \times X$	35 °C
			5 mm	$2 \times X$	27 °C
2	1 MHz	763 mW/cm^2	3 mm	$2 \times X$	35 °C
			5 mm	$1 \times X$	27 °C
3	45 kHz	10 mW/cm^2	3 mm	$4 \times X + 1 \times Z$	35 °C
			5 mm	$1 \times X, 2 \times Z$	35 °C

Table 3.8: Test conditions of each Duoson Mode.
Separation distance between transducer and hydrophone; number of scans in X-axis, Z-axis or both, and temperature.

The resulting line scans of rms pressure were plotted in Excel to illustrate beam shape. The manufacturer's data was estimated from the rms pressure beam profiles as detailed in 3.2.1.2. Parameters for Modes 4 and 6 were predicted by multiplying the Mode 3 results by the square root of the intensity gain.

To further illustrate the expected shape of the 45 kHz beam incident on the cell layers during *in vitro* exposures, the 45 kHz peak-negative pressure results were extrapolated to a 2D raster scan by first calculating an averaged half-line scan, then rotating the half-line scan around the zero point to model the axisymmetric beam shape.

3.2.2.2 Duoson Acoustic Characterisation Results

The rms pressure beam profiles of the Duoson device are illustrated in Figure 3.6. The 45 kHz Mode 3 results show the average ± one standard deviation (σ). Figure 3.7 illustrates line scans of peak-negative pressure of Mode 3 at 3 mm and 5 mm separations, with extrapolated raster colourmaps showing extent of 6-well plates or petri dish used in the University of Birmingham studies. Table 3.9 compares the parameters derived from line scans with manufacturer's data.
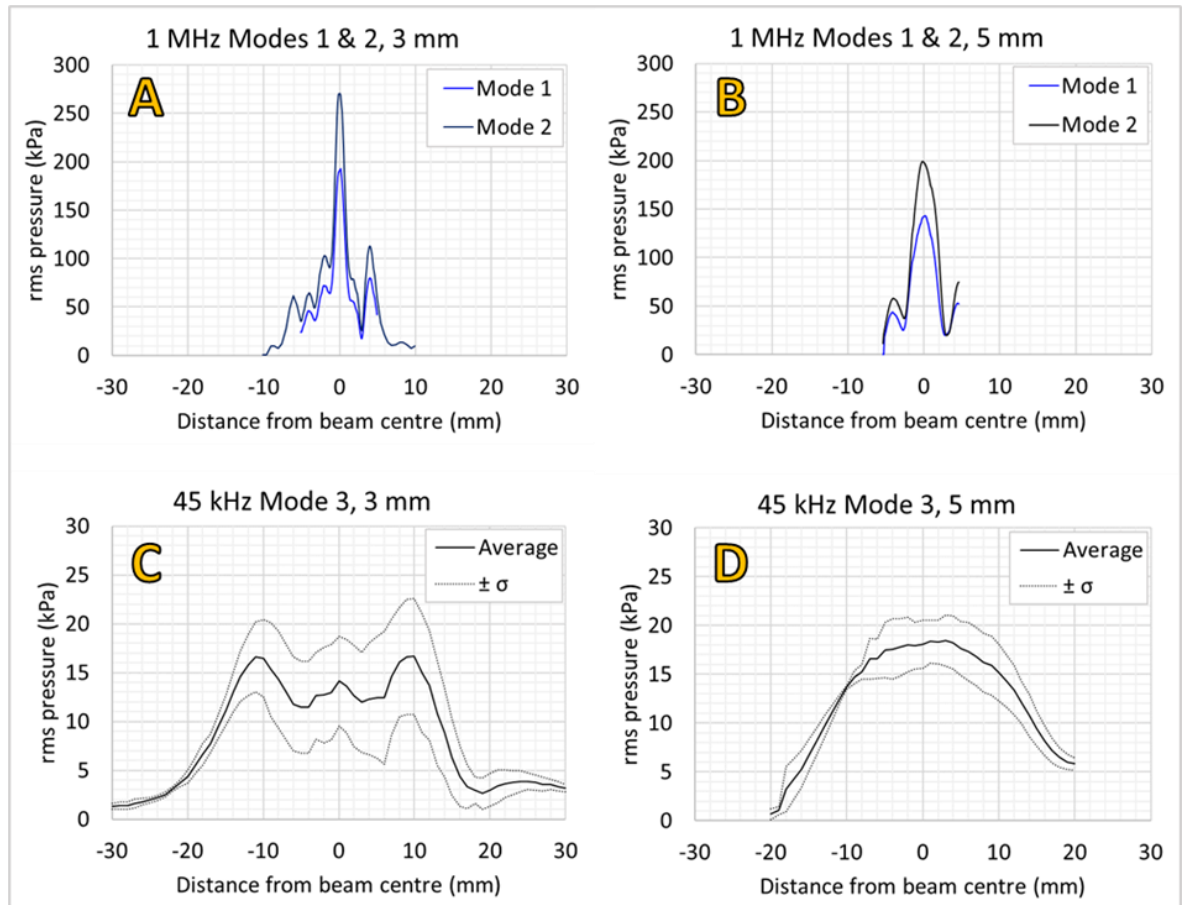
Figure 3.6: Duoson rms pressure beam profiles.
A: 1 MHz Modes 1 and 2 at 3 mm separation; B: Modes 1 and 2 at 5 mm; C: 45 kHz
Mode 3 at 3 mm separation; D: 45 kHz Mode 3 at 5 mm separation. Dotted lines in C & D
indicate one standard deviation (σ) from the mean (n = 5 at 3mm, n = 3 at 5 mm).
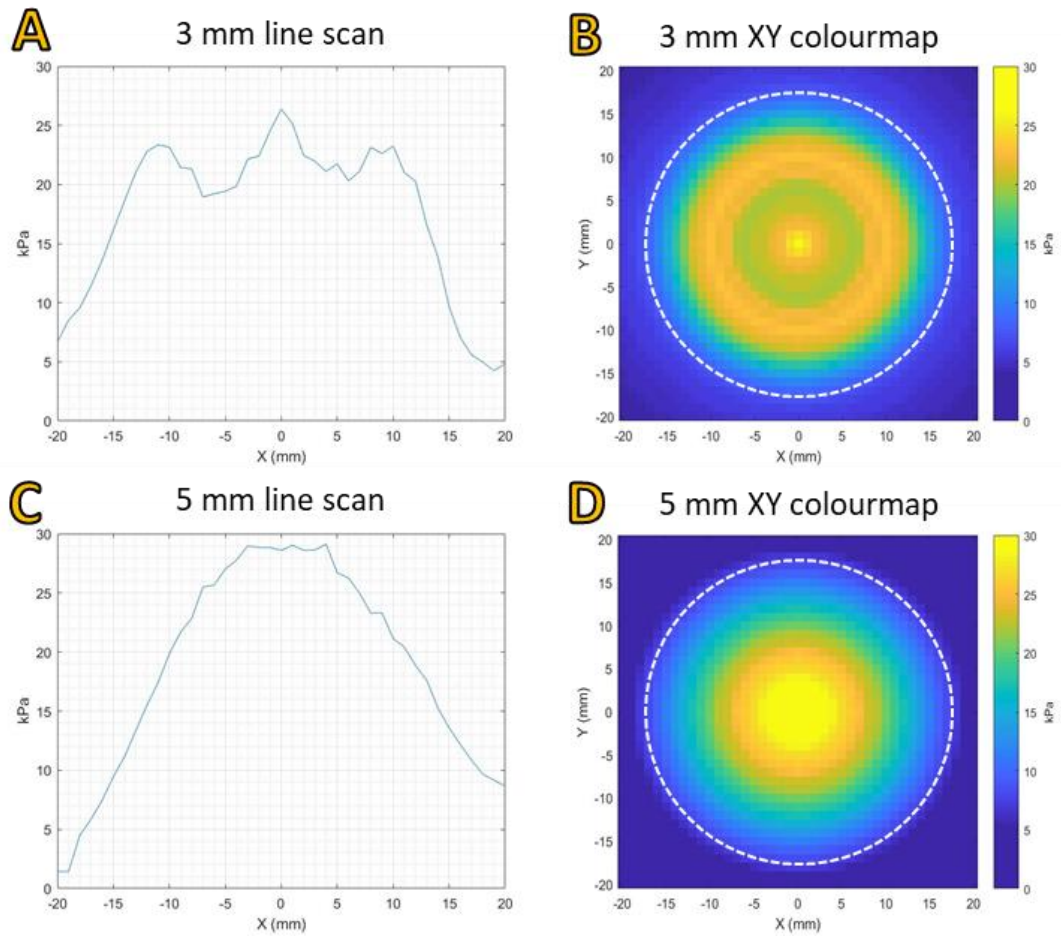
Figure 3.7: Average Peak-negative pressure line scans and colourmaps
A&C: average peak-negative pressure from line scans presented in Figure 3.6C & D, at
3mm and 5mm distance from the front face. B&D: colourmaps of average peak negative
pressure at the same distances, estimated by axisymmetric extrapolation of the line scans.

Mode	Frequency	$\hat{p}_{rms}$(kPa)	$\hat{p}_-$ (kPa)	MI (MI$_{LF}$)	P (mW)	$I_{SATA,AER}$ (mW/cm^2)
1	1 MHz	193	271	0.27	30 (14)	400 (191)
2	1 MHz	271	383	0.38	60 (58)	790 (763)
3	45 kHz	17	26	0.12 (0)	110 (159)	7 (10)
4	45 kHz	26	42	0.20 (0)	(406)	(25)
6	45 kHz	46	72	0.34 (0)	(1217)	(75)

Table 3.9: Acoustic parameters of Duoson device at 3mm separation.
Maximum rms and peak-negative pressures; MI (MI$_{LF}$); Power; I$_{SATA,AER}$. Manufacturer's
P and I$_{SATA,AER}$ in brackets. Modes 4 & 6 pressures are predicted.

3.2.2.3 Discussion

When examining the pressure fields of the Duoson at 1 MHz and 45 kHz, the most obvious difference is in the widths of the main beams. The -6 dB (or half-pressure) beam width at 1 MHz, 5 mm separation is 3.8 mm, almost twice as large as the beam width at the 3 mm separation, 1.7 mm. At 45 kHz the beam width does not change as much between separations (30 mm at 3 mm separation, 28 mm at 5 mm) but this is at least seven times greater than the beam width at 1 MHz. This disparity makes it difficult to compare cellular responses between the frequencies, because the areas of exposure are not the same across the cell layer. It was therefore concluded that the Duoson was not a suitable device for comparing cellular responses to LIPUS fields. Instead, when comparing LIPUS at different frequencies, transducers should be chosen, or designed, to have similar beam widths so that the area of cells exposed, and therefore the cell numbers, are comparable.

3.2.3 LIPUS field study #2: Custom-built LIPUS transducer

This second LIPUS field study investigated the field of the Exogen LIPUS transducer (Bioventus, US), the most common transducer used in the LIPUS *in vitro* study literature. An Exogen device was requested from Bioventus for the purposes of this study but the request was declined. Instead, a LIPUS transducer was designed and built with dimensions based on those given in the manufacturer's data. The design and construction of the custom-built LIPUS transducer is described in Appendix C.

3.2.3.1 Acoustic Characterisation of Custom LIPUS Transducer for in vitro Pressure Amplitude Study

The custom-built LIPUS transducer provided the LIPUS field in the Pressure Amplitude Study described in Section 4. A frequency of 1 MHz was chosen for this study because it would lower the uncertainty of the pressure measurement (as no interpolation of sensitivity data was required) and it matched the frequency of previous studies in the literature, comparing 1 MHz and 45 kHz LIPUS [6, 19, 40, 45].

The device was fully characterised for the conditions required in the study at the far field distance of 100 mm, with the scanning tank heated to 37 °C ± 1 °C. It was clamped in the same way as in previous measurements and placed in the scanning tank. The drive system consisted of a signal generator (33250A, Agilent, US) and power amplifier (2100L, E&I,

US). All measurements were conducted with an oscilloscope (DPO7054, Tektronix, US) and the HF scanning system described in 3.2.1. The signal generator was set to output 20 cycles at 1 MHz with a burst period of 10 ms.

After alignment, a brief axial scan confirmed the last axial maximum (determined in Appendix C) had not been altered by the change in temperature. The drive voltages required to produce maximum peak-negative pressures ($\hat{p}_-$) of 10 kPa, 100 kPa, 200 kPa, 350 kPa and 500 kPa were determined at the centre of the beam. XY raster scans were then conducted for all drive voltages, with spans ±30 mm in 1 mm steps in the 350 kPa and 500 kPa settings, to provide higher resolution for estimation of BS 61689 and LIPUS dose parameters, and 2 mm steps at all others.

Post processing was conducted in MATLAB according to the processes described in 3.2.1.2 and 3.2.1.3. The spatial-average LIPUS dose parameters were computed over a 50 mm diameter area (the area of the cell layer in the pilot study). This computation can be seen in the example MATLAB script *Analyse_XY_Scan_SACellArea.m* in Section B.1.1 of Appendix B. Figure 3.8 shows line scans extracted from the XY raster scans to illustrate beam shapes.

The beam patterns at 100 kPa or greater were within ±0.3 dB in the main beam and ±0.9 dB throughout. The 10 kPa beam had very low signal levels so measurements outside the main beam were affected by background noise. The beam shapes were not quite symmetrical, with the same flattening of the mean beam in negative Y as observed in previous measurements. The -6dB beam widths were also similar to those measured previously: 11.7 mm in X and 13.3 mm in Y.

Table 3.10 presents the drive voltages required to achieve the pilot study peak-negative pressures. As the 10 kPa field was near the noise floor, the minimum peak-negative pressure chosen for the pilot study was 50 kPa. The pressure output was linear with drive voltage, therefore the signal generator voltage for 50 kPa was derived by interpolation.
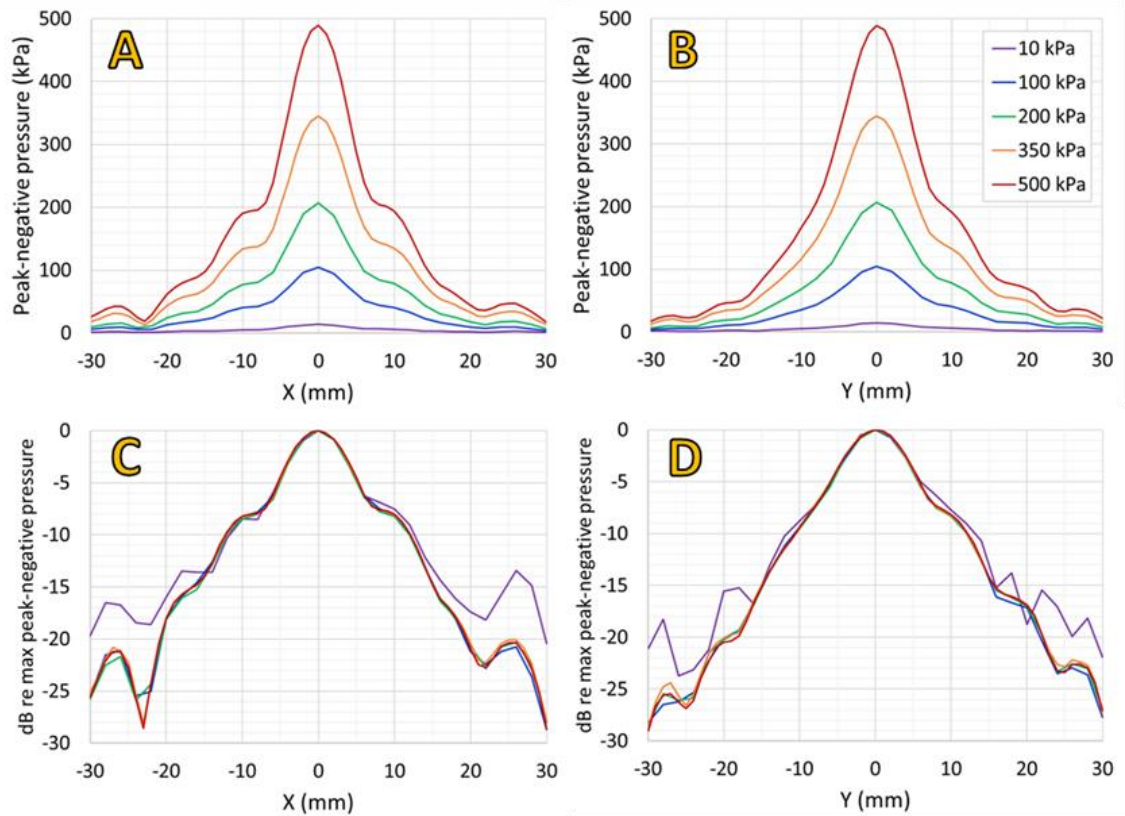
Figure 3.8: Line scans showing beam shapes of the Custom-built LIPUS transducer at maximum peak-negative pressures 10 kPa, 100 kPa, 200 kPa, 350 kPa and 500 kPa. A and B: peak-negative pressure in X and Y planes. C and D: peak-negative pressure in dB re maximum peak-negative pressure, showing shape of beam is not affected by amplitude (the lower pressure settings are subject to background noise outside the main beam).

	Peak-negative pressure (kPa)				
	50	100	200	350	500
Signal generator voltage (mVpp)	30	60	125	222	327

Table 3.10: Drive voltages for pilot study maximum peak-negative pressures

A standard deviation of 5.7 % in the resulting measured peak-negative pressures was observed from 25 repeat measurements across the range. The random uncertainty assumed for the pressure is therefore 11.4 % for a 95% confidence level. Combining this with the sensitivity uncertainty from Table 3.5, the combined uncertainty is 18 %.

Table 3.11 shows the LIPUS dose and BS 61689 parameter results for all peak-negative pressure settings. The 50 kPa results were extrapolated from the results at other pressures.

				Nominal $\hat{p}_-$ (kPa)			
	Parameter	50 kPa	100 kPa	200 kPa	350 kPa	500 kPa	Units
LIPUS dose Maxima	$\hat{p}_-$	-	105	208	345	489	kPa
	$\widehat{MI}$	0.05	0.11	0.21	0.35	0.49	-
	$\hat{I}_{PA}$	92	368	1501	4344	9356	mW/cm^2
	$\hat{I}_{TA}$	18	74	300	869	1871	mW/cm^2
LIPUS dose Spatial-average	p_{-,SA,A_c}	9.7	21.1	42.3	71.4	101	kPa
	MI_{SA,A_c}	0.01	0.02	0.04	0.07	0.10	-
	I_{SAPA,A_c}	5.2	24.8	100	294	623	mW/cm^2
	I_{SATA,A_c}	1.0	5.0	20.0	58.8	125	mW/cm^2
BS 61689	Power	20.7	99.7	405	1193	2527	mW
	A_{ER}	-	5.2	5.4	5.5	5.3	cm^2
	R_{BN}	-	3.8	4.0	4.0	3.9	-
	$I_{SATA,AER}$	4.0	19.3	75.1	216	475	mW/cm^2
	$I_{SAPA,AER}$	20.1	96.4	376	1079	2375	mW/cm^2

Table 3.11: LIPUS dose and BS 61689 parameters of LIPUS transducer Calculated from XY raster scans. 50 kPa values are predicted by linear extrapolation.

The 100 kPa results were used to derive the equivalent values of BS 61689 parameters for the power rating of the Exogen, to compare performance of the custom-built device with that of a commercial device (Table 3.12). Equalising the power to 117 mW, the power gain was then used to predict the intensities and peak-negative pressure of the custom-built LIPUS transducer if driven at the same power. Another prediction set the $I_{SATA,AER}$ of the LIPUS transducer to that of the Exogen (30 mW/cm^2).

In the equalised power results, the intensities were lower than the Exogen but within 25% of the Exogen values. To achieve the Exogen $I_{SATA,AER}$ the LIPUS transducer had to be driven at 131 mW power. This is most likely due to The A_{ER} of the custom-built transducer was 36% larger. This may be due to measuring the A_{ER} in the far field instead of at 3 mm separation. The beam of the transducer was slightly divergent so the A_{ER} would increase

with distance from the front face. Finally, the R_{BN} was up to 4.0, which did not quite meet the < 4 Exogen criterion, but still meets the <8 requirement of BS 61689

	Power (mW)	$I_{SATA,AER}$ (mW/cm^2)	$I_{SAPA,AER}$ (mW/cm^2)	A_{ER} (cm^2)	R_{BN} -	$\hat{p}_-$ (kPa)
Exogen	117	30	150	3.88	< 4.0	-
LIPUS transducer (equalising power)	117	23	113	5.3	≤ 4.0	114
LIPUS transducer (equalising $I_{SATA,AER}$)	155	30	150	5.3	≤ 4.0	131

Table 3.12: Comparison of Custom-built LIPUS transducer characteristics with those of the Exogen device. Firstly if the power output is equalised (row 2), and secondly if the effective intensity (or $I_{SATA,AER}$) is equalised. The A_{ER} is larger, indicating the custom-built transducer emits over a wider area than the Exogen.

3.2.3.2 Discussion of the custom-built LIPUS transducer performance

The results of the characterisation of the custom-built LIPUS device indicated the pressure output was linear with drive voltage, it was stable and could be driven to produce the required LIPUS fields. The comparison with the Exogen device showed it could produce the same $I_{SATA,AER}$, although the field distribution was likely to be different. The device meets the safety criteria of BS 61689 at 100 mm distance, so was deemed safe to use *in vitro* at that distance. To fully comply with the standard the A_{ER} would have to be determined at a distance of 3 mm, so it is not conclusive that the device could be cleared for clinical practice. However, the results proved the device was suitable for *in vitro* exposures in the far field.

Unfortunately, after the device was used successfully in the Pressure Amplitude Study, a fault developed. While driving the device for a subsequent study, the output reduced to almost zero. An impedance measurement suggested the impedance was almost purely capacitive, with the capacitance about the same as expected for the length of coaxial cable. It was concluded that the connection to the back of the piezoelectric disc had somehow come loose. Because the connection was potted into the casing with backing material, there was no way of investigating further without destroying the device. An alternative off-the-shelf 1 MHz transducer was therefore chosen for subsequent *in vitro* trials. This transducer, and the transducer used to produce 45 kHz LIPUS, are described in the next section.

3.2.4 Devices for *in vitro* Exposures

3.2.4.1 45 kHz Transducer

It was proposed in Section 3.2.2 that, in order to compare cellular responses to LIPUS of different frequency, it is desirable to equalise the shape of the beam as much as possible, to equalise the LIPUS dose experienced across the exposed cell layer. A short study was conducted using the MATLAB toolbox Field II (v3.20, 2010, [189, 190]), to investigate front face topographies and dimensions that might produce similar beam widths to the custom-built LIPUS transducer. A piezoelectric disc transducer was not practical due to the thickness of the material required for resonance in the tens of kHz range. Focussing the beam with an acoustic lens was considered, but the dimensions of a conventional lens would not be practical to fit in a small tank. Field II modelling suggested that the required beam width, approximately 12 mm, could be achieved close to the front face of a flat circular piston of diameter 3 mm. The Langevin transducer design, with low longitudinal resonant frequencies, could provide the desired frequency with a smaller front face.

The Langevin design consists of a number of piezoelectric rings sandwiched between a front mass and back mass, and the resonant frequency is defined by the longitudinal resonance of the entire structure. A previous study by researchers at the University of Glasgow involved the design of a number of miniature Langevin transducers to optimal performance for medical applications (Li et al. [191]). The smallest Langevin transducers used in the study had four PZT4 rings, titanium back mass and front mass, with various front mass horn shapes, all tapering to a final front-face diameter of 2.5 mm, a diameter which might produce the required beam widths.

The conductance of the devices was measured with an impedance analyser (Agilent 42941A) and five devices were found to have peak conductance, and therefore resonant frequencies, close to 45 kHz: the frequency used in previous studies of low frequency LIPUS [6, 19, 40, 45]. Figure 3.9 shows the different horn shapes – stepped, catenoidal exponential, cone and cosine and the conductance results for each.
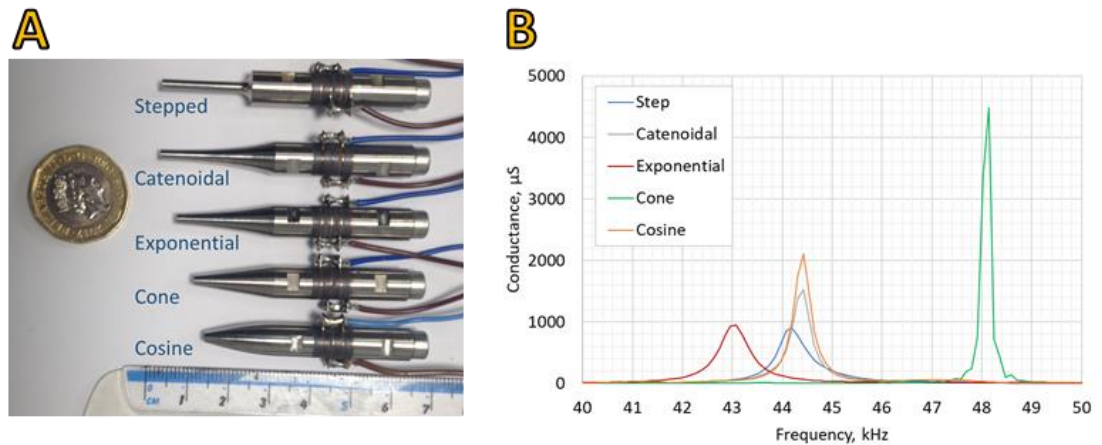
Figure 3.9: Candidate Langevin transducers for 45 kHz device
A: Devices and horn shapes. B: Conductance, showing resonance peaks

The transducer chosen was the device with the cosine-shaped horn, because it had a relatively high conductance peak and a resonant frequency close to 45 kHz (44.4 kHz). The device was rewired with a coaxial cable and BNC connector, and water-proofed with PTFE tape. The device was placed in water and the impedance at the end of the cable measured. The impedance magnitude of the device was high (2966 Ω at 45 kHz) and the phase close to zero, so a matching transformer was designed to step down the impedance to 50 Ω. The turns ratio, T_R, of the transformer was determined by:

$$T_R = \frac{N_P}{N_S} = \sqrt{\frac{Z_P}{Z_S}} \tag{3.16}$$

Where N_P and N_S were the number of turns on the primary and secondary windings, Z_P was the primary impedance (the 50 Ω output of the power amplifier) and Z_S the secondary impedance (the 2966 Ω of the transducer). This led to a required turns ratio of 0.13, achieved by setting $N_P = 3$ and $N_S = 23$. The matched impedance magnitude was 57.5 Ω, and the phase was slightly increased to 1.1°. Although not exactly 50 Ω, the power amplifier was designed to absorb any reflected energy from a load, so the small discrepancy would have minimal effect.

The pressure field of the transducer and matching circuit was measured using the LF scanning tank system described in 3.2.1. The drive system consisted of an Agilent signal generator (33220A) and E&I power amplifier (2200L). Initial line scans were conducted to determine the approximate beam widths at a range of separations (Figure 3.10).
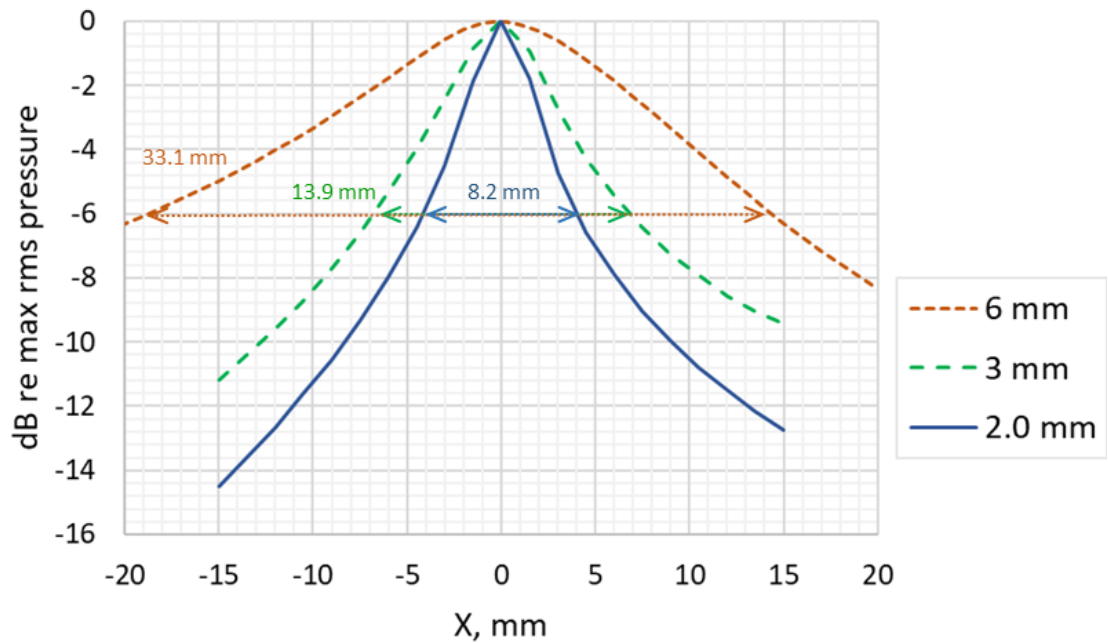
*Figure 3.10: X line scans of cosine transducer at 45 kHz
at 6 mm, 3 mm and 2 mm separations, in dB re maximum rms pressure. -6 dB (half
pressure) beam widths are indicated. The beam widens as the separation increases.*

The line scans indicated that a separation of between 2 mm and 3 mm would result in a
beam width comparable with the LIPUS transducer (12 mm). This separation required the
placement of the cell growth surface of the custom culture vessel (known as the biocell and
described in Chapter 4) directly in front of the transducer. In early *in vitro* trials, cells in
this orientation were shaken off the surface, possibly by the vibration of the membrane due
to the cyclic radiation force of the LIPUS pulse (see Figure 3.11A). It was therefore
necessary to position the cell growth surface on the opposite side, so the radiation force
acted to push the cells back against the membrane rather than pushing them off. This meant
that the shortest distance possible between the transducer front face and the cell layer was
6 mm (Figure 3.11B).

At 6 mm the -6 dB beam width was 33.1 mm, more than double that of the Custom LIPUS
device. This was not ideal as such a wide beam width was not likely to be achieved with a
conventional transducer at 1 MHz. Section 3.2.4.2 discusses the methods adopted to
maximise the 1 MHz beam width to make it more comparable to the 45 kHz beam width.
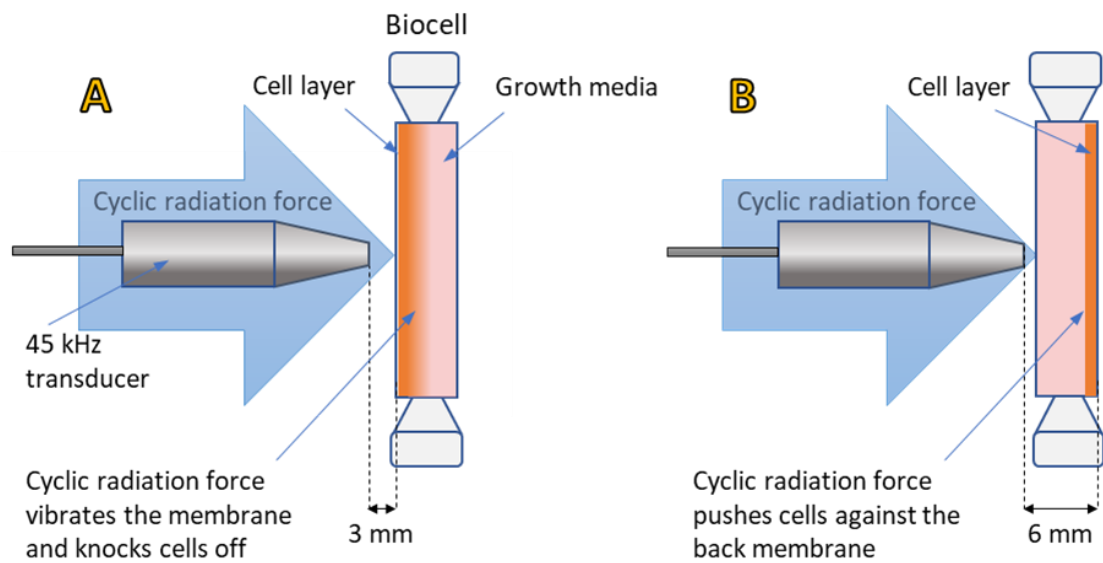
Figure 3.11: Factors affecting separation and beamwidth of 45 kHz LIPUS exposure. A. A separation of 3mm, ideal for equalising beam widths at 45 kHz and 1 MHz, resulted in cell detachment during exposures. This is thought to be due to the cyclic radiation force vibrating the adjacent membrane and knocking the cells off. B. Orienting the culture vessel / biocell so the layer is at the back membrane furthest from the transducer front face results in a wider beam width but the cells stay attached as the cyclic radiation force now pushes the cells against the growth surface.

The cosine transducer was used in the Frequency Study detailed in Chapter 4, which compared 45 kHz and 1 MHz LIPUS. The transducer and its matching circuit were fully characterised for all required drive conditions at 6 mm separation. The same drive system (the signal generator and power amplifier mentioned earlier) was used throughout characterisation and subsequent *in vitro* exposures to maintain conditions.

As it was known that the threshold of cavitation differed with frequency, the drive conditions required to achieve maximum peak-negative pressures corresponding to the mechanical index (*MI*) of 0.05, 0.10, 0.15 and 0.2 were determined. The hypothesis was that comparing fields with the same *MI* would induce comparable mechanical stimulus of the cells at different frequencies. This first trial used the *MI*, not the MI_{LF} as the measure of mechanical effects because at the time the issues with the Mechanical Index at low frequency were not fully appreciated.

The signal generator was set to burst mode with pulse width 200 µs (9 cycles at 45 kHz) and the repetition rate (*prr*) to 1 kHz (period 1 ms), as in the standard 1 MHz LIPUS pulse. The drive voltages required to achieve the above *MI* settings were then established and a XY raster scan was conducted at 0.2 *MI* over the span ±40 mm in 2 mm steps. A series of

detailed line scans in X and Y were also conducted at all *MI* settings over the span ±40 mm in 1 mm steps. The line scans and raster scan were then used to derive the LIPUS dose parameters detailed in 3.2.1.3 for all *MI* settings. The results are detailed in Table 3.13.

Signal generator voltage (mVpp)	Average $\hat{p}_-$ (kPa)	Average $\widehat{MI}$	% σ	%Uncertainty
62	10.9	0.051	2.5	4.9
117	21.2	0.100	0.4	0.7
179.2	31.6	0.149	0.5	1.0
243.3	42.4	0.200	0.1	0.2

Table 3.13: Cosine transducer drive conditions
for nominal $\widehat{MI}$ = 0.05, 0.10, 0.15 & 0.20. The required signal generator output is provided, along with the resulting average $\hat{p}_-$, $\widehat{MI}$, percentage standard deviation (% σ) and % random uncertainty of measurement.

Figure 3.12 shows a colourmap of the peak-negative pressures (and *MI*) measured in the raster scan, indicating the overall shape of the beam.
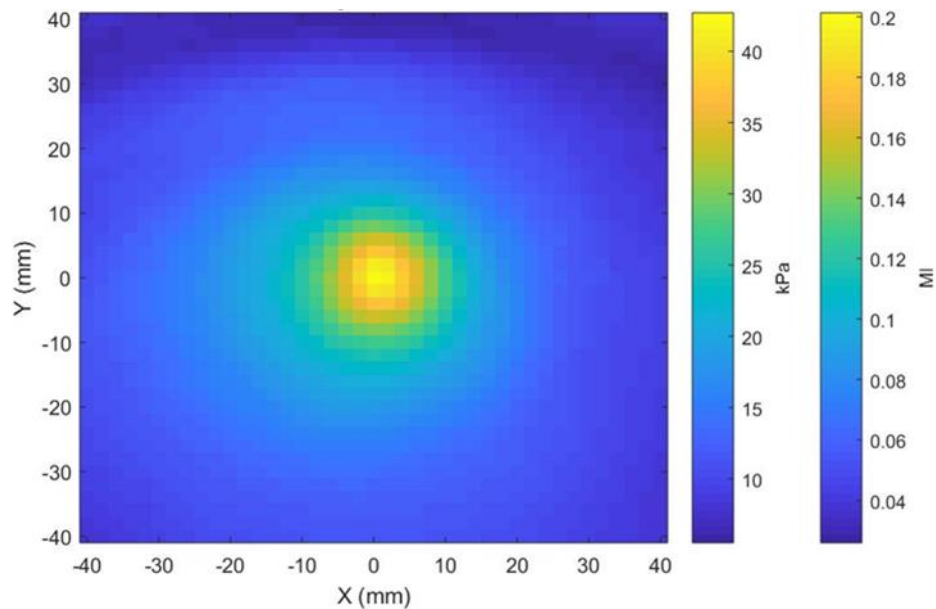
Figure 3.12: Colourmap of peak-negative pressure / MI beam shape of cosine transducer at MI = 0.20

Figure 3.13 presents the line scan results in X and Y. The results suggest the beam is not axisymmetric, especially in the positive Y direction. The -6dB beam widths were 33.1 mm in X and 30.9 mm in Y (average 32.0 mm). The narrower beam width in the Y-plane might

be an effect of the clamp holding the transducer reducing vibration of the device in the vertical plane. To reduce any effects of variation in clamping, the transducer was left in the clamp until required for the Frequency Study.
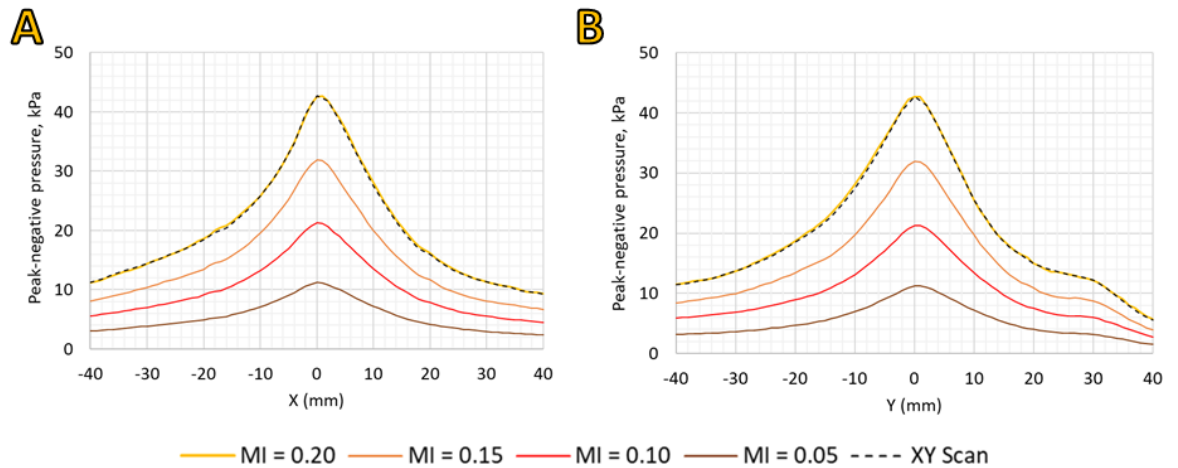
Figure 3.13: Line scans of cosine transducer
A: X-plane; B: Y-plane. X and Y line scans extracted from the XY raster scan (MI = 0.20) are also plotted.

Table 3.14 presents the LIPUS dose parameters calculated from raster and line scans. The MI_{LF} is not reported, but was effectively zero at all settings, so the mechanical effects were likely over-estimated for these peak-negative pressures.

	Nominal $\widehat{MI}$				
	0.050	0.100	0.150	0.200	Units
$\hat{p}_-$	11	21	32	43	kPa
$\widehat{MI}$	0.053	0.100	0.150	0.201	-
$\hat{I}_{PA}$	3	10	21	38	mW/cm^2
$\hat{I}_{TA}$	0.5	1.9	4.2	7.5	mW/cm^2
p_{-,SA,A_c}	4.4	8.3	12.4	16.6	kPa
MI_{SA,A_c}	0.021	0.039	0.058	0.078	-
I_{SAPA,A_c}	0.5	1.8	4.1	7.2	mW/cm^2
I_{SATA,A_c}	0.1	0.4	0.8	1.4	mW/cm^2

Table 3.14: LIPUS dose parameters of the 45 kHz transducer.

3.2.4.2 1 MHz Transducer

An off-the-shelf 1 MHz device replaced the faulty LIPUS transducer. The V303 (Olympus, Japan) was a 12.5 mm diameter transducer designed primarily for non-destructive testing applications. The V303 impedance magnitude was high (389 Ω at 1 MHz) so a step-down transformer was designed to match the impedance to the 50 Ω drive system. The resulting impedance magnitude of the matching circuit and transducer was 39 Ω.

To equalise the 1 MHz and 45 kHz beam widths as much as possible, the separation between the cell layer and V303 was set to 60 mm, the largest distance at which the transducer and matching circuit could sustain the maximum MI of 0.2 without saturating the transformer. The V303 was then characterised at the same MIs as the 45 kHz device, i.e., 0.05, 0.10, 0.15 and 0.20. The determination of distance and characterisation were conducted with the LF scanning system and 0.5 mm needle hydrophone described in 3.2.1. When setting the drive conditions, the matching transformer heated up while being driven, so that the initial peak-negative pressures were lower than those measured over the 20-minute duration. Table 3.15 shows the drive conditions set to achieve an average *MI* within 1.5 % of the required value. The stepped scan process allowed the transformer to cool down between measurements, therefore the results of these scans agreed with the initial peak-negative pressures shown below. Line scans were conducted over ± 40 mm in 1 mm steps and are reported in Figure 3.14. XY raster scans were conducted at 0.2 *MI,* with one scan over the range ±40 mm, step size 2 mm, and a more focussed scan over the range ±10 mm in 0.5 mm steps (Figure 3.15).

	Nominal $\widehat{MI}$				
	0.05	0.1	0.15	0.2	Units
Signal generator voltage	126	200	275	390	mVpp
Initial $\hat{p}_-$	45	80.1	118.3	176.9	kPa
Average $\hat{p}_-$	50.1	100.5	150.6	202.8	kPa
Average $\widehat{MI}$	0.0501	0.1005	0.1506	0.2028	-

Table 3.15: Drive Conditions for V303 Transducer.
Scan results were closer to the initial readings shown in the table, but the average readings over the 20-minute drive duration are more representative of the LIPUS dose.
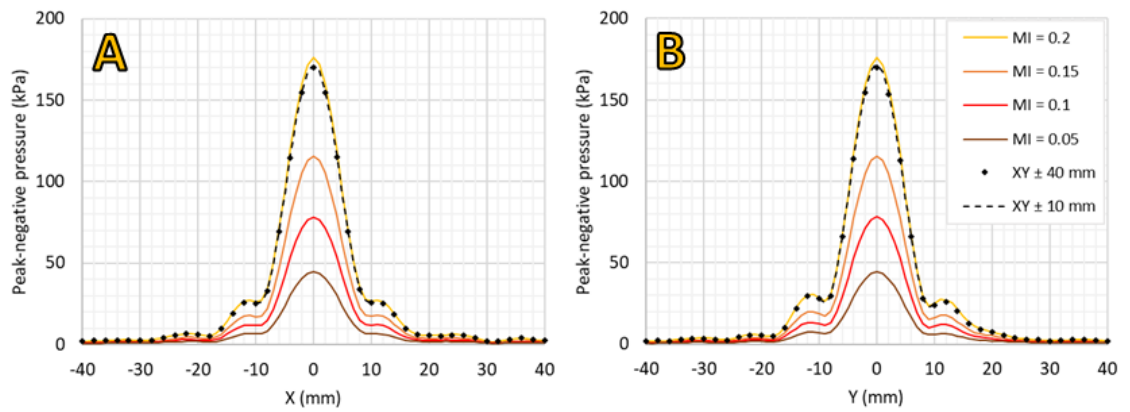
Figure 3.14: V303 (1 MHz) transducer line scan results.
A: X-plane; B: Y-plane. Line scans extracted from XY scans are included for comparison.
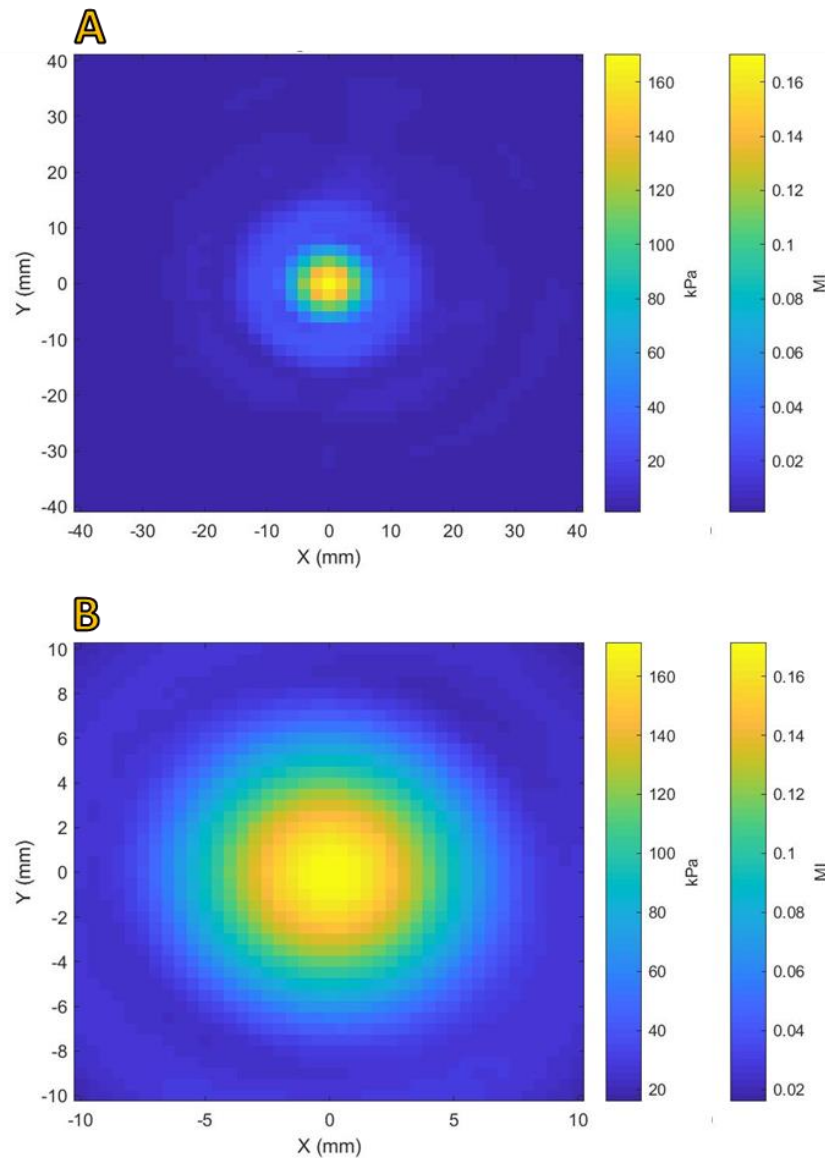
Figure 3.15: Raster Scans of V303 (1 MHz) transducer
at nominal MI = 0.2 with MI and peak-negative pressure scales. A: large area scan (±40
mm, 2 mm steps); B: focussed scan (±10 mm, 0.5 mm steps).

The $\widehat{MI}$ in the 0.2 *MI* line scan was 3.5% higher than XY scan results. This is likely due to the timing of the scans. The 0.2 MI / 200 kPa line scan was conducted after the XY scan, when the transformer was warmer. The LIPUS dose parameters were computed from both XY scans combined according to the calculations described in 3.2.1.3. The MATLAB code written to perform these calculations, *Process_XY20_XY80.m*, is given in Section B.1.2 of Appendix B. Table 3.16 presents the results.

			Nominal $\widehat{MI}$			
LIPUS Dose Parameters		0.050	0.100	0.150	0.200	units
Maxima	$\hat{p}_-$	50.1	100.5	150.6	202.8	kPa
	$\widehat{MI}$	0.0501	0.1005	0.1506	0.2028	-
	I_{SPTP}	83	321	736	1418	mW/cm^2
	I_{SPTA}	17	64	147	284	mW/cm^2
Global (Spatial average)	p_{-,SA,A_c}	3.2	6.3	9.5	12.8	kPa
	MI_{SA,A_c}	0.0032	0.0063	0.0095	0.0128	-
	I_{SAPA,A_c}	1.6	6.5	14.5	26.3	mW/cm^2
	I_{SATA,A_c}	0.3	1.3	2.9	5.3	mW/cm^2

Table 3.16: LIPUS dose parameters of V303 transducer
derived from XY raster and line scans. Amplitudes and parameters were corrected for
expected gain during 20-minute run

3.2.4.3 Comparison of 1 MHz and 45 kHz beam shapes

The beam shapes of the two devices used in the *in vitro* LIPUS exposure studies are compared in Figure 3.16. The beam of the 45 kHz transducer is much wider than that of the 1 MHz device, with average -6 dB (half-pressure) beam width 32.0 mm, compared with the V303 1 MHz beam width of 10.3 mm.
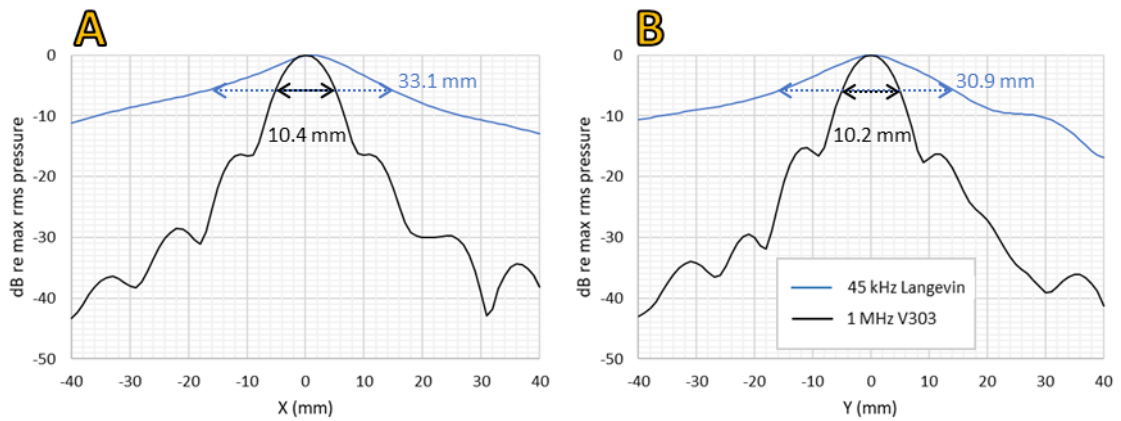
*Figure 3.16: Beam shapes of 45 kHz Langevin transducer and V303 1 MHz transducer
A: X line scans; B: Y line scans, with indication of -6 dB (half-pressure) beam widths.*

Comparing the values of the LIPUS dose parameters in Table 3.14 and Table 3.16, the maximum parameters of the 45 kHz transducer are much lower than the 1 MHz device (due to equalising the $\widehat{MI}$). However, the spatial averages are less, due to the very wide beam width of the 45 kHz device relative to the 1 MHz device. In fact, there is some overlap between the spatial average peak-negative pressure (p_{-,SA,A_c}) values. The p_{-,SA,A_c} of the 45 kHz device at 0.15 MI is 12.4 kPa, which is very close to the p_{-,SA,A_c} of the 1 MHz device at 0.2 MI.

A comparison of the spatial parameters of the Custom 1 MHz LIPUS transducer and the V303 1 MHz transducer is also provided in Table 3.17. The values compared are for each transducer driven to produce a maximum peak negative pressure of $\hat{p}_-$ 200 kPa. The narrower beam of the V303 transducer results in a halving of the spatial average pressure and intensity values, even though the maximum pressure in the beam is the same.

	Custom LIPUS (Ø 50 mm)	V303 1 MHz (Ø 50 mm)	Units
$I_{SAPA,Ac}$	100	49	mW/cm^2
$I_{SATA,Ac}$	20	10	mW/cm^2
$p_{-,SA,Ac}$	42	21	kPa

*Table 3.17: Spatial Average Intensities and peak negative pressures
of Custom LIPUS and V303 transducers over cell growth surface areas of 50 mm
diameter, at $\hat{p}_-$ 200 kPa.*

3.3 Chapter Conclusion

This chapter presented the materials and methods used for cell culture and ultrasonic devices in the course of this PhD. The cell line was presented along with reasons for the choice, and cell culture and immunocytochemistry methods described. The RNA extraction and RT-PCR processes used to assess genetic markers for mechanotransduction and mineralisation were also described.

Two scanning systems were developed to enable detailed and accurate acoustic pressure field characterisation of transducers at high frequency (greater than 500 kHz) and low frequency (less than 500 kHz), which were critical to the investigations that follow in Chapter 4 and 5. The performance requirements for physiotherapy devices set out in the IEC / British Standard 61689 were described and discussed. As a result, a set of LIPUS dose parameters were proposed as measures to enable meaningful comparison against methods of quantifying cellular responses, and to compare those responses against controlled investigations *in vitro*.

A study of clinical LIPUS devices was conducted by measuring the pressure fields of a commercial dual-frequency LIPUS device and a custom-built device based on the Exogen 4000 LIPUS system. After evaluation of device performance, the commercial device was considered unsuitable for controlled *in vitro* exposures at the two operating frequencies of 1 MHz and 45 kHz due to the significantly different beam widths and the inability to control pressure amplitudes. The formation of bubbles on the front face when immersed was also a factor, as this severely disrupted the acoustic field. The conclusion of this study was that clinical LIPUS devices may not be suitable for use in controlled *in vitro* tests, especially when comparing LIPUS fields of different frequency.

A new custom-built LIPUS device was designed, built and its acoustic pressure field characterised. The performance was compared with the available data for the commercial LIPUS device, the Exogen (Bioventus, US) and found to be similar in performance. The custom-built device also met the requirements for safety, as set out in the IEC and British Standards. This device was used to provide the LIPUS field in the Pressure Amplitude Study (Section 4.3).

Two more devices were chosen for use in controlled *in vitro* trials comparing LIPUS at 1 MHz and 45 kHz: the 45 kHz Langevin transducer and the V303 1 MHz transducer (Olympus, US). The Langevin transducer had a front face diameter of 2.5 mm, which was chosen to minimise the beam width at 45 kHz. Although the goal of achieving equal beam widths at both frequencies was not realised, the difference in beam width was minimised as much as possible with the available devices. The 45 kHz Langevin transducer and the 1 MHz V303 transducer were used in the Frequency Study (Section 4.4). The 1 MHz V303 transducer was also used in the Rise Time Study (Section 4.5) and 3D Scaffold Feasibility Study (Section 4.6).

These studies establish the clear need for custom devices that allow full control of the LIPUS dose delivered in order to conduct reliable *in vitro* investigations of LIPUS mechanisms, especially when these include the comparison of significantly different LIPUS frequencies. The proposal of a standard set of LIPUS dose parameters attempts to solve the issues of comparing results between investigations conducted in other laboratories or using different devices. The parameters attempt to describe the acoustic field in terms that are relevant to the biological methods commonly used to quantify cellular responses. It is proposed that these standard parameters might be adopted by all LIPUS researchers in future, such that they can begin to build a consolidated body of work that can be compared with studies by other laboratories in a quantifiable manner. The availability of such data will significantly aid future understanding and the ability of the LIPUS research community to definitively identify the physical and cellular mechanism stimulated by therapeutic LIPUS.

CHAPTER 4
IN VITRO ULTRASOUND EXPOSURE METHOD DEVELOPMENT

This chapter describes the design and development of the *in vitro* ultrasound exposure methods adopted for this study. A custom culture vessel, the biocell, was developed to allow growth of cells and controlled exposure to LIPUS fields in one vessel (4.1). An ultrasound exposure tank system was developed to allow exposure of the cells in the biocell to controlled LIPUS fields (4.2). An early version of the system was tested with the Pressure Amplitude Study (4.3) and further developed when employed in a Frequency Study (4.4), where cells were exposed to LIPUS at 45 kHz and 1 MHz.

The fully developed exposure methods described in 4.1 and 4.2 were employed in an extensive study of the effects of LIPUS with fast and slow rise times to determine if the rate of change of the cyclic radiation force applied to the cells was a significant factor in the stimulation of healing effects (4.5). Potential healing effects were assessed by measuring cell proliferation via cell counts before LIPUS exposure and at 24 hours and 48 hours post-exposure; PGE2 protein expression and cox-2 mRNA expression; and RNA markers of mineralisation.

The Scaffold Feasibility Study (4.6) investigated the potential for growing and exposing MC3T3-E1 preosteoblasts in 3D culture environments to better mimic *in vivo* conditions. Section 4.7 summarises the chapter and describes contributions to the field.

4.1 Custom culture vessel: the biocell

A custom cell culture vessel, the biocell, was designed to allow cell monolayers to be cultured and exposed to controlled LIPUS fields within the same vessel. This section details the development of the biocell.

The biocell (Figure 4.1A) was developed to allow the culture of cells in a monolayer (Figure 4.1B), and exposure of that monolayer to LIPUS fields (Figure 4.1C). The basic design incorporated a 3D-printed frame forming a circular aperture. Thin film was

stretched over both sides with the aim of forming an optically and acoustically transparent window. Access funnels on opposing sides were designed to fit off-the-shelf self-sealing septa (Suba-Seal, Sigma-Aldrich, UK) to allow injection of cells and growth media.
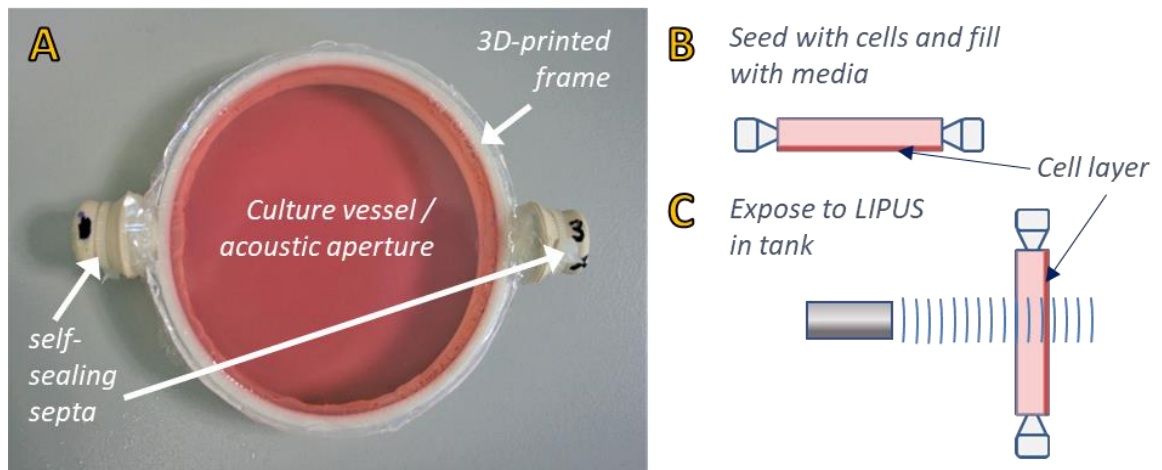
Figure 4.1: The biocell design.
A: Features of the biocell. A pair of septa allow injection of growth media and cells. The thin membranes stretched across the 3D-printed frame provide an acoustic 'window' or aperture, plus a cell growth surface. B: The biocell can be laid flat to grow and incubate cells on one surface. C: The biocell can then be mounted in a tank of water to allow exposure of the cells to LIPUS fields with minimum disturbance to the field.

The design was based on existing vessels such as the Opticell (Thermo Fisher Scientific, US) or the CliniCell (Mabio, FR) shown in Figure 4.2.
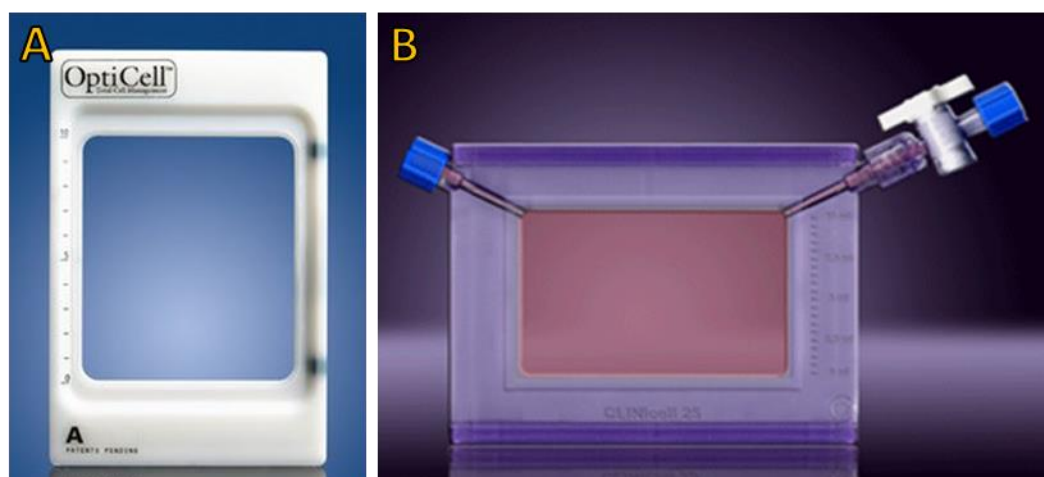
Figure 4.2: Commercially available cell culture vessels used in ultrasound exposures.
A: The OptiCell (Thermo Fisher Scientific, US, discontinued); B: The CliniCell (Mabio, FR). Images reproduced with permission from the manufacturers.

The OptiCell and CliniCell have been used in a number of *in vitro* ultrasound exposure studies, most often in studies of ultrasound-mediated drug delivery in the presence of

microbubbles [192, 193]. Both are of similar cassette-like design, consisting of a rectangular frame with two thin membranes. The thinnest possible membranes are usually chosen for ultrasound tests (75 µm for Opticell and 50 µm for Clinicell) as a thickness much less than the wavelength of the frequency of interest are assumed to make the membrane acoustically transparent (though as discussed in Section 1.3, plate modes should still be considered).

Beekers et al. [194] measured the pressure amplitude drop of an Opticell with 75 µm polystyrene membranes and a Clinicell with 50 µm polycarbonate membranes over the frequency range 1 MHz to 4 MHz. They placed their focussed test transducers at a 45° angle to the front membrane to direct any reflections away from the front face of the transducer. The pressure amplitude was assessed using a novel technique where the oscillatory response of well-characterised microbubbles in the presence of the ultrasound was monitored and quantified using a high-speed camera. They found the pressure amplitude across the frequency range 1 MHz to 4 MHz dropped by 5.4 dB on average in the Clinicell and 5.1 dB in the Opticell.

The Biocell design improved on the Clinicell and Opticell designs by using a significantly thinner membrane (6 µm Mylar, Goodfellow, UK) to minimise the effect on the ultrasound field. A circular aperture was considered more appropriate to accommodate the beam shapes of most ultrasound transducers, which tend to be axisymmetric. The circular aperture also simplified the prediction of vibrational modes across the membrane (calculated in Section 4.1.2.2) and 3D printing the frame allowed the aperture of the vessel to be customised for any ultrasound beam width. The following sections describe the other design aspects considered when developing the biocell, starting with the 3D-printed frame.

4.1.1 The 3D-printed Frame

The 3D-printed frame of the biocell consisted of a circular frame with two funnels designed to fit off-the-shelf self-sealing septa (SubaSeal[TM], Sigma-Aldrich, UK). The design was created in the Solidworks Computer-Aided Design (CAD) package (Figure 4.3A). Prototype frames were printed in a number of candidate 3D-printing materials (Figure 4.3B) to assess their performance against the following requirements:

- The biocell frame shall be watertight and have low water absorption to withstand prolonged immersion in the exposure tank and moist conditions in the incubator.

- The biocell frame shall have good chemical resistance to the sterilisation agent 70% ETOH.

- The biocell frame shall maintain shape and rigidity at temperatures up to 37 °C.

- The biocell frame should have a smooth finish to aid cleaning and sterilisation.
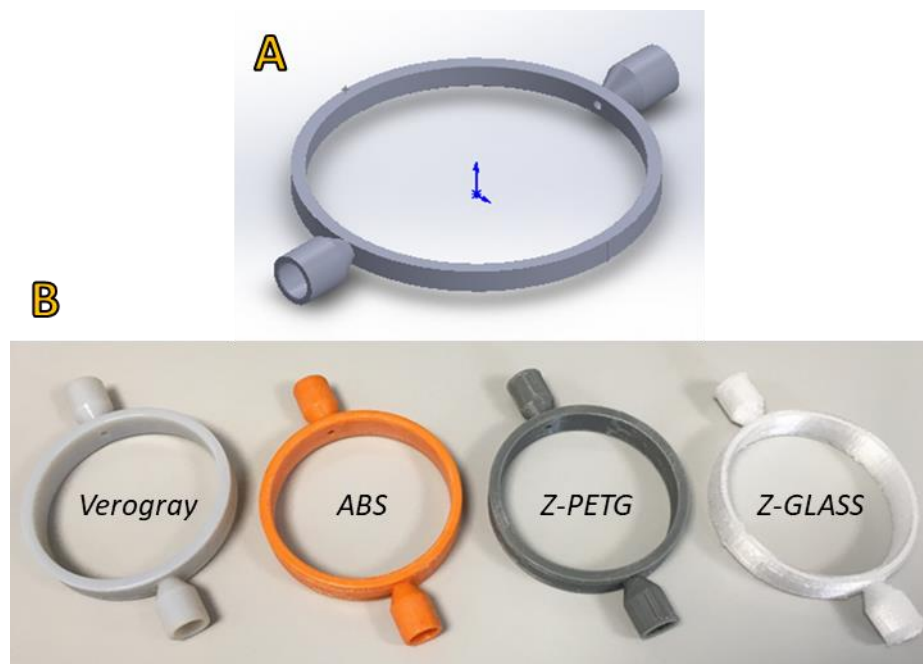
Figure 4.3: Biocell CAD design and prototype biocell frames.
A: 3D CAD representation of the Biocell design. B: Prototype frames in four 3D-printing materials (50 mm × 10 mm aperture).

The performance of each sample was assessed in the lab by exposure to these conditions, with reference to the available manufacturers data summarised in Table 4.1. The 3D printers used were either UV curing or Fused Deposit Modelling (FDM) types. FDM printers extrude thermoplastic material through a heated nozzle and lay it down layer by layer, with layer thicknesses down to 0.2 mm. UV cured 3D printers cure a liquid polymer one layer at a time with UV light, offering fine resolution down to tens of microns. Low resolution or layer thickness does not necessarily equal a better print: printer quality and printing techniques all affect the final print quality. As well as printer type and layer thickness or resolution, Table 4.1 details:

- The glass transition temperature (Tg) and/or the heat deflection temperature (HDT), which indicate the temperature at which the polymer loses rigidity[1].
- The water sorption, which is a measure of how the material takes up water by surface adsorption and bulk absorption combined. Required so the material could resist prolonged immersion and the humid environment in the incubator.
- The flexural and tensional moduli, which measure a material's resistance to bending under a load.

	Verogray[TM]	**ABSplus-P430**	*Z-PETG*	*Z-GLASS*	***Strong-X***
Manufacturer	Stratasys, US	**Stratasys, US**	Zortrax S.A., PL	Zortrax S.A., PL	**Liqcreate,**
3D printer	Objet30	**F270**	Zortrax M300	Zortrax M300	**Elegoo Mars**
Printing technique	Polyjet (UV cure)	**FDM**	FDM	FDM	**UV + post cure**
Layer thickness / resolution	30 µm	**0.2 mm**	0.2 mm	0.2 mm	**35 µm**
Glass transition temperature (Tg)	52 - 54 °C	**108 °C**	-	78 °C	**128 °C**
Heat Deflection Temperature, (0.455 MPa)	45 – 50 °C	**96 °C**	70 °C	-	**-**
Water sorption	1.1 – 1.5 %	**0.05 – 1.0 %**	-	-	**0.45 %**
Tensile modulus	2 - 3 GPa	**2.2 GPa**	-	-	**2.5 GPa**
Flexural modulus	2.2 – 3.2 GPa	**1.65 – 2.1 GPa**	2.1 GPa	1.2 GPa	**3.25 GPa**

Table 4.1: Properties of 3D printing polymers considered for biocell frame
Data from manufacturer's data sheets.

The tensile and flexural moduli were very similar for all materials, with most in the region of 2 – 3 GPa. Water sorption was low across the board, where the data was available, with the ABS and Strong-X materials the lowest.

---

[1] Polymers have an amorphous structure and therefore do not have a defined melting point as is the case for crystalline solids. Instead, they transition from a solid to a more flexible state at the glass transition temperature (Tg). Tg is not fixed and depends on the degree of crystallisation in the structure. Another measure of melting point is the Heat Deflection Temperature, i.e., the temperature at which the polymer begins to bend under a given load.

The Z-PETG and Z-GLASS prototypes were not water-tight due to printing imperfections and so were rejected. The Verogray™ prototype had a smooth finish and was waterproof. However, at 37 °C it was prone to warping when attempts were made to stretch the mylar membrane across the aperture. The ABS material did not have as smooth a finish but was waterproof, resistant to the sterilisation chemicals and remained rigid even at incubator temperatures. Therefore, the ABS was chosen as the most suitable material.

Some later frames were printed in the Strong-X material, due to the university 3D printing service being unavailable (see COVID impact statement at the front of this thesis for details). The Strong-X biocell frames were tested in the same manner and performed as well as the ABS frames.

4.1.2 The Biocell as an Acoustically Transparent Aperture

This section details the aspects of the biocell design relating to providing an acoustically transparent aperture. The requirements were as follows (with the relevant section number in brackets):

- The biocell aperture shall be wide enough to accommodate the main LIPUS beam in order to minimise reflections off the inside edges of the frame (4.1.2.1).
- The biocell aperture size shall be designed to avoid radial vibration modes in the biocell membrane that coincide with the LIPUS frequencies of interest (4.1.2.2).
- The biocell aperture membrane shall be designed to minimise reflections (4.1.2.3).
- The biocell aperture membrane shall be designed to minimise transmission loss through the membrane (4.1.2.4).

4.1.2.1 Biocell Aperture / Frame Diameter

The frame diameter was set to 70 mm as this was the width at which the 45 kHz beam was 10 dB below the maximum pressure. The 1 MHz beam was over 30 dB below the maximum pressure at the frame edges. Ideally the amplitude of the beam should be at least 20 dB (100 times) below the maximum pressure at the beam centre to ensure any reflections from the frame have minimal effect on the field experienced by the cells. Figure 4.4A and B illustrate the beam shapes of the 45 kHz and 1 MHz transducers, with the locations of frame edges indicated, assuming the beam is accurately centred.
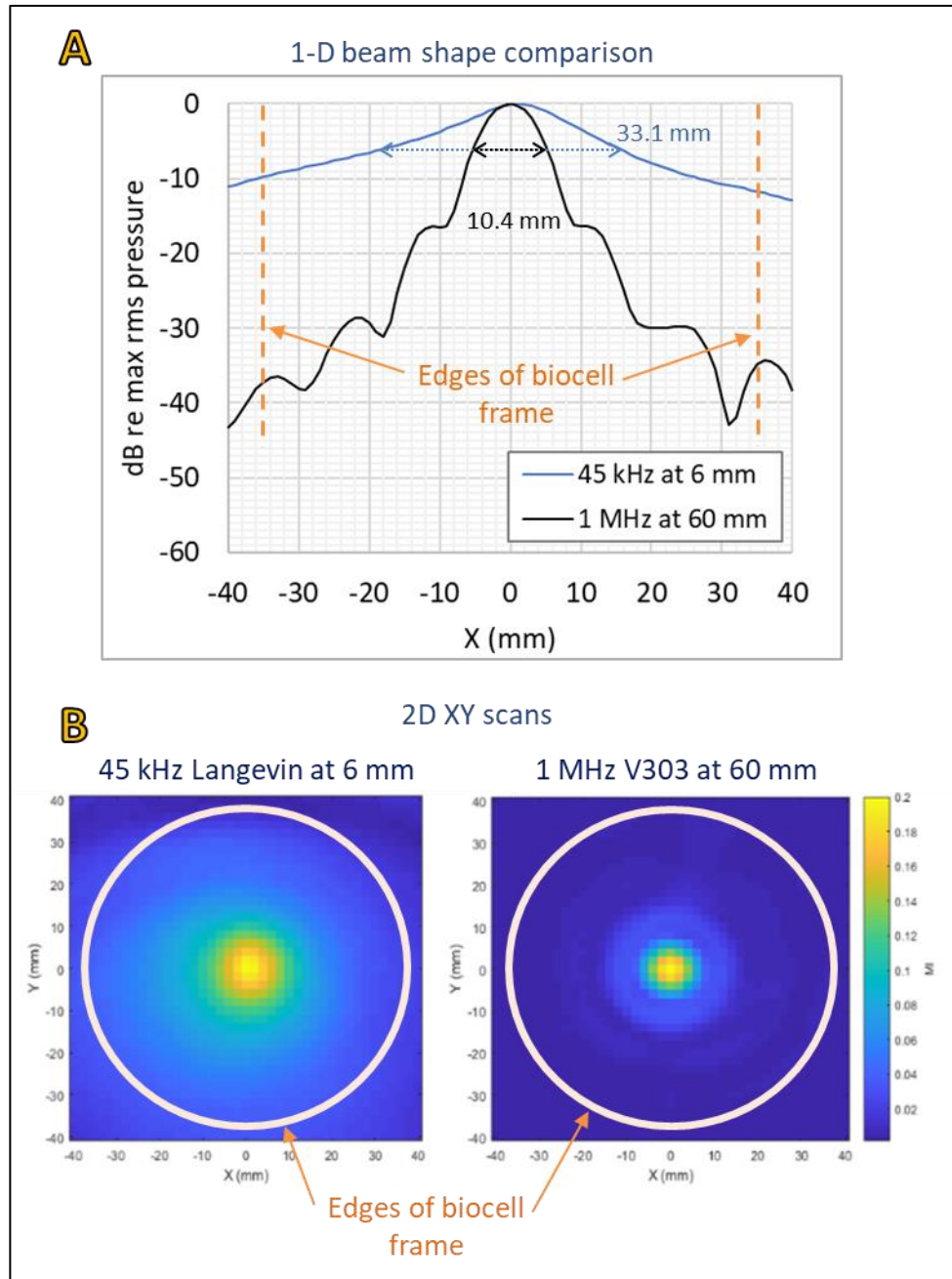
Figure 4.4: Illustration showing edges of biocell frame in comparison with beam widths of ultrasound fields used in the in vitro studies. A: Line scan results showing beam shapes of transducers used in this study in horizontal (X) plane with indication of biocell frame edges (70 mm diameter). B: 2D beam patterns in X-Y plane. The transducers and separations were: 45 kHz Langevin device at 6 mm separation; 1 MHz V303 device at 60 mm separation.

4.1.2.2 Radial Modes of the Mylar Membrane

Another factor to take into account was the possible excitation of radial modes of the Mylar membrane. Frequencies coinciding with radial modes must be avoided to minimise the secondary effects from direct vibration. For a circular membrane fixed rigidly at its

edges, the first radial mode, or fundamental frequency of vibration, f_0, occurs at the frequency:

$$f_0 = {}^c\!/_{2d} \qquad\qquad (4.1)$$

where d is the diameter in metres (m) and c is the speed of sound in the material in metres per second (m/s). The diameter of the membrane in the final biocell design is 70 mm (0.07 m) and the speed of sound in Mylar is 2540 m/s [60], giving a fundamental frequency (f_0) of 18.1 kHz, with first and second harmonics at 36.2 kHz and 54.4 kHz. As vibration modes occur only at integer multiples of the fundamental frequency, it is unlikely that vibration modes will be excited by fields at 45 kHz ($2.5 \times f_0$) and 1 MHz ($55.1 \times f_0$).

4.1.2.3 Predicted Reflection Coefficient of Biocell Membrane

6 µm BoPET (Mylar) film (Goodfellow, UK) was chosen as the membrane material for the acoustic aperture of the biocell. To assess the effects of the material on the ultrasound field, the reflection coefficient, |R|, of 6 µm Mylar was predicted by Equation 1.2, and compared to that of the Opticell (75 µm Polystyrene / PS) and Clinicell (50 µm Polycarbonate / PC). Figure 4.5 presents the results and values of |R| are given for 45 kHz and 1 MHz, the frequencies of interest in this study.

	45 kHz	1 MHz	dB re Biocell
Opticell	0.0046	0.1001	+9.6
Clinicell	0.0039	0.0858	+8.9
Biocell	0.0005	0.0112	0.0
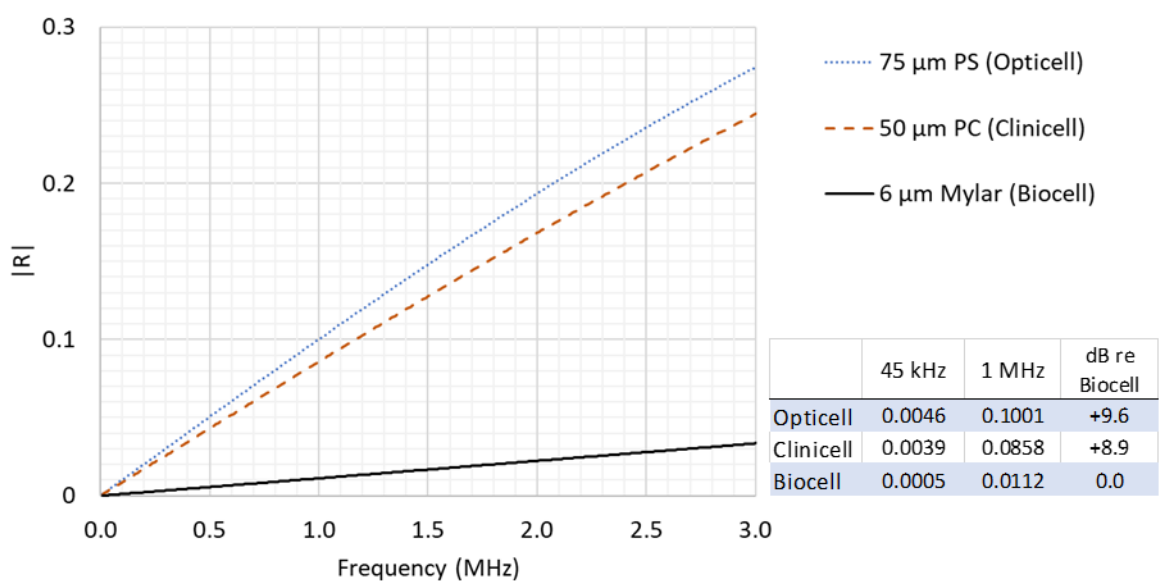
Figure 4.5: Reflection coefficients of the Opticell membrane, Clinicell membrane and 6µm Mylar, up to 3 MHz. Predicted via Equation 1.2.

The 6 μm Mylar membrane has a significantly lower predicted reflection coefficient (*R*) than the Opticell and Clinicell membranes, at 9 times (or 9.6 dB) lower than the Opticell membrane and 7.7 times (or 8.9 dB) lower than the Clincell membrane. *R* is consistently low (<< 0.1) at the lower frequency, so it would be possible to use the Clinicell and Opticell vessels for a study at 45 kHz provided the window area allows the entire beam to pass through. At 3 MHz, another common LIPUS frequency, the *R* of the Clinicell and Opticell rise to 0.24 and 0.27 respectively, meaning 24 – 27 % of the pressure amplitude is reflected. The *R* of the 6 μm Mylar remains low at 0.03 (i.e., 3% reflected).

4.1.2.4 Transmission Loss through the Acoustic Aperture

The Transmission loss through the 6μm Mylar membrane was measured using the scanning tank system described in 3.2.1, with water held at 37 ± 2 °C. A mock-up biocell fitted with one 6 μm Mylar membrane was immersed in the tank, brushed with a soft brush to remove any air on the surface and left for at least 1 hour to wet.

The 45 kHz Langevin device and V303 1 MHz device described in 3.2.4 were each aligned in turn to the centre of the biocell front window, at the distance at which each device was fully characterised. A needle hydrophone (detailed in Table 3.2) was positioned 2 mm behind the centre of the membrane and aligned to the ultrasound source using the alignment techniques described in 3.2.1. A line scan was conducted in the horizontal (X) plane, orthogonal to the propagation, spanning ±10 mm either side of the beam centre in 1 mm steps. The voltage output of the needle hydrophone at each scan point was saved as comma delimited text files and the peak negative pressure derived using the methods described in Section 3.2.1.1. The mock-up biocell with one membrane was then removed, taking care not to move the transducer or hydrophone, and the scan repeated to measure the acoustic pressure field without the membrane.

The difference between the two measurements gives a measure of the transmission loss due to the membrane. The results are presented in Figure 4.6, showing the peak negative pressure (*p-*) through the membrane and in the free field (Figure 4.6A & B). The transmission loss in dB is given in Figure 4.6C.
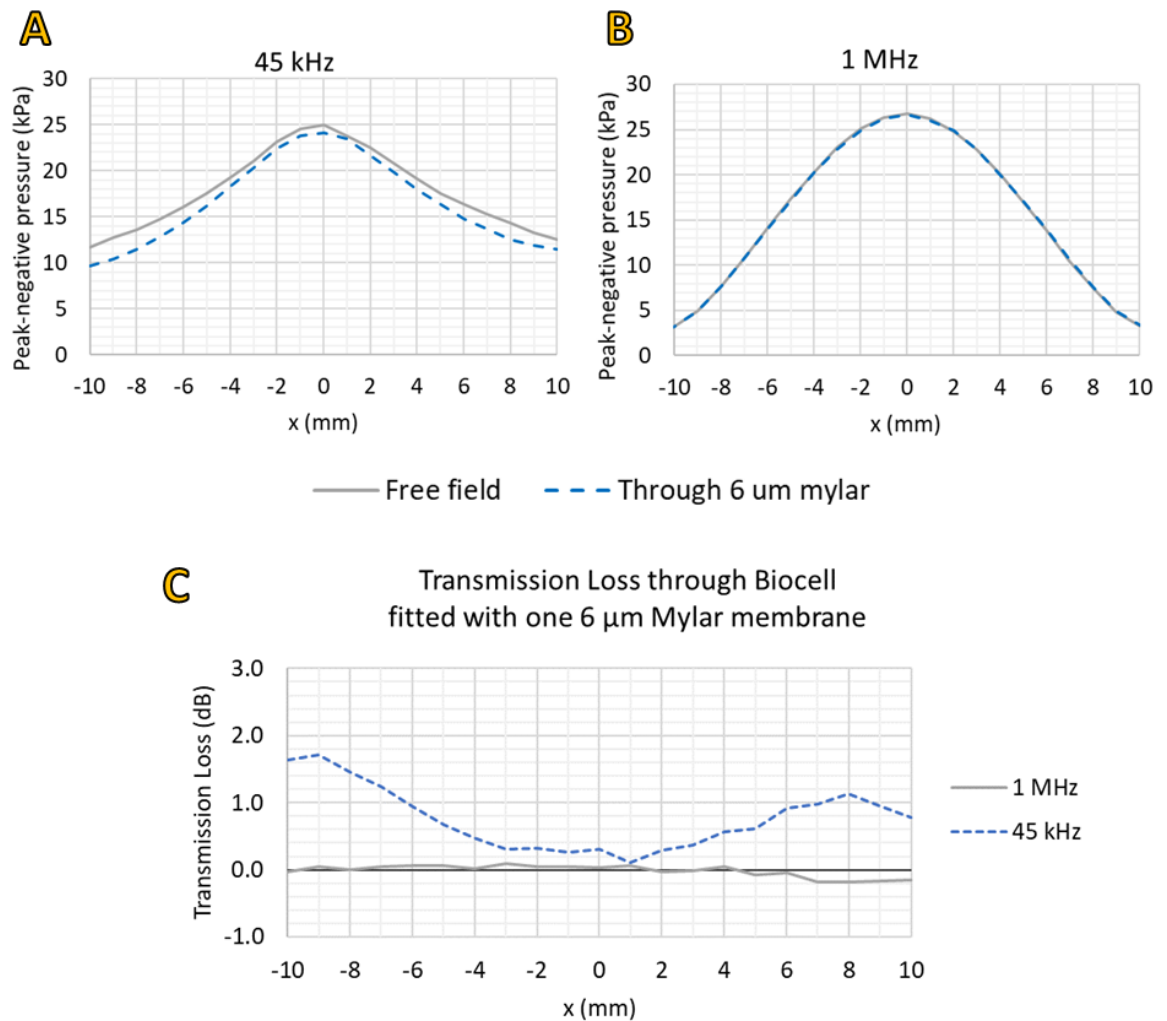
Figure 4.6 Transmission Loss through Biocell fitted with one membrane.
A: 45 kHz; B: 1 MHz; C: Transmission Loss in dB.

The 45 kHz transmission loss due to mylar indicated p_- dropped by 0.3 dB (3.5 %) in the beam centre and the beam width appeared to narrow. The free field -6 dB (half-pressure) beam width reduced from 18.2 mm in free field conditions to 15.7 mm with the biocell and membrane in place. I suspect this narrowing of the beam was caused by the membrane acting as an acoustic lens, focussing the ultrasound. During ultrasound excitation the membrane was observed to bow slightly in the centre, probably due to the radiation force acting on the membrane. The resulting concave shape likely caused the focussing effect. Note the degree of curvature, and therefore the focussing effect, may change due to variation in membrane tension.

The transmission loss at 1 MHz was 0 dB at the centre of the beam, with worst case of 0.1 dB (-1 %) at the -3.5 mm scan point. Negative transmission losses from 5 mm to 10 mm of down to -0.2 dB indicate an effective gain, but this was more likely to be due to

either random variation in the measurement or to a slight difference in the rotational alignment of the transducer, which could easily have occurred when removing the mock-up biocell from the tank. We can therefore conclude that the 1 MHz ultrasound field was effectively unchanged by the presence of the biocell fitted with one Mylar membrane.

As the LIPUS field is unchanged by transmission through the Mylar membrane, and the reflection coefficient of the 6 µm Mylar is effectively zero, I have therefore assumed that the cells are exposed to a LIPUS field that is the same as characterised in Chapter 3. In the case of the 45 kHz field, this was only used for the Frequency Study, which was limited in scope. If further 45 kHz LIPUS studies were to be run in future, the LIPUS dose parameters would have to be recalculated taking the focussing effects into account.

4.1.3 The Biocell as a Culture Vessel

4.1.3.1 Gas permeability

As well as the nutrients contained in growth media and a stable temperature and humidity, cells require a particular balance of gases to grow well *in vitro*. Incubators are designed to provide this, providing a mix of 95% air and 5% carbon dioxide (CO_2). To maintain these optimal levels for the cells, the Opticell and Clinicell membranes are designed to be gas permeable: allowing air and CO2 to pass through.

In the case of the polycarbonate Clinicell membrane, the manufacturer quotes a CO_2 gas transfer rate of 1.075 ml/mil/100in^2/24h/atm, which is equivalent to 16.7 ml/m^2/24h in SI units. The CO_2 transfer rate of 50 µm-thick Mylar is 5.9 ml/m^2/24h [195], and this is likely to rise for the thinner 6 µm film. Therefore, it was concluded that the biocell membrane would have suitable gas permeability for cell growth and incubation purposes. As a precautionary measure, in case the gas transfer was not sufficient, any growth media used to seed or fill the biocells was stored in a culture flask (with filter cap) in the incubator for at least one hour beforehand, to take up CO_2 prior to being encapsulated.

4.1.3.2 Cell adhesion

Early attempts to culture cells on the Mylar membrane indicated cell adhesion might be poor. Cells were easily washed off during DPBS washes and low cell counts after initial exposures suggested the cells were being knocked off the surface by the LIPUS field.

One of the indications of good cell adhesion properties of a surface is its ability to attract or repel water. The water contact angle is a measure of the wetting capability of the surface and depends on a variety of factors but most significantly on surface roughness and surface charge. A hydrophobic surface repels water and has a water contact angle of greater than 90° (Figure 4.7A). A hydrophilic surface attracts water and has a water contact angle of less than 90° (Figure 4.7B). A hydrophilic surface also encourages the deposition of extracellular matrix, cells and proteins and therefore improves cell adhesion [196].
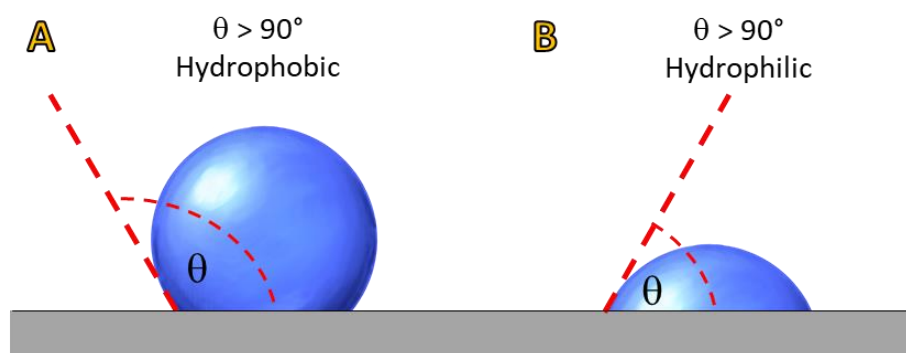
Figure 4.7: Water contact angle (θ) of surfaces.
A: hydrophobic (water repelling) surfaces have θ > 90°. B: hydrophilic (water attracting)
surfaces have θ < 90°.

Mylar has a water contact angle of approximately 80° so is mildly hydrophilic [197]. Glass and Tissue Culture Polystyrene (TCPS) have a water contact angle of approximately 40°. Plain Polystyrene (PS) has a water contact angle of approximately 70°. To transform it into TCPS, a variety of surface treatments are applied. The most common surface treatments are chemical etching with acids or plasma treatment, which aim to increase surface oxidation and roughness [196]. Plasma treatment was attempted with a handheld corona plasma device but this technique was too destructive for such a thin film. Chemical etching was also considered too destructive and difficult to control. Gas plasma treatment is a more controlled plasma treatment method and therefore could improve the surface with less damage [196], but this treatment was not available at the time.

Using ECM materials such as fibronectin and collagen have also been shown to improve adhesion of cells on artificial implants [198]. Collagen was considered the most appropriate for this study because (1) it is the major constituent of the extra cellular matrix in bone and (2) collagen coatings have been shown to improve adhesion of osteoblasts [198]. Growing preosteoblasts and osteoblasts on collagen has been shown to subtly

change the expression of mineralisation markers [199]. However, as all the biocell membranes would be treated the same, the relative expressions in response to LIPUS exposure could still be assessed.

A cell adhesion study assessed the adhesion of cells to biocell membranes coated with collagen. Six biocells were prepared with one membrane and coated with two concentrations of collagen solution (Collagen Type 1, from rat tail, C3867, Sigma-Aldrich, DE) as follows:

- 3x biocells at 10 μg/cm^2 Dilute 134 μl Col Type 1 solution in 6 ml DPBS.
- 3x biocells at 15 μg/cm^2 Dilute 200 μl Col Type 1 solution in 6 ml DPBS.

2 ml of the required collagen solution was added to each biocell with two concentrations of collagen coating and three seeding densities. The biocell frames used for the study had a 50 mm diameter aperture (19.6 cm^2 cell growth area). The assembly of the biocells was completed in the usual way (described in 4.1.5) and seeded with MC3T3-E1 (passage 20) at three cell densities: 10,000, 20,000 and 30,000 cells/cm^2 to ascertain if cell density might also affect adhesion. After 24 hours incubation the biocells were live-stained as described in 3.1.2.1 and imaged in 5 central areas with a fluorescent microscope. Two biocells were found to be leaking and discarded. Images were saved in JPEG format for cell counting in the image processing software ImageJ [179, 200]. After imaging, the biocells were washed vigorously with 3 x 10 ml DPBS (D8537, Sigma-Aldrich, DE) applied via 20 ml syringe and 1 ml diameter needle, then imaged again in the same areas.

The hypothesis of the study is that vigorous washing would detach any cells that are poorly adhering to the membrane and cell counts would drop, as was observed in early studies with no collagen coating. Examination of the images before and after washing found that the number of dead cells was very low, with a maximum of 1 dead cell in each image. Live/dead cell counts were used to determine the effects of the wash. These counts were obtained via the ImageJ process macro *Count_all_FUNA.ijm* in Section B.2.1 of Appendix B. The five cell counts, from the five captured images of each biocell before and after washing, were averaged and are presented in Figure 4.8.

The chart data corresponds to the following table:

Collagen concentration.	10 µg/cm²	10 µg/cm²	10 µg/cm²	15 µg/cm²
Seeding density	10 k/cm²	20 k/cm²	30 k/cm²	10k/cm²
%difference (After wash vs. Before)	-2.5 %	-10.8 %	+1.7 %	-28.0 %
P (Student's t-test, After wash vs. Before)	0.43	0.22	0.37	0.27
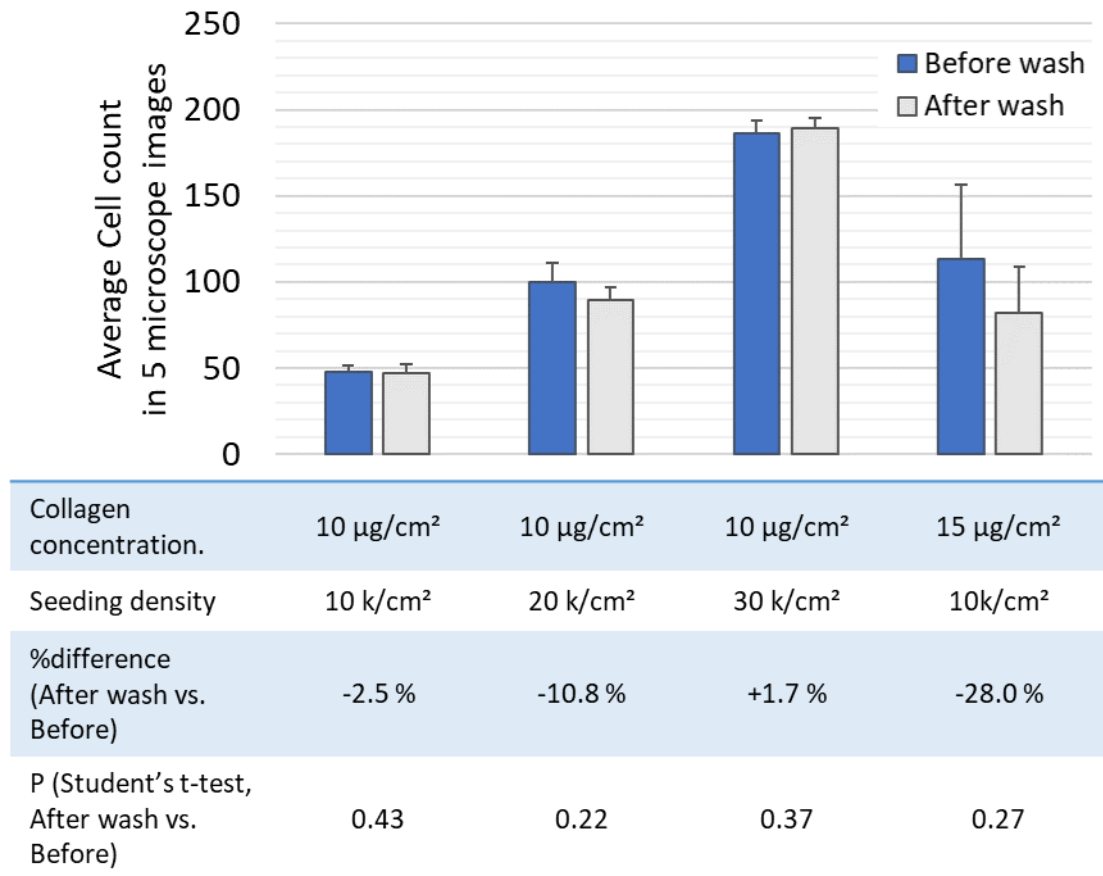
Figure 4.8: Average cell counts over five images in four biocells coated with collagen with concentration 10 µg/cm² or 15 µg/cm² and seeding density 10, 20 or 30 thousand cells per cm². Table shows percentage difference in cell counts after vigorous washing with DPBS. Error bars are Standard Error of the Mean (SEM). The Before Wash and After Wash cell counts were analysed with the Student's t-test and no significant difference was found (p > 0.05) in cell counts after vigorous washing, indicating adequate cell adhesion in all conditions tested.

The results show good cell adhesion with a coating concentration of 10 µg/cm² consistently showing no significant difference in cell counts as tested via a Student's t-test. The single biocell with higher coating concentration saw a drop in cells after washing, but this was not significant and was likely due to the higher variation in cell counts between images. The results showed that the standard coating concentration of 10 µg/cm² provided adequate cell adhesion for the purposes of the study and that seeding density did not affect cell adhesion.

4.1.4 The Final Biocell Design

Briefly, the final biocell design consisted of a 3D-printed ABS (or Strong-X) frame forming a 70 mm diameter circular aperture. 6 µm BoPET (Mylar) film (Goodfellow, UK) was stretched over both sides, forming an optically and acoustically transparent window.

Access funnels on opposing sides were fitted with self-sealing septa (Suba-Seal, Sigma-Aldrich, UK) to allow injection of cells and growth media. The funnels and mylar frame were sealed with marine grade silicone sealant (Bond It, UK) to ensure a watertight seal. Cells were grown on one of the Mylar surfaces, pre-treated with a 10 µg/cm^2 coating of Collagen Type I (C3867, Sigma, UK) to improve adhesion.

4.1.5 Biocell Assembly and Seeding Process

The final biocell design required a meticulous construction protocol to maintain a sterile and hospitable environment for cells to grow and ensure the biocell was watertight. On day 1 of construction, the parts involved in assembly were gathered and cleaned by scrubbing in hot soapy water. Each biocell assembly required the following components and equipment (illustrated in Figure 4.9):

Components:
- Biocell frame × 1 (CAD illustration in Figure 4.3A)
- Film stretcher × 1 (CAD illustration in Figure 4.10A)
- 10 cm x 10 cm mylar film × 2
- SubaSeal^{TM} Rubber Septa (Merck, DE) × 2

Equipment:
- Biocell stand: 70 mm diameter, cut from 5 mm-thick polystyrene craft board) × 1
- Rubber bands ×2
- Scissors
- Tweezers
- Marking stencil (CAD illustration in Figure 4.10B)

| Rubber bands | Biocell stands (polystyrene) | SubaSeal™ rubber septa | Biocell frames and film stretchers | 6 µm mylar squares (10cm x 10cm) |
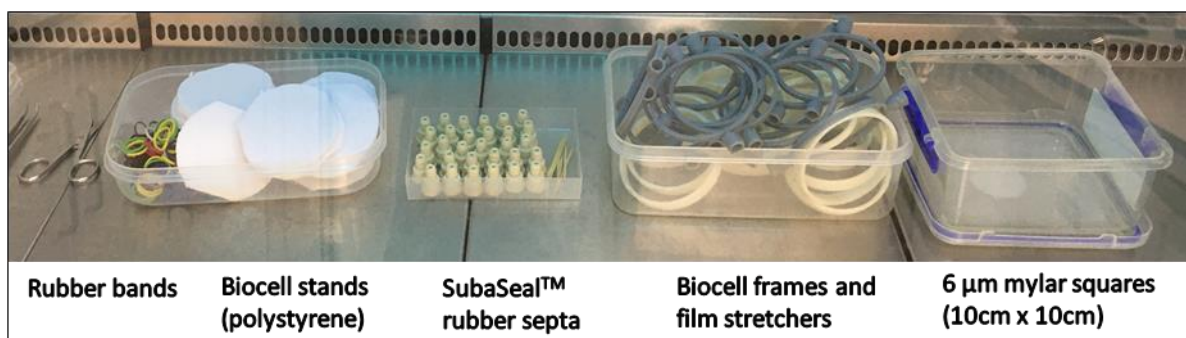
Figure 4.9: Biocell assembly day 1
Prepare biocell parts, soak in 70% ethanol and expose to UV in biological safety cabinet for 30 minutes.
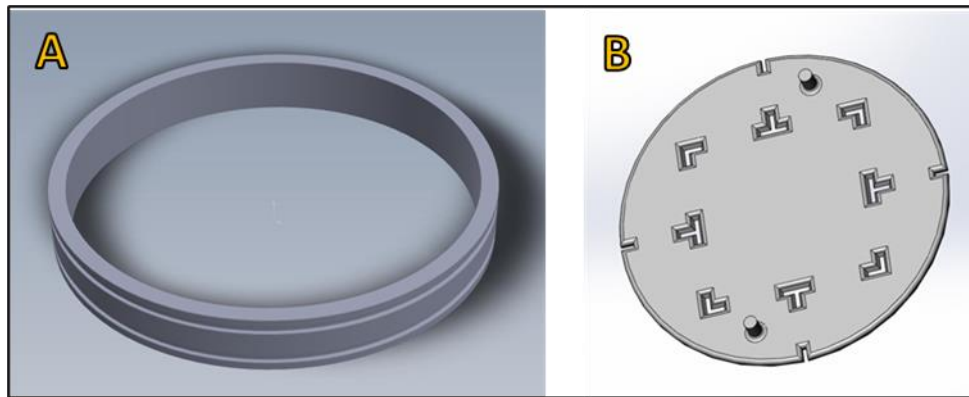
Figure 4.10: 3D CAD files of 3D-printed parts involved in biocell assembly. A: biocell film / membrane stretcher is the same diameter and thickness of the biocell circular frame, with ridges to hold the membrane in place with elastic bands during stretching. B: the marking stencil allowed uniform marking of the biocell membrane for correct alignment during US exposures and in the scanning microscope.

All parts were soaked overnight in 70 % ethanol, placed in the biological safety cabinet (BSC) and exposed to UV for at least 30 minutes. On day 2 (Figure 4.11), the septa and first mylar membrane were fitted. First the septa were folded over in preparation for fitting to the funnels of the biocell frame, and a 10 cm x 10 cm mylar square was stretched across the 3D-printed stretcher and fixed in place with a rubber band. Once any residual 70% ethanol had evaporated off, a non-toxic silicone sealant, here HA6 Marine Grade RTV silicone sealant (Bond-It, UK), was applied using a syringe in and around the funnel and along one edge of the circular biocell frame. Finally, septa and mylar membrane were fitted in place. The sealant acted as an adhesive and ensured the biocell was waterproof. The assembly was then exposed to 30 minutes UV and left overnight in the BSC to cure.
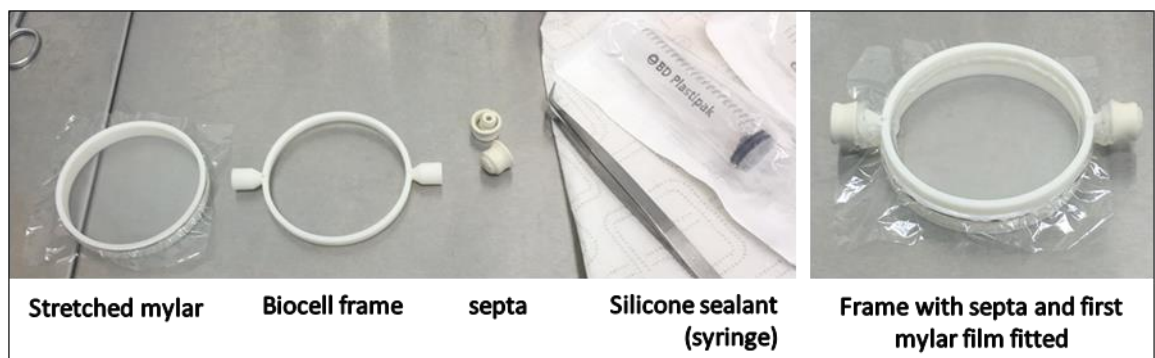
Figure 4.11: Day 2: stretch first mylar film and fit to biocell frame with septa.

On day 3 a collagen coating was applied to the inside of the first membrane, which would constitute the cell growth surface. First the membrane was washed 3 times with 5 ml DPBS to remove any residual ethanol deposits. Then 4 ml of collagen solution (containing 90 µl

rat tail collagen) added to each biocell to give a collagen coating concentration of $10\,\mu g/cm^2$ as established in the cell adhesion trial. The biocells were soaked in the solution in the BSC overnight until dry (Figure 4.12A). The biocells were not exposed to UV light during the collagen soak as this can denature the collagen while in solution.
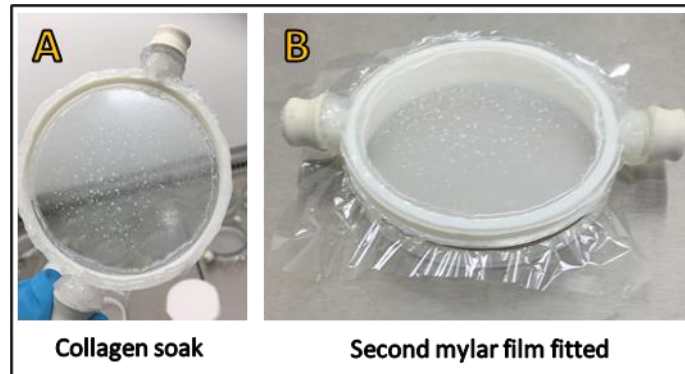
Figure 4.12: Biocell assembly days 3 and 4:
Collagen soak and second mylar film.

On day 4 the second Mylar membrane was fitted by stretching it over the stretcher and fitting the frame with silicone sealant (Figure 4.12B). Silicone sealant was also applied around the base of the funnels as this area was prone to leakage (caused by small flaws in the 3D printing in this area of the frame). The final assembly was exposed to 30 minutes UV and left in the BSC overnight to cure.

On day 5 (Figure 4.13) the outside of the biocell growth surface was marked with a sharpie using the marking stencil, aligned to the centres of the funnels, to ensure the marks were uniform and in the correct orientation.
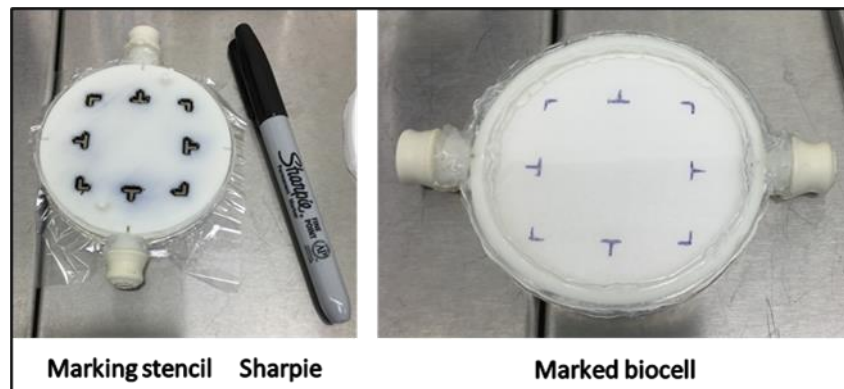
Figure 4.13: Day 5: Marking the biocell with 3D-printed stencil.

Finally, the biocell was washed thoroughly three times with DPBS. The first wash involved filling the biocell with 20 ml DPBS and refreshing the air inside to remove any residual deposits or fumes of acetic acid, a by-product of the silicone sealant curing process. Then two further washes with 10 ml DPBS washed off any remaining ethanol or acetic acid residue and any loosely attached collagen from the collagen coating.

The process of injecting liquids into the biocell was a simple one but required great care to ensure it was done correctly – especially immediately prior to US exposure where the presence of any bubbles could invalidate the results. Two needles and syringes were required. Large diameter needles were used (1 mm / 19G) to minimise damage to cells during injection. Figure 4.14 shows a still from the biocell filling process, in this case injecting fresh growth media prior to a US exposure.

When filling the biocell the top syringe extracted the air as the bottom syringe injected the liquid. This equalises the pressure within the biocell. The process was carried out slowly to avoid sudden pressure changes, as large pressure differentials may damage the seal around the edges of the membrane. Working slowly and smoothly also minimised the formation of bubbles in the liquid, both in drawing up the liquid into the syringe and injecting it into the biocell. The process was reversed when draining the biocell.
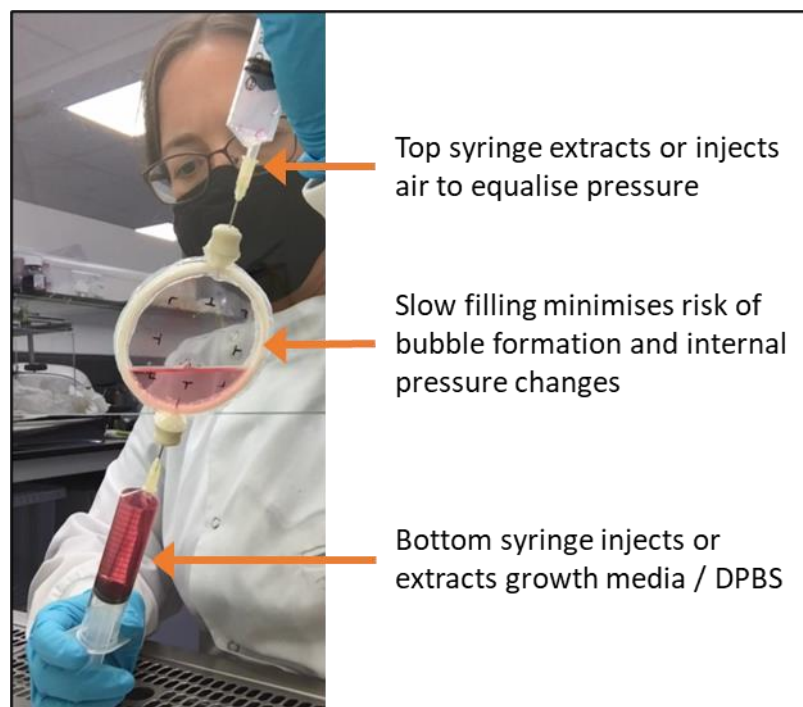
Figure 4.14: Filling or draining the biocell.

When seeding, the biocell was oriented as horizontally as possible so that the cells were more likely to fall to the coated growth surface rather than land and potentially adhere to the top membrane. After injection of the cell and media mix the biocell was agitated to spread the cells evenly around the growth surface, left for a few minutes for the cells to settle then the uniformity of cell density across the membrane checked under a phase contrast microscope. To ensure the cells had the correct CO_2 / air mix from the start, the growth media was placed in a culture flask and put in the incubator for at least 1 hour to take up gases prior to mixing with the cells.

4.2 Ultrasound Exposure Tank System

An ultrasonic exposure tank system was designed and built to expose the biocell to controlled LIPUS fields. This section details the design of the tank (4.2.1), the positioning system and alignment techniques (4.2.2) and *in-situ* temperature measurements used to determine potential temperature rises within the biocell (4.2.3).

4.2.1 The Tank

An off-the-shelf acrylic tank (L 40 cm x W 22 cm x H 25 cm) was used for LIPUS exposures. The small tank dimensions allowed the system to fit inside a BSC to maximise sterility of the setup. The setup is shown in Figure 4.15.

The tank was filled with deionised, degassed water and heated to a temperature of 36 - 37 °C using a thermostatically controlled heater and small pump to mix the water. The pump and heating element were switched off during US exposures to avoid temperature differentials in the water and flow effects on the cells. During US exposures the water temperature stayed within the aforementioned temperature limits, unless otherwise mentioned.
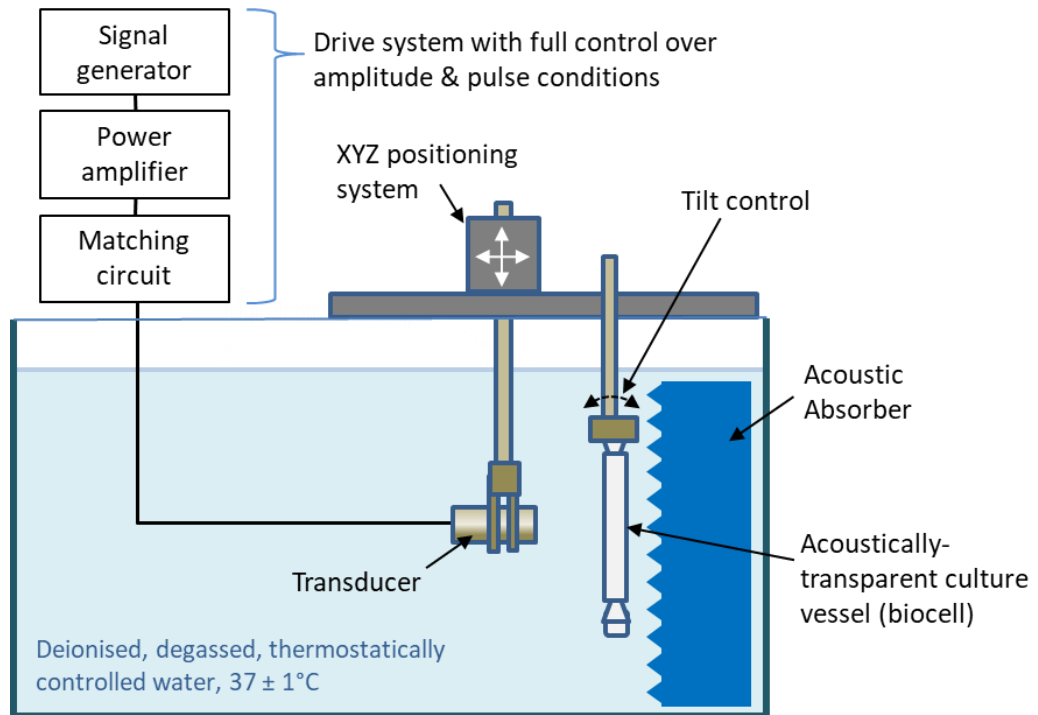
Figure 4.15: US Exposure tank system

The transducer and biocell were mounted in the tank on the positioning system detailed in 4.2.2. The biocell was placed 1-2 cm from an acoustic absorber (Apltile SF5048, Precision Acoustics, UK) with insertion loss greater than 22 dB at 45 kHz (meaning a 44 dB reduction in any reflection off back wall of tank). The insertion loss at 1 MHz is not given in the data sheets but is likely to be much greater than 22 dB. The front of the tile is shaped to diffuse any reflections off the surface. The transducers and drive systems were as described in 3.2.4.

4.2.2 Positioning System and Alignment Technique

In the Pressure Amplitude and Frequency studies, detailed in Sections 4.3 and 4.4, the transducer and biocell were held using simple lab clamps. The transducer was aligned to the centre of the biocell window with aid of measurements made with digital callipers. However, a more precise positioning system was required for the Rise Time study due to the counting of cells within bins of equal pressure, as detailed in Section 4.5.

LIPUS exposures took place with the tank inside the BSC, where space and ability to align were severely limited. A custom positioning system was designed and built to allow accurate alignment of the transducer with the centre of the biocell window on a three-sided

mock-up of the tank on the lab bench. Once alignment was achieved the system could be lifted into the BSC and placed on top of the exposure tank, with the transducer and biocell hanging underneath (Figure 4.16).
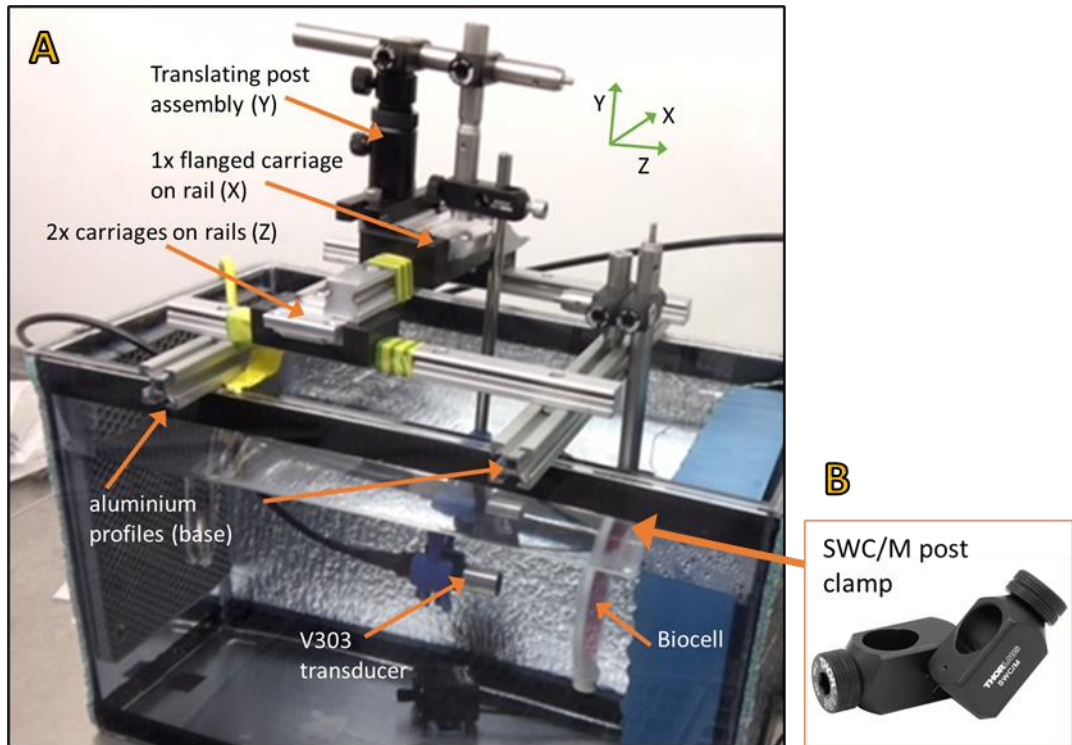
Figure 4.16: Tank Positioning System.
A: labelled assembly and B: hidden SWC/M Clamp (Thorlabs, US) with adjustable tilt to correct ant tilt in biocell position.

The tank positioning system consisted of a base formed by two 20 mm x 20 mm x 280 mm aluminium profile pieces (KJN, UK). On top of these were two aluminium guide rails 15 mm wide by 240 mm (L1018.15-0240, Automotion, UK) upon which two flanged carriages (L1018.F15, Automotion, UK) allowed smooth adjustment of the Z position of the transducer. The Z position determined the separation between the transducer front face and the biocell growth surface (the back membrane). On top of these Z carriages, another rail was fixed (L1018.20-0180, Automotion, UK) with another carriage (L1018.F20, Automotion, UK) to allow the transducer to be moved in the X direction. The transducer was suspended from a translating post assembly (PH2T/M, Thorlabs, US) which allowed fine adjustment of the transducer's vertical (Y) position by up to 11.4 mm.

The dimensions of the system were carefully controlled to allow it to be lifted in and out of the BSC. When not in the tank, the positioning system rested on a 3-sided Perspex frame

with similar width and height to the US exposure tank. An open end allowed easy adjustment of the transducer and biocell positions (Figure 4.17A).
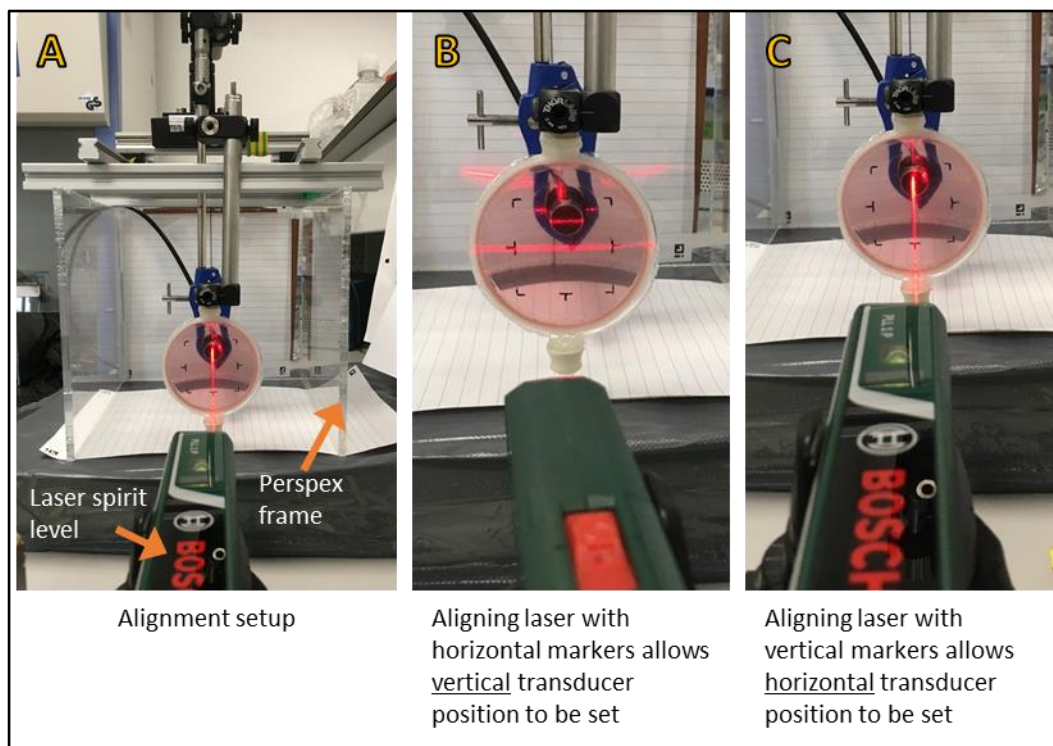
Figure 4.17: Alignment procedure of the transducer and biocell.
A: Positioning system with transducer and biocell fitted, resting on perspex frame.
B: Transducer-biocell vertical alignment with laser spirit level set to horizontal plane.
C: Transducer-biocell horizontal alignment with laser spirit level set to vertical plane.

A laser spirit level ensured accurate horizontal and vertical alignment of the biocell and transducer. First careful measurement of the positioning system position was made to ensure it was square with the back of the Perspex frame. Lined paper was also set up and made square with the back of the frame to provide guide lines to ensure the laser was not pointed at an angle. Vertical guide lines were also drawn on the side of the Perspex frame to assist in adjusting the tilt of the transducer and biocell. The laser spirit level was set up on an adjustable stand which ensured it was also level on the bench. Once this was all set up, alignment could be carried out. First the biocell was fitted into its clamp (by squeezing one septum into the rod space and tightening if necessary). Then its rotation was adjusted so its front membrane was aligned with the positioning system base. The tilt was then adjusted using the SWC/M clamp so it was in line with vertical guidelines drawn on the Perspex with a sharpie pen. The transducer rotation and tilt were adjusted manually using the base rails and sharpie pen lines as a guide. Finally, the horizontal and vertical position of the transducer was set up using the horizontal and vertical laser lines produced by the

laser spirit level as in Figure 4.17B & C. After final checks and adjustments, the separation between transducer front face and biocell back membrane was set and measured with digital callipers. Positions of the carriages were marked with tape to ensure no movement when placing the system in the BSC.

The laser was Class 2 with wavelength 635-650 nm and power <1mW. The absolute maximum intensity of the laser was in a point source of area 0.025 cm^2, which would produce a maximum intensity of 400 mW/cm^2. Studies have shown that cells can withstand 640 nm light intensities up to 1 kW/cm^2 for several minutes before any damage occurs [201]. The maximum possible intensity experienced by the cells was 1/2500 of that intensity. Therefore, it is highly unlikely to have caused any damage to the cells during alignment. The light may also have induced subtle effects in the cells but the actual area of cells exposed was so small that any light effects would not affect overall results.

4.2.3 *In Situ* Temperature Measurements

A set of measurements were conducted to ascertain if a temperature rise was induced in the cells during ultrasound exposure. One membrane was fitted to a biocell frame and a fibre-optic hydrophone (FOH, FP179-20T, Precision Acoustics, UK) fixed in placed with silicone sealant so its tip was adjacent to the centre of the membrane: the position along the cell layer that would be exposed to the highest level of ultrasound energy (Figure 4.18). A second membrane was fitted the next day and allowed to cure overnight.
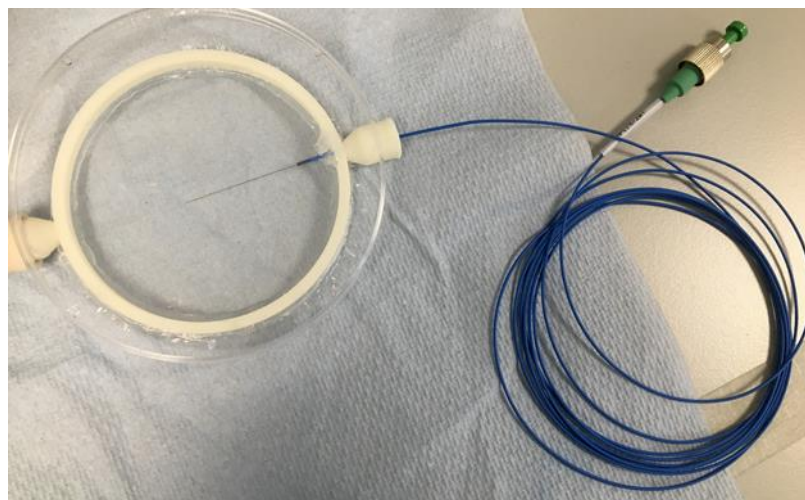
Figure 4.18 FOH in mock-up biocell

On the day measurements took place, the ultrasound exposure tank was set up with deionised, outgassed water and with the acoustic absorber in place. The tank water was held at 37 °C to simulate *in vitro* exposure conditions. The mock-up of the biocell was filled with tank water and set up in the tank just in front of the absorber, as would be the case in the *in vitro* ultrasound exposures (Figure 4.15). The test transducers (the 1 MHz V303 and 45 kHz Langevin) were set up in turn and driven in the same way as in the ultrasound exposures, with drive voltages corresponding to the 0.2 MI settings established in Chapter 3.

The FOH consisted of a thin polymer film at the tip of an optical fibre sensor downlead. Changes in the polymer thickness, induced by either acoustic pressure or temperature changes, are detected by laser vibrometry. Both pressure and temperature were monitored during exposures.

The temperature data was saved as a delimited text file and the MATLAB program *Process_Temperatures.m*, given in Section B.1.3 of Appendix B, was written to read, analyse and present the results. The voltage output of the FOH was monitored via oscilloscope (DPO7054, Tektronix, US) and the rms and peak negative voltages recorded throughout. Drive conditions corresponded to maximum peak negative pressures at the centre of the membrane of 42 kPa in the case of the 45 kHz device, and 200 kPa for the 1 MHz device. The temperature results are presented in Figure 4.19.
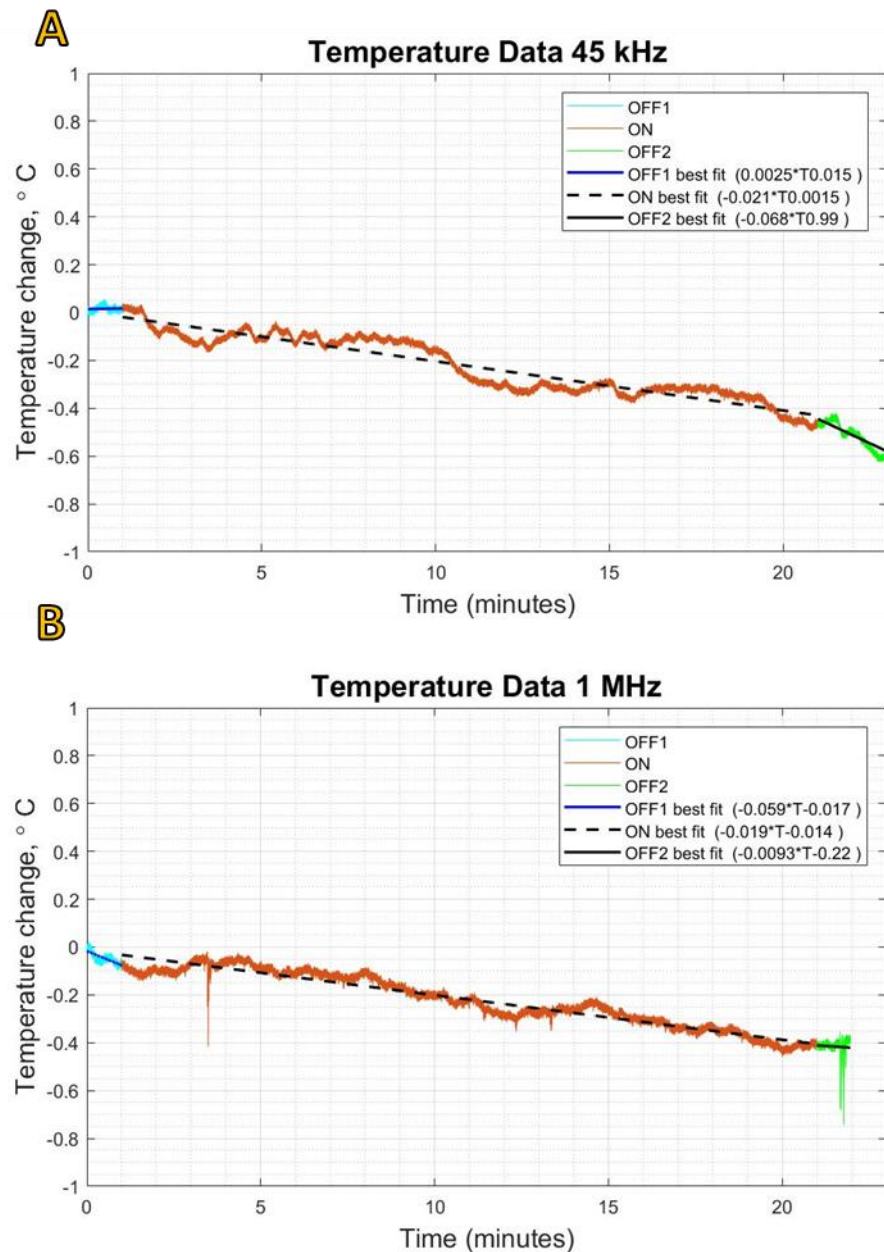
Figure 4.19 Temperature change measured by FOH at back biocell membrane during ultrasound exposures. A: 45 kHz, B: 1 MHz.

The thermostatically controlled tank heater was switched off during the temperature measurements so it did not switch on and affect results. Consequently, the water was cooling during testing. Therefore, the temperature gradients before and after exposure were compared with the temperature gradient during exposure to assess any potential temperature changes while the LIPUS field was on. The gradients were computed in MATLAB via a least squares best fit algorithm. In the case of 45 kHz, the temperature gradient before exposure (OFF1 in Figure 4.19A) was -0.0025 °C/min, and after exposure (OFF2) was -0.021 °C/min. When the 45 kHz transducer was ON the average gradient

was -0.068 °C/min, meaning the temperature was dropping at a faster rate during LIPUS exposure. Therefore, it was concluded that the 45 kHz field did not induce a temperature rise in the membrane.

In the case of 1 MHz LIPUS, the temperature gradient before exposure (OFF1 in Figure 4.19B) was -0.059 °C/min, and after exposure (OFF2) was -0.0093 °C/min. During exposure (ON) the temperature gradient was -0.019 °C/min. Comparing the before / OFF1 gradient with the ON gradient, the ON gradient has increased by 0.04 °C/min, which equates to a worst-case temperature rise over 20 minutes of 0.8 °C. Comparing the after / OFF2 and the ON gradients results is an estimated temperature rise of 0.2 °C. Therefore, any temperature rise due to the 200 kPa, 1 MHz LIPUS field is likely to be within 0.2 °C and 0.8 °C. This is low but could still possibly induce subtle thermal effects in the cells.

4.3 Pressure Amplitude Study: The Effect of LIPUS Peak Negative Pressure on PGE2 Expression and Proliferation of Preosteoblasts

This was the first study attempted using biocells and the ultrasound exposure tank system, which at the time were at an early stage of development. The study had a dual purpose: to establish and assess the method, and to investigate the peak negative pressure (p_-) at which cellular responses associated with healing were stimulated. The cellular responses assessed were PGE2 expression and proliferation. The method differed from the main methods described earlier in this chapter and was as follows.

Six biocells were sterilised by exposure to UV and overnight soaking in 70% ethanol. The membrane growth surface was pre-treated by soaking in Foetal Bovine Serum (FBS, Gibco 10270-106) for 1 hour. Excess was removed and allowed to air dry.

The biocells were seeded with MC3T3-E1 osteoblasts (Passage 19). The growth media consisted of 89 % MEMα (Gibco A1049001), 10 % FBS and 1 % Penicillin-Streptomycin 10,000 U/mL (15140-122). After overnight incubation (37°C, 5% CO_2) each biocell was filled with media and mounted in the test tank with cell growth surface facing the custom built LIPUS transducer detailed in 3.2.3, at a distance of 100 mm. The custom-built LIPUS transducer detailed in 3.2.3 was driven for 20 minutes to produce LIPUS fields with frequency 1 MHz, pulse width 200 µs, repetition rate 1 kHz and maximum peak-negative

pressures up to 489 kPa. Controls were treated the same but with no transducer output. During the exposures the tank water temperature was held at 37 °C ± 2 °C.

After exposure, the biocell was removed from the tank and all but 5 ml of media removed. After 20 hours incubation, the media was harvested and stored at -20 °C. Once all exposures were complete the PGE2 concentration in the media was measured with an Enzyme-linked Immunosorbent Assay (ELISA ab133021, Abcam, UK) as detailed in 3.1.2.4.

Bright field images of cells were captured with the IX73 inverted microscope (Olympus, JP) immediately before ultrasound exposure and after 20 hours incubation to assess proliferation by means of cell counts. The total number of cells after 20 hours was also assessed by hemocytometer by the process described in Section 3.1.1.2. Three repeats of the entire procedure were conducted (Groups A, B & C).

Only Group B results could be used because Group A suffered from very low cell numbers due to low cell adhesion to the Mylar film and in Group C the LIPUS transducer developed a fault which resulted in no output during exposures. The Group C control was also used, making the number of replicates n=1 for LIPUS-treated samples and n=2 for sham-treated controls.

4.4 Frequency Study: The Effect of LIPUS Frequency on Preosteoblast Proliferation and PGE2 Expression

The Frequency Study was conducted to compare cellular responses to LIPUS fields at 45 kHz and 1 MHz. 45 kHz LIPUS has been shown to stimulate expression of PGE2 in osteoblasts [40], suggesting the frequency of excitation is not the main factor in the LIPUS stimulus. The aim of this Frequency Study was to test that hypothesis.

In this Frequency Study, improvements and modifications highlighted by the Pressure Amplitude study were incorporated. These included the use of collagen coating of the Mylar, use of biocell microscope supports to flatten the membrane while capturing images (thus minimising focussing issues), and the use of fluorescent staining to conduct cell counting before and after LIPUS exposure. The Frequency Study protocol is summarised in Figure 4.20.
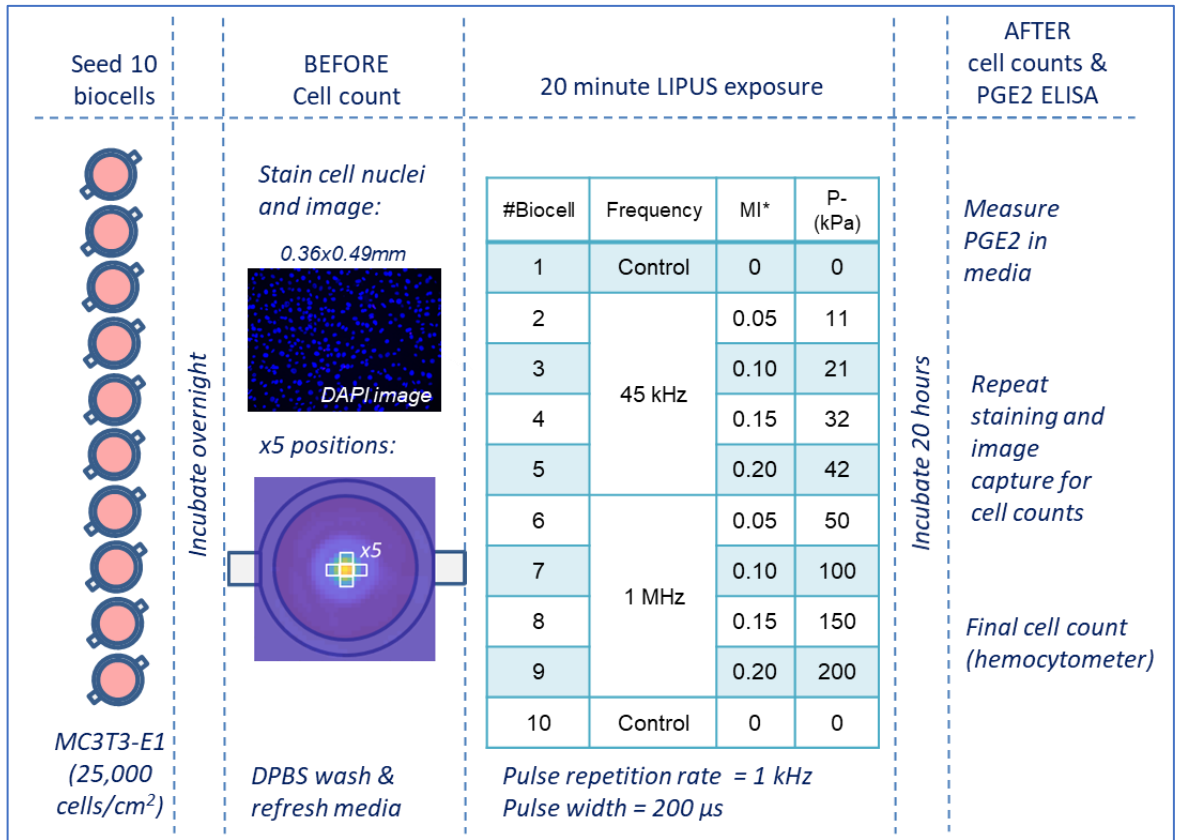
Figure 4.20: Frequency Study Protocol.

Ten biocells were seeded with MC3T3-E1 cells, passage 19, cell density 25,000 cells/cm^2 following the cell culture protocols described in 3.1.1. Cells were grown to near confluency in culture flasks and up to three biocells seeded from each flask (Figure 4.21).
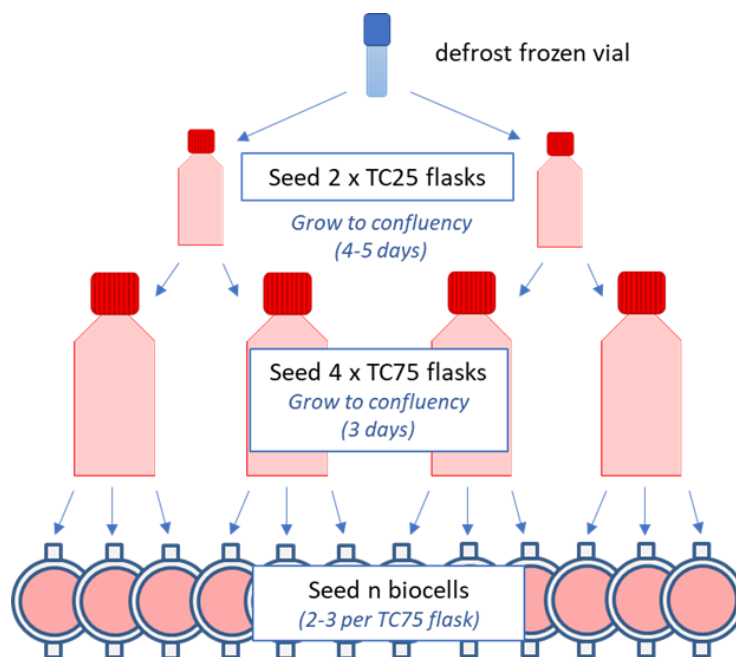
Figure 4.21: Seeding process for LF-HF Study.

All cells (nuclei stained with Hoechst dye) were captured with a DAPI fluorescent filter. Dead cells (nuclei stained with Propidium Iodide dye) captured with the RHOD fluorescent filter on the DMi8 microscope (Leica, DE). Following imaging, the media and dye mix were removed and the biocells washed two times with 10 ml DPBS. The biocell was filled with media warmed to 37 °C, then exposed to LIPUS in the tank exposure system. In this investigation, a low power aquarium heater was used to stabilise the temperature. Note that the tank water was cooler than would be ideal for *in vitro* work during the Frequency Study, at 32 °C ± 1 °C. The media within the biocell was warmed to 37 °C prior to filling, to mitigate the effect on cells, with an expected gradual cooling from 37 °C, rather than being subjected to 32 °C for the full 20 minutes of the LIPUS exposure.

The table in Figure 4.20 summarises the LIPUS exposure conditions, which are also described in full in the characterisation of each transducer in 3.2.4. The Mechanical Index was used as an indicative measure to attempt to equalise the potential for mechanical effects induced by the very different ultrasonic frequencies. It is recognised that this is not the intended use of the MI and that the MI is also not valid at frequencies below 1 MHz. The p_- is also given in the table and is quite different for the 45 kHz device compared with that of the 1 MHz device. The maximum p_- at 45 kHz was 42 kPa compared to the 200 kPa maximum of the 1 MHz device.

After exposure, the biocells were dried and incubated. After 20 hours (the optimal period for osteoblast PGE2 production found by Reher et al. [40]) the media was collected and 5 ml stored in vials at -20 °C until required for the PGE2 ELISA (see 4.4.1). The biocells were then stained with the live ReadyProbe stains and imaged at five points using the same positioning process as in the pre-exposure counts in an attempt to capture the same areas of the biocell growth membrane in order to assess changes in cell counts (and therefore proliferation). Following image capture the cells were detached with trypsin-EDTA and a final cell count was conducted with Trypan blue staining and hemocytometer.

The entire protocol was repeated three times, to give up to n=3 for each condition and up to n=6 for controls. Some biocells were discarded due to excessive changes in conditions, such as accidental damage, accidental dropping of the biocell during exposures or excessive leakage. Once complete, the number of viable cells in each microscope image was counted as described in 4.4.2.

4.4.1 PGE2 ELISA

The media samples were tested for PGE2 concentration via the ELISA kit and protocol described in 3.1.2.4. A ln-ln power regression provided the best fit to PGE2 standards, and its equation (given in Figure 4.22) used to convert optical density (*OD*) of all media samples to PGE2 concentration (C_{PGE2}) in pg/ml.
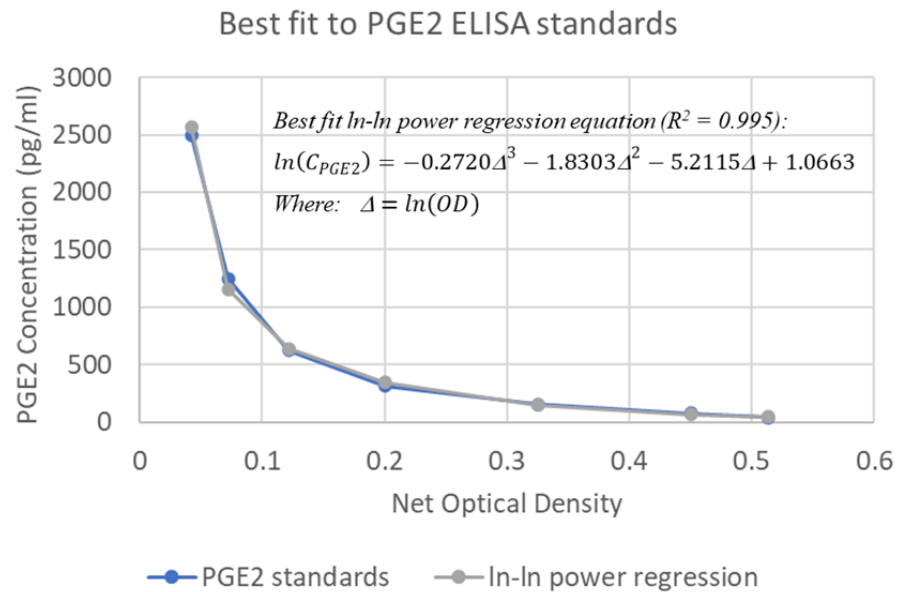
Figure 4.22: Best fit to PGE2 ELISA Standards in LF-HF Study.
The best fit was a ln-ln power regression, conducted in MS Excel, with R-squared value 0.995. The best fit equation was used to determine the PGE2 concentrations of study samples from ELISA net optical densities measured via plate reader.

The measured PGE2 concentrations were averaged at each LIPUS condition and plotted to assess PGE2 expression in LIPUS-treated samples versus sham-treated controls. To correct for total number of cells exposed to the LIPUS field, the PGE2 concentrations were also normalised to the total number of cells pre-exposure and plotted on a separate chart. The total number of cells is estimated by extrapolating the average pre-exposure cell count per microscope image (an area of 0.0058 cm^2) to fill the total biocell growth area of 38.5 cm^2.

4.4.2 Cell Counting in ImageJ

Viable cells were counted by performing two cell counts with ImageJ on each of the 5 images taken in the DAPI and RHOD fluorescent filters. ImageJ macros *Count_DAPI.ijm* and *Count_RHOD.ijm*, given in Sections B.2.2 and B.2.3 in Appendix B, were written to automate the process. A brief description follows.

The DAPI images captured the live + dead cell nuclei stained with the Hoechst dye (Figure 4.23). For each image file, the original 16-bit image (Figure 4.23A) was converted to 8-bit greyscale and the contrast enhanced automatically with ImageJ tools 'Enhance Contrast' and 'Subtract Background' (Figure 4.23B). The enhanced image was then converted to binary by comparing to a threshold intensity level, setting the background to white (Figure 4.23C). The ImageJ tools 'Fill Holes' filled any holes within the nuclei spots.
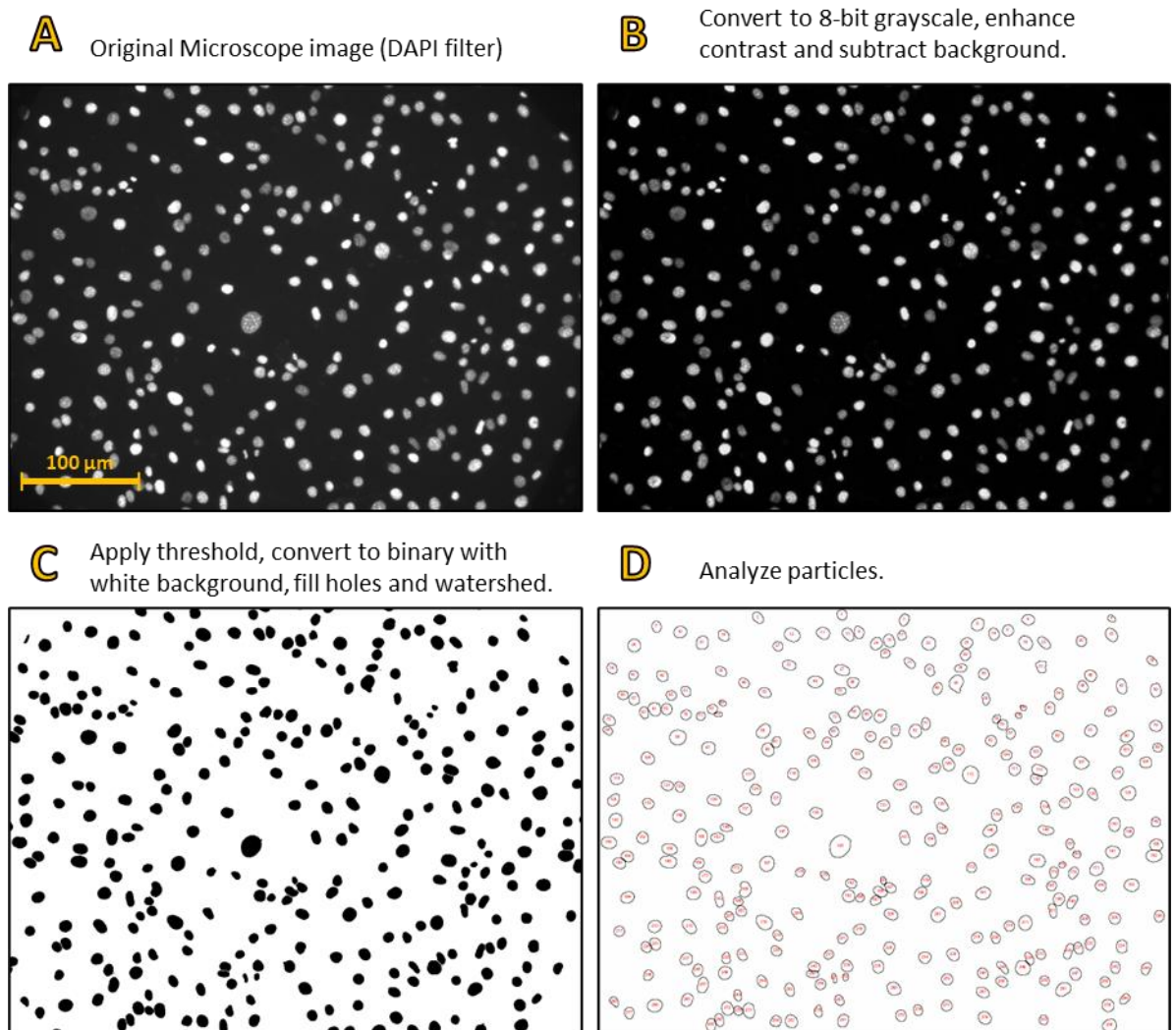
Figure 4.23: Live + dead cell counting in ImageJ.
A: Original image showing cell nuclei stained with blue Hoechst dye, with approximate scale. B: After image enhancement. C: Converted to binary (white background). D: Cells counted with ImageJ 'Analyze Particles' tool.

'Watershed' identified adjacent nuclei spots that were touching and drew a single pixel line to separate them so they would not be counted as one item in the final cell count. Finally, the counting was conducted with the 'Analyze Particle' ImageJ tool, which

counted the number of nuclei (Figure 4.23D). The cell count number was recorded in a comma delimited text file for import and analysis in Excel.

The process was developed using a subset of representative images, then the settings were incorporated into macros to run through the remaining files. Accuracy of the cell counts was verified by running through the process step by step and manually adjusting the contrast and Subtract Background settings to optimise the image, then comparing these 'manual' cell counts with the cell counts produced by the macro. The automated dead cell counts were more prone to error because there were very few dead cells present in the samples (as in Figure 4.24A).

Figure 4.24: Dead cell counting with ImageJ.
A: Original image (no dead cells), showing approximate scale. B: Enhanced image showing background fluorescence (false positives in automated counts). C: Original image with some dead cells (same scale); D: Enhanced image (accurate dead cell count).

This resulted in the ImageJ 'Enhance Contrast' tool artificially enhancing the background fluorescence of the image (Figure 4.24B), potentially leading to many false positives. The viable cell counts were calculated by subtracting the dead (RHOD filter) cell count from the live + dead (DAPI filter) cell count. The cell counts produced for each biocell, pre- and post-exposure, were then compared to assess cell proliferation at each LIPUS exposure condition.

The significance of viable cell counts of LIPUS-treated samples compared to sham-treated controls were tested with a one-tailed, equal variance Student t-test. The results of the Pressure Amplitude Study are reported in Section 5.2. The next section reviews the methods of the Frequency Study, the lessons learned, and measures taken to improve study methods.

4.4.3 Frequency Study Method Review

The assessment of cell counts and proliferation in the Frequency Study was based on imaging of live stained cells over a very small area of the cell growth surface. The total area imaged was $5 \times 0.0058 \text{ cm}^2 = 0.029 \text{ cm}^2$ per biocell, which was less than one thousandth of the total growth area of 38.5 cm^2. Such a small sample would be prone to localised variations in cell population.

To illustrate the extent to which the cell counts were affected, Figure 4.25 compares the total post-exposure cell counts of each biocell estimated via hemocytometer with those estimated from the live-stained cells. The hemocytometer method, if conducted correctly, is likely to provide a more representative estimate of the total viable cell population because all cells are detached from the growth surface and a count is conducted from a known volume of a homogenous mix of cells and growth media.
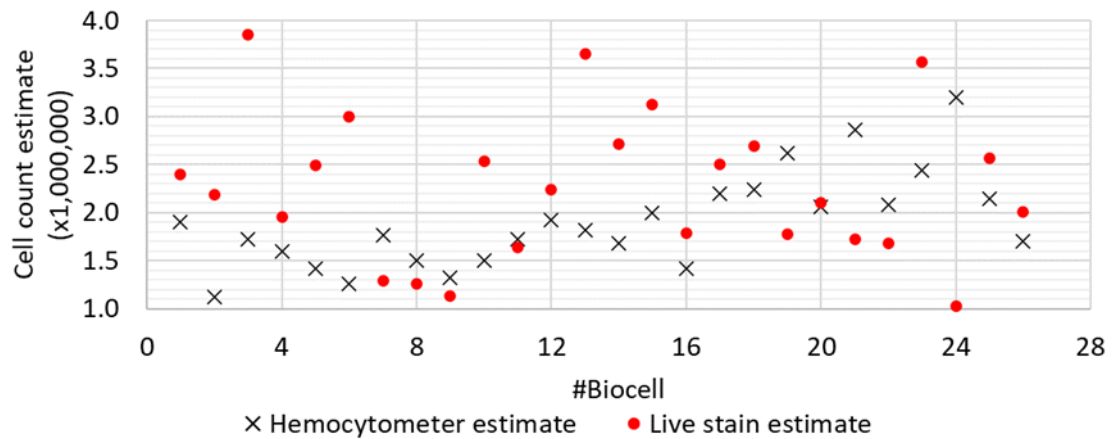
Figure 4.25: Comparison of post-exposure total viable cell counts across entire biocell growth area (38.5 cm^2) estimated via hemocytometer and live-stained cell counts, for all biocells in the Frequency Study

The total cell counts estimated by live staining differed greatly from those estimated by hemocytometer by -68% to +138%. This illustrates the need for a more representative means of estimating cell counts. This was achieved by using an automated scanning microscope to sample a much larger area of the biocell growth area, a technique which also enabled cell counting within pressure bins (described in detail in Section 4.5.3). Staggered biocell seeding, described in 4.5.2, equalised incubation times prior to LIPUS exposure.

An overall positive bias in live stain estimates as compared to hemocytometer estimates suggested cell density was higher in the centre where the counts took place. This was possibly due to bowing of the biocell membrane during incubation, causing more cells to migrate attach to the centre during seeding and incubation. This effect was minimised in subsequent trials by supporting the biocell membranes on flat polystyrene biocell stands.

Results may have also been affected by exposure to the live cell stains and light from the microscope, both of which have a degree of toxicity. For instance, the live dye Hoechst 33342 is known to cause DNA damage and alter cell behaviour and sensitivity to ultraviolet light [202]. Exposure times were minimised throughout the study but were not uniform and could contribute to variation. Subsequent trials switched from live dyes to the use of replicates and staining of fixed samples as opposed to live staining.

Seeding methods were also improved. As described in Section 4.4, in the Frequency Study, two to three biocells were seeded at a time using cells from one 75 cm^2 culture flask. As only one exposure could be conducted at a time, and each exposure took approximately

one hour to complete, incubation times prior to exposure varied by up to 5 hours. This time difference almost certainly contributed to variance in pre-exposure cell numbers between biocells and likely propagated through to the post-exposure cell counts, thus affecting overall proliferation results. An improved seeding method was devised to minimise these timing effects, and this new method is described in the next section, which describes the methods of the Rise Time Study.

4.5 Rise Time Study: The Effect of Rate of Change of Pressure Amplitude on Preosteoblast Proliferation, PGE2 Expression and RNA Markers for Mechanotransduction and Mineralisation.

During the Frequency Study it was noted that the rise time of the 45 kHz pulse was greater than that of the 1 MHz pulse. Transducers commonly take a period of time (or number of cycles) to reach a steady state at the onset of a drive pulse, as the driving vibration overcomes the inertia of the transducer structure and surrounding medium. After a 200 µs pulse width the 45 kHz had evidently not reached its steady state (Figure 4.26A). By contrast, the 1 MHz pulse reached steady state at around within about 7 to 8 µs (or number of cycles) (Figure 4.26B).
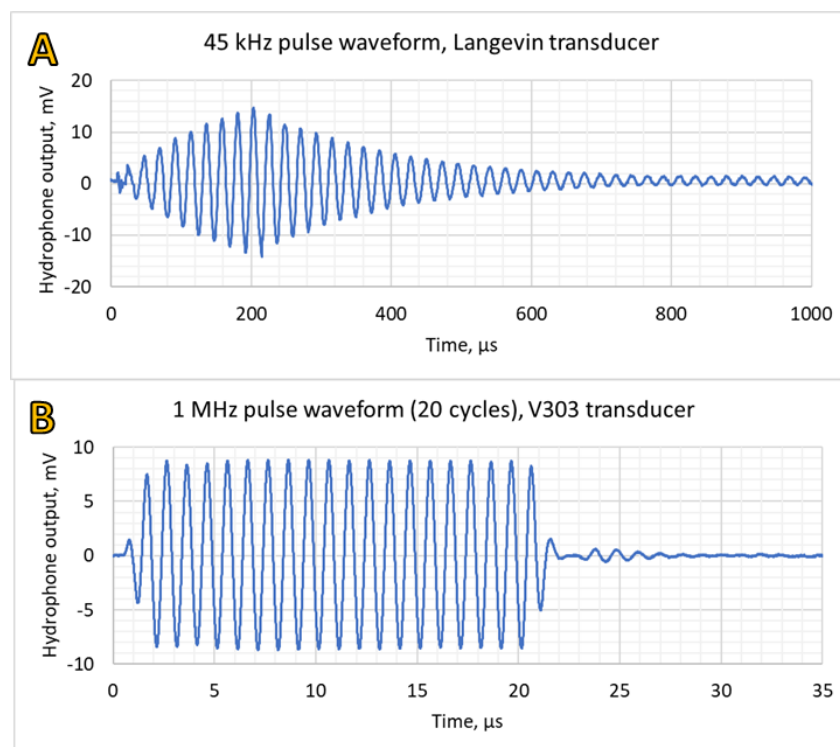
Figure 4.26: A: 45 kHz and B: 1 MHz pulse waveforms.

Note also the ringing down of the 45 kHz transducer after the 200 µs drive pulse ends, which continued on past 1000 µs, i.e., when the next pulse was due to start. This is likely due to the resonant Langevin design of the transducer, which has very little damping. By contrast, the 1 MHz V303 transducer likely has damping incorporated in its design, which might explain the rapid reduction of the pulse amplitude when the drive signal stops.

This large discrepancy between device characteristics, including the differences in beam widths already described in Chapter 3, led to a re-evaluation of the techniques used. A new approach was developed to use the same device but to effectively use the 1 MHz drive frequency as a carrier pulse and modulate the amplitude to simulate the excitation at lower frequencies.

Cell responses to vibration (e.g. integrins or vibration-induced cation channels) have a latency period of the order of milliseconds while the channels return to their pre-stimulation state [203]. So, the assumption is that the 1 µs period at 1 MHz has too short a duration to make a difference to the cellular response, leading to the hypothesis that it is the pulse envelope that is more influential in the stimulation of the mechanotransduction pathways than the carrier frequency itself.

A 1 MHz pulse with a slow rise time would have a more gradual application of the radiation force, and a standard 1 MHz pulse, with a relatively fast rise time, would result in a rapid switch-on of the radiation force. The following sections describe the experimental protocol developed to investigate this hypothesis.

4.5.1 Fast and Slow Rise Time Drive and Pulses

The 1 MHz V303 transducer was driven in two ways:

- Fast rise time (RT). A 1 MHz burst consisting of 200 cycles, repetition rate 1 kHz with no amplitude modulation, resulting in a rise time of 1.4 µs.
- Slow RT. An amplitude-modulated 1 MHz burst, repetition rate 1 kHz, with longer rise and fall times of 40.5 µs.

The peak-negative pressure (p_-) was set to 100 kPa in each case. This pressure amplitude was chosen because it had produced optimum proliferation and PGE2 expression in the previous trials. The modulated burst was designed to rise/fall between zero and 100 kPa in 50 µs. The pulse width was increased to 267 µs to maintain the same temporal-average intensity (I_{TA}). The drive waveforms are shown in Figure 4.27.
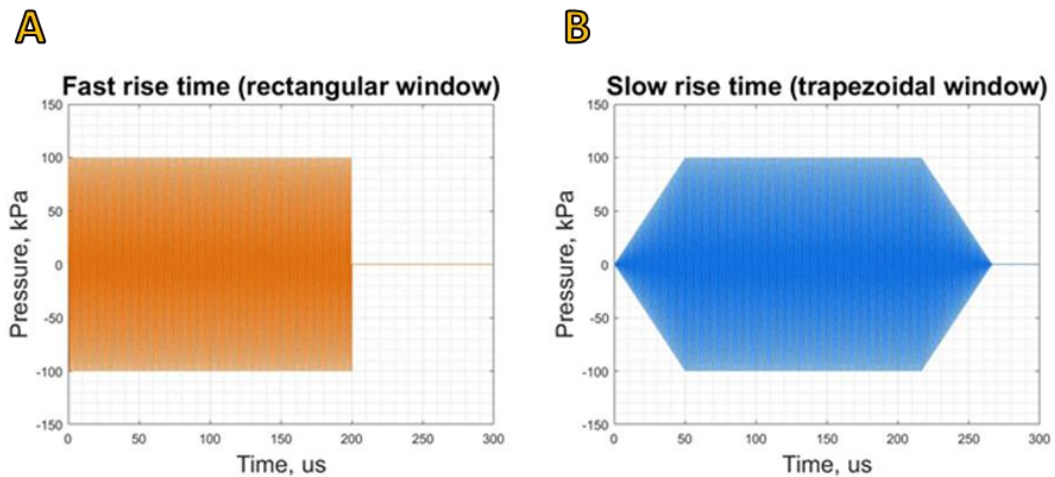
Figure 4.27: Drive signals of 1 MHz Transducer for radiation force trial.
A: standard burst with fast rise time of 1.4 µs (rectangular window). B: Modulated burst with slow rise time of 40.5 µs (trapezoidal window).

The pressure waveforms of the resulting outputs from the test transducer could not be measured directly due to interference caused by internal reflections between the needle hydrophone and the scanning tank. Instead, the drive voltages were analysed. The minimum voltage, Vmin, indicates peak-negative pressure, and the sum of the squared-voltages indicates the temporal-average Intensity, I_{TA}. These are presented in Table 4.2. The percentage differences between the two applied conditions are within 0.5 %.

The first 95 µs of the pressure waveforms, shown in Figure 4.28, were not affected by the diffraction and reflection features, and so could be used to calculate the rise times (defined as the time taken for the signal amplitude to increase from 10 % to 90 % of the steady-state pressure amplitude). As expected, the rise time of the modulated burst was 29 times longer than the standard, unmodulated burst. These are summarised in Table 4.2.
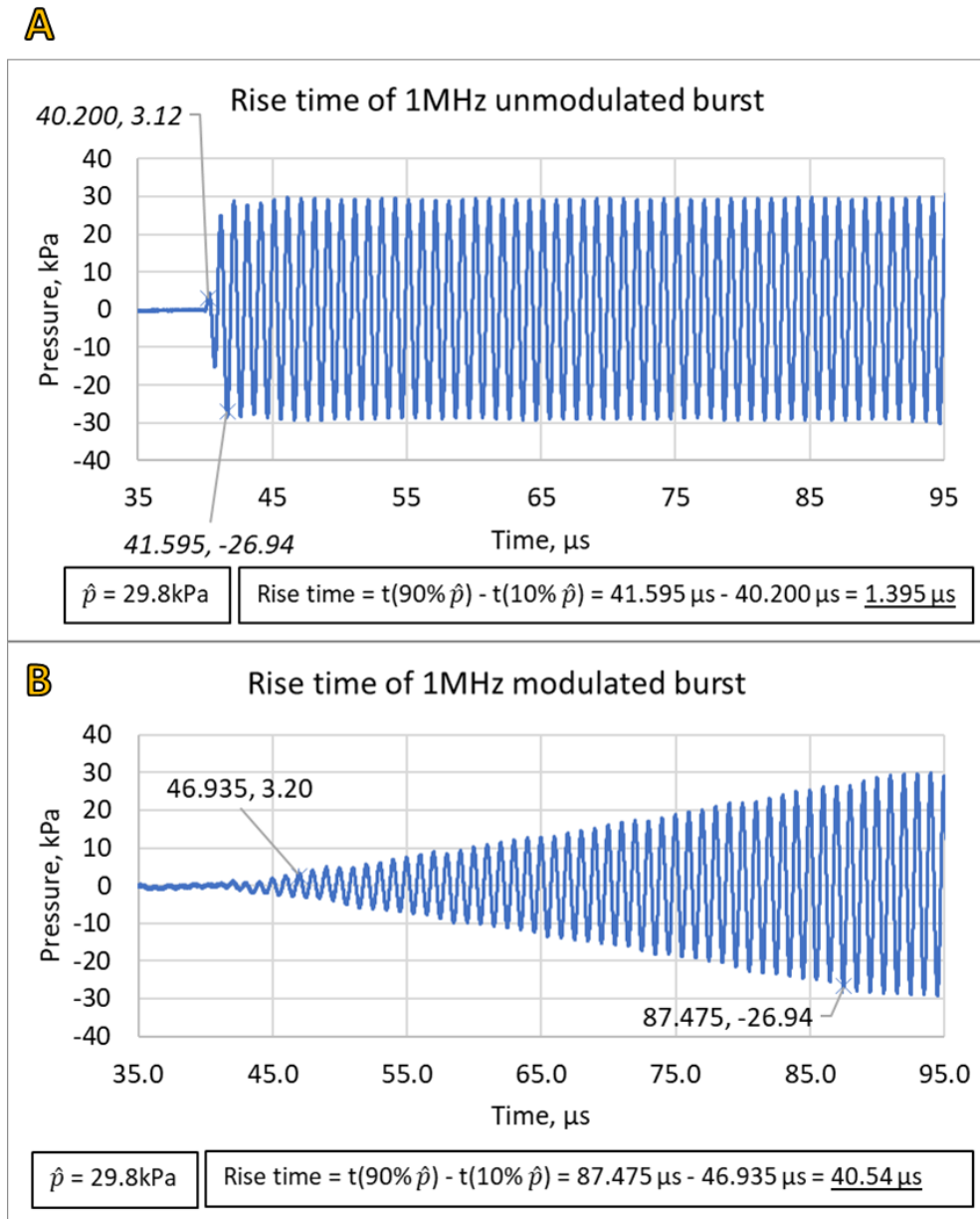
Figure 4.28: Rise times of the A: standard and B: modulated pressure waveforms.

	Standard burst	Modulated Burst	Percentage Difference
V_{min}	2.38 V	2.37 V	0.2 %
$\sum V^2$	116664 V^2	116136 V^2	0.5 %
Rise time	1.4 µs	40.5 µs	2906 %

Table 4.2: Comparison of Drive voltage Vmin and sum of voltage-squared with percentage differences.

This rapid switch-on would also have the effect of creating an impulsive stimulus, with the energy spread across a wider frequency range. This may make it more likely to excite the modes of cellular structures (as well as the potential to excite plate modes of culture vessels or membrane growth surfaces). To illustrate, the idealised pulses in the top two charts of Table 4.2 were analysed by Fast Fourier Transform in MATLAB via the program *Modulation_Drive_Calcs.m*, provided in Section B.1.4 of Appendix B. The FFT results in Figure 4.29 clearly show the reduced frequency content of the modulated (slow rise time) burst.
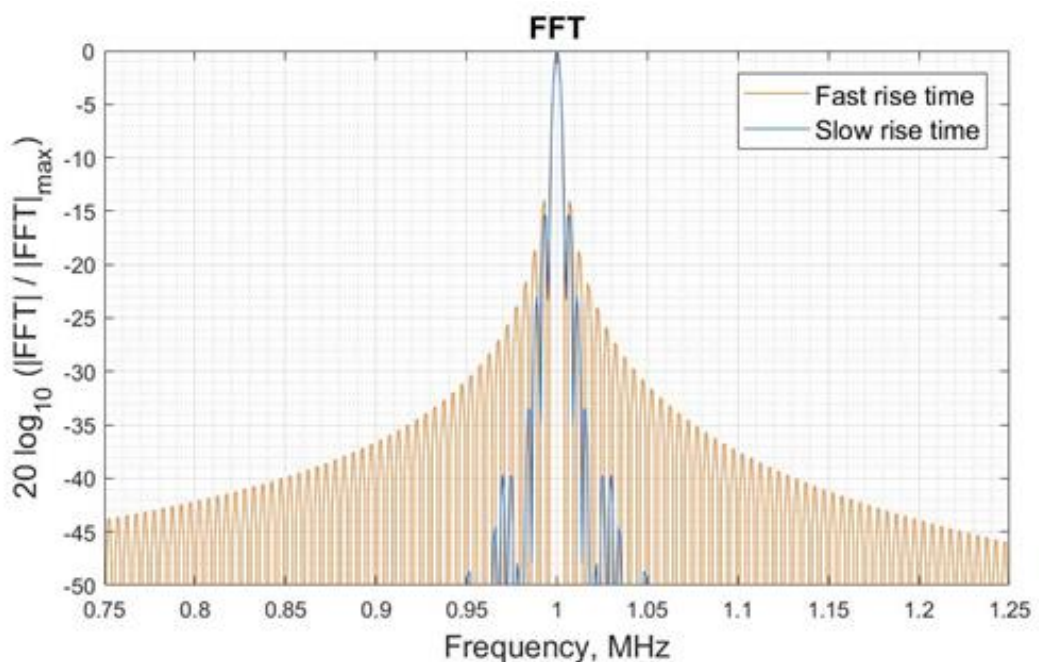
Figure 4.29: FFT of Fast and Slow Rise Time Pulses.
The rapid switch-on of the Fast RT pulse increases the broadband frequency content. The impulsive nature of the switch-on would be more likely to excite vibrational modes of cellular structures, plates or membranes. A slow rise time would reduce these effects.

4.5.2   Improving biocell seeding and incubation prior to LIPUS exposure

Improved cell biology techniques were adopted for the Rise Time Study. An automated scanning fluorescent microscope, the Evos FL Auto 2 (Invitrogen, US) allowed image capture and cell counting over a much larger area than in previous studies: a 40 mm by 40 mm square. Secondly, cells were fixed prior to imaging (as described in 3.1.2.2). Fixing the cells prior to imaging has the advantage of avoiding the potentially toxic effects of dyes and UV light exposure on the cells. The cells could also be stored and imaged later, which was an advantage given that the scanning microscope was situated in different laboratory to the one used for US exposures. However, fixing the cells meant that the use of replicates

was required, i.e., each condition required at least three samples to be treated in exactly the same way. Another consequence was the conditions of seeding, especially the timing between seeding and US exposure, had to be tightly controlled to ensure repeatability. This was done by following the procedure summarised in Figure 4.30: the main improvement being the use a separate culture flask to seed each biocell. This allowed seeding of biocells to be staggered in time to equalise the incubation time between seeding and exposure.
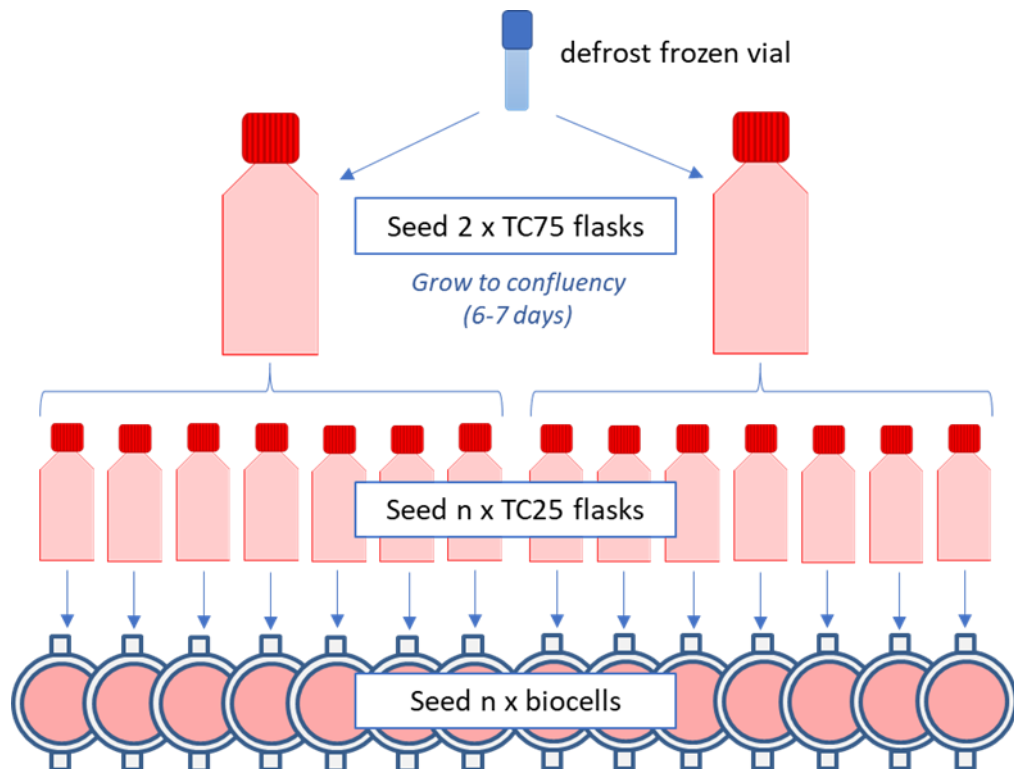
Figure 4.30: Improved biocell seeding technique
adopted for fast/slow rise time trials. Seeding with one flask per biocell allowed staggered seeding and equalisation of incubation times prior to LIPUS exposure.

Only two conditions could be evaluated in one measurement set due to the large numbers of biocells required to produce the appropriate number of replicates. However, the use of the scanning microscope meant that cell counting could be carried out across a wider area of the beam. A strategy was devised to separate the beam into areas exposed to the same range of pressure (pressure bins). This way cell counts, and therefore proliferation, could be assessed for changes due to the pressure dose experienced in the local area.

4.5.3 Cell counting in Pressure Bins

The use of the EVOS scanning microscope allowed a large area of cells to be counted. With accurate alignment assured from the positioning system and alignment techniques,

the scanned area could be separated out into pressure bin areas. The aim was to assess the relationship between ultrasonic pressure and cell proliferation across the cell growth area.

First, the two-dimensional XY scans of p_- were converted to suitable pressure bins within the proposed scan area. The XY raster scans from Figure 3.23 were combined to create a single XY scan of p_- (Figure 4.31A). The MATLAB program in Section B.1.5 of Appendix B, *Pressure_Mask_from_XY_Scan.m,* reads in the combined scan and allocates each pixel to a pressure bin, with p_- ranges of <10 kPa, 10-25 kPa, 25-50 kPa, 50-75 kPa and 75-100 kPa (the contour plots in Figure 4.31B shows the resulting pressure bin shapes).
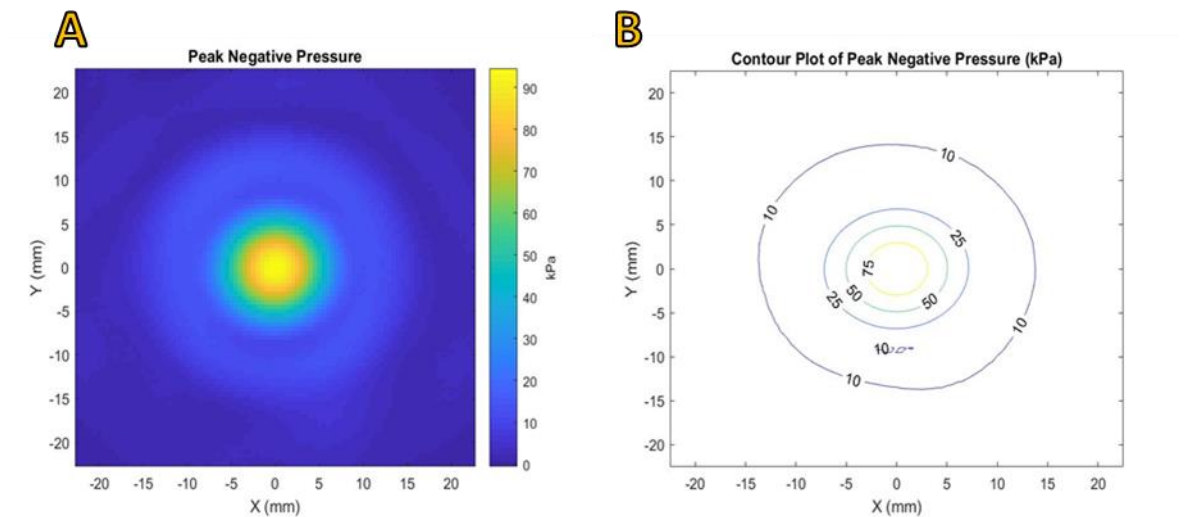
Figure 4.31: Dividing the V303 2D scan into pressure bins.
A: combined XY scan of V303 p- at 100 kPa output. B: resulting contour plot showing pressure bins.

The bin sizes were chosen to create an area within the smallest, central bin that was large enough to accommodate sufficient numbers of cells to allow statistical assessment of any changes in the cell numbers. The MATLAB routine produced a series of comma delimited mask files, containing matrices of the same dimensions as the XY scan area (± 20 mm in X and Y dimensions, in 0.5 mm steps). Scan steps falling within the mask had the value 1, and the rest had zero value to black out (or set to zero intensity) the areas outside the pressure bin. Figure 4.32 shows the resulting masks.
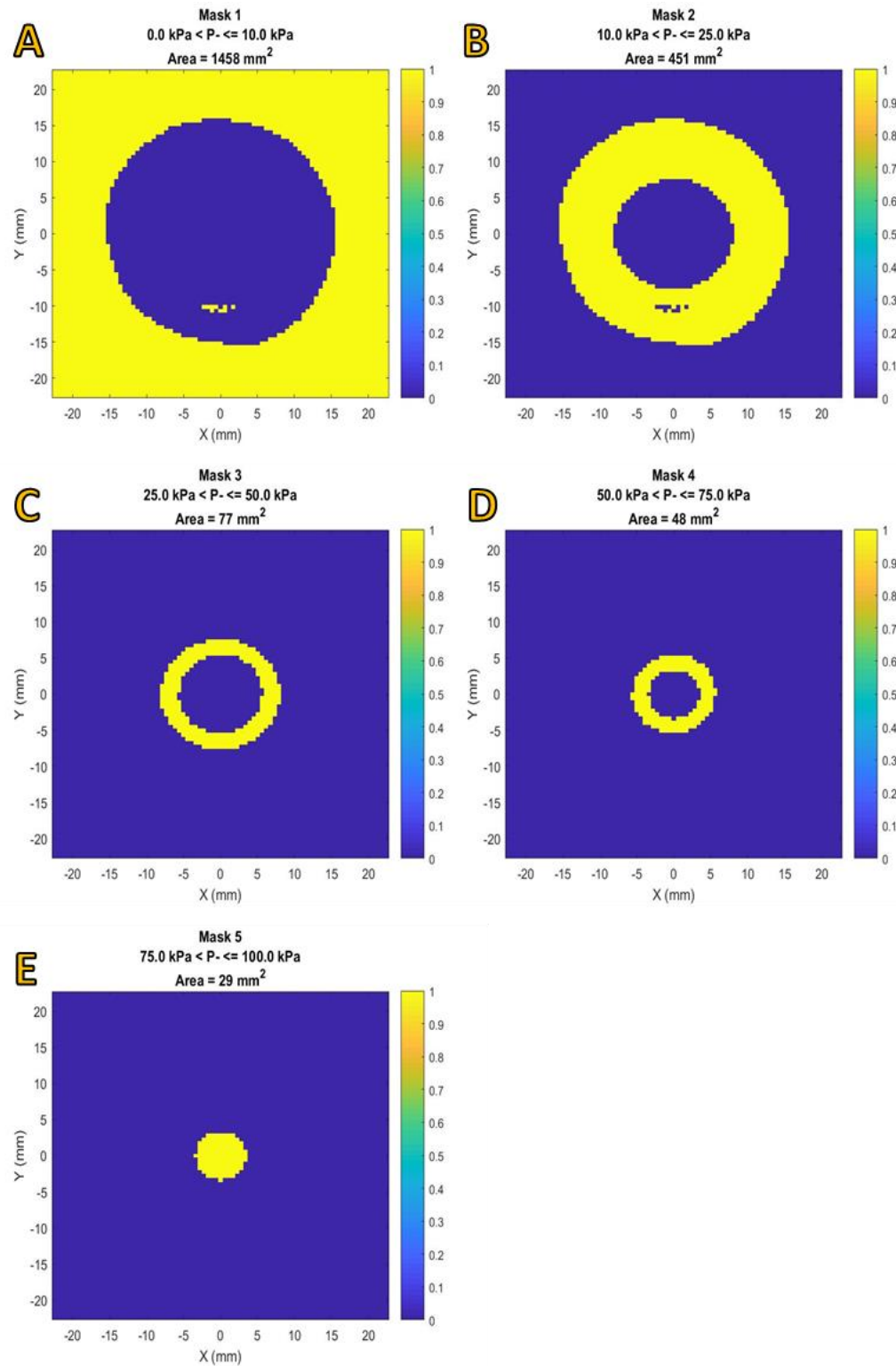
Figure 4.32: Masks of 1 MHz V303 pressure bins.
Pixels within the bin have value=1 and those outside are zero value. A: Mask 1,
p_-<10 kPa. B: Mask 2, p_- 10-25 kPa. C: Mask 3, p_- 25-50 kPa. D: Mask 4, p_- 50-75 kPa.
E: Mask 5, p_- 75-100 kPa.

In comparison to the Frequency Study, the areas captured were much larger. The total area

captured in the Frequency Study was 0.88 mm^2, whereas the total area captured here was

40 mm × 40 mm = 1600 mm^2, with the smallest pressure bin area 29 mm^2. Provided the biocells were seeded uniformly across the membrane, this would much improve the validity of cell count results as local clusters would have less effect on variation.

Microscopy was conducted using the EVOS FL Auto 2 scanning microscope (Invitrogen, US). Accurate positioning and orientation of the biocell was essential for the pressure bin cell counting to be valid. This was ensured by marking the clamped septa and aligning membrane markings to the edges of a custom microscope stand with a 40 mm × 40 mm square window (Figure 4.33). Images through the DAPI filter (for live/dead Hoechst staining), CY5 (for dead phalloidin staining) and bright field were captured for each scan, in darkened conditions and with the same intensity, to ensure uniformity of brightness and contrast throughout the scanning period.
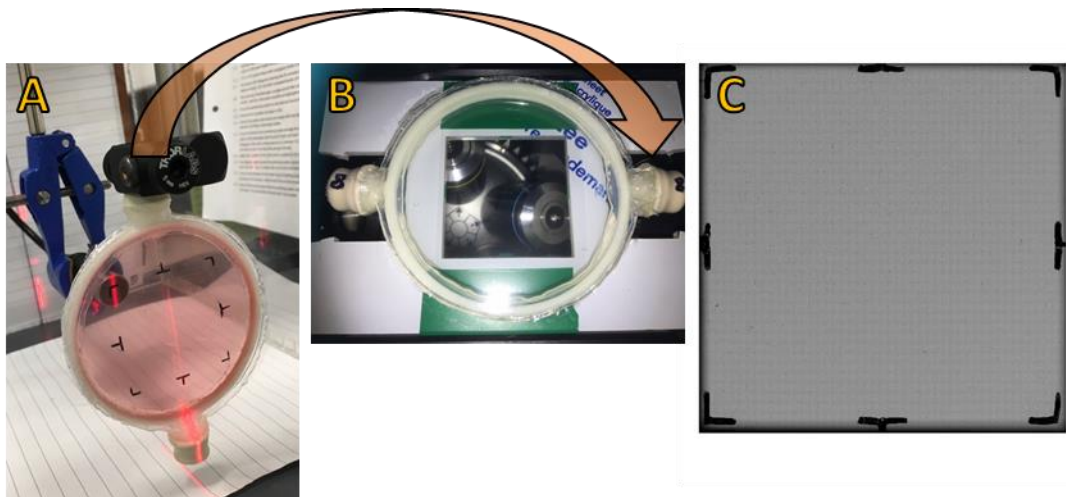
Figure 4.33: Positioning of biocell on the scanning microscope.
A: After alignment the top septa was marked with permanent marker. B: The biocell was placed on the custom microscope stand so that the marked septa was positioned on the right. C: The markings on the membrane aligned with the edges of the 40 mm × 40 mm square scan area.

The MATLAB programs *Apply_Masking_DAPI.m* and *Apply_Masking_CY5.m* were written to apply the pressure bin masking to the microscope images. *Apply_Masking_DAPI.m* is provided in Section B.1.6 of Appendix B. The CY5 version was the same as the DAPI version except that it created masked images with CY5-specific filenames). First the programs displayed the bright field images captured at the same time as the fluorescent filter scans (Figure 4.34A).
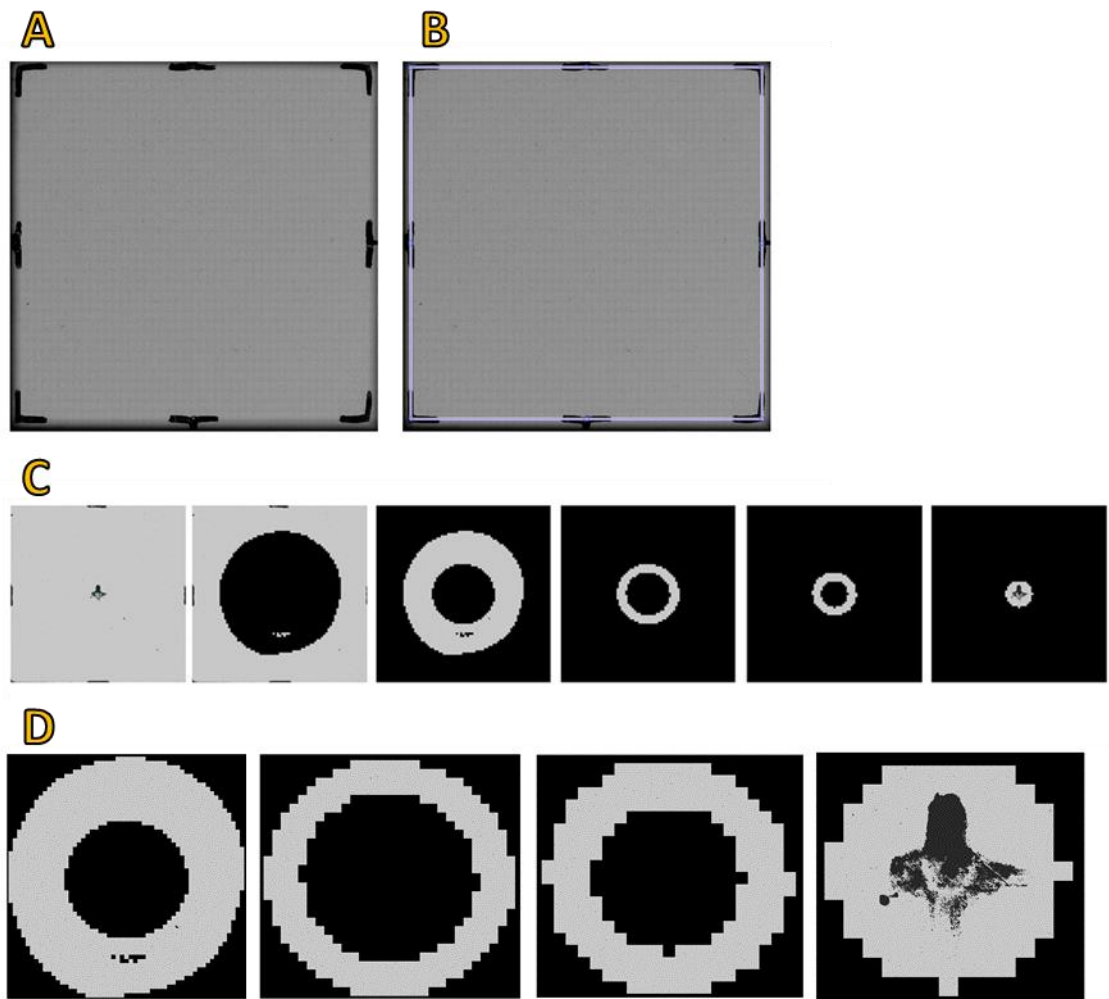
Figure 4.34: Applying pressure bin masks to microscope images.
A: MATLAB displays the bright field image containing marker points. B: User selects the region of interest via an interactive box, aligning with guidelines marked on membrane. C: The program was tested on a bright field image with centre marked. The resulting images correlated with masked areas. D: The images cropped.

An interactive box allowed the user to select the region of interest from the scan by aligning the edges to the marks on the biocell membrane. The program then computed the centre point in pixels (accurate to within ±48 pixels) and the scale (accurate to within ±1 pixels per mm). Next, masking was applied to each pixel by finding the nearest XY scan point for each of the pressure bin masks. Note, the masking in Figure 4.34C shows the resulting masked images for a bright field test image with the centre point marked. Next, the images were cropped to reduce image size and memory requirements (Figure 4.34D). Images appear pixelated because the XY scan was in 0.5 mm steps. Accuracy could be further enhanced by interpolating the scan results, but as the transducer alignment accuracy was estimated to be of the same order (±0.5 mm) this was considered adequate for the purposes of the image processing and cell counting.

This masking was applied to all microscope images. The images were pre-processed, and cells counted in ImageJ [179]. As well as masked images, the full microscope scan image (the global image) was also processed.

4.5.3.1 Live / dead Cell Counting (Hoechst stain / DAPI filter)

Cell counting was more complex than in the Frequency Study because (a) images were so large, (b) they included artificial zero values from the masking, and (c) denser cell populations were involved (because cells were cultured for up to 48 hours after exposure). This meant that the automatic contrast enhancing and background removal routines used for the Frequency Study cell counts were not as effective, and manual checking of counts was more difficult.

In the case of the live/dead DAPI images, with more cells to count, a similar process to that used in the Frequency Study was adopted (see Figure 4.23), except that the automatic contrast enhancement was adjusted to take into account the ratio of the pressure bin versus zero-value pixels. An example ImageJ macro, *Count_DAPI_m5_recursive.ijm*, is provided in Section B.2.4 of Appendix B. Briefly the process consisted of running the following ImageJ commands, which were already described in previous sections: Subtract Background; Enhance Contrast; Convert to 8-bit Grayscale; Threshold value 50.

The threshold value was chosen by examination of cell count results and images for sparsely populated and densely populated example images, as illustrated in Figure 4.35.

As in the Frequency Study, there were very few dead cells present in most samples. This was either due to fewer cells dying, or due to dead cells being washed off the membrane during the fixing and staining process. Because there were so few dead cells, the scanning microscope was set to focus on the bright field image during a scan. This resulted in the scanned images of the fluorescent filter often being slightly out of focus (as the focal points of each were slightly different).
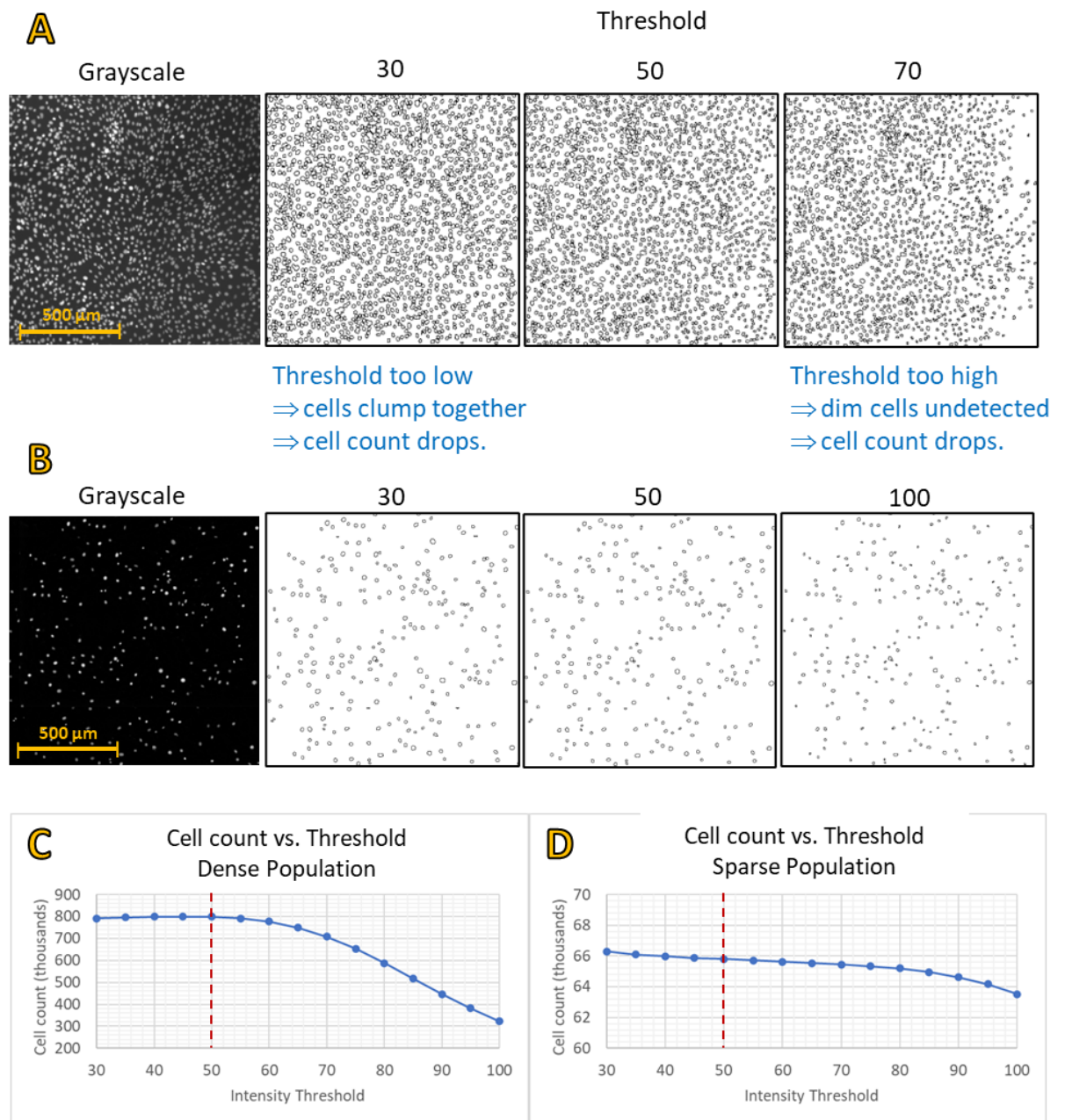
Figure 4.35: Finding the optimum threshold level for DAPI live/dead cell counts. Small representative sections of A: densely and B: sparsely populated images were chosen and cells counted with threshold values from 30 to 100. C: Densely populated images showed more pronounced reliance of cell count accuracy on threshold value and D: sparsely populated images less so. Optimum threshold value for both cases was 50 (marked with red dashed lines). Approximate scales are provided on original images.

In addition, the ABS polymer and silicone sealant used to construct the biocells were found to be auto-fluorescent in the dead cell images, particularly in the case of the green stain. Small smears of adhesive and any tiny particles of ABS scraped off by the needle and not washed out of the biocell would show up in the images and result in false positives. The number of false positives was reduced by removing the watershed feature (see Figure 4.36)

and introducing a maximum particle size of 500 in the cell count routine (this limits the cell counts to features with areas less than or equal to 500 pixels).
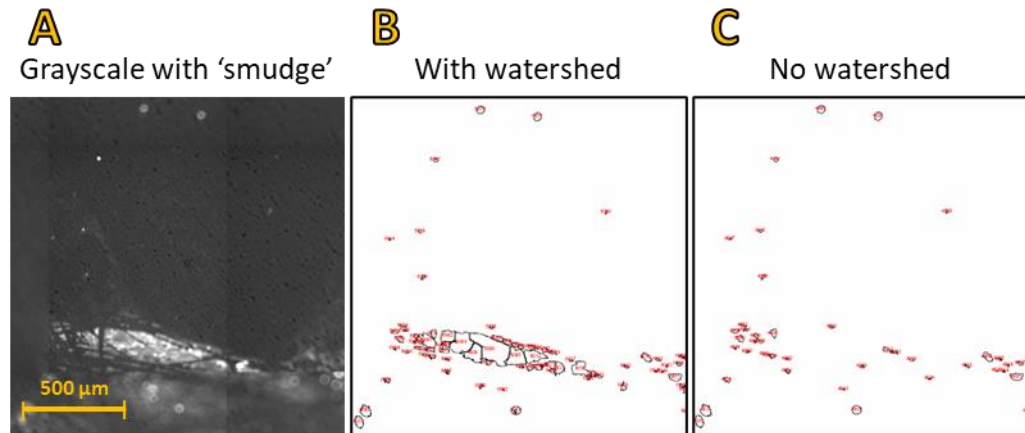
Figure 4.36: Effect of watershed routine on cell count accuracy.
A: Grayscale shows smudge of auto-fluorescent adhesive (with approximate scale).
B: Water shedding segmented the smudge and increased false positives. C: With no
watershed and maximum particle size false positives reduced significantly.

In the second proliferation trial, the use of the far-red stain reduced the effects of the ABS and adhesive auto-fluorescence. As in the Frequency Study, the low dead cell count in most biocells resulted in increased false positives. However, the size of the images meant that manual counts of dead cells was not practical. Instead, the number of false positives in the automatic cell count was minimised by removing the automated Enhance Contrast step. An example ImageJ macro, *Count_CY5_m5_recursive.ijm,* is given in Section B.2.5 of Appendix B.

Checks on accuracy of the dead counts were limited to checking the highest counts, as they were the most likely to contain false positives. These cell counting procedures were used throughout the Rise Time Study trials described in the next section.

4.5.4   Rise Time Study protocols

The Rise Time Study consisted of three trials. The first two trials assessed proliferation and PGE2 expression of MC3T3-E1 preosteoblasts cultured in base media (Trial A) and osteogenic media (Trial B). The results from cells grown in base media indicate preosteoblast response to LIPUS and allow direct comparison to the results of the Pressure Amplitude and Frequency studies, both conducted in base media. MC3T3-E1 cells grown in osteogenic media differentiate to mature osteoblasts and mineralise. The results from

cells grown in this media indicate whether differentiation and mineralisation are further stimulated by LIPUS exposure. The third (Trial C) assessed expression of genetic markers for mechanotransduction pathways and mineralisation. The protocols for Trial A and B are summarised in Figure 4.37. Trial C protocol is summarised in Figure 4.38 on page 161.

4.5.4.1 Proliferation and PGE2 in base media (Trial A)

In Trial A, 14 biocells were seeded with 500,000 MC3T3-E1 preosteoblasts (seeding density 13,000 cells/cm^2). After 24 hours incubation untreated controls (x2) were fixed and stained with Hoechst and the live/dead Green fixable stain (Invitrogen L34969). These provided the pre-exposure, or 'before' cell counts. The remaining biocells were filled with fresh base media (89% αMEM, 10% FBS and 1% PS) and exposed to LIPUS in the custom tank system. Four were sham-treated (no drive to the transducer), four exposed to standard, Fast RT LIPUS and four exposed to modulated, Slow RT LIPUS. After exposure the biocells were dried and incubated for either 24 hours (x2 for each condition) or 48 hours (x2 for each condition). After incubation, a 1 ml sample of growth media was removed and stored at -20°C until required for the PGE2 ELISA. The cells in the biocell were fixed and stained as described in 3.1.2.2 (with the Green live/dead stain) and imaged. Images were masked into pressure bins and the cells counted as described in 4.5.3. The whole process was repeated to achieve four replicates of each condition (i.e., Pre-exposure, 24-hours and 48 hours post-exposure to sham-treated LIPUS; 24 hours and 48 hours post-exposure to fast rise time LIPUS and 24 hours and 48 hours post-exposure to slow rise time LIPUS. Proliferation is then assessed by comparing the cell counts pre- and post-exposure to LIPUS. PGE2 expression is assessed by PGE2 ELISA, detailed in 3.1.2.4. MC3T3-E1 cells grown in base media maintain their preosteoblast phenotype, with fast proliferation (confluence in 2-3 days) and no mineralisation.
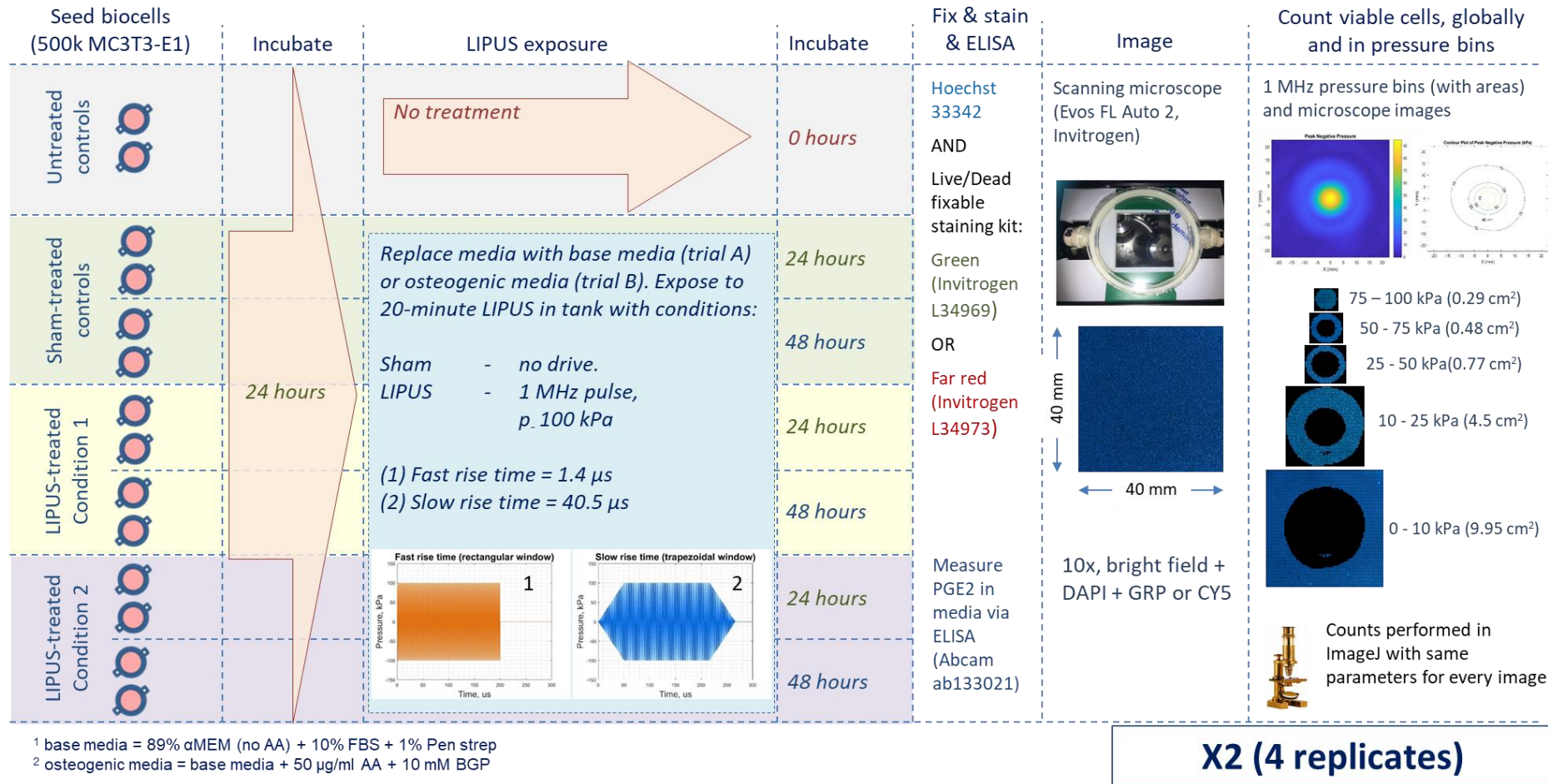
Figure 4.37: Protocol for Rise Time Study Cell proliferation and PGE2 expression in base media and osteogenic media (Rise Time Trials A and B)
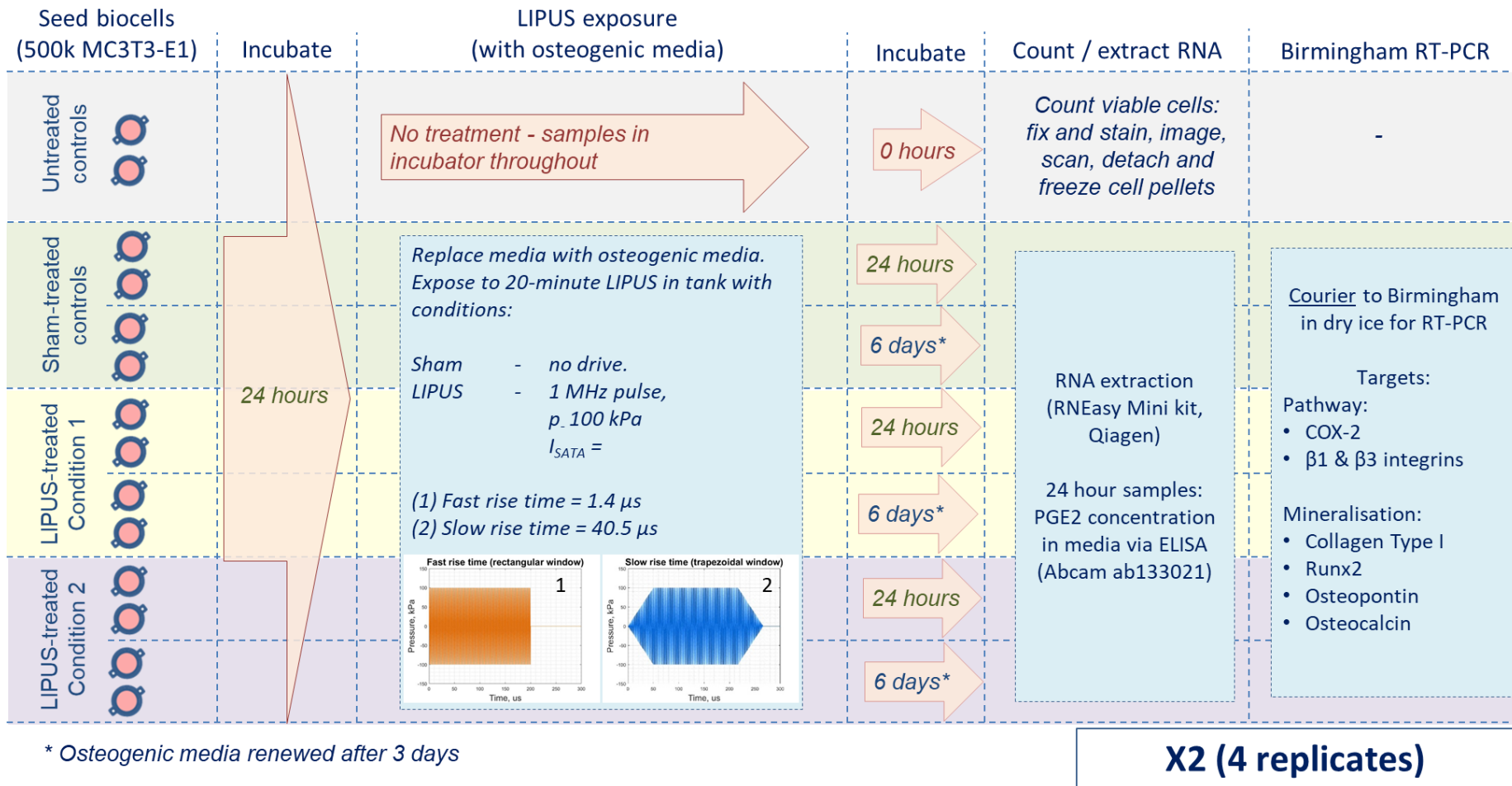
Figure 4.38: Protocol for Rise Time Genetic Markers study
(Trial C)

4.5.4.2 Proliferation and PGE2 in osteogenic media (Trial B)

Trial B followed the same process as Trial A, except biocells were filled with osteogenic media (base media plus 50 µg/ml AA and 10 mM BGP) immediately prior to US exposure. The dead cell count was carried out using the far red live/dead stain, to reduce the number of false positives. Cell count accuracy was also improved by not marking up the centre of the biocell membrane during this trial, as this had affected some of the cell counts in the central bin of Trial A. The use of osteogenic media also allowed direct comparison of proliferation and PGE2 expression with expression of genetic markers for mechanotransduction and mineralisation, assessed using the protocol described in the next section.

4.5.4.3 Genetic Markers for Mechanotransduction and Mineralisation (Trial C)

The protocol for assessing RNA markers for mineralisation, COX-2 and PGE2 in response to Fast and Slow RT LIPUS is summarised in Figure 4.38. The first few steps were the same as for the proliferation trials. Biocells were seeded in the same way, incubated for 24 hours and exposed to LIPUS. A pre-exposure set was fixed, stained and cells counted in the same way as for the proliferation trials, to make sure the same numbers of cells were exposed. Prior to US exposure the media was refreshed with osteogenic media. Two replicates of each LIPUS exposure condition (Fast RT, Slow RT and sham) were then incubated for 24 hours, and two were incubated for 6 days, renewing the osteogenic media on day 3. The 6-day incubation period allowed the cells to begin the process of mineralisation (see Table 3.1 in Chapter 3), so that the expression of mineralisation markers in response to LIPUS exposure could be assessed. After incubation, RNA was extracted using the RNEasy mini kit (Qiagen, DE) as described in 3.1.3. The extracted RNA was then stored at -80 °C until all samples were collected for RT-PCR. Samples of the media in the biocells incubated for 24 hours post-exposure were taken and stored at -20 °C for assessment of PGE2 concentration by ELISA (see 4.5.4.4). The whole process was repeated to achieve four replicates for each condition, and the frozen RNA was analysed by real-time PCR (protocol described in 3.1.3) for the mineralisation markers cox2, integrin β5, collagen Type I, runx2, osteocalcin and osteopontin.

4.5.4.4 Fast/Slow Rise Time Trials: PGE2 ELISA

The media samples from all three trials were tested for PGE2 concentration via two ELISA kits with the protocol described in 3.1.2.4. Four-Parameter Logistic Regressions (4PL) [204] provided the best fit to the PGE2 standards in both ELISAs (see Figure 4.39). The regressions were used to convert optical density (*OD*) to PGE2 concentration (C_{PGE2}) in pg/ml.
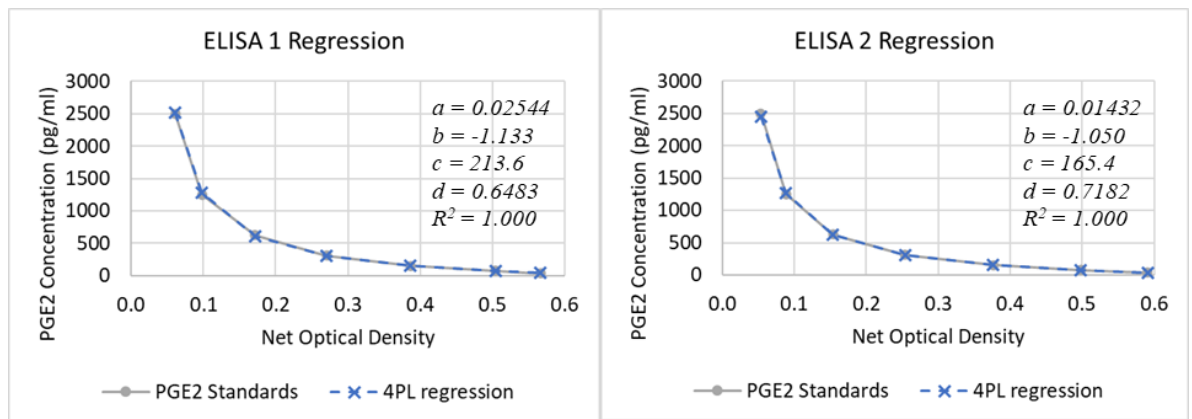
$$\text{Best fit 4PL regression equation:} \quad C_{PGE2} = c \left(\frac{a-d}{OD-d} - 1 \right)^{1/b}$$

Figure 4.39: Best fit to PGE2 ELISA Standards in the Rise Time Study.
Best fit was a 4PL regression with above equation, conducted with the MATLAB function '4PL' [204]. The best fit equations were used to derive PGE2 concentrations from Optical Densities (ODs) measured via plate reader (as described in 3.1.2.4).

The PGE2 results and all other results from the Rise Time Study are presented in Chapter 5. The final method is reviewed in the general discussion in Chapter 6. The next section describes the 3D scaffold feasibility study.

4.6 3D Scaffold Feasibility Study: A method allowing investigation of cellular responses to LIPUS in a 3D growth environment

Section 2.3.2.4 presented the hypothesis that the most likely physical mechanism of LIPUS is the movement of bone induced by the cyclic radiation force of LIPUS, which in turn stimulates the mechanotransduction pathways of osteocytes and osteoblasts by either direct vibration or the increased fluid flow in the lacuna-canalicular system. This triggers the healing and strengthening responses of bone that are normally induced by exercise. If this hypothesis is true, any *in vitro* study must attempt to replicate the physical conditions *in*

vivo. 3D-printed scaffolds could be used to create a bone mimic that can be designed to reproduce some or all of the structures of bone in order to reproduce the effects of LIPUS on bone. In addition, bone cells such as preosteoblasts, osteoblasts and osteocytes display differences in morphology and cellular behaviours in 3D environments compared to standard two-dimensional culture vessels. Therefore, even simple structures could change general cellular behaviour and their responses to LIPUS exposure. The studies described in this section test the feasibility of using 3D-printed scaffolds to investigate the cellular responses of MC3T3-E1 preosteoblasts to LIPUS in a 3D culture environment. The 3D environment chosen was a 3D-printed scaffold design developed by the University of Glasgow for a trial assessing coatings for bone implants [205].

A secondary aim of this study was aligned to the aims of the Ultrasurge project [EP/R045291/1], a collaborative project investigating the use of robotic and miniaturised ultrasonic cutting tools and including assessments of the effects of these cutting tools on cells. For this reason, the study included cutting the 3D scaffolds with an ultrasonic cutting tool with the aim of studying cell recovery, migration and proliferation into the cut site, and whether LIPUS could accelerate the recovery. Local cell death would be expected with a tool such as this, along with the risk of cavitation of any media surrounding the sample. To limit the risk of cavitation, the samples were removed and air dried for a short period before cutting.

The 3D scaffolds consisted of a lattice structure of Polycaprolactone (PCL) doped with 20 % hydroxyapatite (HA) particles. The Young's modulus of the scaffold material was 70-90 MPa which is comparable to that of bone (133 MPa longitudinal, 51 MPa transverse [206]). The scaffolds used were cylindrical with diameter 8 mm (to fit in a 48 well plate) and 8 vertical lattice layers of 0.3 mm height, making the total height 2.4 mm. The gap size between lattice struts was 0.5 mm and angle between layers 60° (Figure 4.40). The gap size and angle were chosen because they had been shown to be optimal for culturing MSCs of similar size to the MC3T3-E1 cells (15–30 µm) in the previous study by the University of Glasgow [205].
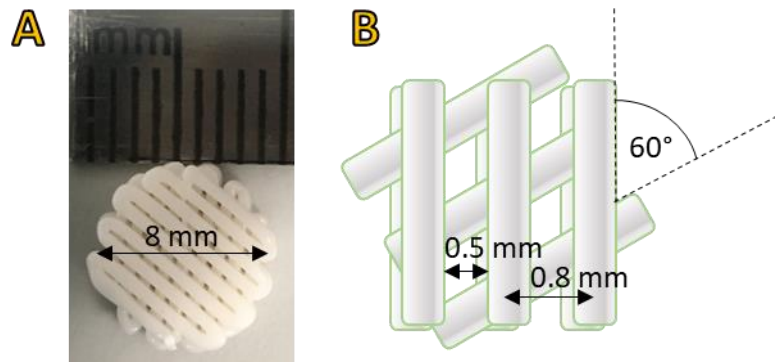
Figure 4.40: The 3D-printed scaffold.
A: Photograph showing scaffold scale. B: Dimensions of lattice structure. 0.5 mm gap size
(0.8 mm between centre of lattice struts). 60° angle between adjacent vertical layers, of
which there are 8. Total scaffold height is 2.4 mm.

4.6.1 3D Scaffold Preliminary Study: Seeding, Cutting and Cell Migration

This preliminary study established protocols for seeding, cutting and staining of the 3D printed scaffolds with MC3T3-E1 cells. The work was carried out in collaboration with a visiting PhD student from Drexel University in Philadelphia. Seven scaffolds were placed in 48 well plates and sterilised by soaking in 70 % ETOH then exposing to UV light for 30 minutes each side. The scaffolds were washed with 1 ml DPBS three times and soaked in 90 µg/ml concentration rat tail collagen (C3867, Sigma, DE), sealed with parafilm and incubated at 4 °C overnight to allow the collagen to coat the scaffold.

The next day excess collagen was removed and the scaffolds washed with 1 ml DPBS three times. The scaffolds were seeded with 1×10^6 MC3T3-E1 cells in 1 ml growth media and incubated for 24 hours at 37 °C, 95 % humidity and 5 % CO_2. One scaffold was not seeded so the fluorescence of the scaffold alone could be assessed.

On day 3, three scaffolds were removed from their wells, placed on the inside lid of the culture plate and cut using a handheld 20 kHz ultrasonic cutting tool with a curved tip while being held with tweezers (Figure 4.41A, B & C). The cut depth was approximately half way through the scaffold strut, approximately 0.1 to 0.2 mm deep, and varied in length. The cut showed evidence of melting, with ridges of scaffold material deposited on the edges (Figure 4.41D). Three controls were not cut. One cut sample and one control sample were immediately fixed and stained (the 0-hr group). The remaining samples were placed in a new 48 well plate with 1 ml fresh growth media and incubated for 24 hours. After incubation, these samples were also fixed and stained (the 24-hour group).
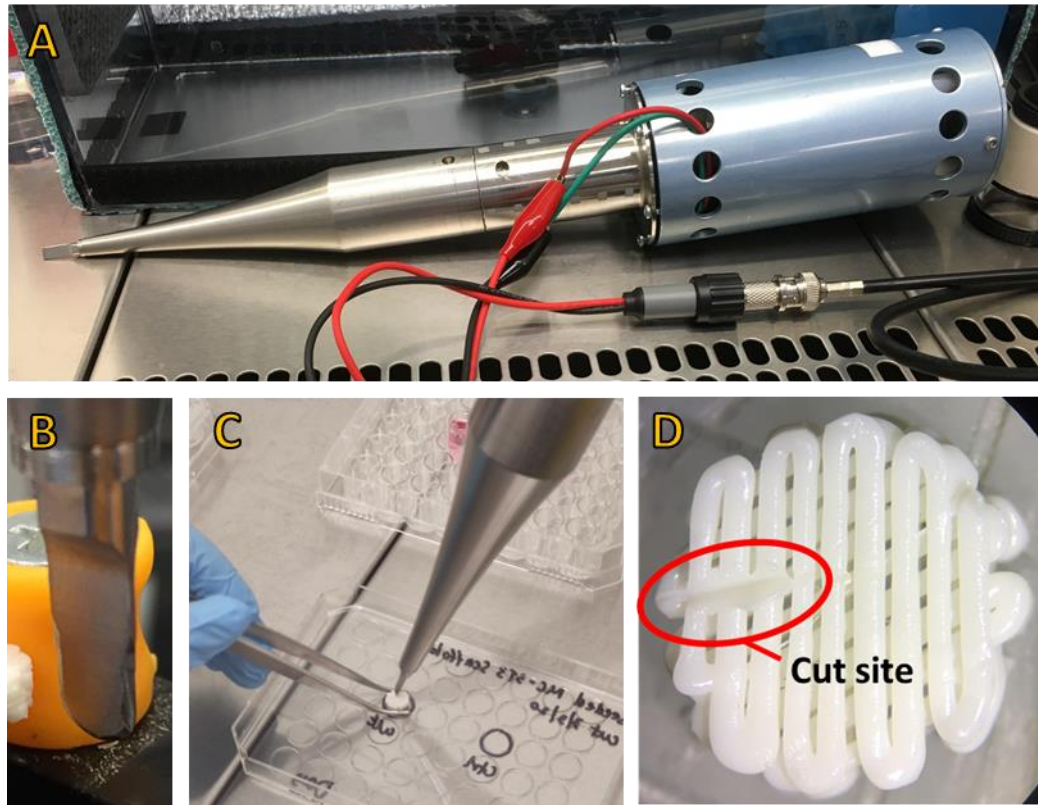
Figure 4.41: Ultrasonic cutting of 3D scaffolds seeded with MC3T3-E1 cells.
A & B: the cutting tool. C: Cutting a scaffold. D: Cut site under magnification (unseeded).
Localised melting leaves ridges of material either side of cut site.

To fix and stain cells, first growth media was removed from each well and the scaffolds washed with 1 ml DPBS. Cells were fixed with 1 ml of 4 % PFA at room temperature for 10-30 minutes. The PFA was removed and the scaffolds washed 2-3 times with DPBS. 500 µl of 0.1% Triton X-100 in DPBS was added and the scaffolds were incubated at room temperature for 3-5 minutes to increase cell membrane permeability. The Triton mixture was then removed and the scaffolds washed 2-3 times with DPBS. Next, samples were blocked by adding 500 µl of 1 % BSA to each scaffold and incubating at room temperature for 30 minutes. After incubation the 1 % BSA was removed and the scaffolds washed 2-3 times with DPBS. Finally, the cells were stained with rhodamine phalloidin (R415, Invitrogen, US) and Hoechst dyes. The Hoechst stained the nucleus and the phalloidin stained actin to image the cell membranes.

The phalloidin was diluted to 1:100 concentration in DPBS, then 2 drops per ml of Hoechst dye was added. 1 ml of the phalloidin-Hoechst mixture was added to each scaffold and incubated for 60-90 minutes at room temperature, wrapped in aluminium foil to protect samples from light. Next the dye solution was aspirated and each well filled with DPBS-

Tween solution and incubated for 5 minutes at room temperature. This was repeated two more times for a total of three DPBS-T washes. The scaffold was then moved to a 48 well imaging plate, DPBS added, and stored wrapped in aluminium foil at 4°C until time for imaging. Imaging was conducted using the DMi8 fluorescent microscope (Leica, DE). The results of the preliminary study are given in Section 5.4.1.

4.6.2 3D Scaffold LIPUS Exposure Study

The preliminary study indicated that MC3T3-E1 cells could attach and grow on 3D scaffolds coated with collagen. The aim of the 3D scaffold LIPUS exposure study was to assess if LIPUS exposure of the cut sites might encourage the cells to migrate at a faster rate, as found in 2D scratch assays in a previous LIPUS study [45]. Migration of preosteoblasts to a fracture site is one of the processes of bone healing, and speeding up this process might in turn speed up the laying down of mineralised matrix of bone.

The protocol is summarised in Figure 4.43. Ten scaffolds were sterilised, coated with collagen and seeded in 48 well plates using the protocol established in the preliminary study, then incubated for 24 hours. All scaffolds were then cut with a 20 kHz cutting tool.

Figure 4.42A & B illustrate the blade used for cutting, which was a different shape from the blade used in the preliminary study. The aim was to make a shallow cut of approximately 0.1 – 1 mm in the top layer of the seeded scaffolds but if the blade was held against the material for more than 2 seconds, a deep cut of approximately 2 - 3 mm would result (see Figure 4.42C). It is suspected that the vibration of the cutting tip was causing localised heating, resulting in the blade melting the polymer material. During cutting it was noted that any growth media remaining on the samples would occasionally froth, indicating the presence of cavitation. The samples were left to air dry for approximately five minutes prior to cutting to reduce the risk of this harmful phenomenon, but frothing still occurred in some samples.

After cutting some samples were exposed to LIPUS in the tank exposure system to assess if LIPUS stimulated cell migration into the cut site. Scaffolds were secured to the back membrane of a biocell then the second membrane attached before filling with growth media and exposing to LIPUS.
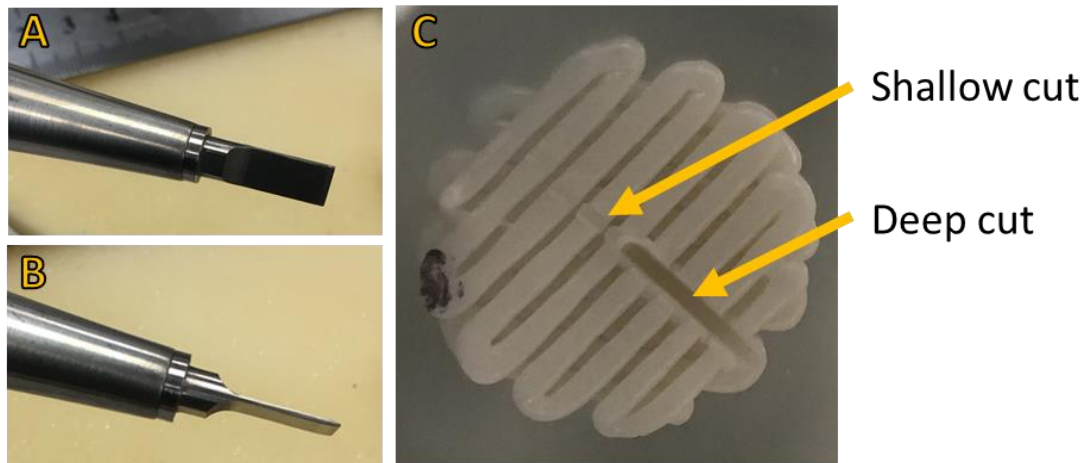
Figure 4.42: Cutting blade used in 3D scaffold LIPUS trial, with resulting cut.
A & B: Cutting blade had square edges approximately 0.5mm thick. C: Shallow cut and
deep cut in the 3D scaffold. If the cutting tip was held on the scaffold for longer than
2 seconds, a deeper cut of 2-3 mm was made, due to local heating of the polymer material.

The remaining scaffolds were glued to the back membrane of a biocell with medical grade cyanoacrylate adhesive (Liquidskin), then the second membrane was fitted to the biocell.

Problems occurred when trying to fix the second membranes to the biocells. The silicone adhesive used to seal the biocells could not be used in this case due to its long cure time. Initial benchtop trials using Liquidskin had been successful, but during the trial this method only worked with one biocell. It is suspected that increased moisture on surfaces during the trial adversely affected the ability of the Liquidskin to cure. After many failed attempts the rest of the biocell membranes were fitted with a fast-curing epoxy. This was a last resort, since epoxy is cytotoxic, but allowed the LIPUS exposure method to be assessed.

LIPUS exposure was conducted using the 1 MHz V303 transducer (Fast RT, 200 µs, p_- 100 kPa, *prr* 1 kHz). The biocell containing the scaffold and transducer were clamped in the positioning system and aligned with the transducer close to the scaffold. Then the transducer was moved back to the required distance of 60 mm from the front of the scaffold. The apparatus was then placed in the tank in the BSC and the LIPUS exposure conducted. The biocell was then dried and placed in the incubator.
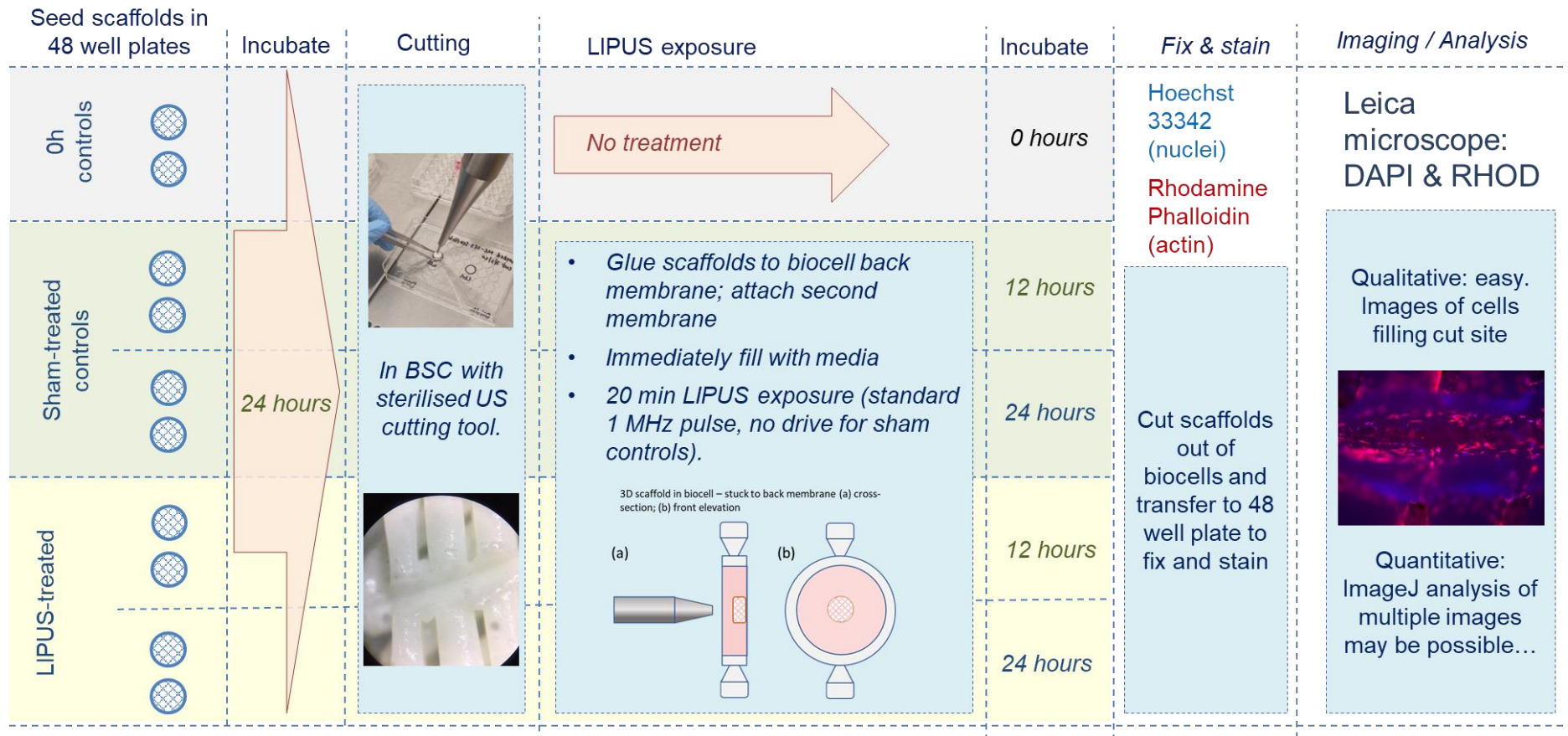
Figure 4.43: Protocol of Seeding and Cutting trial

Zero-hour controls were fixed and stained immediately after cutting with Phalloidin and Hoechst dyes using the protocol established in 4.5.1. Cells were stained with live Hoechst dye and imaged at regular intervals to monitor cell migration, beginning at 12 hours post-exposure. Once migration was established, samples were fixed and stained at regular intervals and imaged. The images can then be examined qualitatively, and quantitatively via ImageJ to assess the rate of migration into the cut site Post-exposure to LIPUS or sham treatment. The full results of both studies are detailed in 5.6.

4.7 Chapter Summary

A custom culture vessel, the biocell, was developed to allow growth of biological cells and exposure to ultrasound *in situ*. The biocell design was based on existing vessels (the Clinicell and Opticell) but with a thinner membrane (6 µm mylar) to minimise the effect on the ultrasonic field. The 3D printed frame and off-the shelf components meant the vessel was cheap and easy to reproduce, and the diameter of the circular frame could be adjusted to accommodate varying ultrasonic beam widths. The biocell offered an improvement over existing off-the-shelf culture vessels (the Opticell and Clinicell) because its thin membrane had effectively zero effect on the pressure amplitude of the ultrasonic beam, whereas the Clinicell and Opticell reduce it by more than 5 dB (nearly half).

A custom tank exposure system was developed, consisting of a thermostatically controlled water tank with an acoustic absorber positioned behind the biocell to minimise reflections off the tank walls. A positioning system that spanned the top of the ultrasonic exposure tank allowed alignment of the transducer and biocell outside the BSC, and the apparatus could then be lifted in to place above the tank for the LIPUS exposures. Alignment was conducted with the aid of a laser spirit level and external ink markings made on the Mylar membrane.

The Pressure Amplitude Study tested the *in vitro* exposure methods and investigated the pressure amplitudes of 1 MHz LIPUS that would result in cellular responses, in terms of cell proliferation and PGE2 expression. The Frequency Study compared cellular responses to 45 kHz and 1 MHz LIPUS and aided further development of the methods.

The Rise Time Study investigated cellular responses to LIPUS fields with fast and slow rise times, i.e., quick and slow onset of the pulse amplitude. This had the aim of assessing

whether the sudden (fast) onset of the radiation force provided the mechanism for stimulating healing responses, in the form of proliferation, PGE2 expression and expression of genetic markers associated with mechanotransduction and mineralisation. Finally, 3D scaffolds were assessed for supporting cell growth and more closely replicating conditions found *in vivo* during LIPUS exposures.

The methods developed in this chapter offer a set of controlled *in vitro* LIPUS investigations that can be replicated in other laboratories, with 3D-printed custom culture vessels that are cheap to produce (though they require time and care to build). These biocells, coupled with the custom tank exposure system, and the potential to incorporate 3D growth structures, together make a powerful suite of LIPUS exposure methods to provide the basis for detailed, controlled studies of LIPUS mechanisms.

CHAPTER 5
PREOSTEBLAST RESPONSES TO LIPUS EXPOSURE

This chapter presents the results of the *in vitro* studies investigating the cellular responses of MC3T3-E1 preosteoblasts to LIPUS fields via the methods described in Chapters 3 and 4. The Pressure Amplitude Study (5.1) assesses the cell proliferation and PGE2 protein expression of cells exposed to 1 MHz LIPUS at maximum peak negative pressures ($\hat{p}_-$) up to 489 kPa. The Frequency Study (5.2) compares the same cellular responses to 45 kHz and 1 MHz LIPUS with $\hat{p}_-$ up to 203 kPa. PGE2 protein expression and preosteoblast proliferation are chosen as early markers of healing effects up-regulated in past LIPUS studies, as discussed in Chapter 2. PGE2 protein expression is assessed in all studies by ELISA using the protocol in Section 3.1.2.4. Proliferation is assessed by counting viable cells pre- and post-exposure.

The Rise Time Study (5.3) is an in-depth investigation of cellular responses to rate of change of pressure amplitude in the LIPUS pulse. As well as cell proliferation and PGE2 protein expression, the Rise Time Study investigates expression of RNA markers associated with mineralisation and a mechanotransduction pathway linked to up-regulation of PGE2. Finally, the 3D scaffold study (5.4) investigates the feasibility of using 3D-printed matrices to assess cellular responses to LIPUS in growth environments more representative of *in vivo* conditions.

5.1 Pressure Amplitude Study: The Effect of LIPUS Peak Negative Pressure on PGE2 Expression and Proliferation of Preosteoblasts

The Pressure Amplitude Study investigates the peak negative pressures required to stimulate a potentially healing response in MC3T3-E1 preosteoblasts, in the form of PGE2 expression and proliferation. The study also assesses the initial methods and protocols for ultrasound exposure, described in Section 4.3. PGE2 concentration in the growth media and cell count results are presented in Figure 5.1. Two out of three sample sets were

discarded due to low cell numbers in one and a faulty LIPUS transducer in the other.

Therefore, the results presented are for one sample set only.
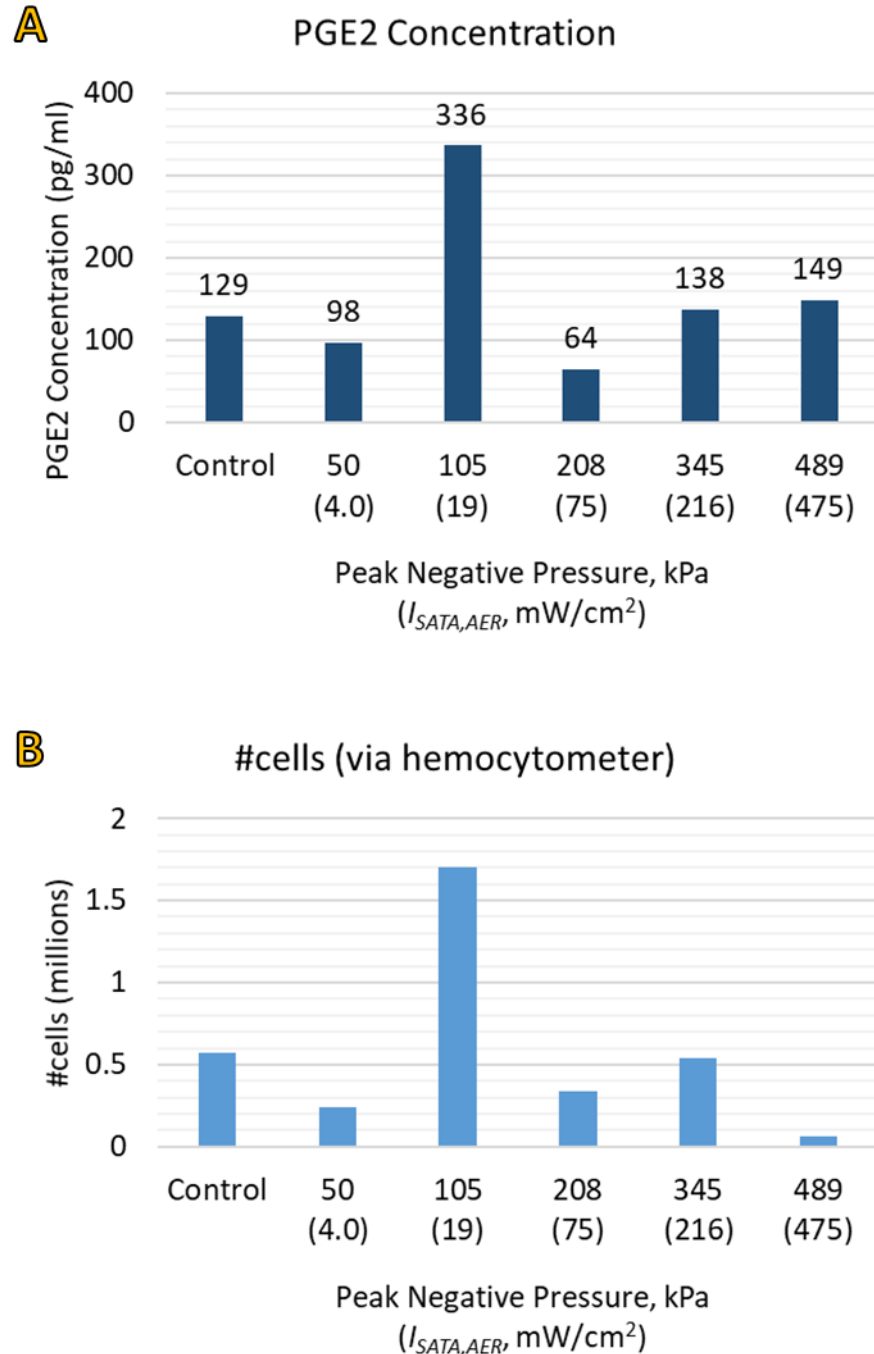
Figure 5.1: Pressure Amplitude Study Results 20 hours post-exposure to 1 MHz LIPUS at $\hat{p}_-$ 0 kPa (sham-treated control), 50 kPa, 105 kPa, 208 kPa, 345 kPa and 489 kPa. A: PGE2 Concentration in the growth media. B: Total number of cells (determined by hemocytometer) 20 hours post-exposure.

Figure 5.1A shows a peak in PGE2 concentration in the sample exposed to LIPUS at $\hat{p}_-$

105 kPa. PGE2 concentration peaked at the same pressure, at 336 pg/ml, 2.6 times higher

than that of the sham-treated control (Figure 5.1B). At the pressure $\hat{p}_-$ 105 kPa the LIPUS transducer used in the Pressure Amplitude Study produced a spatial-average, temporal average intensity of 19 mW/cm^2 $I_{SATA,AER}$, which is within the range of optimal intensities found in LIPUS studies in the literature (see 2.3.1.4) [19, 38, 44, 124, 125]. However, with no replicates it is not possible to conclude that the increased cell count and PGE2 expression are due to LIPUS exposure or are within experimental variance and have occurred by chance.

5.2 Frequency Study: The Effect of LIPUS Frequency on Preosteoblast Proliferation and PGE2 Expression

The Frequency Study investigates cellular responses of MC3T3-E1 preosteoblasts to controlled LIPUS fields at 1 MHz with $\hat{p}_-$ up to 203 kPa and 45 kHz with $\hat{p}_-$ up to 43 kPa. LIPUS has been shown to stimulate expression of PGE2 in osteoblasts at 1 MHz and 45 kHz [40], suggesting the frequency of excitation is not the main factor in LIPUS stimulus. The range of peak negative pressures at 1 MHz was also chosen to include the peak response observed at 105 kPa in the pilot study, with finer steps to investigate if a smooth trend could be established. The aim is to confirm if this finding can be replicated with a controlled exposure method that isolates the ultrasound and minimises secondary effects of the apparatus, and to determine whether frequency affects cellular responses. The methods and protocols are described in Chapters 3 and 4. The 1 MHz results are presented in 5.2.1, and 45 kHz results in 5.2.2.

5.2.1 Proliferation and PGE2 Expression in response to 1 MHz LIPUS

Figure 5.2A shows the average number of viable MC3T3-E1 cells over each set of five microscope images of live-stained cells, captured pre-exposure and 20 hours post-exposure to 1 MHz LIPUS with $\hat{p}_-$ up to 203 kPa. Error bars indicate standard error of the mean (SEM), which is 14% in the sham-treated controls (n = 6) and up to 45% in LIPUS-treated samples (n = 2). High variance in all cell counts, both pre- and post-exposure, is likely due to the effects of the biocell seeding techniques discussed in Section 4.5.2 and the small sample area of cells counted in the five microscope images (a total area of just under 0.03 cm^2). The average cell counts do not exhibit any statistically significant trends with pressure amplitude due to the high overall variance between each set.
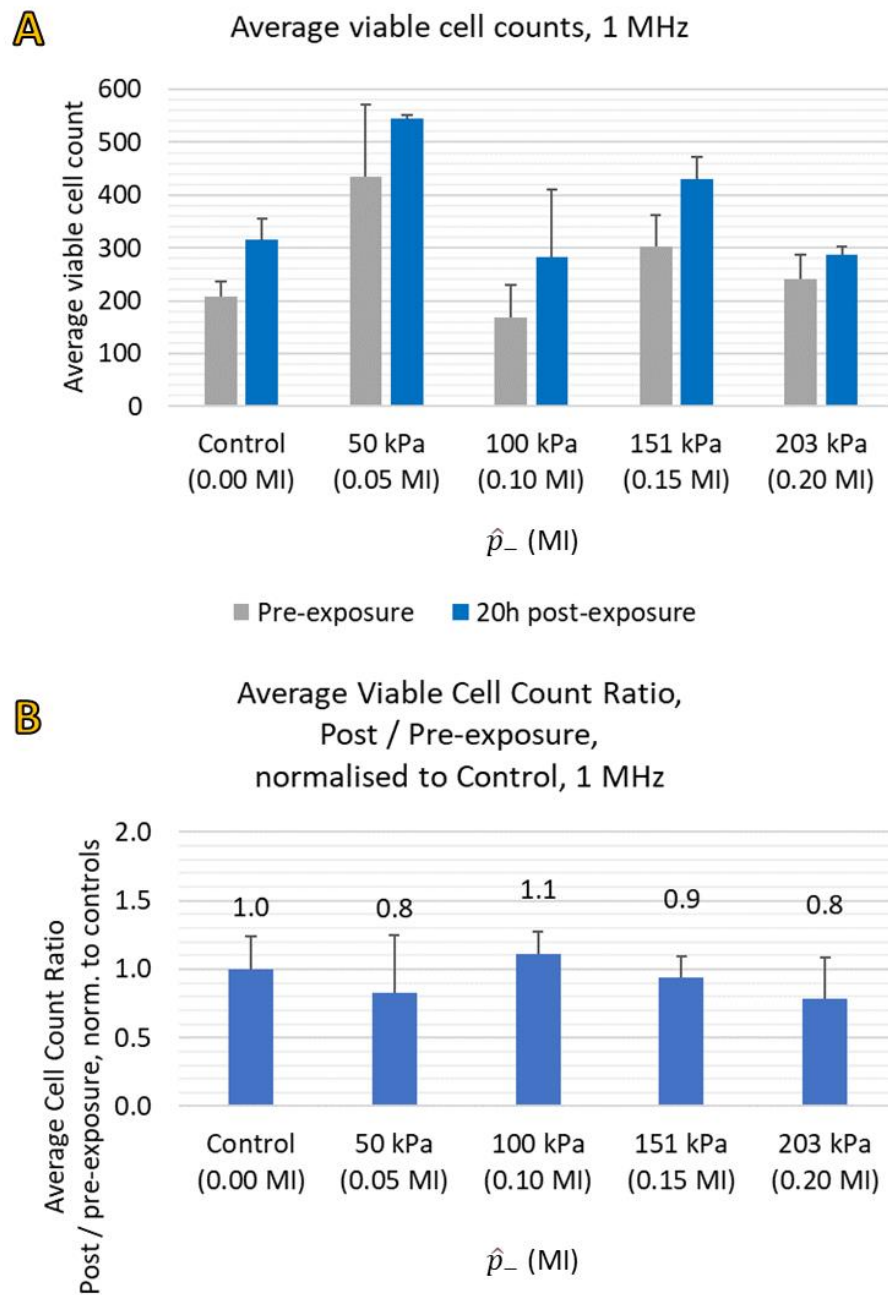
Figure 5.2 Frequency Study viable cell count results.
A: Average viable cell counts pre-exposure and 20 hours post-exposure to 1 MHz LIPUS
at $\hat{p}_-$ 0 kPa (sham-treated controls), 50 kPa, 100 kPa, 151 kPa and 203 kPa. Error bars
are SEM, n (controls) = 6; n (LIPUS) = 2. B: Average viable cell count ratios, post- versus
pre-exposure, normalised to sham-treated controls.

Figure 5.2B presents the viable cell count ratios, normalised to sham controls, 20 hours

post-exposure versus pre-exposure. Cell counts in samples exposed to LIPUS at $\hat{p}_-$ 50 kPa,

151 kPa and 203 kPa show less increase in cell counts compared to controls, indicating

reduced proliferation at those pressure amplitudes. The average cell count in samples

exposed to LIPUS at $\hat{p}_-$ 100 kPa increases by 11 % with respect to control, suggesting a

small increase in proliferation may occur after exposure to LIPUS at this pressure. There is no statistical significance ($p < 0.05$) in any LIPUS cell counts compared to those of sham-treated controls due to the high overall variance in cell counts.

Figure 5.3A shows the PGE2 protein concentrations in the growth media at 20 hours post-exposure to 1 MHz LIPUS. Error bars indicate SEM. PGE2 expression in all LIPUS-treated samples are higher than in sham-treated controls and reach a peak of 741 pg/ml at $\hat{p}_-$ 151 kPa, which is 29 % above the average PGE2 concentration in sham-treated controls (574 pg/ml). At $\hat{p}_-$ 100 kPa the PGE2 concentration is 24 % above the control.
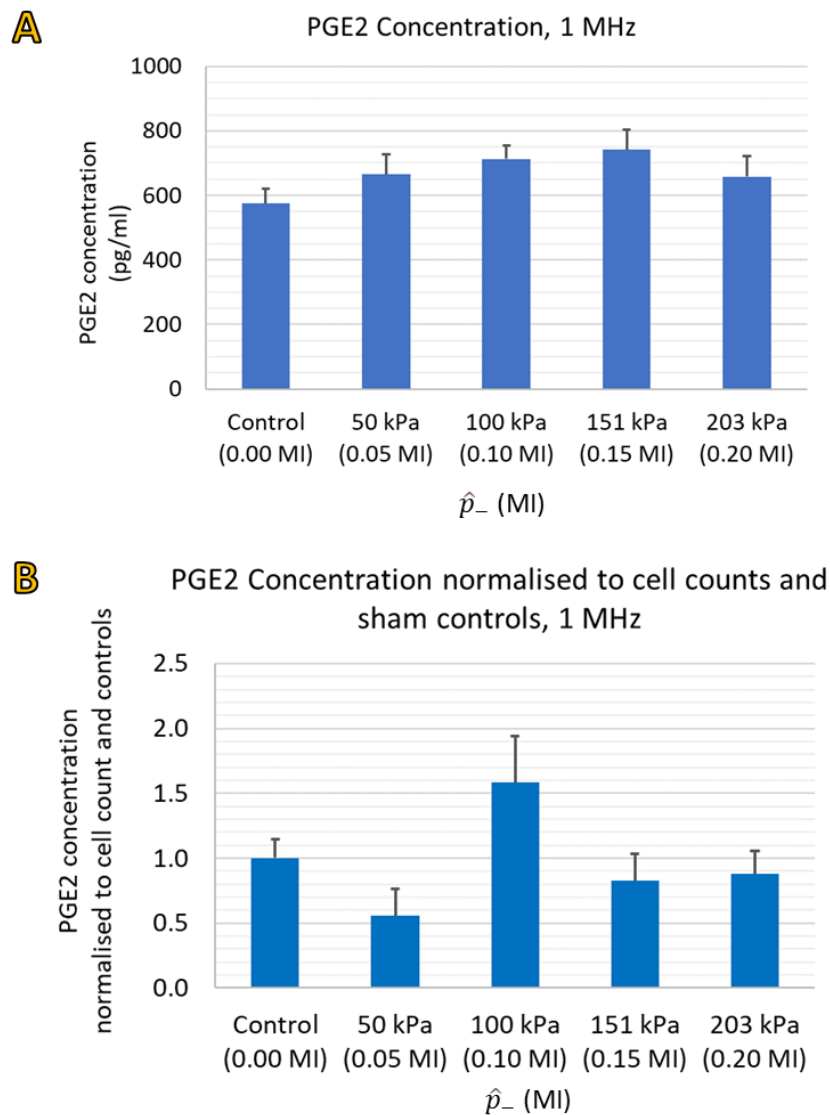
Figure 5.3: PGE2 concentration in growth media 20 hours post-exposure to 1 MHz LIPUS With $\hat{p}_-$ 0 kPa (sham control), 50 kPa, 100 kPa, 151 kPa and 203 kPa. A: Measured PGE2 protein concentration. B: PGE2 concentrations normalised to pre-exposure cell counts and sham controls. Error bars are SEM, n (controls) = 6; n (LIPUS) = 2.

Figure 5.3B shows the PGE2 concentrations normalised to the pre-exposure cell counts and sham-treated controls. A clear peak in normalised PGE2 concentration is apparent in the samples treated with LIPUS at $\hat{p}_-$ 100 kPa, where the normalised PGE2 concentration is 58 % higher than that of the sham-treated control.

None of the LIPUS-treated PGE2 concentrations, measured or normalised, were statistically significant with respect to controls (p < 0.05). Despite the lack of statistical significance, the trends suggest 1 MHz LIPUS with $\hat{p}_-$ 100 kPa to 151 kPa up-regulates PGE2 expression in MC3T3-E1 preosteoblasts and this coincides with the peaks in PGE2 expression and cell counts observed at $\hat{p}_-$ 105 kPa in the pressure amplitude study.

5.2.2 Proliferation and PGE2 Expression in response to 45 kHz LIPUS

Figure 5.4A shows the average number of viable cells over the five microscope images captured pre-exposure and 20 hours post-exposure to 45 kHz LIPUS with $\hat{p}_-$ up to 43 kPa. Error bars indicate SEM, which was 14% in sham-treated controls (n = 6) and up to 37% in LIPUS-treated samples (n = 3). Figure 5.4B presents the ratios of average viable cell counts 20 hours post-exposure versus pre-exposure, normalised to sham controls.

Samples exposed to LIPUS at $\hat{p}_-$ up to 32 kPa exhibited smaller increases in viable cell counts, indicating reduced proliferation with respect to controls. The number of viable cells in samples treated with LIPUS at $\hat{p}_-$ 43 kPa increased by 20 %, suggesting proliferation was up-regulated at this pressure. Statistical significance of these trends could not be proven by student t-test (p < 0.05).
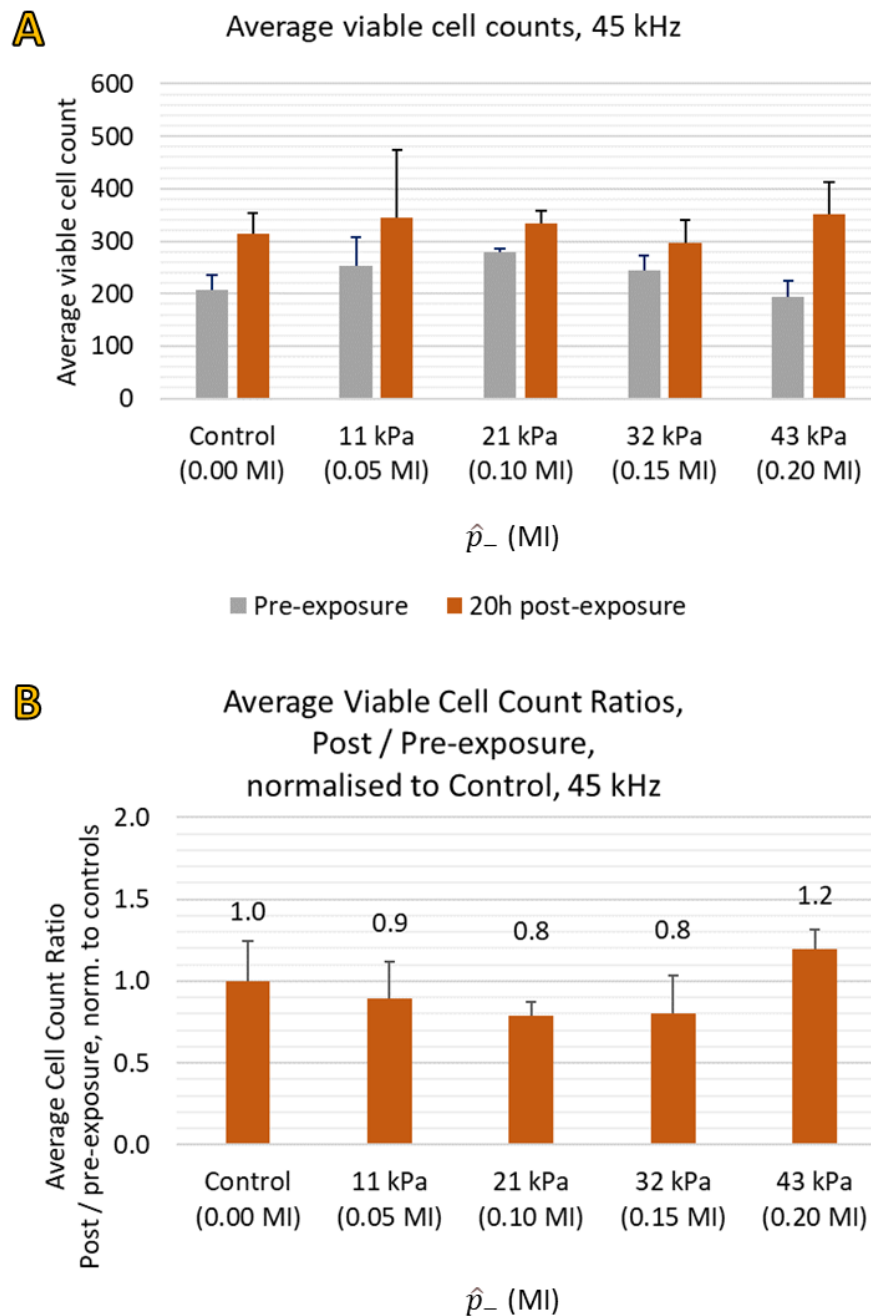
Figure 5.4 Viable cell count results, 45 kHz LIPUS at $\hat{p}_-$ 0 kPa (sham-treated controls), 11 kPa, 21 kPa, 32 kPa and 43 kPa. Average viable cell counts pre-exposure and 20 hours post-exposure. Error bars indicate SEM, n (controls) = 6; n (LIPUS) = 3. B: Ratio of average viable cell counts, 20 hours post- vs. pre-exposure, normalised to sham controls.

Figure 5.5A presents the PGE2 protein concentrations in the media determined by ELISA. The PGE2 concentrations of 45 kHz LIPUS-treated samples were all marginally higher than the sham-treated controls, with the highest PGE2 concentration in LIPUS-treated samples 17 % above controls (674 pg/ml at 21 kPa compared with 574 pg/ml in sham-treated controls). A student t-test could not establish statistical significance (minimum p-value was 0.11 at $\hat{p}_-$ 21 kPa).
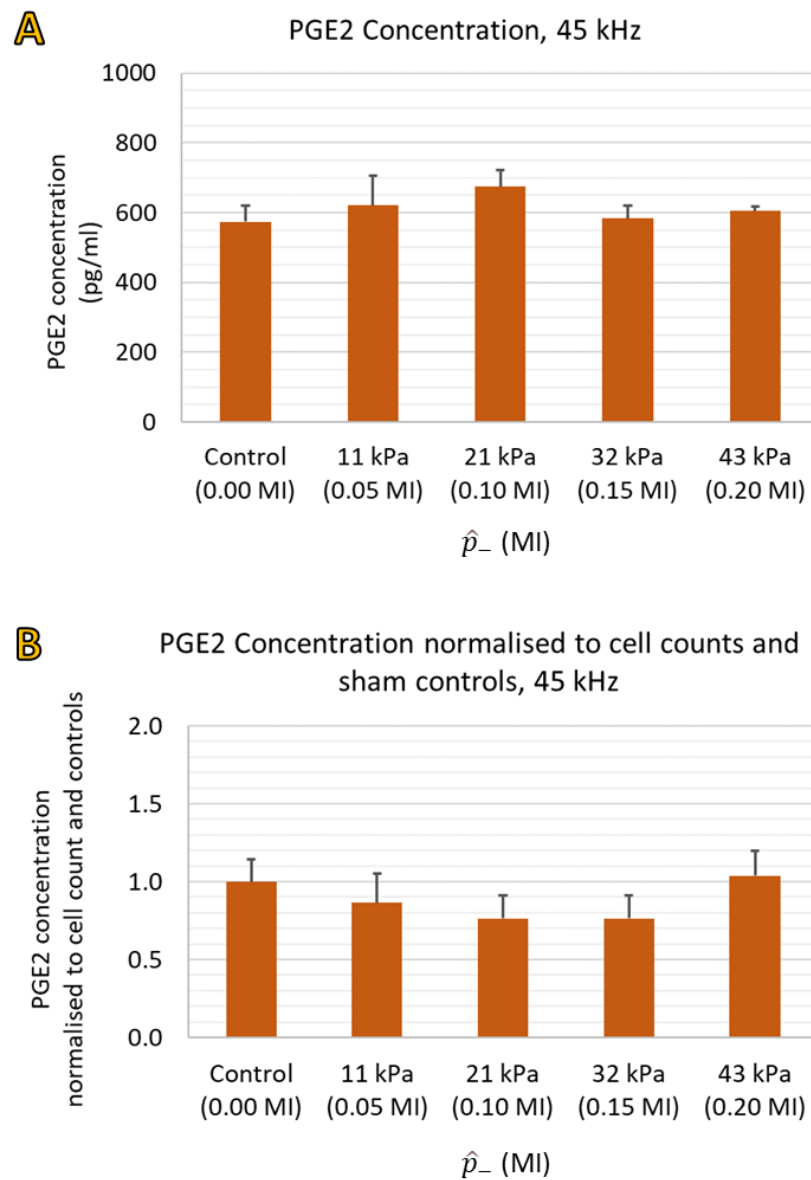
Figure 5.5: PGE2 protein concentration in media 20 hours post-exposure to 45 kHz LIPUS at $\hat{p}_-$ up to 43 kPa. A: PGE2 concentrations measured via ELISA in pg/ml. B: PGE2 concentration normalised to pre-exposure cell counts and sham control. Error bars are SEM, n (control) = 6; n (LIPUS) = 3.

Figure 5.5B presents the PGE2 concentrations normalised to the total number of viable cells pre-exposure and sham-treated control. In these normalised results the LIPUS treated samples show reduced PGE2 concentration compared to control, except for the 43 kPa result, which exhibits a modest increase of only 4%. Overall, the PGE2 results suggest that 45 kHz LIPUS up to $\hat{p}_-$ 43 kPa has no effect on PGE2 expression.

5.3 Rise Time Study: The Effect of Rate of Change of Pressure Amplitude on Preosteoblast Proliferation, PGE2 Expression and RNA Markers for Mechanotransduction and Mineralisation

The Rise Time Study tests the hypothesis that the rate of change of pressure amplitude applied to bone cells influences cellular responses associated with healing, the main mechanism of stimulus being the rapid switch-on of radiation force that would result from a fast pressure amplitude rise time.

A secondary aim of the study is to further investigate whether cellular effects are influenced by secondary effects such as temperature rise and plate vibrations likely induced by the exposure apparatus in previous trials in the literature. Thirdly, the same pressure setting found to be optimal in the Pressure Amplitude and Frequency Study is used to further explore and verify the hypothesis that LIPUS fields with $\hat{p}_-$ 100 kPa up-regulate proliferation and PGE2 expression.

To test the first hypothesis, cells are exposed to LIPUS fields with relatively fast and slow rise times (Figure 5.6), as described fully in Section 4.5.1. Only the rise time was altered and both pulses delivered the same $\hat{p}_-$ (100 kPa) and I_{SATA} (10 mW/cm^2 over a 50 mm diameter circular area – see Table 3.21). The equalisation of I_{SATA} was achieved by increasing the duration of the trapezoidal window of the Slow RT LIPUS pulse.
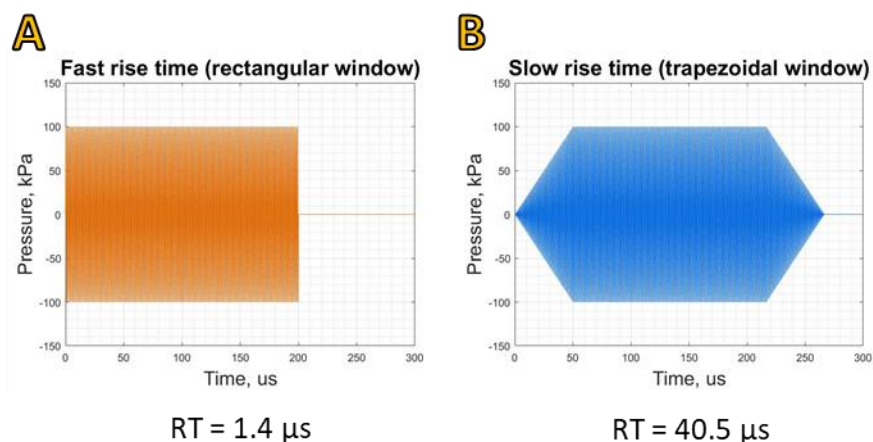
Figure 5.6: Fast and slow rise time (RT) LIPUS pulses.
A: 'Fast' RT LIPUS with rectangular window and rise time of 1.4 μs; B: 'Slow' RT LIPUS with trapezoidal window and rise time 40.5 μs.

Proliferation and PGE2 expression of MC3T3-E1 cells are assessed with cells growing in two formulations of cell growth media, introduced immediately prior to LIPUS exposure. The two media types, described fully in Section 3.1, are base media (89% αMEM, 10% FBS and 1% PS) and osteogenic media (Base media plus 50 µg/ml AA and 10 mM BGP). MC3T3-E1 cells grown in base media maintain the preosteoblast phenotype, with fast proliferation and no mineralisation. The results from cells grown in this media indicate preosteoblast response to LIPUS and allow direct comparison to the results of the Pressure Amplitude and Frequency studies, which were both conducted in base media. MC3T3-E1 cells grown in osteogenic media differentiate into mature osteoblasts and mineralise. The results from cells grown in this media indicate whether differentiation and mineralisation are stimulated further by LIPUS exposure.

The Rise Time Study consists of three trials. Trial A and B assesses proliferation and PGE2 expression in base media and osteogenic media respectively. Trial C assesses RNA markers of mechanotransduction and mineralisation in cells grown in osteogenic media only. Methods and markers are described fully in Chapters 3 and 4.

Section 5.3.1 examines the pre-exposure, or zero-hour, cell count results to assess if improvements to seeding and imaging methods resulted in reduced cell count variance. Proliferation results are presented and briefly discussed in 4.5.4.1. PGE2 protein expression results are presented in 5.3.3. RT-PCR results for the genetic markers associated with mechanotransduction and mineralisation are presented in 5.3.4.

5.3.1 Pre-exposure / Zero-hour Cell Counts

The frequency distribution of the pre-exposure, zero-hour (0h) global viable cell counts throughout all the rise time trials (a total of 13 samples) are presented in Figure 5.7. The figure also shows a standard normal distribution curve with the same mean and standard deviation as the 0h sample set. The frequency distribution of the cell counts correlates well with a normal distribution. The Skewness (a measure of the distribution symmetry, zero for a normal distribution) and Kurtosis (a measure of the relative weight of the distribution tails) of the sample set were calculated in Microsoft Excel and found to be within ±0.5, indicating it is acceptable to assume the sample set has a normal distribution. Skewness was 0.44 and Kurtosis was -0.44. A range of Student's t-tests were carried out on the cell counts of each trial compared to the other two trials and none were found to be

significantly different. From this evidence it can be concluded that the number of cells exposed to LIPUS in each trial were effectively within the same normal distribution.
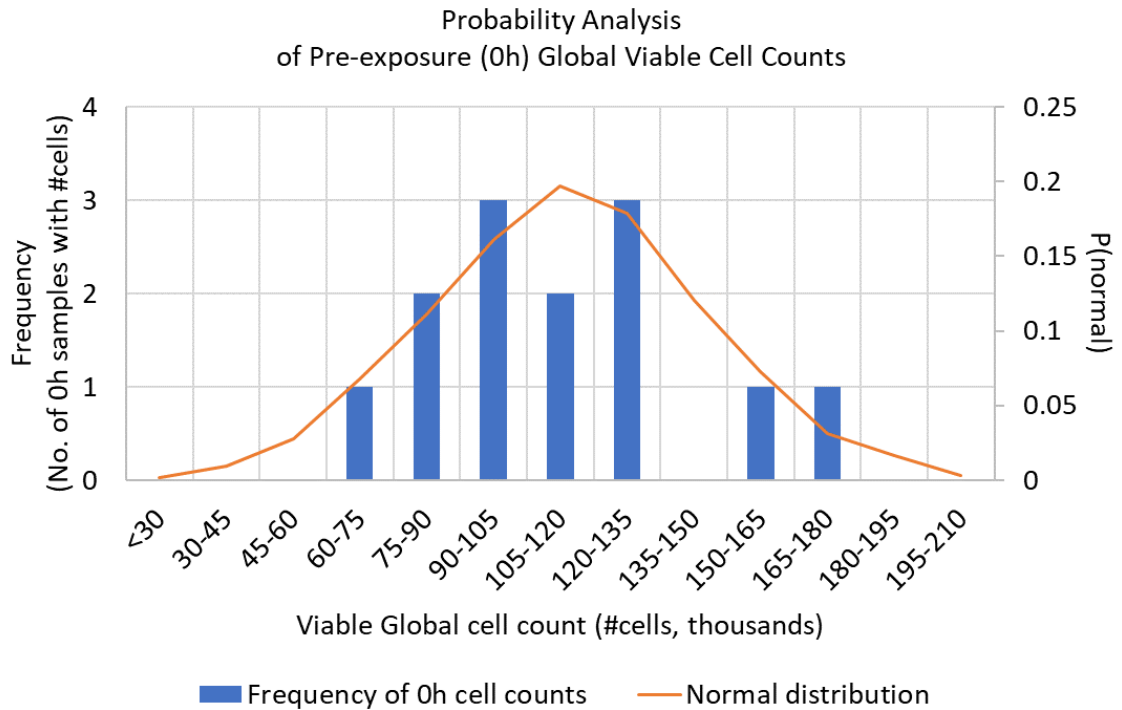
Figure 5.7: Frequency distribution of pre-exposure global viable cell counts across all trials within the Rise Time Study (n=13). The histogram is plotted against a normal distribution of the same mean and standard deviation to check the fit to the curve.

The maximum percentage standard deviation, %σ, in the Frequency Study was 64 % (with percentage Standard Error of the Mean, %SEM, up to 45 %). The %σ in the Rise Time study was 27 %, with maximum %SEM 15 %. This drop in variance is likely due to the improved seeding techniques detailed in Section 4.5.2.

5.3.2 Proliferation

The proliferation results of the Rise Time Study are presented in the following sections as viable cell densities (in #cells/cm^2), calculated by dividing the viable cell count by the area of each pressure bin, and globally across the entire 4 cm by 4 cm scan area. Results are presented for 24 hours and 48 hours post-exposure to Fast RT LIPUS, Slow RT LIPUS or sham treatment. The results are also presented as percentage differences in LIPUS-treated samples versus the equivalent sham-treated controls to highlight any changes that may be due to LIPUS exposure. Section 5.3.2.1 presents the results for samples incubated in base

media (Trial A) and Section 5.3.2.2 presents results for samples in osteogenic media (Trial B). Section 5.3.3.2 compares the global results in both media types.

5.3.2.1 Proliferation in Base Media (Trial A)

Figure 5.8 presents the results of samples incubated in base media, 24 hours post-exposure.
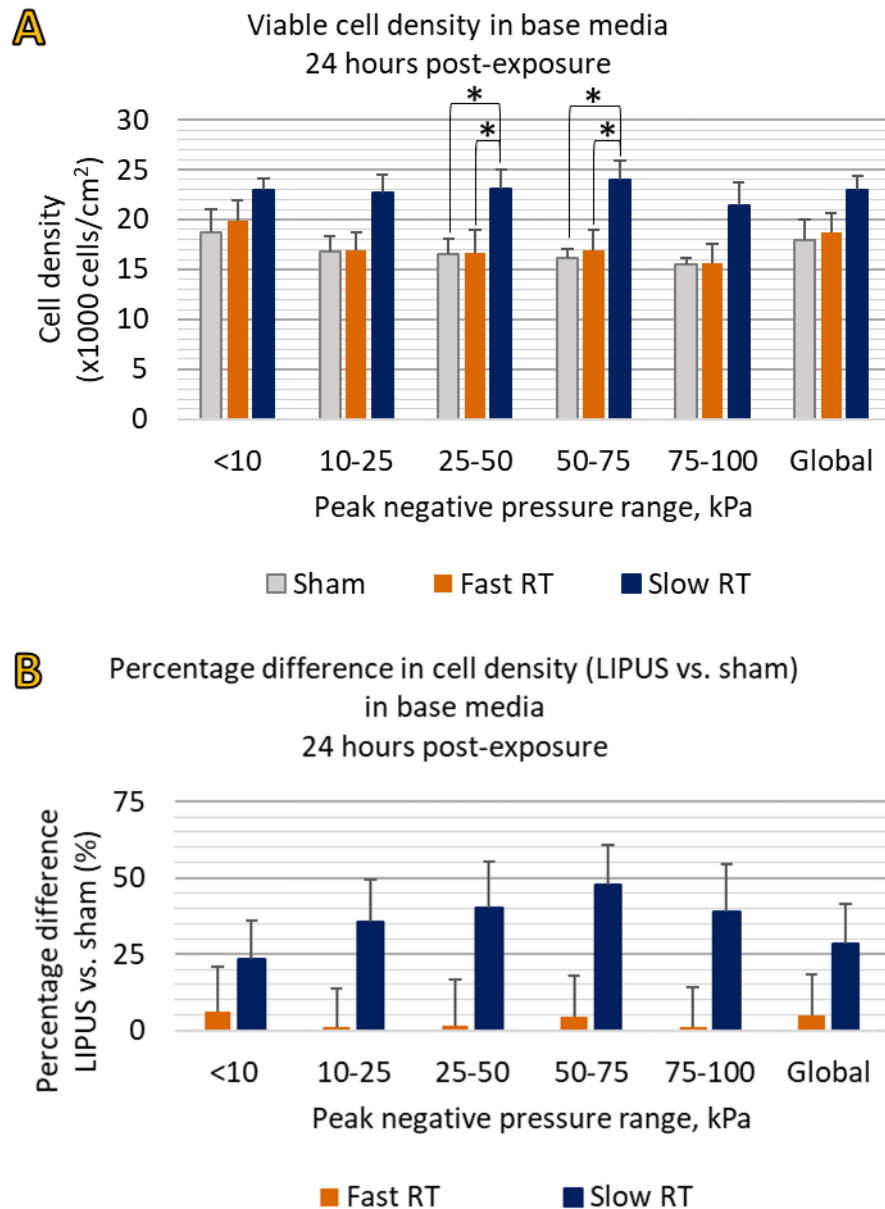
Figure 5.8: Viable cell densities in base media 24 hours post-exposure to sham, Fast RT or Slow RT LIPUS, computed across each pressure bin and entire growth surface (Global). A: Viable cell densities. B: Percentage difference in cell density, LIPUS vs. sham-treated controls. Error bars are SEM, n (sham) = 2; n (LIPUS) = 4. '' indicates significance versus sham controls (p < 0.05)*

Figure 5.8A presents cell densities and Figure 5.8B the percentage differences for each peak negative pressure bin. The average cell densities of samples treated with Fast RT LIPUS are within 6 % of those of the sham-treated controls, indicating Fast RT LIPUS has no significant effect on proliferation.

The viable cell densities of samples treated with slow RT LIPUS are 23 % to 48 % higher than controls. Those in the 25–50 kPa and 50–75 kPa bins are significantly higher than both controls and samples treated with Fast RT LIPUS (Figure 5.8A). The 10-25 kPa bin and global results are also very close to achieving significance ($p = 0.054$). This increased proliferation occurs across the entire growth surface, with optimum p_- range of 50–75 kPa.

Slow RT LIPUS therefore up-regulates proliferation in the cell population as a whole, suggesting the cells are responding to a global stimulating factor, such as vibration of the membrane, rather than local pressure amplitudes. The optimal pressure bin could correspond to the optimal vibration displacement experienced by the cells. This is discussed further in Chapter 6.

Figure 5.9 presents the cell density and percentage difference of LIPUS-treated samples versus sham-treated controls incubated for 48 hours post-exposure in base media. All the LIPUS-treated samples exhibit reduced cell densities compared to those of the sham-treated controls. The most pronounced drop is 20 % in the 75–100 kPa pressure bin of the samples exposed to Fast RT LIPUS, which is statistically significant compared to sham-treated controls ($p < 0.05$). The results suggest exposure to Fast RT LIPUS has a detrimental effect on proliferation after 48 hours in base media.

The cell densities of samples treated with Slow RT LIPUS are also less than those of the sham-treated controls. The drop is not as pronounced as samples treated with Fast RT LIPUS, with a worst case of 10%, and is not statistically significant. This result contrasts with the significant rise seen in Slow RT LIPUS cell densities at 24 hours, and suggests that any up-regulation of proliferation is temporary. The effect occurs throughout the growth surface, indicating the effect may be more dependent on a global stimulus rather than local pressure. This is discussed further in Chapter 6.
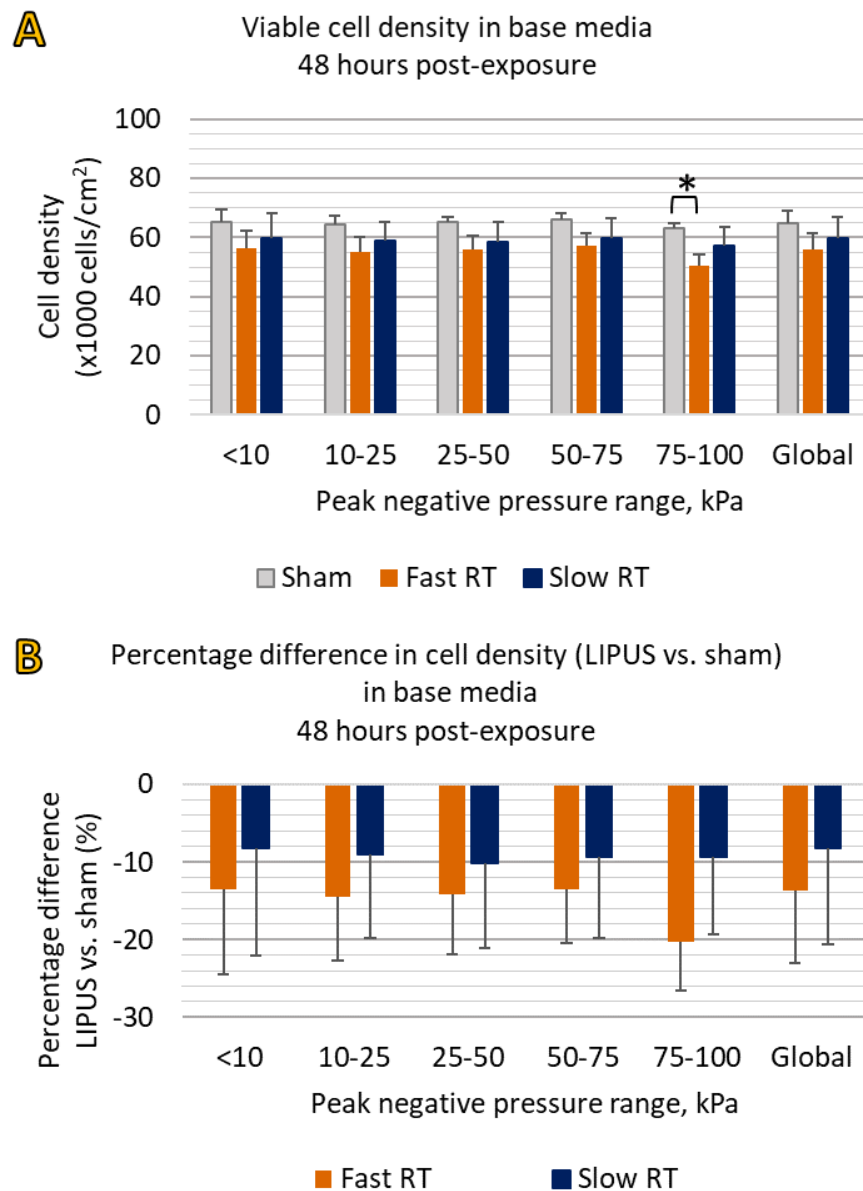
*Figure 5.9: Viable cell densities in base media, 48 hours post-exposure
to sham, Fast RT or Slow RT LIPUS, across each pressure bin and Global growth surface.
A: Viable cell densities. B: Percentage difference in cell density LIPUS vs. sham-treated
controls. Error bars are SEM, n (sham) = 3; n (LIPUS) = 4. '*' indicates significance
versus sham-treated controls (p < 0.05)*

5.3.2.2 Proliferation in Osteogenic Media (Trial B)

Figure 5.10 presents the cell densities and percentage difference results for samples treated
with sham, Fast RT or Slow RT LIPUS and incubated for 24 hours in osteogenic media.
All average cell densities of LIPUS-treated samples show a modest increase compared to
those of the sham-treated controls, up to a maximum of +10 % in the Fast RT group (in the
25-50 kPa and 75-100 kPa bins) and up to 9 % in the Slow RT group (in the 10-25 kPa
bin). The small increases are not statistically significant (p < 0.05), suggesting proliferation

is not up-regulated by LIPUS in osteogenic media, though further repeats are required to overcome the relatively high cell count variance and verify this finding.
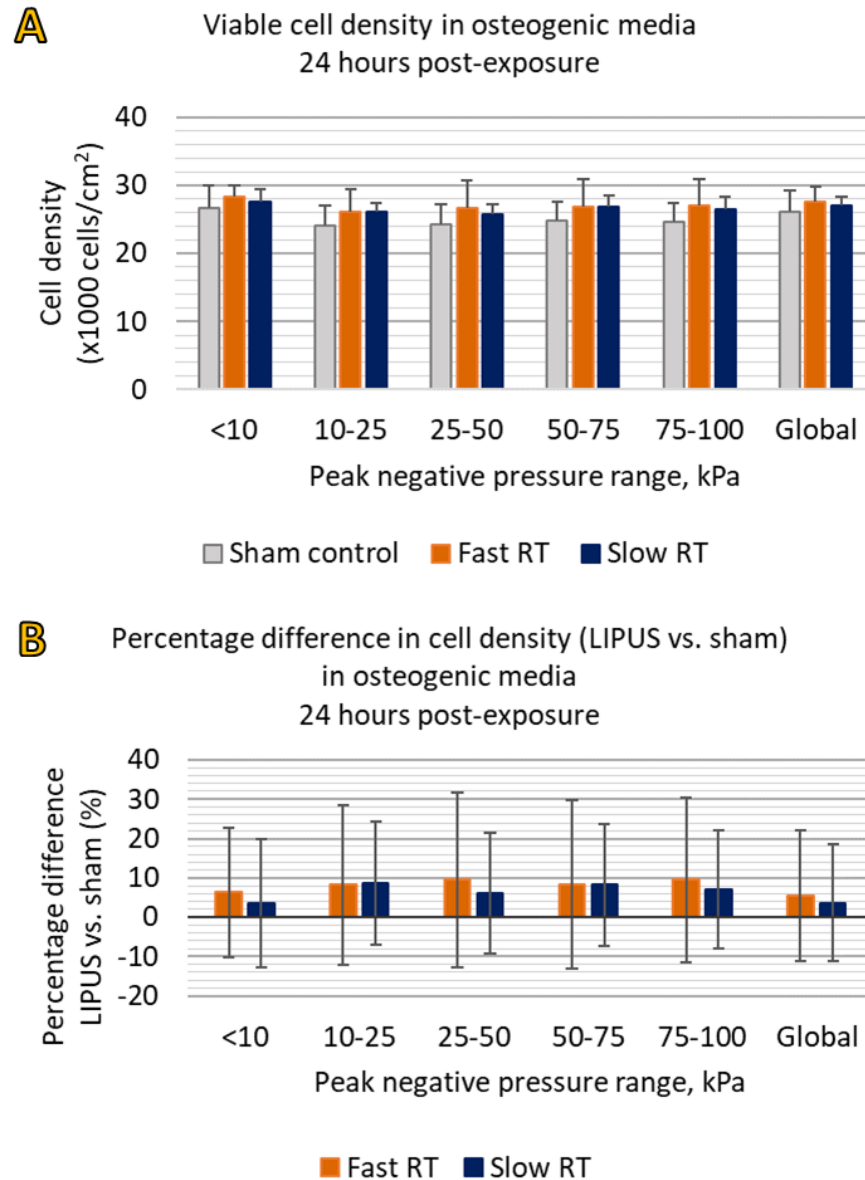
Figure 5.10: Viable cell densities in osteogenic media 24 hours post-exposure to sham, Fast RT or Slow RT LIPUS, across each pressure bin and Global growth surface. A: Viable cell densities. B: Percentage difference in cell density LIPUS vs. sham-treated controls. Error bars are SEM, n (sham) = 5; n (LIPUS) = 4.

This contrasts with the 24-hour post-exposure results in base media, where proliferation of Slow RT LIPUS samples is up-regulated. The Global base media and osteogenic media results are compared directly in 5.3.2.3 and discussed further in Chapter 6.

Figure 5.11 presents the cell density and percentage difference results for samples treated with sham, Fast RT or Slow RT LIPUS and incubated for 48 hours in osteogenic media.
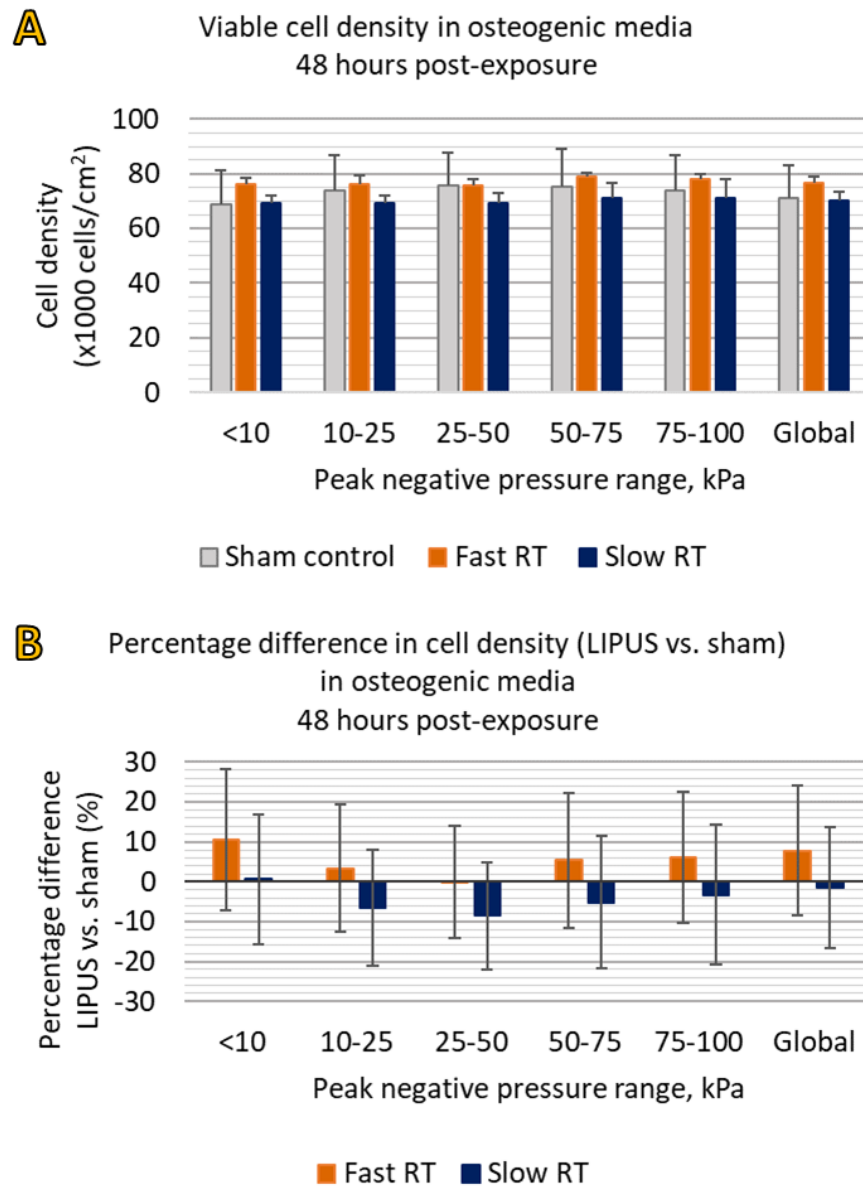
Figure 5.11: Viable cell densities in osteogenic media, 48 hours post-exposure to sham, Fast RT or Slow RT LIPUS, across each pressure bin and Global growth surface. A: Viable cell densities. B: Percentage difference in cell density LIPUS vs. sham-treated controls. Error bars are SEM, n (sham) = 3; n (LIPUS) = 4.

48 hours post-exposure, the cell density in Fast RT LIPUS-treated groups is overall slightly larger than those of sham-treated controls, with percentage differences up to +11 % in the 10-25 kPa pressure bin, and a global rise of 8 %. The cell density of the Slow RT LIPUS-treated group is generally slightly lower than controls, with percentage differences down to -8.5 % in the 25-50 kPa bin, and -1 % globally. ranging from increases by 2 % to 11 % (Figure 5.11B). These results are not statistically significant, partly due to the high

variance in the sham-treated group. The results suggest that the rate of proliferation of MC3T3-E1 cells incubated in osteogenic media is not affected by a single exposure to LIPUS fields with $\hat{p}_-$ up to 100 kPa.

5.3.2.3 Comparison of Global Cell Densities

Global cell densities are plotted in Figure 5.12 to assess and compare the effect of growth media and LIPUS exposure conditions on proliferation. Figure 5.12A presents the global cell densities and Figure 5.12B the percentage differences in cell density of LIPUS-treated samples compared to those of sham-treated controls.
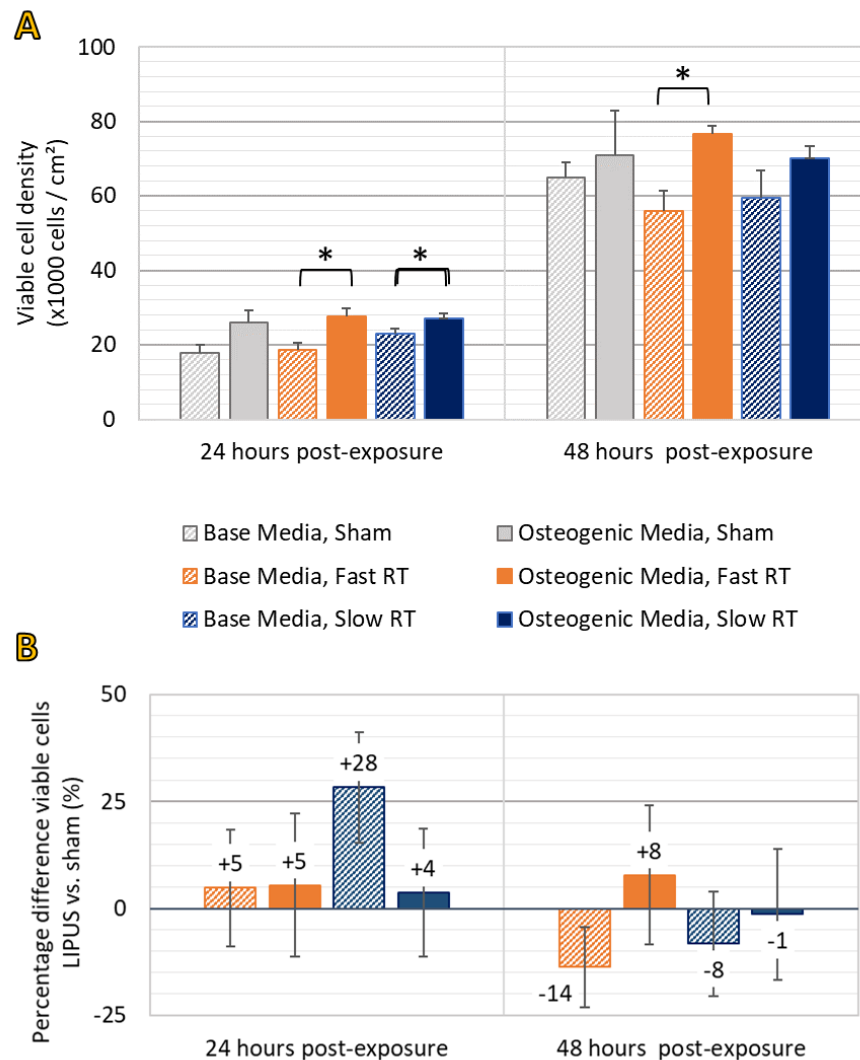
Figure 5.12: Comparison of Global cell densities in base and osteogenic media, 24 hours and 48 hours post-exposure to sham, Fast RT or Slow RT LIPUS. A: Viable cell densities. B: Percentage difference LIPUS vs. Sham Controls. Error bars are SEM, n (LIPUS) = 4; n (base media, sham, 24h) = 2; n (base + osteogenic media, sham, 48h) = 3; n (osteogenic media, sham, 24h) = 5. '*' indicates significance (p ≤ 0.05).

At 24 hours post-exposure the average cell densities in osteogenic media are higher than those in base media, by up to 47 % in the Fast RT group. This increase is statistically significant in the LIPUS-treated groups (p < 0.05). The average cell density of the sham controls increases by 46 % but does not achieve significance due to higher standard deviation in the osteogenic media sham group (not reflected in the SEM error bar in the chart because the number of replicates was higher in this group, n = 5). These results indicate proliferation is up-regulated by osteogenic media, which is as expected from the literature [172] and discussed in Chapter 3.

48 hours post-exposure, the LIPUS-treated groups in osteogenic media again have higher cell densities, up to 37% higher in the Fast RT group. The sham controls in osteogenic media have average cell density 9% higher, though this is likely affected by the high variance in the osteogenic media sham.

Examining the percentage differences of cell densities in LIPUS-treated groups compared to sham controls in Figure 5.12B, Fast RT LIPUS has no significant effect on cell densities at 24 hours post-exposure, with only +5 % difference compared to controls in both growth media types. The Slow RT LIPUS group at 24 hours post-exposure has cell density 28 % higher than controls in base media, but in osteogenic media only a 4 % rise is seen, similar to the Fast RT groups. It could be that the introduction of the osteogenic media suppresses the cellular response to Slow RT LIPUS. With sample sizes so low, repeats are required to establish if these results can be replicated. The possible mechanisms for this result are discussed further in Chapter 6.

At 48 hours post-exposure, proliferation in base media is down-regulated compared to sham-treated controls by up to 14 % in the Fast RT LIPUS-treated group. By contrast, LIPUS appears to up-regulate proliferation in osteogenic media, with Fast RT LIPUS resulting in the higher stimulus of +20 % compared to controls. Again, these global increases are not statistically significant and the trends require verification with further repeats. A study conducted over a longer period, with multiple daily exposures, may also amplify any short-term or minor stimulatory effects of LIPUS exposure. The proliferation results are further discussed in Chapter 6 and compared with previous findings from the literature. The next section presents the results for the expression of PGE2 in the media.

5.3.3 PGE2 Expression

PGE2 protein concentration measured in the media 24 hours and 48 hours post-exposure to Fast RT LIPUS, Slow RT LIPUS or sham treatment are presented in the following sections. The results are presented as measured PGE2 concentrations and in percentage difference in measured PGE2 of LIPUS-treated groups compared to sham-treated controls. The PGE2 concentrations are not corrected for the number of cells exposed as in the Frequency Study, because the improved seeding techniques and use of replicates means the number of cells exposed is effectively the same throughout the Rise Time Study.

The Trial A PGE2 results are affected by degradation of PGE2 in the growth media due to prolonged storage, as described in the COVID impact statement at the beginning of this thesis. For the purposes of this study, it is assumed that percentage differences with respect to controls are comparable.

5.3.3.1 PGE2 Expression in Base Media (Trial A)

Figure 5.13 presents the results of Trial A PGE2 protein concentrations in base media. Figure 5.13A shows the measured PGE2 concentrations and Figure 5.13B the percentage difference in LIPUS-treated groups compared with sham-treated controls.

Examining the PGE2 concentrations of samples treated with Fast RT LIPUS, the PGE2 concentration increases by 25 % at 24 hours post-exposure as compared to sham controls. This increase is not statistically significant ($p < 0.05$). At 48 hours post-exposure the PGE2 concentration in the Fast RT group is 7 % below sham-treated controls. The apparent up-regulation at 24 hours and drop to normal levels at 48 hours matches the expected trends, observed in previous studies by Doan et al. and Tang et al. [30, 38].

Slow RT LIPUS has no effect on PGE2 expression at 24 hours post-exposure, with only 1% difference compared to sham-treated controls. 48 hours post-exposure, PGE2 levels show a modest increase of 9 % compared to controls, again not significant. The increase may be due to the increase in number of cells seen at 24 hours post-exposure (see Figure 5.8), rather than an up-regulation of PGE2.
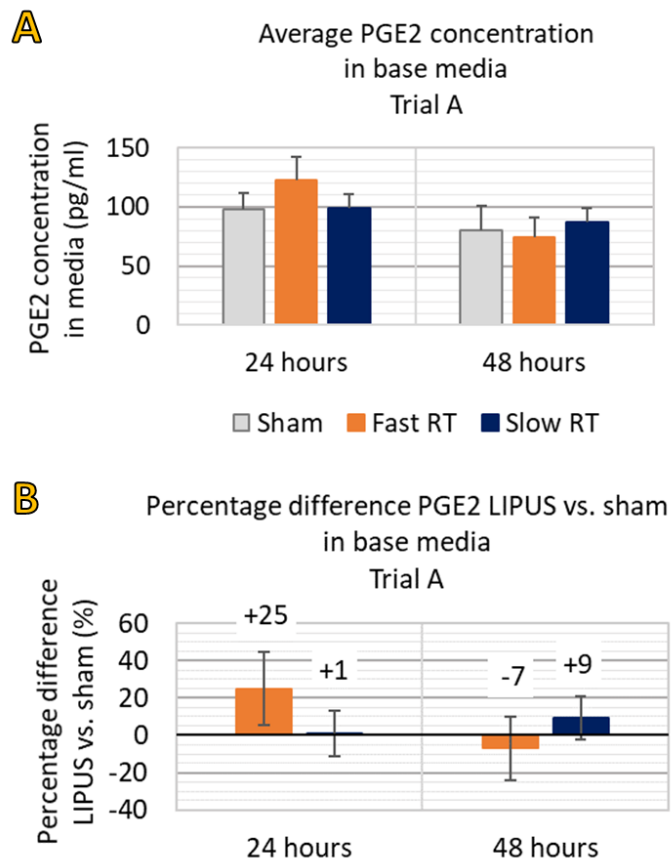
Figure 5.13: PGE2 protein concentrations in base media (Trial A),
24 hours and 48 hours post-exposure to sham, Fast RT or Slow RT LIPUS. A: Average
measured PGE2 concentration. B: percentage difference in PGE2, LIPUS versus sham.
Error bars are SEM, n (sham, 24 hours) = 2, n (sham, 48 hours) = 3, n (LIPUS) = 4.

5.3.3.2 PGE2 Expression in Osteogenic Media (Trial B and C)

Figure 5.14A shows the PGE2 protein concentrations in osteogenic media and Figure 5.14B presents the percentage difference in LIPUS-treated samples compared with sham-treated controls in Trials B and C. Trial C PGE2 results are at 24 hours post-exposure only because samples were incubated for either 24 hours or 6 days in that study, and previous results in the literature suggest any up-regulation of PGE2 is not expected to be present 6 days after LIPUS stimulus.
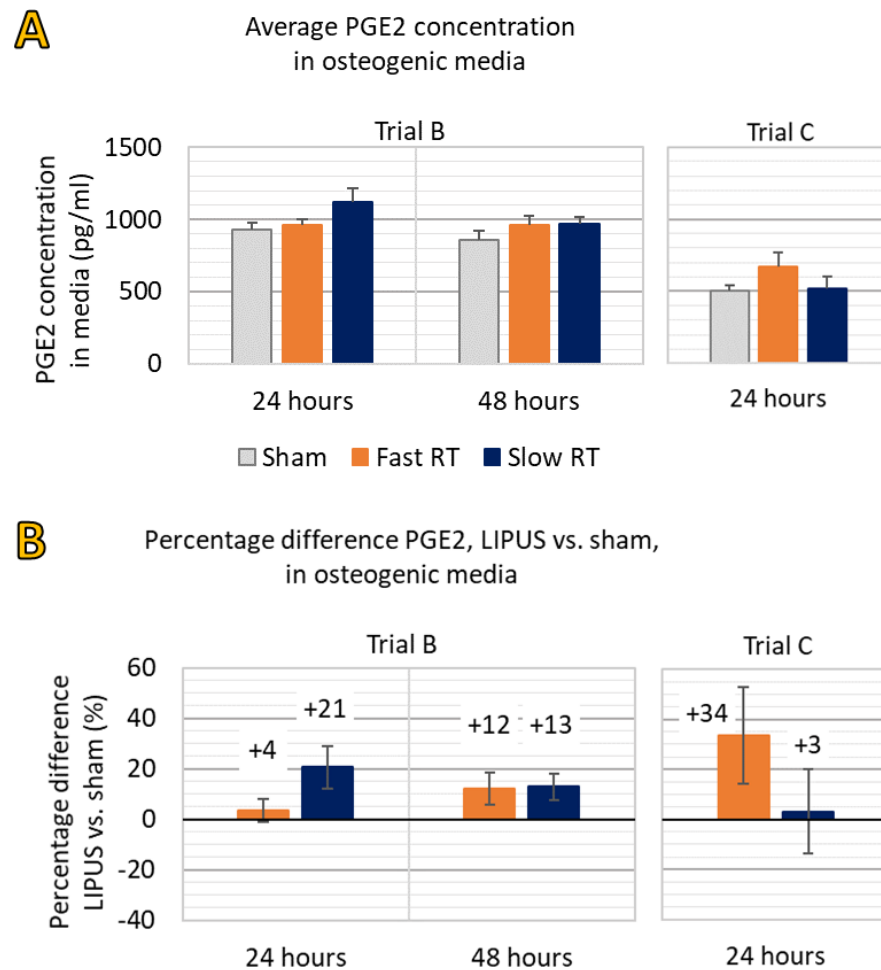
Figure 5.14: PGE2 protein concentration in osteogenic media, 24 hours and 48 hours post-exposure to sham, Fast RT or Slow RT LIPUS. A: Average measured PGE2 concentration. B: percentage difference, LIPUS versus sham. Error bars are SEM, n (Trial B, 24-hour sham) = 5, n (Trial B, all other conditions + Trial C, sham) = 4, n (Trial C, Fast RT) = 3, n (Trial C, Slow RT) = 2.

After 24 hours the Slow RT group in Trial B has an average PGE2 concentration 21 % higher than the control group. The result is not statistically significant (p < 0.05), though it is close, with a p-value of 0.06. The Fast RT group in Trial B is effectively the same as controls, with only 4 % difference in PGE2 compared to that of the sham-treated control group. This trend is reversed in the Trial C PGE2 results at 24 hours, where the Fast RT group has PGE2 concentration 34 % above the control (again not significant with p-value of 0.08) and the Slow RT group has effectively no change with 3 % difference. This reversal of trends in samples that have received the same treatment, coupled with the lack of statistical significance, suggests that both the Fast RT and Slow RT LIPUS fields have no effect on PGE2 expression in MC3T3-E1 preosteoblasts in osteogenic media.

In Trial B at 48 hours post-exposure the LIPUS-treated sample sets have a modest gain of 12 % to 13 % in PGE2 concentration with respect to controls. Overall, results suggest LIPUS exposure makes no significant difference to PGE2 expression in MC3T3-E1 preosteoblasts. The results and their implications are discussed further in Chapter 6.

5.3.4 Genetic Markers for Mechanotransduction and Mineralisation (Trial C)

This section presents the results of an investigation of expression of genetic markers associated with mechanotransduction and mineralisation in response to LIPUS at 24 hours and 8 days post-exposure. Detailed descriptions of the methods used in this trial are given in Chapters 3 and 4. Section 4.5 details the LIPUS exposure protocols and Section 3.1.3 describes the RT-PCR analysis. The genetic markers are described in Section 2.4 and briefly described below. The expression over time of the markers associated with mineralisation in preosteoblasts and osteoblasts are presented in Table 3.1 of Section 3.1.1.1 along with the expected timescales of expression in the MC3T3-E1 cell line. The markers and how they indicate a potential healing response are briefly described below:

- Integrin β5 mRNA, associated with exercise-induced mechanotransduction in bone (through up-regulation of the hormone irisin in muscles rather than direct stimulus of bone cells – see the covid impact statement and Section 2.4 for more detail) [165].

- Expression of Cyclo-oxygenase 2 (cox2) mRNA. COX-2 is a protein that is a direct pre-requisite of PGE2 and is expected to correlate with PGE2 concentration. PGE2 is up-regulated in the early inflammatory stage of bone healing and is expected to be stimulated within 24 hours of LIPUS exposure.

- The early mineralisation marker Runt-related Transcription Factor 2 (runx2) regulates osteogenic differentiation of MSCs and preosteoblasts. Increased expression of runx2 within the first 1 to 6 days following LIPUS exposure would expect to induce increased mineralisation and preosteoblast differentiation to osteoblasts further downstream.

- Collagen Type 1 (col1) is expected to be expressed early in the healing process as this protein is laid down to produce the initial ECM that would constitute the soft

callus in secondary bone healing. Collagen Type 1 was expected to be expressed in high levels from 1 to 12 days after LIPUS exposure, and less so from 9 days on as osteoblasts begin laying down the mineralised bone structure that would make up the hard callus.

- Mineralisation protein markers Osteocalcin (ocn) and Osteopontin (opn) are expressed and laid down later in the mineralisation process. Expression of these proteins varies throughout the healing process but are generally significantly up-regulated during later maturation and mineralisation of osteoblasts. Reported expression varies but ocn is expected to begin increasing from 4 days post-exposure, and opn from 9 days post-exposure.

All results are presented as ratios to the housekeeping gene Beta Actin (ACTB) and normalised to sham-treated controls at 24 hours post-exposure to assess expression due to LIPUS exposure conditions and elapsed time after exposure. Section 5.3.4.1 presents the results associated with mechanotransduction pathways (Integrin β5 and cox2) and Section 5.3.4.2 presents the results for markers associated with osteogenesis, bone healing and mineralisation (runx2, col1, ocn and opn).

5.3.4.1 Mechanotransduction Markers Integrin β5 and COX-2 mRNA

Figure 5.15 shows the RT-PCR results for expression of COX-2 mRNA (cox2) at 24 hours and 6 days post-exposure. Expression of cox2 is up-regulated 24 hours post-exposure to LIPUS fields, significantly in the case of the Slow RT group, with expression 60 % higher than sham-treated controls. The cox2 expression of the Fast RT group shows a greater increase with respect to sham-treated controls (+80 %), but expression is dominated by one data point and therefore significance could not be established. The peak in cox2 up-regulation in the Fast RT group corresponds to the peak in PGE2 expression observed in the same group (recall Figure 5.14). However, the peak in cox2 expression in the Slow RT group has no corresponding rise in PGE2 concentration.
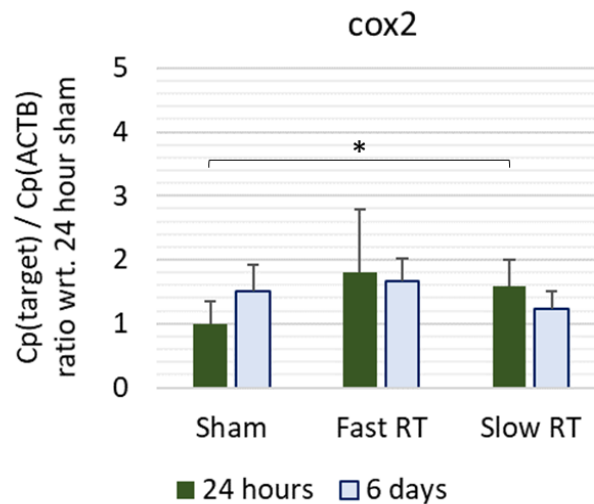
*Figure 5.15: cox2 expression 24 hours and 6 days post-exposure
to Sham, Fast RT or Slow RT LIPUS. Results are normalised to ACTB and 24-hour sham-
treated controls. Error bars indicate SEM, n (24 hours) = 3, n (6 days) = 4. '*' denotes
significance (p < 0.05)*

6 days post-exposure, cox2 expression reduces in LIPUS-treated groups and increases in the sham-treated group, with the Fast RT LIPUS group 10 % higher than controls and the Slow RT group 20 % lower. Overall, the results suggest LIPUS exposure initiates transient up-regulation of COX-2 mRNA in the MC3T3-E1 cells 24 hours post-exposure, which then drops back toward normal levels 6 days post-exposure. This is in line with previous studies examining COX-2 mRNA and PGE2 protein expression [40, 41]. More repeats are required to determine if this result is repeatable and establish significance with more confidence. Adding an assessment of COX-2 protein expression would provide further supporting evidence of COX-2 expression.

Figure 5.16 shows the expression of Integrin β5 mRNA (itgb5) normalised to the 24-hour sham-treated control group. At 24 hours post-exposure, expression of itgb5 is less in LIPUS treated groups compared to controls, with a drop of 14 % in the Fast RT group and 19 % in the Slow RT group. These drops are not statistically significant.

At 6 days post-exposure, expression is up-regulated in all groups compared to expression at 24 hours. This up-regulation is significant in the LIPUS-treated groups. Significance was not achieved in the sham group due to high variance of the 6 days post-exposure results. Integrins are involved in cell attachment as well as mechanotransduction, so the overall increase in expression may be due to improved cell adhesion to the growth surface over time. Expression of itgb5 in LIPUS-treated groups is not significantly different to the sham

results at either time period, therefore LIPUS exposure has no significant effect on expression of Integrin β5.
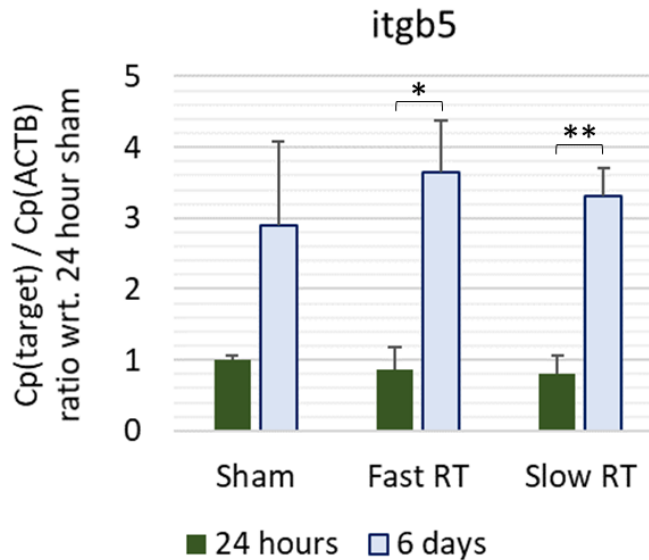
Figure 5.16: Integrin β5 mRNA (itgb5) COX-2 mRNA (cox2) expression 24 hours and 6 days post-exposure to Sham, Fast RT or Slow RT LIPUS. Results are normalised to sham-treated controls, 24 hours post-exposure. Error bars indicate SEM, n (24 hours) = 3, n (6 days) = 4. Significance is denoted by '' (p < 0.05) or '**' (p < 0.01)*

5.3.4.2 Mineralisation Markers

Figure 5.17 presents the gene expression of the mineralisation marker Collagen Type 1 (col1) at 24 hours and 6 days post-exposure to Sham, Fast RT or Slow RT LIPUS. Expression of Collagen Type 1 is similar at 24 hours post-exposure in all LIPUS exposure conditions. The col1 expression of the Fast RT group is 1 % lower than in the sham group, and the Slow RT group is 10 % greater. No significant differences in LIPUS-treated versus Sham-treated groups suggest LIPUS has no short-term effects on col1 expression.

At 6 days post-exposure, col1 expression increases significantly in the LIPUS-treated groups but not in the sham group, which has a greater increase but high variance in results. The fast RT LIPUS group has col1 expression 20% lower than sham and the Slow RT group is 50 % lower. The results are not statistically significant compared to controls, again due to the high variance, but col1 expression in the Slow RT group is significantly lower than found in the Fast RT group. Therefore, exposure to LIPUS either has no effect on, or reduces, Collagen Type I expression in MC3T3-E1 preosteoblasts. These results are discussed further in Chapter 6.
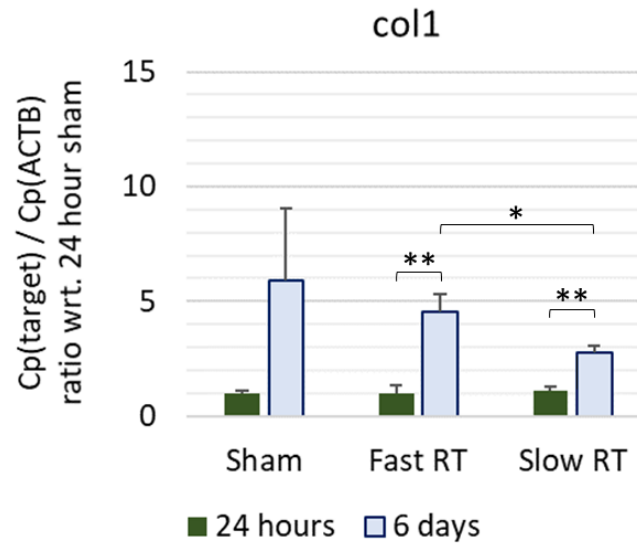
Figure 5.17: Collagen Type I mRNA (col1) expression 24 hours and 6 days post-exposure to Sham, Fast RT or Slow RT LIPUS. All results are normalised to ACTB and 24-hour sham-treated controls (and so will include up-regulation due to increased incubation period in osteogenic media). Error bars indicate SEM, n (24 hours) = 3, n (6 days) = 4. Significance is denoted by '' (p < 0.05) or '**' (p < 0.01)*

Osteocalcin (ocn) expression, shown in Figure 5.18, has a similar pattern to col1 expression at 6 days post-exposure, with highest expression in the sham-treated group, next highest the Fast RT group then lowest the Slow RT group. Expression at 6 days post-exposure is 67 to 129 times higher than expression at 24 hours post-exposure and all achieve significance compared to the 24-hour results (p < 0.05). No statistical significance was found between any of the 6-day post-exposure LIPUS-treated samples compared with the sham controls.

With reference to Table 3.3, ocn expression increases in the early stages of differentiation to the osteoblast phenotype. The ocn expression suggests LIPUS exposure either has no effect on, or reduces, ocn up-regulation compared to sham controls.

The ocn expressions of LIPUS treated groups relative to sham-treated groups is consistent at 24 hours and 6 days post-exposure, with ocn expression in the Fast RT LIPUS group 23 % to 30 % below that of controls, and expression in the Slow RT LIPUS group remaining at 48 % below. This suggests the effects of the LIPUS stimulus remain regardless of elapsed time post-exposure.
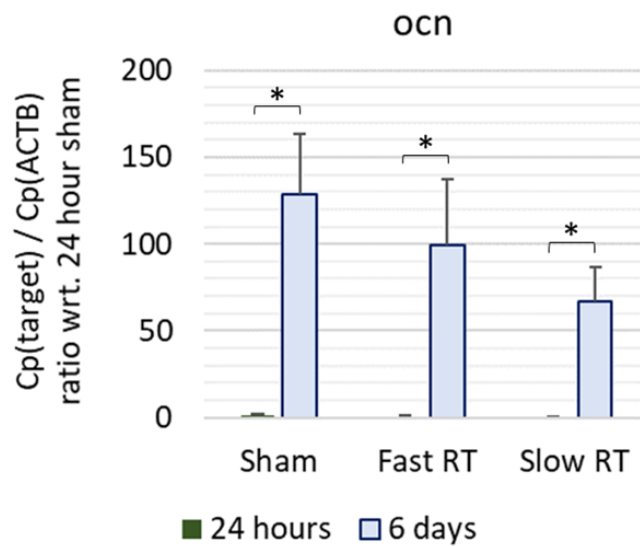
Figure 5.18: Osteocalcin mRNA (ocn) expression 24 hours and 6 days post-exposure to Sham, Fast RT or Slow RT LIPUS. Results are normalised to ACTB and 24-hour sham-treated controls (and so will include up-regulation due to increased incubation period in osteogenic media). Error bars indicate SEM, n (24 hours) = 3, n (6 days) = 4. Significance is denoted by '' (p < 0.05)*

Osteopontin (opn) expression is presented in Figure 5.19. Expression of opn is also up-regulated at 6 days compared to 24 hours post-exposure, but only significantly so in the Sham-treated controls.
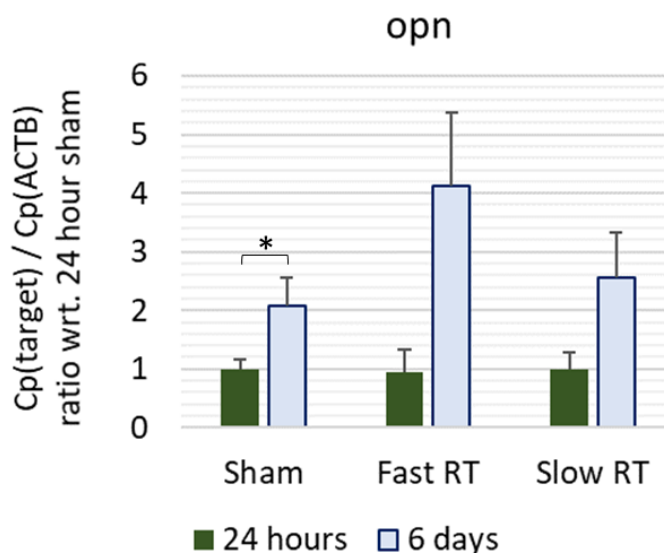
Figure 5.19: Osteopontin RNA (opn) expression 24 hours and 6 days post-exposure to Sham, Fast RT or Slow RT LIPUS. Results are normalised to ACTB and 24-hour sham-treated controls (and so will include up-regulation due to increased incubation period in osteogenic media). Error bars indicate SEM, n (24 hours & 6 days Fast RT) = 3, n (6 days sham and Slow RT) = 4. Significance denoted by '' (p < 0.05)*

Expression of opn is similar to controls at 24 hours post-exposure and is up-regulated 6 days post-exposure in both LIPUS-treated groups. Significance of up-regulation cannot be established but the Fast RT LIPUS result is very close (p = 0.07), and the opn expression is 2 times higher than that of the sham control group. The increase is less marked in the Slow RT group, which is 22 % higher than controls.

Expression of Runt-related Transcription Factor 2 (runx2), is presented in Figure 5.20. Expression of runx2 is similar in all conditions at 24 hours post-exposure, with no significant differences between LIPUS conditions. At 6 days post-exposure expression is up-regulated significantly compared to 24 hours post-exposure in all LIPUS conditions, with expression increasing 7-fold in sham-treated controls and Slow RT groups, and 14-fold in the Fast RT group.

Expression in the Fast RT group at 6 days post-exposure is 2 times that of the control group and this achieves statistical significance (p < 0.05). The Slow RT LIPUS group is not up-regulated, showing only an 11 % increase compared to controls. The results suggest exposure to Fast RT LIPUS significantly increases runx2 expression in MC3T3-E1 preosteoblasts. This result is discussed further in Chapter 6.
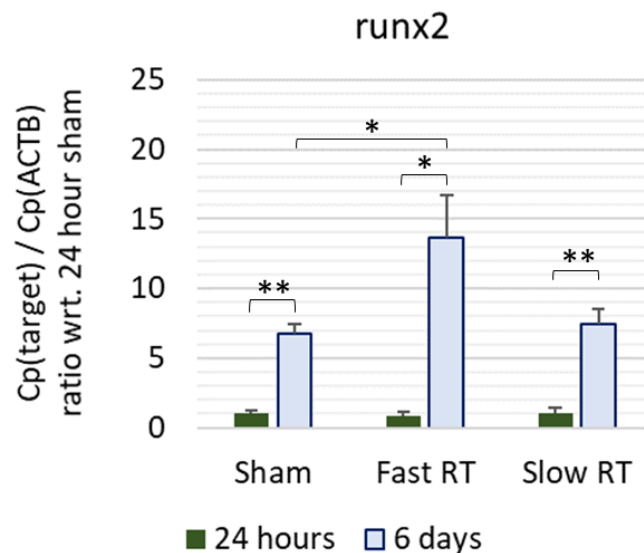
Figure 5.20: Runt-related Transcription Factor 2 RNA (runx2) expression 24 hours and 6 days post-exposure to Sham, Fast RT or Slow RT LIPUS. Results are normalised to ACTB and 24-hour sham-treated controls (and so will include up-regulation due to increased incubation period in osteogenic media). Error bars indicate SEM, n (24 hours) = 3, n (6 days) = 4. Significance denoted by '' (p < 0.05) and '**' (p < 0.01)*

Figure 5.21 summarises and compares the relative expressions of mineralisation markers normalised to sham controls at both time periods post-exposure, to remove the dependency on elapsed time and highlight the effects of LIPUS exposure.
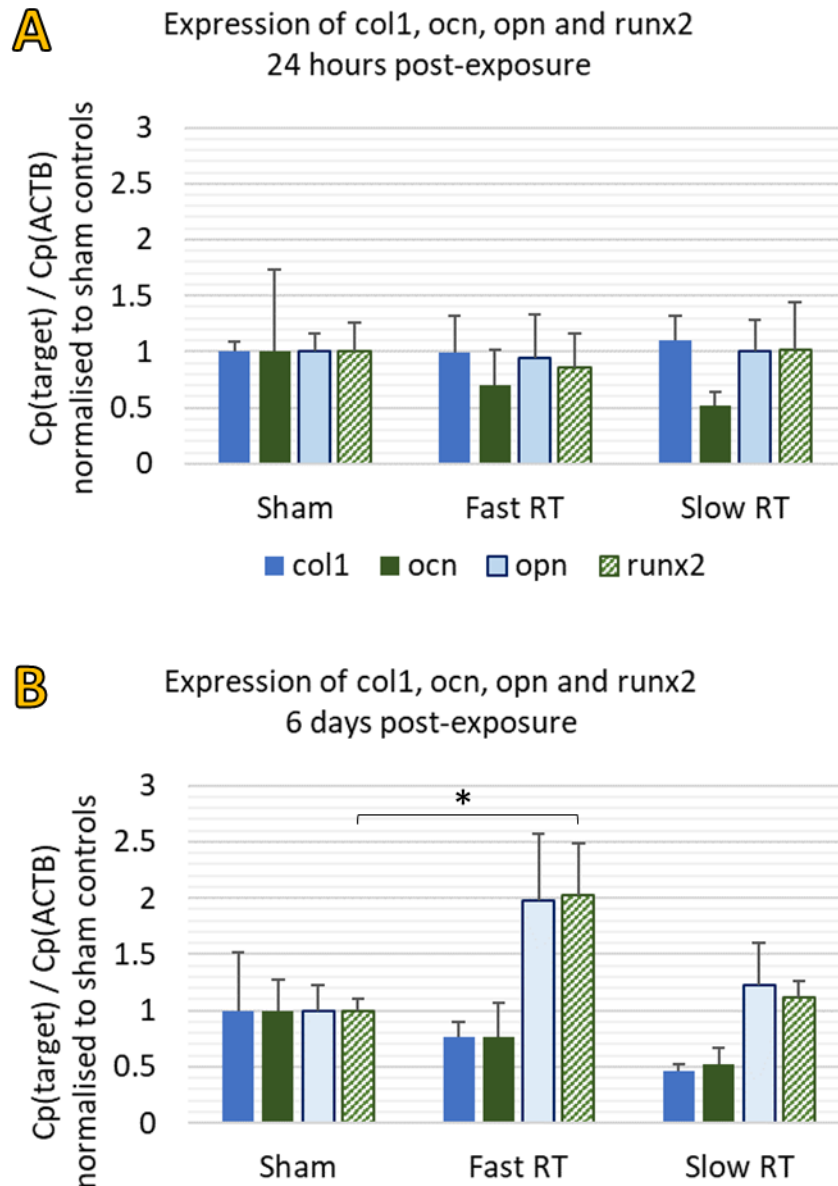
Figure 5.21: Expression of col1, ocn, opn and runx2
at A: 24 hours post-exposure relative to 24-hour sham and B: 6 days post-exposure
relative to 6-day sham. Error bars indicate SEM, n (24 hours) = 3, n (48 hours) = 4. ''*
denotes significance with respect to controls (p < 0.05).

Expression of runx2 correlates with expression of opn at both 24 hours and 6 days post-exposure, exhibiting no significant change at 24 hours and a marked increase at 6 days, though only the runx2 increase in expression is statistically significant. Col1 expression also shows no change at 24 hours in all LIPUS conditions with respect to controls, and at 6

days the col1 of Fast RT LIPUS is less than controls and that of the Slow RT LIPUS group is lower still. This trend is seen in the expression of ocn at both 24 hours and 6 days post-exposure. Overall, the results suggest that Fast RT LIPUS up-regulates opn and runx2 at 6 days post-exposure, significantly so in the case of runx2, whereas col1 and ocn expressions are reduced. Slow RT treatment results in a small increase in opn and runx2, which is not statistically significant.

The morphology of samples indicate differentiation towards mature osteoblasts at day 6 post-exposure. Figure 5.22 shows phase contrast images of cells at 24 hours post-exposure (Figure 5.22A) and 6 days post-exposure (Figure 5.22B). Cell outlines show morphology is changing from elongated fusiform shape towards a more cuboidal shape characteristic of mature osteoblasts.
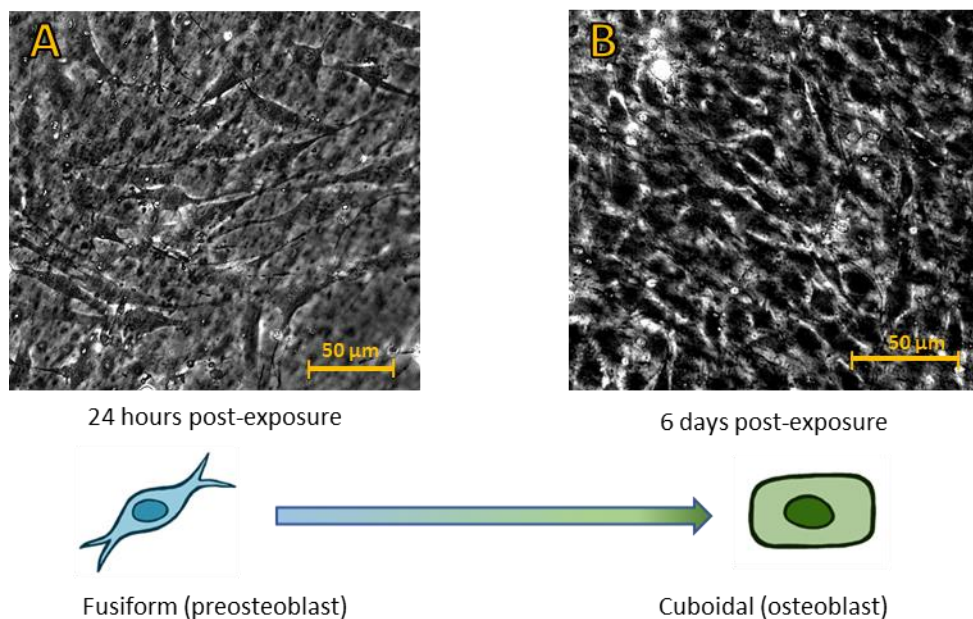
Figure 5.22 Phase contrast images of cells in sham-treated controls.
A: 24 hours post-exposure. Fusiform morphology. B: 6 days post-exposure. Cell shapes
are more cuboidal. Scales are approximate.

The indications in the morphology were reinforced when cells were detached with Trypsin after 6 days prior to the RNA extraction process. The cell / collagen layer appeared more opaque and thicker than those incubated for 24 hours, suggesting that some mineralisation had taken place. This could be verified in future by staining samples with Alizarin-red dye.

The full implications for the results observed in the Rise Time Study are discussed in Chapter 6. The next section moves on to the results of the 3D Scaffold Feasibility Study.

5.4 3D Scaffold Feasibility Study: A method allowing investigation of cellular responses to LIPUS in a 3D growth environment

This section describes the results of the 3D scaffold study, which assesses the feasibility of growing cells on 3D-printed scaffolds in an attempt to introduce a growth environment closer to *in vivo* conditions. The full methods are described in Section 4.6. Briefly, the method is a 3D version of the 2D scratch assay [207], which is used to test healing and cell migration *in vitro*. The seeding and cutting study (5.4.1) investigates if MC3T3-E1 preosteoblasts can be grown on the 3D scaffolds, survive a cut made in the scaffold using an ultrasonic cutting tool, and can proliferate and migrate into the cut site. The method is described in Section 4.6.1.

The seeding, cutting and LIPUS exposure study (5.4.2) performs the seeding and cutting, and exposes the samples to Sham and Fast RT LIPUS treatment within the biocells using the ultrasound exposure tank system. This study tests the hypothesis that LIPUS up-regulates cell migration, another healing marker found to be stimulated in the LIPUS literature [45]. The method is described in Section 4.6.2.

5.4.1 3D Scaffold Preliminary Study: Seeding, Cutting and Cell Migration

Figure 5.23 compares cut sites of scaffolds immediately after cutting (0h) and 24 hours after cutting (24h). The images show that at 0h no cells are present in the cut site, suggesting cell death and detachment in the immediate area. 24 hours after cutting, the presence of cells in the cut site indicates that neighbouring cells survive the cutting procedure and are able to proliferate and migrate into the cut site.

The migration of cells into the cut site 24 hours after cutting validates the cell seeding technique, seeding density, cell seeding attachment timing and fluorescent dye concentrations used in the study.
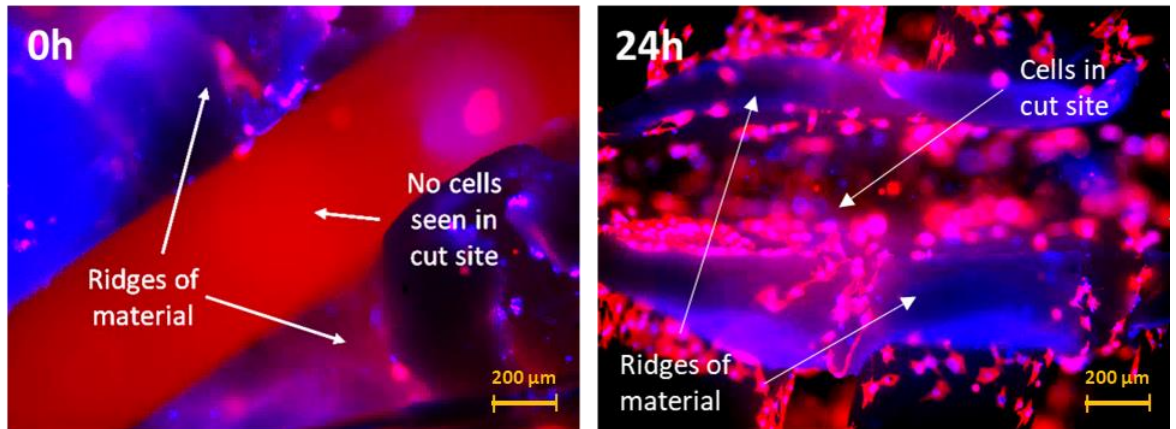
Figure 5.23: Cut site on 3D scaffolds 0h and 24h post-cut.
At 0h no cells were seen in cut site. 24 hours after, cells had migrated into the cut site,
despite the ridges at the sides. Scales are approximate.

5.4.2 3D Scaffold LIPUS Exposure Study

Figure 5.24 presents the fluorescent microscope images of the scaffold fixed and stained immediately after cutting. No intact cells are present in the cut site immediately after cutting (Figure 5.24A) and the adjacent areas show signs of cellular damage and detachment. Cells farthest from the cut site appear intact (Figure 5.24B).
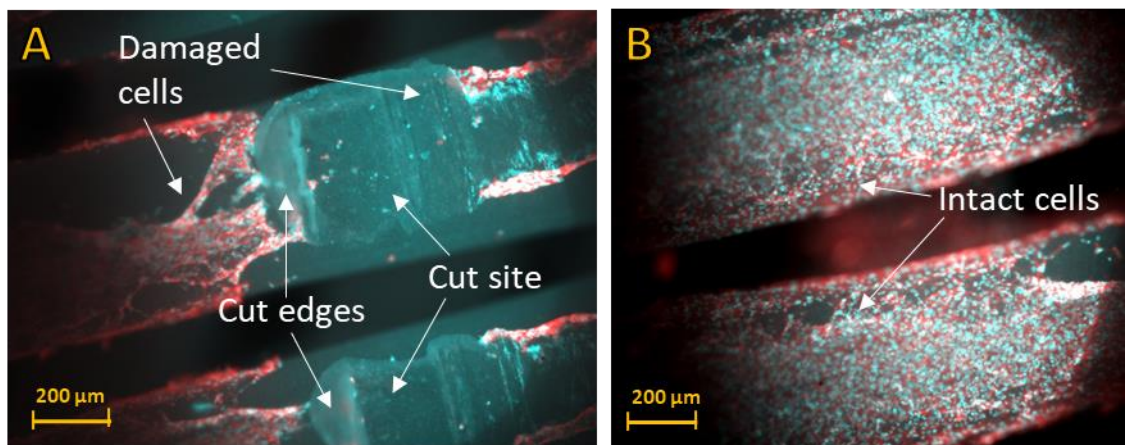
Figure 5.24: Sample stained immediately after cutting.
A: Cells around cut site show obvious signs of damage and detachment. B: Cells farthest
from cut site appear intact. Red staining is actin (cell membranes), Cyan indicates cell
nuclei. Scales are approximate.

Due to the difficulties with adhesives detailed in Section 4.6.2, only one sample could be exposed to LIPUS in the tank system. Figure 5.25A, B & C show fluorescent microscope images of the cut site in this sample at 12 hours, 18 hours and 24 hours post-exposure, live-stained with Hoechst dye. After 24 hours there is no change in number and positions of cells, indicating no proliferation or migration. Figure 5.25D shows the cells stained with

Hoechst and Propidium Iodide (PI), which stains the nuclei of dead cells. The PI staining confirms all cells in the 3D scaffold are dead. The cause of death cannot be ascertained but it is likely due to cavitation or localised heating during the cutting procedure. Adhesive toxicity could also be a factor. The adhesive used for the biocell featured in Figure 5.25 was Liquidskin, which is non-toxic *in vivo* but may be cytotoxic.

Although the initial testing of this method resulted in cell death, the method still shows promise for use in LIPUS investigations. Improvements and modifications required to make the method work are discussed further in Chapter 6.
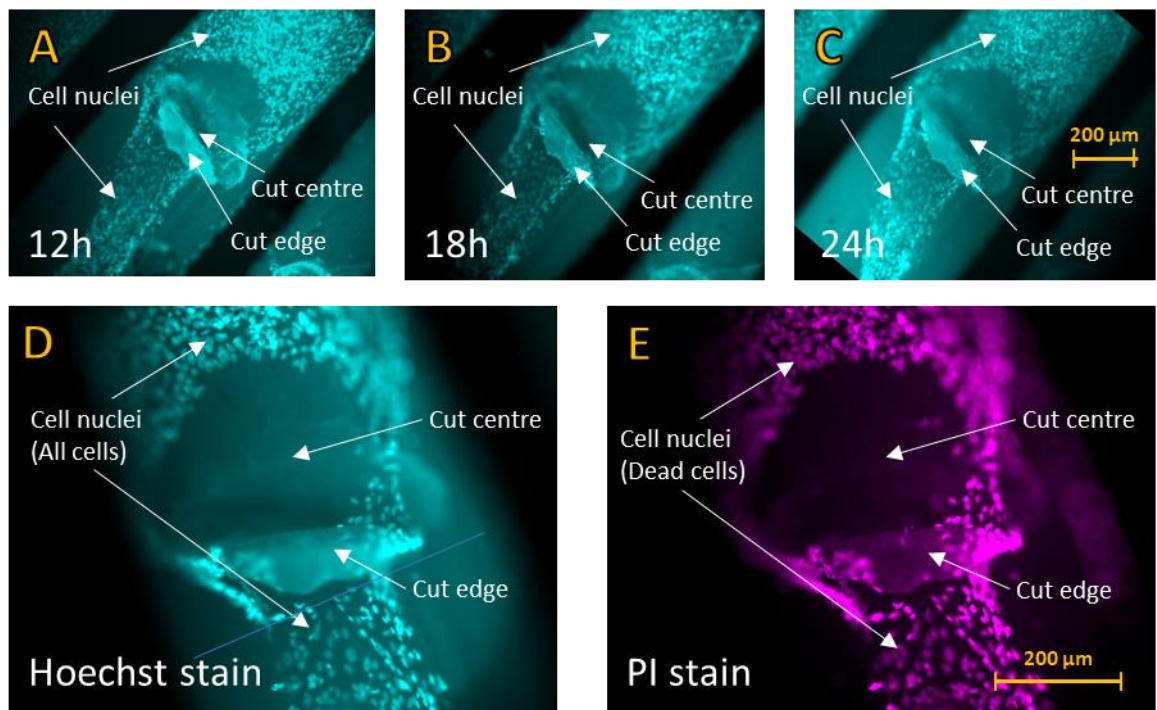
Figure 5.25: Microscope images of biocell sealed with Liquidskin.
A, B & C: cells stained with Hoechst and imaged 12 hours, 18 hours and 24 hours post-exposure respectively. No change observed in pattern of cell nuclei around cut site. D: Hoechst stain showing all cells and E: PI staining confirmed all nuclei stained indicating all cells were dead (as PI only stains cells with compromised membranes). Scales are approximate.

5.5 Chapter Summary and Contribution to the Field

The results of *in vitro* trials involving exposure of preosteoblasts to LIPUS were presented in this chapter. All trials were conducted in a controlled manner in the biocell, the custom culture vessel described in Section 4.1, which enables cells to be grown and exposed to controlled LIPUS fields in one culture vessel. Exposures took place in the ultrasound

exposure tank system described in Section 4.2. The result was a set of *in vitro* tests that assessed the cellular responses of MC3T3-E1 preosteoblasts with fully controlled and characterised LIPUS fields, allowing the effect of the ultrasound alone on cellular responses to be assessed, with secondary effects such as plate vibrations and heating minimised.

The Pressure Amplitude Study tested initial LIPUS exposure methods and compared cellular responses of LIPUS fields with maximum peak negative pressures ($\hat{p}_-$) up to 489 kPa. The results indicated that proliferation and PGE2 expression of MC3T3-E1 preosteoblasts may be up-regulated by LIPUS fields with $\hat{p}_-$ 105 kPa.

The Frequency Study further tested and informed the methods, and assessed proliferation and PGE2 expression in response to controlled exposure to LIPUS fields with frequency 1 MHz, $\hat{p}_-$ up to 203 kPa, and frequency 45 kHz, $\hat{p}_-$ up to 43 kPa. The results indicated that proliferation and PGE2 expression may be up-regulated by LIPUS fields at 1 MHz and $\hat{p}_-$ 100 kPa to 151 kPa. The 45 kHz results indicated that proliferation may be stimulated at $\hat{p}_-$ 43 kPa but PGE2 expression was not. The results of the Frequency Study led to the hypothesis that the rapid switch-on of the 1 MHz LIPUS pulse, and the corresponding rapid switch-on of the radiation force, was the main stimulus affecting cellular responses.

The Rise Time Study tested this hypothesis by exposing MC3T3-E1 preosteoblasts to Fast RT LIPUS (with rise time 1.4 µs), Slow RT LIPUS (with significantly longer rise time of 40.5 µs) and sham-treatment. The Fast RT pulse was predicted to stimulate the mechanotransduction pathways regulating mineralisation.

The fast / slow rise time trial tested the cellular responses of the MC3T3-E1 cell line in terms of cell counts and PGE2 protein regulation 24 hours and 48 hours post-exposure to fast RT, slow RT or sham LIPUS fields. RNA Markers for the mechanotransduction pathway associated with PGE2 up-regulation and mineralisation were also tested using RT-PCR techniques. There were few statistically significant results in these trials. Nevertheless, a significant up-regulation in the mineralisation marker RUNX2 was observed in samples treated with fast RT LIPUS, despite mixed results in cell count and PGE2 protein concentrations. The results and their implications are fully explored in the next chapter.

Finally, a feasibility study assessed the potential of using 3D printed scaffolds to assess cellular responses to LIPUS in growth conditions more like the *in vivo* environment. The 3D scaffold results demonstrated that cells could be grown and could also be used to test cellular responses to cutting. The studies also indicated that, once appropriate adhesives can be found to attach the scaffolds to the Mylar membrane and seal the membrane to the biocell frame, and with careful cutting techniques and power settings, the 3D structures could be exposed to LIPUS fields within the biocell apparatus, thus enabling the possibility of testing LIPUS fields with cells grown in structures designed to mimic the *in vivo* environment.

CHAPTER 6
DISCUSSION OF *IN VITRO* RESULTS

The *in vitro* studies investigated cellular responses of MC3T3-E1 preosteoblasts to LIPUS fields in controlled conditions designed to minimise the secondary effects of the ultrasound exposure. These secondary effects (plate vibrations, reflections, standing waves and local temperature rise) are likely to occur to some degree *in vivo*, but by exposing the cells to the direct ultrasound alone we can begin to explore whether it is the direct stimulus or the secondary effects induced in the apparatus that are producing the cellular responses observed in the literature. This chapter discusses the methods, results, outcomes and limitations of the *in vitro* studies and describes their contribution to the field of LIPUS research. Sections 6.1 to 6.3 discuss the results of the Pressure Amplitude, Frequency and Rise Time Studies, grouped by cellular response. The outcomes of the 3D *in vitro* feasibility study are discussed in Section 6.4 and the chapter conclusions are summarised in Section 6.5.

6.1 Cell Counts and Proliferation

Proliferation of preosteoblasts at the fracture site is essential for bone healing. Some studies in the literature found proliferation of preosteoblasts was up-regulated by LIPUS exposure [129] and others found no effect [132]. These mixed outcomes suggest the proliferation results might be influenced more by the secondary effects induced in the exposure apparatus rather than the ultrasound itself. All the *in vitro* studies described in the previous chapters assessed proliferation by counting the number of viable cells pre- and post- exposure to LIPUS fields and comparing these with sham-treated controls.

The results of the Pressure Amplitude Study (5.1) suggested a maximum peak-negative pressure ($\hat{p}_-$) 105 kPa, or intensity 19 mW/cm^2 $I_{SATA,AER}$, was optimal for proliferation 20 hours post-exposure to 1 MHz LIPUS. In the Frequency Study (5.2), proliferation increased by 11% above controls at the maximum peak-negative pressure, $\hat{p}_-$, 100 kPa. This pressure corresponded to a lower I_{SATA}, approximately half that applied in the Pressure Amplitude Study, due to the narrower beam of the 1 MHz V303 transducer used in that study (see Table 3.21: I_{SATA} was 10 mW/cm^2 as opposed to 20 mW/cm^2 over a 50 mm

diameter surface area). In both studies, significance of increased proliferation could not be established due to high cell count variance but the apparent correlation of proliferation up-regulation at $\hat{p}_-$ 100 kPa suggested the pressure amplitude provided the physical stimulus rather than the spatial and time-averaged intensity.

The Frequency Study also assessed proliferation of the cells in response to 45 kHz LIPUS. The results indicated a 20 % increase in viable cells with respect to controls at the highest $\hat{p}_-$ of 43 kPa and a decrease at lower pressures. Significance of this result could not be established due to high variance in cell counts, so future studies could provide more repeats to establish whether this increase was real and investigate cellular responses to 45 kHz LIPUS at higher pressures.

With no clear trends in cellular responses when exposed to 45 kHz LIPUS, the final Rise Time Study (5.3) was conducted at 1 MHz only and at the optimum pressure established in the Pressure Amplitude and Frequency Studies ($\hat{p}_-$ 100 kPa). Viable cells were counted in pressure bins and converted to cell densities to compare populations directly between bins. Although modest trends were observed, cell densities remained uniform across all the pressure bins in most sample sets, suggesting a global mechanism was acting on the cells. The global cell densities are presented in Figure 5.12 to assess global trends.

Figure 5.12A illustrates that the introduction of osteogenic media had a significant effect on proliferation of sham and LIPUS treated groups 24 hours post-exposure. This agrees with the findings of previous studies in the literature [172]. As well as up-regulating proliferation across all samples, the results indicate the growth media type might influence cellular responses to LIPUS. The 24-hour post-exposure groups generally show small (4 % to 5 %) rises in viable cell densities compared to controls. The Slow RT / base media group (discussed in further detail later) bucks the trend with a 28 % rise. At 48 hours post-exposure the cell densities of both base media groups drop compared to controls (14 % in those exposed to Fast RT and 8 % in the Slow RT group). The cell density of the osteogenic media / Fast RT group increases by 8 % with respect to controls and the density of the osteogenic media / Slow RT group drops only slightly, by 1 % compared to sham. None of these global differences in LIPUS-treated groups achieves statistical significance when comparing against controls. Further repeats would establish beyond doubt if these modest changes are significant or simply due to experimental uncertainty.

The Slow RT LIPUS / base media / 24 hours group exhibited the only significant results in terms of up-regulation of proliferation compared to controls. This group was also the only group to exhibit any noticeable trends in proliferation between pressure bins (see Figure 5.8B). The percentage difference in average number of viable cells peaked at +48 % versus sham-treated controls in the 50-75 kPa bin and tapered off smoothly at lower and higher pressures. Statistical significance was achieved in this pressure bin and in the 25-50 kPa pressure bin. Significance could not be established in the global results or in other pressure bins, though the increases in cell counts were still higher than in other groups. A repeat study would confirm the results, but if real, they suggest Slow RT LIPUS might have a stimulatory effect in the absence of osteogenic nutrients. Perhaps Slow RT LIPUS enhances preosteoblast proliferation in a fracture site lacking nutrients due to inadequate blood supply. This effect might be short-lived, as evidenced by the drop in proliferation in the same group at 48 hours post-exposure.

I hypothesised the trends across pressure bins were due to cells responding to vibration of the membrane induced by the cyclic radiation force of the LIPUS exposure. Cells at or near the centre of the membrane would experience more displacement than those in the outer areas, which are fixed to the biocell frame. This sample set may have included biocells with a lower membrane tension, and therefore would experience higher displacements than other sample sets. The lower proliferation in the centre may indicate that higher displacement at the centre was producing a detrimental response in the cells. This is discussed further in the sources of uncertainty Section 6.1.1.

Comparing these results with the literature, Katiyar et al. [129] found proliferation of MC3T3-E1 preosteoblasts in α-MEM medium containing ascorbic acid increased by 30 % to 50 % (measured via BrdU and MTS assays) after two daily 30-minute exposures to 1.5 MHz LIPUS (200 µs, prr 1 kHz), I_{SATA} 5 to 74 mW/cm^2. This study used the benchtop dip technique with media depth close to an integer-multiple of the wavelength, increasing the likelihood of standing waves and other secondary effects. Tassinary et al. [46] grew MC3T3-E1 cells in osteogenic media, using the direct coupling technique to expose the cells to 30 minutes LIPUS (1 MHz, 200 µs, 1 kHz, I_{SATA} 200 mW/cm^2). They found proliferation increased by approximately 20 % at 48 hours post-exposure (assessed by cell count). By contrast, Tabuchi et al [132] found no significant change in cell counts when exposing MC3T3-E1 cells, in the same medium used by Katiyar et al., to 20 minutes of

1.5 MHz LIPUS (30mW/cm^2, 1 kHz, 200 µs) using the same direct coupling technique. The fact that similar apparent intensities and growth conditions can produce either no change or a significant up-regulation of proliferation strongly suggests the proliferation was influenced by secondary effects peculiar to each apparatus. I suspect this is also the case in my studies.

The mixed nature of the proliferation results across all the *in vitro* studies reported in Chapter 5 suggests that my results were also influenced by secondary effects. No results achieved statistical significance, except for the up-regulation observed in pressure bins 25-50 kPa and 50-75 kPa in the 24-hour post-exposure, base media, Slow RT LIPUS group and a down-regulation in the 75-100 kPa pressure bin of the Fast RT LIPUS base media group at 48 hours post-exposure. I hypothesised that this high variance was due to variations in the conditions in individual biocells, discussed in the next section.

6.1.1   Sources of Uncertainty

This section describes the potential sources of systematic uncertainty in the *in vitro* studies that might have contributed to the high variance in cell counts between biocells. The possible effects on cellular responses are discussed, along with ways to mitigate the effects in future studies.

6.1.1.1 *Increased Acidity in the Growth media due to inadequately cured adhesive*

During the biocell assembly the biocell funnels are filled with adhesive to aid in sealing the biocell when the rubber septa are fitted. The chosen adhesive, HA6 Marine Grade RTV silicone sealant (Bond-It, UK), is non-toxic once cured but the acetic acid is released during the curing process. As the curing only occurs through contact with air, it is likely that some adhesive remained uncured within the sealed funnel. The assembly process was adjusted in an attempt to minimise this, but it was occasionally observed via the phenol red pH indicator contained in the growth medium that the contents of the biocell were acidic. This acidity was diluted when the biocell was filled with 20 ml medium, but it is possible that the first cells injected into the biocell were affected as the acidity would likely be toxic. The collagen layer may also have been compromised by this acidity (collagen is soluble in acidic solutions), which in turn could affect cell adhesion. Even low-level contamination could affect the pH of the growth medium by varying degrees in different

biocells, resulting in subtle changes in cellular behaviour. For instance, PGE2 expression can be up-regulated by acidic conditions [208, 209].

6.1.1.2 Adhesive opacity in UV

Another source of variance relating to the adhesive was observed in the sham control group with the highest standard deviation, in osteogenic media (Trial B) at 48 hours post-exposure. Examination of fluorescent images of the Biocell with the lowest cell count revealed frequent patches of unpopulated areas across the growth area in the DAPI images (Hoechst-stained, Live + Dead cells, Figure 6.1A).
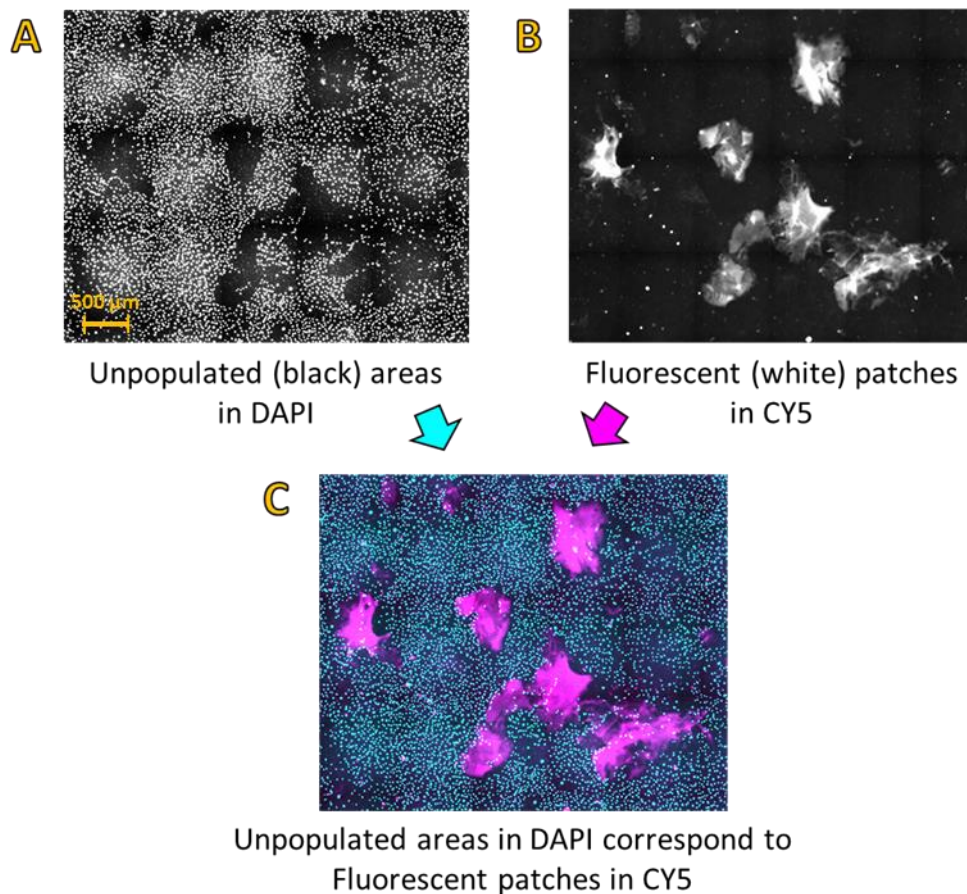
Figure 6.1: Fluorescent microscope images of biocell with lowest cell count in sham-treated controls, 48 hours post-exposure, in osteogenic media. A: DAPI image (Live + Dead) showing dark patches; B: CY5 image (Dead) showing fluorescent patches of adhesive; C: DAPI and CY5 images coloured and overlaid, showing correlation. Scale is approximate.

Comparison of the same area in the CY5 (Dead Cell only) fluorescent image revealed small patches of silicone adhesive on the outside of the growth surface, which were

fluorescent at the CY5 wavelengths (Figure 6.1B). The position, shape and size of these patches correlated with the unpopulated areas in the DAPI image, indicating the silicone adhesive is opaque at the UV wavelengths of the DAPI filter (Figure 6.1C). Closer scrutiny of the same areas in bright field images, where the adhesive was transparent, revealed evidence that cells were present, thus suggesting the cell count in this biocell was underestimated due to being in shadow from the adhesive patches. The results from this biocell were not included in the analysis reported in Chapter 5.

Images from all biocells were examined to determine the impact of this effect on other cell counts, but it appeared that only one biocell was affected significantly. Examining other fluorescent microscope images, most were clear or reasonably clear of adhesive patches and of those with adhesive areas apparent, the cell counts did not appear to be significantly affected. Any future trials must include further measures to ensure there is no adhesive on the membrane, by minimising the amount of adhesive, discarding rubber gloves if they become soiled and cleaning the membrane if deposits are observed.

Some biocells also contained floating particles of adhesive introduced via the syringe during filling and washing of the biocells. These floating pieces are not likely to have affected results as they were detected prior to imaging and their position adjusted so they would not appear in the imaged area. However, taking the above measures to minimise contamination would reduce their occurrence and further improve the imaging quality.

As well as minimising adhesive, the reliance on imaging and cell count accuracy should be reduced in future studies by also assessing proliferation via other methods, such as the Bromodeoxyuridine (BrdU) incorporation assay, which detects DNA synthesis of proliferating cells. This type of assay has the added advantage that it measures proliferation rather than cell number, as a higher cell count may merely mean less cells have died.

6.1.1.3 Mylar Membrane Tension

During biocell assembly the Mylar film was stretched across the film stretcher piece with elastic bands (see Section 4.1.5). Variation in elastic band size, extent of stretching and occasional snapping of elastic bands during overnight curing of the adhesive led to a corresponding variation in membrane tension. As well as altering the stiffness of the growth surface, which has been shown to change cellular responses of osteogenic cells

[210], the variation in tension would result in a corresponding variation of displacement. Lower tension would likely result in larger displacements of the membrane in response to the cyclic radiation force of the LIPUS pulse, especially at the centre of the growth surface, and higher tension would give rise to lower displacement. It is strongly suspected that this was the main source of variance in cellular responses between biocells and should be minimised in future tests.

One method to improve tension uniformity would be to exploit the 'shrinkage' properties of plastic films when heated. Plastic films are cooled under tension during the manufacturing process, sealing in a stretch tension that is relaxed when reheated. Once the mylar is fixed to the biocell frame, exposing it to heat from a heat gun will shrink it and stretch it further across the frame. If this does not provide adequate control, a more elaborate stretch roller system could be employed to stretch the membrane during fixation.

6.1.1.4 Growth surface topology

Another issue associated with stretching the mylar using elastic bands was the occasional bunching and creasing of the film when caught up in an elastic band that had come loose from the stretcher piece. These creases could still be seen on the mylar when it was stretched again, suggesting the surface topology had changed. This variation in topology of the growth surface may have affected the adhesion of the collagen layer and cells by roughening the texture and very likely making the surface more hydrophilic. The creasing might also compromise the membrane and lead to an increased gas transfer rate of CO_2 across the membrane, further contributing to variance between conditions in the biocells. To reduce variance in future studies, creased membranes should be discarded.

6.1.1.5 Complexity of in vitro protocols and biological response

The behaviours of biological cells are highly dependent on the surrounding environment, nutrient levels and exposure to stresses such as temperature variations, chemical toxicity and vibration. There are also inherent differences in the behaviours of different batches of cells due to factors such as variations in the time taken to defrost a vial of cells after cryogenic storage, the level of confluency reached prior to subculturing, and general viability of the cell population in each batch.

In vitro studies therefore require careful and consistent execution of all protocols to minimise variation in cellular responses. Seeding involves detaching cells by careful and time-limited application of toxins with variations in exposure to low temperature, low CO_2 and low nutrient conditions. Good pipetting technique is essential for mixing cells and media to make homogeneous mixtures for accurate cell counting and seeding. Seeding a biocell requires slow and careful syringing techniques to avoid killing cells. Non-uniformities in these techniques were more likely at the beginning and end of each set: at the beginning due to being out of practice, and at the end due to fatigue. In the Rise Time Study with sets grown in osteogenic media (Trial B), the controls were scheduled at the beginning and end of each set, whereas in the base media sets (Trial A) controls were mixed in throughout. It is therefore strongly suspected that human error contributed to the higher variance in control groups observed in Trial B. This could be mitigated by randomising the order of samples and running fewer samples in each set to avoid fatigue due to prolonged lab work. This highlights a particular issue with such a multi-disciplinary research area, which requires skills and expertise in two very different research domains: that of biology and engineering. A researcher might be well versed in one discipline and not so knowledgeable in the other. Many LIPUS *in vitro* studies are likely to be run by researchers with primary training in the field of biology, with less awareness of ultrasound and vibration. I have come at the subject from the opposite side, and many of the unforeseen challenges have been in my unfamiliarity with tried and tested *in vitro* protocols and conventions.

The list of sources of uncertainty illustrate the difficulties in using non-standard, custom-built culture ware for *in vitro* testing. Standard culture ware was developed over many years to provide the conditions required for cells to survive, grow and proliferate in a stable and consistent manner. The biocell shows promise as a more acoustically transparent, cheaper alternative to specialist vessels such as the CliniCell. But to be cost-effective it will be essential to minimise the aspects of the design and construction process that have a potential effect on cellular responses.

6.2 Prostaglandin E2 (PGE2)

The expression of PGE2 was assessed throughout all the *in vitro* studies. PGE2 regulates inflammation and is considered an essential intercellular signalling protein in bone healing.

It has been shown to be up-regulated in osteocytes and osteoblasts in response to mechanical stress [155, 163], and to regulate the production of osteoclasts [155, 211], which absorb mineralised bone material at the fracture site in Stage 1, and bone remodelling in Stage 4 of the healing process.

The results of the Pressure Amplitude Study suggest treatment with 1 MHz LIPUS at $\hat{p}_-$ 105 kPa increases PGE2 expression by 2.6 times that of controls. The Frequency Study PGE2 results suggest a more modest increase, of 24 % to 29 % above controls with optimal $\hat{p}_-$ 100 kPa to 151 kPa. When PGE2 concentrations are normalised for the estimated cells exposed to LIPUS, the normalised PGE2 concentration is + 58 %, at $\hat{p}_-$ 100 kPa, though this result may have been skewed artificially by cell count errors. Significance could not be established by Student t-test ($p < 0.05$). There were no obvious trends or significant results in PGE2 concentrations of the samples treated with 45 kHz LIPUS, suggesting 45 kHz LIPUS has no stimulatory effect on PGE2 expression up to $\hat{p}_-$ 43 kPa. As mentioned in 6.1, further 45 kHz studies could investigate higher pressure amplitudes to determine if these induce cellular effects.

With reference to the Rise Time Study results in Figure 5.14B and 5.15B, PGE2 expression was generally increased by LIPUS exposure but not significantly. Only one drop was observed, -7 % in the Base media / Fast RT LIPUS group at 48 hours post-exposure. All other results ranged from +1 % to +34 % compared to PGE2 concentrations in sham-treated controls. The groups in base media at 24 hours post-exposure to Fast RT LIPUS had the most consistent results, with the Frequency Study and Rise Time Study showing a rise of 24 % and 25 % respectively, as compared to sham-treated controls (see Figures 5.3A and 5.14A). The PGE2 concentration in the Rise Time Study then dropped to -7% at 48 hours post-exposure.

The Osteogenic media results are more mixed. At 24 hours, Trial B results suggest effectively no change in samples treated with Fast RT LIPUS, and a 21 % rise in PGE2 in samples treated with Slow RT compared to controls. In Trial C samples were subjected to the same process but in this trial the PGE2 concentration of the Fast RT group was 34 % above controls, whereas the Slow RT group exhibited effectively no change at +3 %. This reversal of trend suggests the changes are due to experimental variance rather than a result of LIPUS exposure.

Comparing the differences in PGE2 concentrations observed in these trials with LIPUS studies from the literature, Tang et al. [41] observed five-fold increases in PGE2 expression in LIPUS-treated samples, using the benchtop dip method. Reher et al. [40] found PGE2 concentration increased four-fold 24 hours post-exposure to 1 MHz LIPUS at 100 mW/cm^2 I_{SAPA} (equivalent to approximately 20 mW/cm^2 I_{SATA}) using the tank dip method. Kokubu et al. [128] found PGE2 concentrations increased three-fold 60 minutes post-exposure to LIPUS (1.5 MHz, 30 mW/cm^2 I_{SATA}, 1 kHz, 20 mins) using the absorption tank method with standard multiwell plates. All the above methods would still be prone to thermal effects, plate vibrations and reflections. Given the significant differences in the magnitude of PGE2 up-regulation observed in these past studies compared to the controlled study reported here, I propose the up-regulation in PGE2 is caused by secondary stimuli induced by the apparatus rather than direct LIPUS exposure.

6.3 Genetic Markers for Mechanotransduction and Mineralisation

The following sections discuss the results of the genetic marker study, conducted as part of the Rise Time Study and detailed in 5.3.4. The RT-PCR results are discussed in turn in the following sections and compared to that expected for each genetic marker.

6.3.1 Cyclo-oxygenase 2 mRNA (cox2)

The RT-PCR results in Section 5.3.4.1 suggest expression of Cyclo-oxygenase 2 mRNA (cox2) is up-regulated 24 hours post-exposure to LIPUS, significantly so in the Slow RT LIPUS group. Expression of cox2 then falls back to normal or below normal at 6 days post-exposure, with cox2 expression in the Fast RT group 10 % higher than controls and in the Slow RT group 20 % below controls (see Figure 5.16). LIPUS studies in the literature find a correlation between the expression of COX2 mRNA and protein with the expression of PGE2 [41], [40]. Comparing PGE2 expression with cox2 expression at 24 hours post-exposure, the PGE2 expression of the Fast RT sample sets increased by 34 % compared with controls and the cox2 expression increased by 80 %. The Slow RT sample sets had average PGE2 increase of only 3% compared to controls, whereas the cox2 expression increased by a statistically significant 60%. This apparent disconnect between COX-2 and PGE2 expression was not expected.

Figure 6.2 compares cox2 and PGE2 expression for individual biocells in the PCR trial to investigate. The biocell IDs are in the form (#Set.#Biocell). The cox2 result for sham control 1.16 was discarded due to a labelling error and the PGE2 result for Biocell 2.6 was not available because no media was collected for that sample.
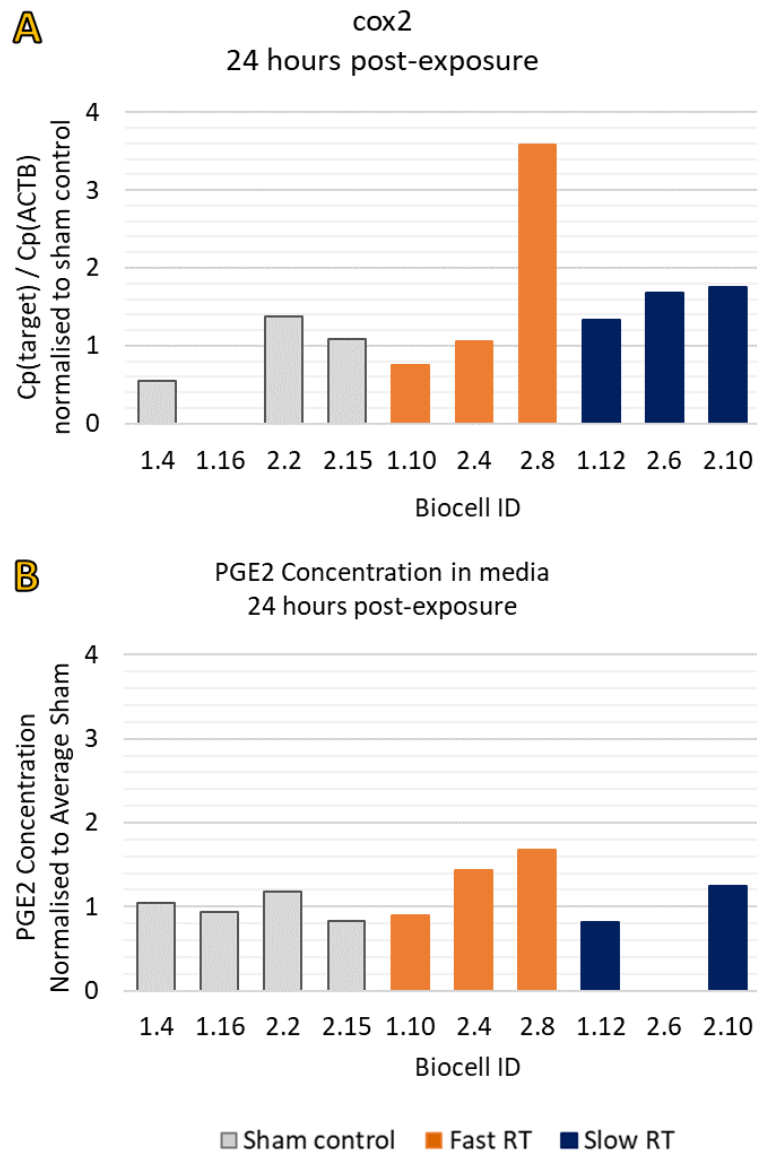
Figure 6.2: Comparison of cox2 and PGE2 expression in individual biocells, 24 hours post-exposure, normalised to average expression in controls. A: COX-2 mRNA (cox2); B: PGE2 Concentration in media.

An approximate correlation is apparent between the cox2 and PGE2 expressions in most individual biocells. The main exception is Biocell 2.8 in the Fast RT LIPUS group, where the cox2 expression is considerably higher, suggesting the elevated average in the Fast RT LIPUS group is due to a single high result. If this result is removed the average cox2

expression in the Fast RT LIPUS group falls from 8% above to 10 % below that of the sham control group, suggesting the cox2 expression is unaffected by LIPUS exposure. In the case of the Slow RT LIPUS treated samples, which are statistically significant, the results are more consistent.

Comparing with the literature, Tang et al. [41] found a 6-fold increase in cox2 expression 6 hours post-exposure and over 4-fold increase in COX2 protein expression 24 hours post-exposure to LIPUS using the benchtop dip method. Kokubu et al. [128] found COX2 mRNA and PGE2 expression peaked at 60 minutes post-exposure to 1.5 MHz LIPUS (200 µs, 1 kHz prr, 20 minutes) using the absorption tube method. The PGE2 expression in the LIPUS-treated group was approximately 3 times that of the control group.

The inconsistency of results, mismatch with PGE2 expressions and low magnitudes of up-regulation compared to the literature suggests controlled LIPUS exposure has no significant effect on cox2 or PGE2 expression. This is consistent with the general findings for PGE2 expression throughout my studies. As before, I propose the secondary effects induced by the apparatus can explain the differences in cellular responses. Again, this supports my hypothesis that direct vibration of the cell growth surface is the most likely stimulus. This is supported by previous studies in the literature showing PGE2 and COX2 expression in osteogenic cells are up-regulated by direct vibration [25].

As mentioned before, these secondary effects would likely be present *in vivo* but their magnitude would be dependent on many factors including the local fracture site structure (especially any mineralised bone present at the site, which can reflect the ultrasound and produce localised thermal effects), transducer orientation and coupling and any movement of the transducer during treatment.

This leads to the proposal that a bone tissue mimic with mineralised structures of comparable dimensions and geometry to fracture sites may provide an *in vitro* environment that can, if designed appropriately, reproduce some of the secondary effects that occur *in vivo*. The 3D Scaffold Feasibility Study investigated the practicalities of seeding cells on 3D printed scaffolds for this reason, and the findings are discussed later in this chapter.

6.3.2   Integrin β5 (itgb5)

The expression of Integrin β5 (itgb5) increased over time but there was no significant difference between LIPUS-treated samples and sham-treated controls. Evidence from studies in the literature suggest Integrin β5 is involved in osteoblast differentiation and mineralisation [212], but not in response to mechanical stimulus. Instead, this Integrin is a chemical receptor for the hormone Irisin, which is up-regulated in muscle tissue during exercise [165]. Future studies should therefore focus on integrins that have been shown to be involved in mechanotransduction: for example β1 and β3, which were the subject of the study by Tang et al. [41] and were implicated in the pathway leading to COX-2 and PGE2 up-regulation. The rise in expression of Integrin β5 is likely due to increased adhesion of the cells to the growth substrate, as integrins are the proteins by which cells bind to the surrounding ECM.

6.3.3   Collagen Type I (col1)

Collagen Type I (col1) expression is high in preosteoblasts and immature osteoblasts and down-regulated in mature osteoblasts as they begin to lay down hard mineralised matrix (Table 3.3). Col1 is therefore a marker for maturation and mineralisation of osteoblasts. The col1 expression results in Section 5.3.4.2 suggest LIPUS treatment has no effect on col1 expression after 24 hours. After 6 days col1 expression increased in all samples compared to 24 hours post-exposure, significantly so for LIPUS-treated samples (Figure 5.18). Both LIPUS-treated samples had reduced levels of col1 expression compared to the sham-treated control at 6 days post-exposure.

The expression of col1 for each biocell is plotted in Figure 6.3A. The sham controls contain one very high result, in Biocell 1.5, which skews the average. Assuming this is an outlier, the new average sham control expression is lower (Figure 6.3B), the Slow RT LIPUS result is similar to controls (only 3 % below) and the Fast RT LIPUS treated samples have col1 expression 60% higher than controls. This increase was close to achieving significance, with a p-value of 0.07, suggesting Fast RT LIPUS may up-regulate col1 expression but further repeats are required to verify and establish significance.
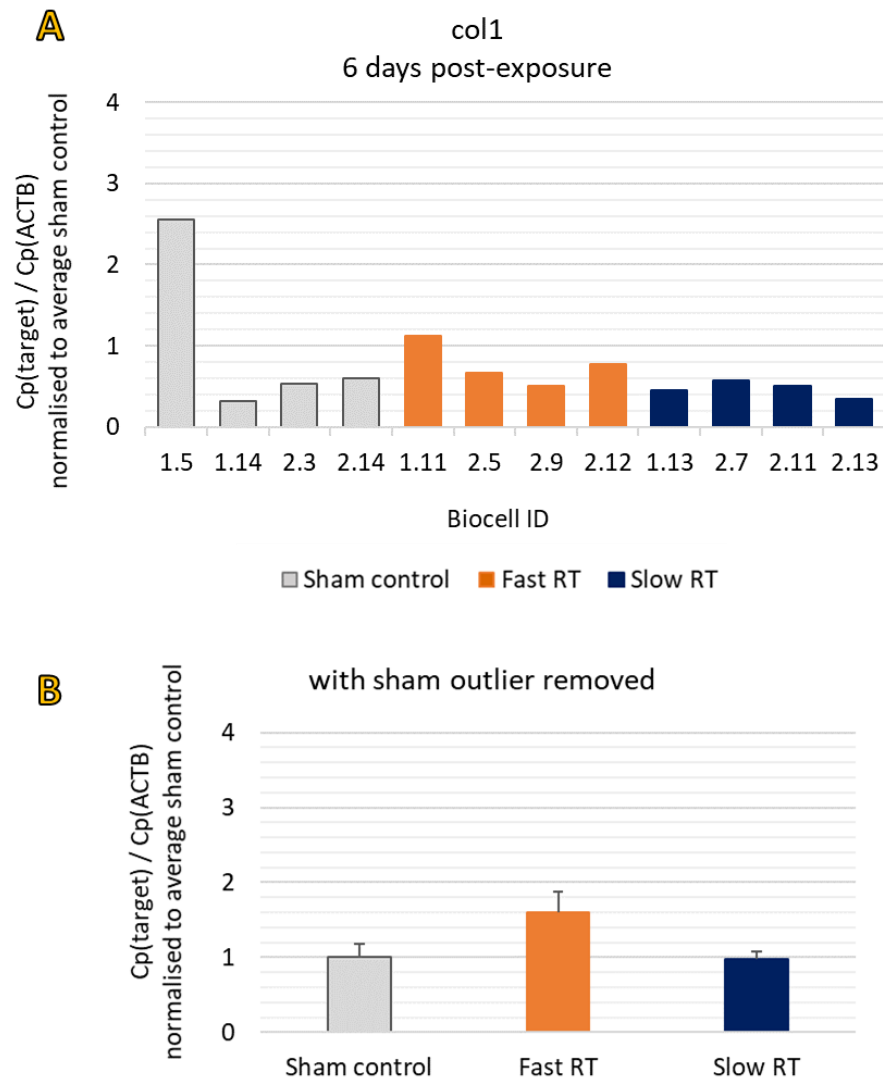
Figure 6.3: Collagen Type I (col1) expression
in A: individual biocells and B: Average expression with sham outlier removed.

Comparing results to those in the literature, Doan et al. [38] exposed human mandibular osteoblasts to 5 minutes of 1 MHz LIPUS (100 mW/cm^2 I_{SAPA}, *pw* 2 ms, *prr* 100 Hz) using the tank dip method and found collagen protein levels increased by approximately 55% compared to sham-treated controls. A well-controlled custom tank study by Harle et al. [140], with MG63 osteoblast-like cells grown and exposed to LIPUS in a standard culture flask but with in-situ characterisation of the LIPUS field, found no significant change in COL1 protein expression 5 days after a 5-minute LIPUS exposure (3 MHz, CW, I_{SATA} 140 to 990 mW/cm^2). Bandow et al. [71] exposed MC3T3-E1 cells, matured for zero to four weeks in osteogenic media, to 20 minutes 1.5 MHz LIPUS (200µs, prr 1 kHz, ISATA 30 mW/cm2) using the absorption tube method and found no significant change in expression of Collagen Type 1 mRNA (Col1a1) compared to controls.

The mixed results in the literature and lack of significant up-regulation in more controlled studies strongly suggest that col1 expression is not stimulated by the direct LIPUS stimulus, but may be more sensitive to secondary effects induced by the exposure apparatus (which will be present to some degree *in vivo*). Expression may also be influenced by growing the cells on a collagen layer, as this has been shown to reduce col1 expression in foetal rat calvarial osteoblasts [199]. This marker, like PGE2 and COX2, could be included in future studies to verify these results and investigate whether higher pressure amplitudes induce a cellular response.

6.3.4 Osteocalcin (ocn), Osteopontin (opn) and Runt-related Transcription Factor 2 (runx2)

Osteocalcin (OCN) and osteopontin (OPN) are markers for mineralisation because they are expressed by maturing osteoblasts and are present in mineralised bone. OCN promotes alignment and binding of hydroxyapatite crystals to the collagen ECM [213]. Osteopontin (OPN) makes up approximately 2 % of non-collagenous bone tissue and is involved cell adhesion via integrins, bone homeostasis and osteoclast regulation [213, 214]. It is generally considered to be a late marker for mineralisation but is also expressed during the proliferative stage of osteoblast maturation. Runt-related Transcription Factor (runx2) was chosen as a marker because it is an early regulator of osteogenic differentiation. Recalling Table 3.3, runx2 is significantly up-regulated in preosteoblasts that are differentiating to mature osteoblasts, and is a precursor to the up-regulation of many downstream mineralisation markers, including opn and ocn.

All three markers, ocn, opn and runx2, were up-regulated at 6 days post-exposure compared to 24 hours post-exposure for all LIPUS exposure conditions (see Figures 5.19, 5.20 and 5.21). This is likely due to the MC3T3-E1 preosteoblasts commencing differentiation to mature osteoblasts in the presence of osteogenic growth media, as seen in previous studies in the literature [172]. The expressions of ocn and runx2 were reasonably consistent across all individual biocells with no obvious outliers, meaning average results were representative of the biocell population. More variation was seen in the opn expressions, reflected in the error bars and the lack of statistical significance.

In Figure 5.22, which compares expression of mineralisation markers in LIPUS-treated groups compared to sham-treated controls, expression of ocn in LIPUS-treated groups was

consistently below controls at 24 hours and 6 days post-exposure. The Fast RT LIPUS group expressions were 70 % and 77 % at 24 hours and 6 days post-exposure respectively, and expressions in the Slow RT LIPUS group were 52 % of control at both time periods. This suggests LIPUS exposure has a detrimental effect on ocn up-regulation and that this detrimental effect is carried through consistently from the short-term to long term.

Expression of opn and runx2 were unchanged with respect to controls at 24 hours post-exposure. At 6 days post-exposure, the opn and runx2 expressions in the Fast RT LIPUS-treated group both increased 2-fold with respect to controls, and this up-regulation was significant in the case of runx2 expression ($p<0.05$). Expressions in the Slow RT group were both marginally higher than controls, at +22 % for opn and +11 % for runx2. The opn result was influenced by a single high result in one biocell, which may have been an outlier. Further repeats would confirm.

The significant up-regulation of runx2 in response to Fast RT LIPUS is an intriguing result and suggests this early regulator of osteogenesis is particularly sensitive to the ultrasound stimulus, unlike other markers like cox2 and PGE2, which appear to be up-regulated by secondary effects such as plate vibrations or heating. As it is only significantly up-regulated by Fast RT LIPUS in my study, I propose it is the vibration induced in the growth surface by the rapid switch on and off of the radiation force that is the primary stimulus.

Comparing with the literature, many studies used the direct coupling method to investigate expression of runx2, ocn and opn in response to LIPUS exposure. Imai et al. [137] investigated the effects of daily 20 minute exposures to LIPUS (1.5 MHz, 200 μs, 1 kHz, 30 mW/cm^2 I_{SATA}) on primary human mandibular fracture haematoma-derived cells (MHCs) in osteogenic medium. Expression of runx2 was significantly up-regulated compared to sham-treated controls on Day 4 and continued to be higher for treatment periods up to 20 days, though not significantly higher than controls. Up-regulation of ocn increased with time and became significant on Day 14 and Day 20 after LIPUS treatment commenced. Up-regulation of opn also increased with time and achieved significance at Day 20. Mineralisation at Day 20, assessed by Alizarin Red S staining, was four times greater in the LIPUS-treated group compared to the sham control group. The timescales of

this study suggest assessing the markers over a longer time period would provide more insight into the cellular responses to LIPUS, particularly the expression of ocn and opn.

Tabuchi et al. [132] exposed MC3T3-E1 cells to 20 minutes LIPUS (1.5 MHz, 30 mW/cm^2 I_{SATA} 200 µs 1 kHz) in MEM-α medium containing ascorbic acid. OCN protein expression was approximately 70 % greater than controls 24 hours post-exposure. There was no significant change in opn expression compared to controls and runx2 expression was not assessed. The OCN protein result contradicts the ocn RNA expression results of my study. It could be this marker has been up-regulated by the secondary effects induced by the apparatus rather than the direct LIPUS stimulus. The expression of opn could also have been influenced by the growth media, which did not contain BGP. Franceschi et al. found adding ascorbic acid alone to media up-regulated expression of OCN but not OPN in MC3T3-E1 preosteoblasts.

Liu et al. [134] also used the direct coupling technique to exposed MSC-like human periodontal ligament cells (hPDLCs) to LIPUS 30 minutes per day for 7 days (1.5 MHz, 200 µs, 1 kHz, I_{SATA} 90 mW/cm^2). In-situ LIPUS field measurements were taken but temperature was not monitored so thermal effects cannot be ruled out. Expression of runx2 in LIPUS-treated samples was 1.4 times controls. Expressions of opn and ocn were up-regulated in a similar manner. The study also found increased mineralisation by Alizarin red staining 21 days post-exposure in LIPUS treated samples.

With the same cell type, apparatus and LIPUS field, Hu et al. [157] found daily stimulation of 20 minutes per day increased expression of runx2 (1.7 times control), ocn (1.5 times those of controls at 7 days) and integrin β1 RNA (1.9 times control). This study also found increased mineralisation after cells were cultured for 21 days in osteogenic media (1.9 times no. of Ca nodules as controls). Up-regulation was suppressed in all markers when Integrin β1 inhibitor was introduced, suggesting mechanotransduction pathways were stimulated via this integrin.

The direct coupling method is prone to plate vibrations and direct heating so the role of direct vibration and thermal effects in the stimulation cannot be discounted. However, the runx2 results do correspond to the results of the Rise Time Study in this thesis.

A tank dip study by Zhang et al. [70] illustrates the possibility that thermal effects might stimulate the same mineralisation markers. This study exposed adipose derived stem cells to 2 MHz LIPUS (200 μs, 100 Hz, 30 mW/cm^2). Expression of genetic markers increased after 14 days of daily LIPUS exposures. Runx2 expression was approximately 13 times controls, ocn expression approximately 16 times and opn approximately 9 times that of controls. The temperature of the medium was observed to rise by 3 °C during exposures and the up-regulation of heat shock protein was noted in the trial. This supports the heating effects reported by Leskinen and Hynynen [58] for this method and might account for the increased up-regulation compared to my study and the direct coupling studies. Although this is an extreme example of the effect of heating on cellular responses, it does illustrate that heating can bring about up-regulation of the same markers as observed in LIPUS studies. Future studies might include monitoring of heat shock protein to assess if small temperature rises during LIPUS exposures (estimated at < 0.3 °C in my study) correlate with other cellular responses.

Lai et al. [44] employed the more controlled absorption tube method and observed up-regulation of runx2 expression (nearly 3 times that of controls) in human mesenchymal stem cells (hMSCs) treated with 3 days of daily 20 minute LIPUS treatments (1 MHz, 2ms, 100 Hz, 200 mW/cm^2 I_{SPTA}). For comparison, the I_{SPTA} (spatial peak, temporal peak intensity) of the V303 transducer used in the Rise Time Study was 64 mW/cm^2 (Table 3.20). The up-regulation of runx2 in my results was less pronounced, at just under 2 times that of sham-treated controls. This might be due to the lower intensity used and the single exposure compared to three.

By contrast, the absorption tube study by Bandow et al. [71], already described in the previous section, saw no significant difference in ocn expression of LIPUS-treated MC3T3-E1 cells compared to controls and also noted an unpublished previous trial had found no difference in expression of runx2. This highlights another issue with LIPUS research, and indeed all research, where studies with a negative or 'no result' are not reported in the literature as they are deemed to be of less value than positive and significant results, which has the risk of leading to a net bias for the positive results that may not be representative of the true population or may even be erroneous.

It is very interesting that Bandow et al. [71] reported no change in runx2 expression in their controlled study. Bandow's apparatus consisted of a six-well culture plate held in a tank of water with six transducers situated directly under the wells. A silicon absorption chamber was placed over the six-well plate and this effectively absorbed and removed any reflections within the wells, as confirmed by pressure measurements with a hydrophone. The use of standard polystyrene culture ware should have made this apparatus prone to plate vibrations. However, if the absorption material used to suppress reflections within the wells was in contact with the plates this may have dampened some of the plate vibrations and reduced the cellular responses. As already discussed, I suspect the Mylar film growth surface used in the biocells was prone to vibrate in response to the cyclic radiation force of the LIPUS field, with displacement amplitude dependent on the tension of the membrane.

Time-course studies of runx2, ocn and opn expression over longer time periods (2 weeks plus), coupled with mineralisation assays such as Alizarin red staining, would verify and further investigate cellular expression of ocn and opn in response to LIPUS exposure. Multiple LIPUS exposures could also be investigated, along with exposing cells seeded on 3D scaffolds to assess cellular effects in conditions closer to the *in vivo* environment. Additional markers for mechanotransduction pathways of interest and associated integrins and calcium ion channels, could be added to the PCR to begin to understand how the cells are being influenced by the stimulation. Ideally these genetic markers should be backed up with assessment of the resulting protein expression.

As already mentioned, the significant up-regulation of runx2 is the most intriguing result of all the *in vitro* studies, and is worthy of further investigation. In the osteoblast lineage, runx2 is expressed at low levels in mesenchymal stem cells and is up-regulated in preosteoblasts. It reaches maximum expression in immature osteoblasts and is down-regulated in mature osteoblasts [215]. Runx2 plays a similar role in human and mouse osteoblastic cell lines [216].

Transcription factors have a regulatory role in cellular biology: they are proteins that control the rate of transcription of genetic information from DNA to messenger RNA, by binding to a specific DNA sequence [217]. They effectively switch the expression of particular genes on and off to control cell behaviour. Runx2 has a number of functions depending on the cell type and the exact nature of its influence is still the subject of much

research, but it is mainly linked with the regulation of proliferation and mineralisation in osteoblasts. Runx2 inactivation in mice prevents ossification and defects in the runx2 gene can result in bone disorders such as cleidocranial dysplasia (CCD).

In the osteoblast lineage, runx2 is expressed at low levels in mesenchymal stem cells and is up-regulated in preosteoblasts (Figure 6.4). It reaches maximum expression in immature osteoblasts and is down-regulated in mature osteoblasts [215]. Runx2 plays a similar role in human and mouse osteoblastic cell lines [216]. Runx2 is linked to numerous pathways implicated in LIPUS research: the PI3K/AkT pathway which regulates cell apoptosis and osteogenesis in response to stress (also linked to COX-2 and PGE2 up-regulation) [41, 218]; the associated wnt pathway [69], and the ERK / p38 / MAPK pathways [41, 114, 119, 123].
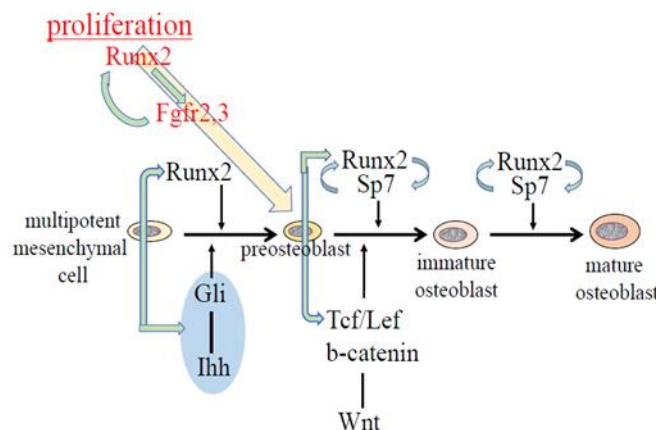
Figure 6.4: Runx2 role in osteoblast lineage, reproduced from [215].
Runx2 promotes differentiation of mesenchymal stem cells into preosteoblasts (in the presence of Indian Hedgehog (Ihh) signalling in endochondral bone formation. Runx2 also regulates preosteoblast proliferation via Fibroblast growth factors (Fgfr2, 3), and their maturation to mature osteoblasts via Sp7 and Wnt / β-catenin signalling.

Higher runx2 in 6-day samples treated with fast RT LIPUS suggest the cells in these samples are maturing into osteoblasts earlier and will therefore likely mineralise earlier than those treated with sham or slow RT LIPUS.

Runx2 is linked to numerous pathways implicated in LIPUS research: the PI3K/AkT pathway which regulates cell apoptosis and osteogenesis in response to stress (also linked to COX-2 and PGE2 up-regulation) [41, 218]; the associated wnt pathway [69], and the ERK / p38 / MAPK pathways [41, 114, 119, 123]. The up-regulation of runx2 may

indicate that the mechanotransduction pathways of the cells are stimulated, which would lead to increased or faster mineralisation of samples treated with fast RT LIPUS.

This should be the focus of future studies, which should employ all the improvements to techniques described in Section 6.1.1 and especially ensuring the mylar film growth surface is tensioned as uniformly as possible. Runx2 can also be investigated in 3D scaffold studies to determine if expression is influenced by growth conditions more like the *in vivo* environment.

6.4 3D *in vitro* Methods

While isolating the ultrasound stimulation alone can begin to provide some clue as to the possible mechanisms acting on the cells, no amount of these controlled studies could fully answer the question of whether LIPUS treatment induces healing effects *in vivo*. As described in Chapter 2, bone cells are known to respond in different ways if grown in 2D or 3D environments [162, 167]. These bone cells live on and around a complex structure of mineralised matrix that will respond to LIPUS stimulus in its own unique set of secondary effects, including vibration, heating and fluid flow in the canaliculae.

A handful of studies highlighted the potential of LIPUS to induce similar conditions in bone to those induced by physical movement and exercise, which is well-established as a stimulus of bone remodelling and strengthening. An *in vivo* study by Greenleaf and Argadine [87] found LIPUS application induced cyclic longitudinal motion in long bone ends at the LIPUS pulse repetition frequency, with strain amplitudes in the range of those known to be induced by physical exercise [150]. Physical exertion can also induce bending motions that result in increased fluid flow in the canalicular structures of long bones. FE modelling has indicated that LIPUS-induced fluid flow in these structures induced wall shear stresses similar to those known to stimulate mechanotransduction pathways of osteoblasts and embedded osteocytes [152-154]. Induced fluid flow can also have the more direct effect of accelerating nutrient delivery and removal of waste products to and from the fracture site, which can also stimulate healing effects.

The results of the above studies strongly suggest that to truly understand the effect of ultrasound on bone we must move to more complex setups. Ideally this would mean measuring the effects of ultrasound exposure *in vivo*, but this introduces practical

difficulties and a large amount of variation due to physiological differences. The method considered, and tested for feasibility in this study, was the use of 3D-printed scaffolds to provide a controllable and repeatable 3D environment in which cells can grow and be exposed to LIPUS in a bone-like structure.

The use of 3D printed scaffolds would have the advantage of providing a uniform structure in which multiple tests of cellular responses could be conducted and compared. The seeding and cutting trial demonstrated that the MC3T3-E1 cells could be grown on these scaffolds and would survive cutting with an ultrasonic cutting tool. This opened up the possibility that the 'healing' process might be tested via these scaffolds – by creating a wound (in this case using an ultrasonic cutting tool) and monitoring the migration and proliferation of cells into the cut site as an approximation of the healing process. This could be extended to longer term monitoring of rates of mineralisation. The intention was to test this with samples exposed to sham or LIPUS treatment and compare the wound closure rates.

Exposing the samples to ultrasound within the biocells proved more difficult than anticipated due to the performance of the adhesives used in the trial. The method required a quick-acting, non-toxic adhesive that would bond to the 3D printed biocell frame and the Mylar film (both smooth surfaces) and render them watertight. The adhesive chosen (Liquidskin – a non-toxic superglue used to seal wounds) did not provide a very good bond despite showing promise in bench tests. Further work is required to find a more suitable adhesive or to precondition the bonding surfaces, e.g., to roughen the biocell frame surface, to improve adhesion. If the adhesive issue were resolved this test method would prove a valuable addition to LIPUS research. More complex 3D printed structures could be designed, to mimic the canalicular structure of cortical bone. The cellular responses could then by analysed via confocal microscopy or histology (i.e., cutting thin slices of a fixed 3D sample in order to view internal structures). This technique has the potential to provide a more accurate glimpse of *in vivo* cellular responses to LIPUS stimulus.

6.5 Chapter Summary

This chapter discussed the results of the *in vitro* studies described in Chapters 3 and 4, grouped by the following cellular responses:

- Proliferation, assessed by comparing viable cell counts pre- and post-exposure.
- PGE2 protein expression in the growth media, assessed by ELISA.
- Genetic Markers for Mechanotransduction and mineralisation, assess by RT-PCR.

45 kHz LIPUS at peak-negative pressures ($\hat{p}_-$) up to 43 kPa did not significantly up-regulate proliferation or PGE2 expression at 24 hours post-exposure. A 20% increase in cell counts was observed at the highest pressure, so it is possible that 45 kHz LIPUS with higher pressures might increase proliferation further. This could be the subject of future studies. All other studies were conducted with 1 MHz LIPUS as the results of the early Pressure Amplitude and Frequency Studies suggested both proliferation and PGE2 might be up-regulated in response to 1 MHz LIPUS at $\hat{p}_-$ 100 kPa to 151 kPa.

The Rise Time Study assessed responses of MC3T3-E1 preosteoblasts to 1 MHz LIPUS $\hat{p}_-$ 100 kPa with Fast (1.4 µs) and Slow (40.5 µs) rise times (RT). The MC3T3-E1 preosteoblast proliferation results were mixed and most changes not significant compared to the relatively high variance in cell counts. One statistically significant up-regulation in proliferation was observed in samples grown in base media, 24 hours post-exposure to Slow RT LIPUS in the 50-75 kPa pressure bin, where cell density was 48 % above that of sham-treated controls. If this result is repeatable, it could mean that Slow RT LIPUS has the potential to increase proliferation of preosteoblasts in fracture sites lacking osteogenic nutrients. Further repeats are required to verify this result.

The generally mixed nature of the proliferation results in my studies are mirrored in the literature, and vary with exposure method. This supports the hypothesis that proliferation is affected by the secondary effects such as plate vibrations and thermal effects induced by the exposure apparatus, rather than the direct LIPUS pulse. These effects can be present *in vivo* but will have significantly differing magnitudes than those in laboratory conditions and between fracture sites.

The sources of uncertainty in the in vitro studies are described in Section 6.1.1, including acidity of the by-products of adhesive curing perhaps affecting the collagen coating and pH of the growth media; adhesive opacity at certain fluorescent wavelengths which affected accuracy of some cell counts; differing mylar membrane tensions resulting in variation of displacement experienced by cells in each biocell; creasing of some biocell membranes

affecting topography of growth surface in some biocells; and general human error in techniques, which were exacerbated by long hours in the laboratory. Mitigation measures were identified for all of the above sources of uncertainty and these could be incorporated in protocols of any future studies.

The expressions of PGE2 protein, and its genetic precursor COX2 RNA (cox2), exhibited conflicting results between groups that were subject to the same processes and conditions. The lack of statistical significance and small magnitude of my PGE2 results as compared to those in the literature suggests cox2 and PGE2 expression is sensitive to secondary effects induced by the exposure apparatus rather than direct LIPUS exposure.

Expression of Integrin β5 RNA (itgb5) increased significantly 6 days post-exposure to all LIPUS conditions and no significant change was observed between LIPUS-treated groups and controls. The up-regulation is likely due to increased adhesion of the cells to the substrate. Future studies will focus on integrins that have established links to mechanotransduction pathways in preosteoblasts and osteoblasts, such as Integrin β1.

Expression of all the markers of mineralisation, ocn, opn and runx2, were significantly up-regulated at 6 days post-exposure compared to 24 hours. This up-regulation over time is likely due to the introduction of osteogenic media. The results suggest ocn is not affected, or even adversely affected by LIPUS exposure. At 6 days post-exposure the expressions of opn and runx2 are 2 times that of the sham treated controls, and the runx2 result achieves statistical significance in a student t-test ($p < 0.05$). Slow RT LIPUS induces a small but not significant up-regulation, by $11 - 20$ % above controls. The significant up-regulation of runx2 is the most intriguing result of the in vitro studies, as runx2 is an essential transcription factor that regulates osteogenesis and facilitates a number of mechanotransduction pathways of interest in LIPUS research. Future research will focus on this transcription factor, which appears to be more sensitive than other markers to controlled LIPUS fields with minimal secondary effects.

I have proposed that the main stimulus acting on the cells during these trials is the vibration of the biocell membrane in response to the cyclic radiation force of the LIPUS pulse. Future studies will attempt to make the tension of the membrane more uniform to

reduce variance, and the main focus will be on the runx2 transcription factor, which was significantly up-regulated by Fast RT LIPUS.

Finally, the outcomes of the 3D *in vitro* feasibility study were discussed. The studies established that MC3T3-E1 preosteoblasts could be cultured on 3D-printed scaffolds, were able to survive cutting of the surface of the scaffold with an ultrasonic cutting tool, and could proliferate and migrate into the cut site within 24 hours. Problems with suitable adhesives to allow quick attachment of the membrane to the biocells hampered attempts to expose the 3D scaffolds to LIPUS, and cutting with a new tip and high-powered drive system meant that all cells died in the LIPUS exposure study. Despite the issues, the 3D-printed scaffolds have great potential to allow testing of cellular responses in a controlled 3D environment approximating *in vivo* conditions.

CHAPTER 7
CONCLUSIONS AND FURTHER WORK

This chapter summarises the main conclusions of this thesis. A summary of the work is provided in 7.1. Contributions to the field of LIPUS research are described in 7.2. The main conclusions regarding mechanisms of stimulus of the LIPUS field are summarised in 7.3. Finally, in 7.4, I recommend further work to expand on the findings of this study.

7.1 Thesis Summary

The main aim of this work was to investigate the healing mechanisms of Low Intensity Pulsed Ultrasound (LIPUS) when applied to fractured bone. Despite being in clinical use, the mechanism of LIPUS healing is still poorly understood and many *in vitro* studies attempted to isolate the mechanism at a cellular level.

Chapter 1 examined LIPUS systems used for bone healing, comparing transducer design, operating frequency, and ultrasound field parameters such as rated intensity (I_{SATA}) and pulse characteristics (1.1). Bone physiology and the post-fracture healing process were described. The possible causes of non-union fractures were presented and compared with LIPUS mechanisms of healing proposed in the literature (1.2). A comprehensive study of *in vitro* LIPUS exposure methods and apparatus led to the conclusion that many of these methods have the potential to introduce secondary effects such plate vibrations, reflections and standing waves within wells, multiple exposures and elevated temperatures (1.3). While these effects are likely to occur *in vivo*, it is highly improbable that comparable effects could be induced in a typical *in vitro* lab apparatus. My approach was to conduct *in vitro* testing with an apparatus designed to minimise the secondary effects, so that the cellular responses to the ultrasound stimulus alone could be assessed. By isolating the ultrasound, we can begin to understand if bone cells are responding to direct ultrasound stimulus or secondary effects induced by the ultrasound interacting with the surroundings. The review also introduced and discussed the merits of using 3D growth surfaces to provide a cell growth environment more analogous to *in vivo* conditions.

Chapter 2 presented a review of the LIPUS literature, from first discoveries and early *in vivo* studies (2.1), to clinical trials and adoption for clinical use (2.2), and on to *in vitro* studies investigating underlying cellular mechanisms (2.3.1 and Appendix A). LIPUS mechanisms identified in the literature were discussed and supporting evidence compared (2.3.2). The mechanotransduction property of bone cells, i.e., their ability to respond to mechanical stress and up-regulate extra-cellular signalling proteins to induce strengthening of the surrounding bone tissue, was identified as the most likely potential mechanism of LIPUS healing effects. Mechanotransduction pathways were the focus of many LIPUS *in vitro* studies and numerous studies found key markers in those pathways were up-regulated.

One such study, by Tang et al. [41], was directly cited on the manufacturer's website of a leading LIPUS device as proof of the healing mechanism of LIPUS. In the study, MC3T3-E1 murine preosteoblast cells were exposed to LIPUS by what I have called the benchtop dip method, where the cells are grown in a standard petri dish and the transducer is dipped in the growth media, with no apparent control or measurement of the ultrasound field. The study found evidence of a direct link between LIPUS stimulus of integrins, which connect the cell to the surrounding ECM, via the FAK/PI3K/Akt & ERK pathway, to a four-fold up-regulation of Prostaglandin E2 (PGE2) 24 hours post-exposure. A similar up-regulation was observed in the protein and mRNA levels of the enzyme Cyclooxygenase 2 (COX-2), which fuels the conversion of activated arachidonic acid to PGE2. PGE2 had also been up-regulated in response to LIPUS at 1 MHz and 45 kHz in a study by Reher et al. [40]. PGE2 was therefore chosen as a basic marker for potential healing in my studies. Cell proliferation was also chosen as a marker due to the mixed results observed in the literature.

The pressure fields of LIPUS devices were investigated in Chapter 3. The pressure fields of a commercial LIPUS dual frequency device operating at 1 MHz and 45 kHz was measured with a precision scanning tank system and needle hydrophone. The pressure fields were found to have significantly different characteristics, which would make it hard to directly compare the cellular response to frequency alone. Recommendations were therefore devised for those studies comparing cellular responses to LIPUS at different frequencies. A LIPUS device with dimensions based on the Exogen device (Bioventus, US) was designed, built and characterised at 1 MHz and 1.5 MHz. Finally, two transducers

were chosen to provide LIPUS fields at 1 MHz and 45 kHz and were positioned and driven to produce comparable beam widths that would pass through the aperture of the biocell with minimal reflections from the edges. Both devices were characterised for spatial pressure properties and the I_{SATA} was calculated (in the case of I_{SATA} across the cell growth area) and estimated (in the case of the I_{SATA} across the effective radiating area (A_{ER}), as defined in the British Standard for physiotherapy devices [14] from the scanned pressures. A set of pressure parameters were also proposed as alternative parameters to report in LIPUS studies that would be more informative than single spatial average characteristics that are most often quoted in studies.

A controlled LIPUS exposure method was devised and apparatus developed and built. The method utilised a custom culture vessel (the biocell) based on existing culture cassettes but with a significantly thinner membrane to minimise transmission loss and reflection effects (4.1). The circular aperture could be tailored to the size of the ultrasound beam. The size of the aperture in the studies reported in this thesis was 50 mm diameter in the case of the Pressure Amplitude Study, and 70 mm diameter in the Frequency and Rise Time Studies. Transducers were carefully chosen and characterised with an ultrasonic scanning system at the frequencies and pulse characteristics used in exposures. The setup allows control over the frequency, amplitude and pulse characteristics of the LIPUS field by driving each transducer with a signal generator and amplifier. The ultrasound exposure was conducted with a tank system, allowing fine adjustment of alignment and separation of the LIPUS transducer and biocell. The ultrasound exposure method allowed the cellular effects of only the ultrasound excitation to be studied, by minimising the secondary effects of heat, reflections and plate mode excitation induced by many *in vitro* ultrasound exposure methods. Transmission loss through the Mylar film was measured on a mock-up of the exposure setup and found to be minimal at 1 MHz (within ±2% at 10 mm from the beam centre) and produce a slight reduction in amplitude (3.5 %) and narrowing of the half-pressure beam width (18 mm to 16 mm) of the 45 kHz device. Temperature measurements were also made over the exposure duration with maximum pressure settings used in the Frequency Study (1 MHz 200 kPa and 45 kHz 43 kPa). The temperature rise was within 0.8 °C.

The Pressure Amplitude study was the first *in vitro* study and served the dual purpose of establishing the method and investigating the optimal peak negative pressures for cellular

responses. The Frequency Study compared cellular responses to 1 MHz and 45 kHz LIPUS fields. The Rise Time Study investigated cellular responses to 1 MHz LIPUS with fast and slow rates of change of the pressure amplitude (the rise time) affected cellular responses. The Rise Time Study included a comparison of MC3T3-E1 cellular responses when cultured in base (proliferative) media or osteogenic media, and an assessment of expression of genetic markers for COX-2, integrin β5 and the mineralisation markers Collagen Type 1 (col1), Osteocalcin (ocn), Osteopontin (opn) and Runt-related Transcription Factor 2 (runx2), assessed via RT-PCR.

The pressure amplitude study and frequency study results indicated that 1 MHz LIPUS with maximum peak-negative pressure ($\hat{p}_-$) 100 kPa stimulated proliferation and PGE2 expression. 45 kHz LIPUS results suggested proliferation may be up-regulated at higher pressures than those tested and no obvious trends were evident in PGE2 expression.

The Rise Time Study assessed responses of MC3T3-E1 preosteoblasts to 1 MHz LIPUS at $\hat{p}_-$ 100 kPa with Fast (1.4 µs) and Slow (40.5 µs) rise times (RT). The MC3T3-E1 preosteoblast proliferation results were mixed and most changes not significant compared to the relatively high variance in cell counts. One statistically significant up-regulation in proliferation was observed in samples grown in base media, 24 hours post-exposure to Slow RT LIPUS in the 50-75 kPa pressure bin, where cell density was 48 % above that of sham-treated controls. This rise was of a similar magnitude to previous studies in the literature that found significant increase in proliferation. If this result is repeatable, it could mean that Slow RT LIPUS has the potential to increase proliferation of preosteoblasts in fracture sites lacking osteogenic nutrients, perhaps where a blood supply has not been fully established. Further repeats are required to verify this result. The general mixed nature of proliferation results in my study and in the literature leads to the hypothesis that proliferation is sensitive to secondary effects induced by the apparatus. I suspect my results were affected by varying membrane tension, where less tension would result in a higher displacement amplitude due to the cyclic radiation force produced by the LIPUS pulses. Further studies with improved membrane tensioning techniques would confirm if this was the case.

No repeatable, significant trends were found in the expression of PGE2 and its precursor COX-2 mRNA expression. Any apparent up-regulation was small compared to the four-

fold increases reported in the literature [41]. This suggests PGE2 and COX-2 expression is also more regulated by secondary effects induced in the apparatus, and not the ultrasound stimulus alone. Any apparent cellular effects could be explained by sources of experimental uncertainty, which included issues of varying pH in the growth media due to acidic bi-products of the adhesive, UV opacity of adhesive deposits on growth surface potentially affecting cell counts, variation in membrane tension and topology due to the stretching techniques, and complexity of in vitro protocols, where small inconsistencies in technique can induce relatively large variations in cellular responses. A series of mitigation measures were identified to minimise systematic uncertainties and these can be adopted in future studies (6.1.1).

Genetic markers for mineralisation were generally up-regulated in all samples including controls 6 days post-exposure, as expected due to the introduction of osteogenic media. Expression of col1 was 60 % higher in samples exposed to Fast RT LIPUS when one outlier was excluded from the analysis, though results were not statistically significant. Expression of Osteocalcin (ocn) was reduced in LIPUS-treated samples (again not significantly). Expression of opn and runx2 increased two-fold compared to controls at 6 days post-exposure to Fast RT LIPUS. Expression of runx2 was significantly up-regulated, suggesting this essential osteogenic transcription factor is sensitive to the LIPUS stimulus alone. If this is the case runx2 could be the key player in LIPUS healing, triggering preosteoblasts and MSCs to differentiate to the osteogenic lineage even without any secondary stimuli. Future LIPUS studies could explore mechanotransduction pathways associated with runx2 to elucidate the particular mechanotransduction 'sensor' (e.g., integrins or calcium-ion channels) stimulated by the LIPUS field.

Two-dimensional *in vitro* testing methods are limited in their ability to predict cellular responses *in vivo*. The use of 3D printed scaffolds showed promise for the development of controlled bone tissue mimics, in which bone cells could be grown in conditions more like the *in vivo* environment, designed to reproduce the physical stimuli within the structures of bone tissue. Such a tissue mimic would provide a more realistic, but controlled and repeatable, environment in which to study the effects of LIPUS on bone.

7.2 Contributions to the Field of LIPUS Research

The following is a summary of the contributions I have made to the field as a result of the work described in this thesis.

- A study of LIPUS exposure methods and potential secondary effects induced by the apparatus, identifying the most controlled methods.

- A review of the literature including comprehensive comparisons of in vitro LIPUS studies and findings (Appendix A).

- Characterisation of the pressure fields of LIPUS devices and proposed parameters for definition of LIPUS dose, including recommended methods of comparing the cellular effects of LIPUS fields with significantly different frequencies.

- A low-cost, 3D-printed custom culture vessel with acoustically transparent membranes was developed to allow the culture of cells and exposure to controlled LIPUS fields in one culture vessel (referred to as the biocell).

- A controlled custom tank method was developed to expose cells growing in biocells to LIPUS fields. The method isolated the ultrasonic stimulation by minimising the secondary effects of reflections, heating and mechanical vibration. Although these effects are likely to occur *in vivo*, I argue it is impossible to recreate the complex interplays of physical phenomena in the *in vivo* environment in a two-dimensional apparatus. Therefore two-dimensional *in vitro* testing should be used to study the simple, controlled case so that we can begin to understand the complex processes involved in ultrasonic stimulation of bone cells.

- This study also proposed that the definition of the LIPUS fields in any LIPUS study should not only include the spatial-average, temporal-average intensity (I_{SATA}), but also report the measured or predicted *in situ* peak acoustic pressure, pressure distribution and temperature to which the cells were exposed, as recommended for bioeffect studies in a paper by ter Haar et al. This would allow cellular responses to be compared between trials and enable meaningful conclusions to be drawn.

- A method for investigating the effects of LIPUS fields on cells grown in 3D printed structures was also explored. The studies showed that the method was feasible provided the practical issues can be resolved: particularly the sourcing of suitable adhesives for attaching the 3D-printed material to the thin film of the biocell. Using 3D printed structures allows the study of cellular responses in environments that are still controlled and repeatable but more like *in vivo* conditions.

7.3 Conclusions Summary

The following is a brief summary of the main conclusions regarding the biological mechanisms of LIPUS in bone healing.

- No significant trends were observed in the proliferation of MC3T3-E1 pre-osteoblasts exposed to 45 kHz LIPUS compared to sham-treated controls. A 20% rise was observed in samples exposed to $\hat{p}_-$ of 43 kPa. Further repeats are required to establish if this rise was significant and investigate the effect of 45 kHz LIPUS at higher pressures.

When MC3T3-E1 murine preosteoblast cells were exposed to a controlled LIPUS field (1 MHz, $\hat{p}_-$ 100 kPa, *pw* 200 µs, *prr* 1 kHz) in the absence of secondary effects, i.e. changes in intensity and pressure amplitudes due to reflections, plate vibrations and thermal effects induced by the test apparatus, these studies found:

- No significant or consistent trends were observed in cell proliferation in samples exposed to LIPUS as compared to sham-treated controls. Any changes seen were thought to be due to variation in the tension of the Mylar film upon which the cells were grown, resulting in varying displacement of the film in response to the cyclic radiation force of the LIPUS field. The mixed nature of proliferation results in the literature also suggest cell proliferation is sensitive to secondary effects and less so to the direct LIPUS stimulation.

- No significant or clear trends were observed in the PGE2 expression of MC3T3-E1 preosteoblasts exposed to controlled LIPUS fields as compared to sham-treated controls. Therefore, it is likely the three to five-fold up-regulation of PGE2 reported

in the literature [40, 41, 128] were due to secondary effects induced by the apparatus rather than direct LIPUS exposure.

- The expression of Cyclo-oxygenase-2 (COX2) RNA showed approximate correlation with PGE2 expression, as expected for an enzyme that is directly involved in converting arachidonic acid to prostaglandins. Again, similar to the general results for PGE2, no clear or significant trends were observed in samples post-exposure to controlled LIPUS fields as compared to sham-treated controls. It is proposed that the expression of COX2 RNA is instead sensitive to vibration of the growth surface induced by the LIPUS cyclic radiation force rather than the ultrasound field itself.

- The effect of LIPUS on expression of the mineralisation protein markers osteocalcin (ocn) and osteopontin (opn) was mixed. 6 days post-exposure, ocn expression reduced in LIPUS-treated samples and opn expression increased. Neither result was significant, partly due to the small sample size. Further repeats of the marker studies, with more replicates and longer time scales of two or more weeks, to allow further mineralisation to occur, are recommended to capture the effects of LIPUS exposure on these markers.

- Expression of RUNX2 RNA was significantly up-regulated by the ultrasound field of LIPUS. It is recommended that this genetic marker and other downstream mineralisation markers be the focus of future studies, as well as mineralisation itself which can be assessed by staining.

- Expression of RUNX2 RNA was significantly up-regulated 6 days post-exposure to LIPUS with fast rise time, and less so by LIPUS with a slow rise time. This suggests that rapid onset of the cyclic radiation force of the LIPUS pulse is the most likely candidate for the physical stimulus behind any healing effects of LIPUS.

7.4 Further Work

The following further work is recommended to verify and progress the research presented in this thesis.

7.4.1 Computer modelling

The LIPUS exposure methods reviewed in Section 1.3 could be modelled using finite element analysis to verify the impact of reflections, plate vibrations and even thermal effects that could be induced by the apparatus. FE modelling could also be used to assess other proposed exposure methods, as well as the exposure method used in this thesis. For instance, modelling the mylar film held at different tensions within the biocell could help to quantify the range of displacements possible in response to the LIPUS pulse, and predict how those displacements would manifest across the extent of the membrane (perhaps exciting particular radial modes of vibration). The model could also be used to test the response of different membrane materials and thicknesses to improve the biocell design: for instance, choosing a thicker membrane or more robust material could allow further treatment to improve topology and hence cell adhesion. Or a stiffer membrane could be chosen to further encourage osteoblast differentiation.

Further computer modelling could be conducted to assess cellular responses in 3D structures, by predicting local pressures, fluid flows and shear stresses in the vicinity of the cells. The modelling could then be used to influence the design of the 3D structure to recreate the fluid flows, pressures and shear stresses expected in cortical bone or fracture sites *in vivo*.

7.4.2 Further two-dimensional in vitro exposures with biocells

Further controlled *in vitro* LIPUS studies should be conducted, incorporating the measures described in 6.1.1 to reduce variations in membrane tension, growth surface topology and the effects of using excessive adhesive. Number of replicates in each study set should be reduced to reduce the effects of human error on uncertainty, by focussing on verifying significant results instead of repeating the full Rise Time Study, i.e., Slow RT LIPUS at 24 hours post-exposure. The genetic marker study should be repeated and focus on runx2 and the components of associated mechanotransduction pathways, such as integrin β1 and

β3, ERK/p-ERK proteins or PI3K / AkT pathways. Longer term studies could then verify any effects of exposure on subsequent mineralisation. Time-course studies of cox2 and PGE2 could be conducted to establish if and when these markers are up-regulated. Cell counts should be conducted. As all the trends in cell count were reflected in the global cell count, only global counts will be required. The cell count evidence should be supported with proliferation assays. Cell counts on creased mylar film surfaces could be compared to those with smooth surfaces to explore if the topology contributed to cell count variation. If so, creased mylar should be discarded. Improvements in the biocell design or stretching techniques could achieve more uniform topologies and growth surface tensions.

Following on from these repeats, the effects of changing other LIPUS parameters could be investigated, such as the duration and number of LIPUS exposures, the pulse repetition rate, higher pressure amplitudes and perhaps smaller steps in amplitude to establish if there are any smooth trends. Future studies could also investigate 45 kHz LIPUS at pressure amplitudes $\hat{p}_-$ greater than 43 kPa, the maximum pressure tested in this thesis.

7.4.3 Further development of 3D in vitro methods

Looking ahead beyond the testing of a monolayer of cells, 3D *in vitro* methods could be further developed to investigate more in vivo- like conditions and cellular responses, mapped to expected physical phenomena within the 3D structures, determined by various modelling methods such as Finite Element Analysis. These 3D structures could be populated with bone cells, ideally with embedded osteocytes if possible, and a mix of preosteoblasts, osteoblasts and even MSCs. As osteocytes are the main source of PGE2, expressing this in response to mechanical vibration, PGE2 could still be used as a marker and monitored over time by harvesting small quantities of media. But other markers such as NO and Calcium, which have also been shown to be up-regulated directly by vibration [25], should also be monitored, to support the healing hypothesis. Long term rates of mineralisation could be measured by alizarin red staining to verify whether any up-regulation of these anabolic regulators leads to increased rates of mineralisation.

Such 3D models have the potential to finally answer the question of whether LIPUS stimulates healing responses in bone and provide controlled study methods that can be repeated between research groups.

7.4.4 Cell-by-cell Analysis

All the results and analysis in this thesis assumed that all the cells exposed to LIPUS were members of one homogeneous population with normally distributed cellular responses. The Rise Time Study included an attempt to distinguish between cells exposed to varying peak negative pressures within the ultrasound beam by separating out areas of the growth membrane and comparing cell counts in those areas to establish and correlate any pattern with the pressure amplitudes.

Cellular biology research in recent years has recognised that this homogeneous assumption is likely to over-simplify the complex nature of biological cells. Cells such as osteoblasts are more and more considered to be a heterogenous population, where within that population there will be a diverse range of roles and phenotypes. In recent years new techniques have evolved to allow each cell to be analysed independently. One such technique is single-cell RNA sequencing, which was adopted in a recent study that revealed a diverse range of osteoblast functional activities and developmental fates, as opposed to the simple assumption of osteogenic differentiation followed by either apoptosis or becoming an embedded osteocyte [219]. Some of these techniques allow RNA analysis to be conducted *in situ* [220], thus it may be possible to analyse the population of cells across the growth area of the biocell after exposure to LIPUS, and map expression of genetic markers, such as Runx2, to the pressure amplitude experienced by each cell. These methods could also be adopted in a 3D culture system, and perhaps even evolve to a 3D bone mimic, with embedded osteocytes, osteoblasts, preosteoblasts and even other phenotypes involved in bone repair, where each cell could be analysed for its response to its environment during exposure.

APPENDIX A
SUMMARY TABLE OF *IN VITRO* STUDIES

This appendix provides a summary table (Table A.2 A.2) of the *in vitro* LIPUS exposure studies discussed in this thesis. The table summarises each paper, ordered by the most relevant stage of fracture repair and cell type. The devices and transducers are detailed, along with a brief description of the LIPUS exposure method. Main results are also given and the final column includes the author, year and reference. The exposure method is indicated by a set of symbols describing the level of control and definition of the LIPUS field. The symbols and their meanings are provided in Table A.1.

The first three symbols (1 star, 2 stars and 3 stars) correspond to levels 1, 2 and 3 recommended as appropriate standards for reporting of ultrasound exposure conditions in bioeffect studies by ter Haar et al. [51]. They recommended that any study attempting to correlate biological effects with exposure to ultrasound must ideally measure the ultrasound fields *in situ*, and that both maxima and spatial distribution of pressure and intensity should be reported.

Level 1 consisted of quoting manufacturer's data about the device with no measurements made of the field and was recommended for indicative, non-quantitative studies only. Level 2 included measurement of the device acoustic output with values of peak intensity, peak pressure and power output, preferably with an estimate of *in situ* intensity and peak-negative pressure, taking into account transmission loss of the path. Level 3 included all the data given in Level 2 with the addition of spatial plots of pressure or intensity, preferably along three orthogonal axes (XYZ) through the region of interest.

As thermal effects should also be considered, a symbol (T) indicates whether temperature has been measured or estimated *in situ*. Multiple exposures and cavitation should also be avoided, so the symbols M and C indicate if these were considered in the method design. All symbols are summarised in Table A.1.

Symbol	Meaning
★	Manufacturer's data only. No measurements conducted for study.
★★	Measurements made of device maximum acoustic output in unperturbed conditions, preferably with an estimate of field *in situ*
★★	As 2 but with additional spatial information about pressure intensity, preferably in three orthogonal planes.
S S	*In situ* ultrasound field has / has not been estimated or measured
T T	The study has / has not considered thermal effects: preferably by measuring temperature at the cell layer.
M M	The study has / has not considered multiple exposures *in situ* and accounted for or mitigated against any effects.
C C	The study has / has not considered cavitation *in situ* and accounted for or mitigated against any effects

Table A.1: Symbols used in Table A.2 as shorthand for level of ultrasound field definition in an in vitro study.

Cell model	US device / exposure	US exposure method	Results	Ref
Stage 1: Inflammation. Fibroblasts help form hematoma. Angiogenesis.				
Fibroblasts (primary human embryonic)	custom transducer (∅ 2 cm) 3 MHz; temporal peak intensity 0.5 W/cm², 2ms on, 8ms off (100 Hz prf), 5 mins duration	★★ S T M C Custom tank method. Cells in suspension in custom-built irradiation vessel (IV) with 130 µm-thick Melinex (mylar) windows. Tank filled with degassed water 25°C and lined with absorber. Transducer attached to one wall with front face 21 cm from IV. Sound field measured in situ with pressure probe, with and without IV present.	↑ **protein synthesis** ↑ **membrane changes** Effects suppressed by exposing cells in 2 atm positive pressure environment – concluded cavitation was present	Webster, Dyson et al. 1978 [72]
Primary human gingival fibroblasts Primary human mandibular osteoblasts Primary human monocytes	5 minutes with two US devices: (1) Therasonic 1032 (EMS, Oxfordshire UK): AER 2 cm²; 1 MHz, pw 2ms prr 100 Hz ISAPA 0.1 – 1 W/cm2. (2) Phys-assist (Orthosonics, UK): AER 12.8 cm² (curved face); 45 kHz, CW, 5 – 50 mW/cm2 (ISATA).	★ S T M C Tank dip method in multiwell plate. Tank lined with absorber and filled with deionised, distilled water held at 37 °C.	Fibroblasts & osteoblasts: ↑ **proliferation** ↑ collagen All cell types: ↑VEGF	Doan, Reher et al. 1999 [38]
Fibroblasts (primary human skin)	Exogen SAFHS (Smith & Nephew, US) 1.5 MHz; *pw* 200 µs; *prr* 1 kHz; I_{SATA} 30 mW/cm² Once for 6-11 minutes	★ S T M C Direct coupling method. 6x SAFHS transducers directly coupled to wells of 6-well culture plate via coupling gel. Calibration method unclear.	↑ **Proliferation** Rho/ROCK/Src/ERK signalling pathway via integrin β1 activation	Zhou et al. 2004 [110]
Gingival Epithelial cell line GE1	BR-Sonic PRO (ITO, Tokyo, Japan). 3 MHz, I_{TA} = 160 & 240 mW/cm², 1:4 duty cycle 15 minutes daily	★ S T M C Direct coupling method. Single transducer coupled to base of 35 mm culture dish via ultrasound gel.	↑ **proliferation** ↑ **migration** (max at 160 mW) ↑ Expression of integrins α6 and β4	Iwanabe et al. 2016 [111]

Cell model	US device / exposure	US exposure method	Results	Ref
HUVECs and HMECs	0.5 MHz; mean intensity = 210 mW/cm^2 mean pressure = 0.5 MPa 1 minute	★ Ⓢ Ⓣ Ⓜ Ⓒ̶ Direct coupling. Ultrasonic field not clearly defined. Single dish so no multiple exposures. Degassed water to reduce cavitation risk. Temperature monitored via temperature test paper	**↑ apoptosis** **↓ viability** Caspase 3, MAPK, ATF-4 and elF2α. Decreased viability. Inhibited angiogenic tube formation.	Su et. al 2019 [112]
Stage 2: Soft callus: MSCs migrate to site, proliferate and differentiate into chondrocytes or preosteoblasts. Chondrocytes lay down soft callus.				
Rat bone marrow derived stromal cells (rBMSC)	Sonic Accelerated Fracture Healing System (SAFHS - THM-Model 2 A-Collimage type, Exogen Inc, US) 1.5 MHz, 200 µs, 1 kHz I_{SATA} = 30 mW/cm^2 20 mins	★ Ⓢ Ⓣ Ⓜ Ⓒ̶ Direct coupling method. six transducers attached to bottom of 12-well culture plate. Multiple exposures likely: calibration method not clear. Temperature of medium monitored. Risk of cavitation not assessed but mentioned in discussion.	3 hours post-exposure: ↑ c-jun ↑ c-myc ↑ COX-2 ↑ Egr-1 ↑ TSC-22 ↑ on ↑ opn	Sena et al. 2005 [113]
Primary Rat bone marrow stromal cells (rBMSC)	Exogen SAFHS 1.5 MHz, 200 µs, 1 kHz, 3 treatment regimens: I_{SATA} = 2, 15, 30 mW/cm^2, 20 mins per day for 3, 5 or 7 days over 8-day period.	★★ Ⓢ Ⓣ Ⓜ Ⓒ̶ Direct coupling method. US beam characterised but in situ intensity not clarified. Temperature not monitored but referred to Sena 2005 trial [113]	↑ ERK1/2 (max at 30 mW/cm^2)& p38 (max at 15 mW/cm^2) pathway ↑ ALP (max +209% at 30 mW/cm^2, 5 days treatment) **↑ mineralisation** (max +225% at 2 mW/cm^2 after 24 days)	Angle et al. 2010 [114]

Cell model	US device / exposure	US exposure method	Results	Ref
Primary human adipose-derived stem cells (hASCs)	Custom LIPUS system – unfocussed transducers 25.4mm diameter (Valpey Fisher, US) driven with sig gen and power amplifier. 1 MHz, ISATA = 30 mW/cm^2 PRF settings 1 Hz, 100 Hz & 1 kHz, 20% duty cycle (pulse width changed I assume) 20 mins per day	★★ (S) (T) (M) (C) Direct coupling method. Transducers coupled to central thin membrane of Bioflex culture dish (Flexcell International Corporation, US) with central thin membrane (thickness 0.5mm). Transmission loss through film measured. Multiwell plate used so multiple exposures possible – though less likely with this plate construction due to decoupling of felxible membrane from surrounding plastic. Temperature not measured.	↓ **Proliferation** ↑ Calcium (max at 1 kHz PRF after 7 days)	Marvel et al. 2010 [115]
Primary human alveolar bone-derived mesenchymal stem cells	Unknown device 1 MHz, 50 mW/cm^2 20% and 50% duty cycles 10 mins per day	★ (S) (T) (M) (C) Direct coupling method. Unknown transducer coupled to 35 mm petri dish via coupling gel	↑ **migration** (max effect 20% duty cycle) ↑ **mineralisation** (max effect 20% duty cycle) ↑**proliferation** (20% duty cycle only)	Lim et al. 2013 [118]
Human bone marrow mesenchymal stem cells	Sonacell device consisting 6 LIPUS transducers designed to directly couple to standard six well plates. Calibration / verification methods unknown. 1.5 MHz, 20% duty cycle, *prr* 1 kHz ISATA = 30, 40, 50, 60 & 80 mW/cm^2. Durations 5, 10 or 20 mins per day for up to 4 days	★ (S) (T) (M) (C) Direct coupling method. Six transducers coupled to 6- or 96-well plates with coupling gel.	↑ **proliferation** (5 mins per day, 50-60 mW/cm^2) ↓ **proliferation** (≥10 mins per day, 50-60 mW/cm^2) via PI3K / Akt pathway	Xie et al. 2019 [65]

Cell model	US device / exposure	US exposure method	Results	Ref
Human adipose-derived stem cells	unknown ultrasound apparatus (Siemens, Germany) 2 MHz, 200µs, 100 Hz (2ms on, 8ms off), Intensity 20 and 30 mW/cm^2	(★) (S) (T) (M) (C) Tank dip method with six transducers positioned 30 mm below wells of a 6-well plate in tank of degassed water. No absorption tube or attempts to mitigate water-air interface. 1mm layer of coupling gel placed under plate. Temperature of medium monitored (rose from 37°C to 40°C over 30 mins exposure – possibly due to standing waves as reported in [58]). Attempts made to define LIPUS exposure but poor understanding of ultrasound demonstrated by confused data reporting.	-**Proliferation** ↑Osteogenic **differentiation** ↑HSP70/90 & ↑BMP. ↑runx2; ↑opn; ↑ocn. ↑p-SMAD Cellular effects very likely to be due to temperature changes caused by setup.	Zhang et al. 2018 [70]
Human periodontal ligament cells (hPDLCs)	Bespoke LIPUS exposure device by Engineering Research Centre of Ultrasound Medicine (Chongping Medical University, China). 6 transducers with diameter 34.8 mm – same diameter as wells in 6-well plate. 1.5 MHz, 200µs, 1 kHz, ISATA 30, 60, 90 mW/cm^2 10, 20 & 30-mins per day for up to 15 days	(★) (S) (T) (M) (C) Direct coupling method. Author claims a flat reponse in the near field but no measurements detailed to verify. Transmission loss (or permeability) through well bottom assessed by ultrasound power meter. No other assessment of in situ ultrasound field.	↑ ALP (max effect 20 mins 90 mW/cm^2) All at 90 mW/cm^2: ↑ Runx2 and Integrin β1 mRNA ↑Osteocalcin ↑**Mineralisation** (All inhibited by Integrin β1 inhibiter)	Hu et al. 2014 [157]

Cell model	US device / exposure	US exposure method	Results	Ref
Dental pulp stem cells (DPSCs) and periodontal ligament stem cells (PDLSCs)	Duoson (SRA Developments, UK). 1 MHz, 3.2 ms, 63 Hz. ISATA = 250 mW/cm2 (DPSCs); 750 mW/cm2 (PDLSCs) 5 minutes	(★) (S) (T) (M) (C) Tank dip method. Device dipped in 6-well plate sitting in an absorbent silicone rubber chamber filled with water. Temperature not monitored.	DPSCs ↑**Proliferation** ↑Piezo 1/2 proteins ↑ERK 1/2 MAPK Piezo ion channel blocker inhibited expression of ERK 1/2 MAPK, suggesting LIPUS activates this pathway via piezo channels. PDLSCs -Piezo 1/2 proteins ↑c-jun; ↑p38 MAPK	Gao et al. 2017 [119]
Primary human mesenchymal stem cells from bone marrow	Sonopuls 490 (Delft, NL) 1 MHz pulse, 2ms, 100Hz, 20 mins daily over 1 – 4 weeks	(★★) (S) (T) (M) (C) Absorption tube method. Device 30 mm from base of well, in situ intensity derived by same method as in Li 2002 [136]. Temperature not measured.	↑ osteogenic **differentiation** (↑runx2)	Lai et al. 2010 [44]
ATDC5 mouse chondrocyte cell line	Exogen fracture repair system (Smith & Nephew, US) – 1.5 MHz, prr 1 kHz; pw 200µs; 160 mW/cm2 (ISAPA). 6x transducers coupled to bottom of 6-well plates Custom-built apparatus 6x Panasonic speakers driven with 1 kHz square wave at 20% duty cycle, calibrated to produce the same displacement of the well bottom as measured with the Exogen system using a scanning laser vibrometer. Treatment 20 mins daily, initiated 3 to 11 days after plating cells, with 6-12 treatments	(★★) (S) (T) (M) (C) Direct coupling method. Displacement amplitudes equalised to 4 nm measured by Vibrometer. Temperature not monitored.	↑ cartilage nodule formation similar up-regulation compared to controls in both 1.5 MHz, prr 1 kHz LIPUS and 1 kHz 20% duty cycle square wave treatment. Initiating treatment on later days resulted in increased effect with 1 kHz compared to 1 kHz prr LIPUS.	Argadine et al. [120]

Cell model	US device / exposure	US exposure method	Results	Ref
Primary human chondrocytes from articular cartilage	Immersion transducer V300 (Panametrics, US), 12.7 mm diameter, 5 MHz, CW, 3mins, spatial average pressure = 14 kPa	★★ Ⓢ Ⓣ Ⓜ Ⓒ Benchtop dip method. Transducer dipped in media, 6mm from cell layer on base of 6-well plates. Not clear if 14 kPa was measured in situ and if this was rms or peak pressure	↑ Integrin-MAPK mechanotransduction pathway via FAK, Src, p130Cas and CrkII	Whitney et al. 2012 [55]
primary rabbit articular cartilage chondrocytes	HT2009-1, Ito, Japan) Intensity = 20, 30, 40, & 50 mW/cm^2 3 MHz, Duty cycle 20% 20 mins daily for 6 days	★ Ⓢ Ⓣ Ⓜ Ⓒ Direct coupling method into single culture dish. Transducer coupled with thin layer of coupling gel.	↑Integrin β1 ↑ p-p38 ↑ Collagen Type II Concludes the Integrin-p38 MAPK pathway plays an important role in LIPUS-mediated ECM production by chondrocytes	Xia et al. 2015 [123]
Primary rat chondrocytes	Custom designed US apparatus 1.0 MHz, 200μs, 1 kHz Average peak-pressure: 88 – 556 kPa 222-230kPa ~ 50 mW/cm^2 ISATA 360 kPa ~ 120 mW/cm^2 2s to 10 mins (Ca2+ experiments) 10 mins daily for 3 days	★★ Ⓢ Ⓣ Ⓜ Ⓒ Inverted tank dip method. Standing waves expected but pressures measured in situ with a membrane hydrophone and depth of media maintained to equalise conditions. Two exposures conducted per plate so multiple exposures likely. 3mm gap between transducers and well bases. Temperature rise estimated but not measured.	-Proliferation ↑aggrecan, mediated by: ↑intercellular Ca^{2+}	Javad & Parvizi et al. 1999 & 2002 [125, 126]
Primary rat chondrocytes (aggregated)	SAFHS-like system (Teijin Institute for biomedical engineering, Tokyo, Japan) 1.5 MHz 200μs 1 kHz 30 mW/cm^2 ISATA 20 minutes daily for 1 to 10 days	★★ Ⓢ Ⓣ Ⓜ Ⓒ Tank system. Culture tube with aggregated cells placed in field at 3 cm distance. Tanks lined with absorber. In situ amplitude in tube measured with hydrophone (85% of direct amplitude)	↑ALP; ↑DNA (↑Proliferation) ↑COL-II, Aggrecan ↓COL-X ↑TGF-β1	Mukai et al. 2005 [124]

Cell model	US device / exposure	US exposure method	Results	Ref
Stage 3: hard callus. Osteoprogenitors and Preosteoblasts mature to osteoblasts and mineralise				
Primary osteoblasts, rat. Murine preosteoblast cell line MC3T3-E1	Exogen 2000 (Bioventus, US) 1.5 MHz, 200 µs, 1 kHz I_{SATA} = 30 mW/cm^2 20 minutes	(★) Ⓢ Ⓣ Ⓜ Ⓒ Benchtop dip. No tank or absorber. No temperature measurements. Risk of cavitation not assessed.	↑ COX-2 ↑ PGE2 Activation of α2, α5, β1 & β3 integrins and Integrin/FAK/PI3K/Akt and ERK pathway by systematic inhibition of processes and testing COX-2 expression.	Tang et al. 2006 [41]
Murine preosteoblast cell line MC3T3-E1	1.5 MHz ISATA = 30 mW/cm^2, prf 1 kHz 20 minutes	(★) Ⓢ Ⓣ Ⓜ Ⓒ Absorption tube method. Six transducers custom-made for 6-well plates. Transducers immersed in tank 20cm from bottom of plate.	PGE2 3xcontrols 60 mins after exposure ↑cox-2 mRNA expression & PGE2 suppressed by COX-2 inhibitor	Kokubu et al. 1999 [128]
Murine preosteoblast cell line MC3T3-E1	0.5 MHz - 5 MHz ISATA = 1 to 500 mW/cm^2; 200 µs, 1 kHz 5, 10, 20 & 30 mins per day for 2 days	(★★) Ⓢ Ⓣ Ⓜ Ⓒ Benchtop dip method. 12-well plates. Transducers characterised in scanning tank but benchtop method means LIPUS exposure uncontrolled. No temperature checks and no cavitation checks	↑ **Proliferation** (BrdU & MTS assays, 24h after 2nd treatment) increased wrt controls. Optimal proliferation (+50%) wrt controls occurred at: 1.5 MHz, 30 mins exposure, ISATA 74.3 mW/cm^2 (approx. +50%). ISATA of 464 mW/cm^2 resulted in decreased proliferation and cell death	Katiyar et al. 2014 [129]

Cell model	US device / exposure	US exposure method	Results	Ref
Murine preosteoblast cell line MC3T3-E1	Sonic Compact (HTM, BR) 1 MHz, 20% I_{SATA} = 200 mW/cm^2 30 minutes	⭐ Ⓢ Ⓣ Ⓜ Ⓒ Direct coupling. Single transducer coupled to bottom of single culture plate with ultrasound gel. Acoustic field in culture well not evaluated – electrical resistance / current monitored instead. Culture media temperature incorrectly monitored via infrared (this does not travel through water).	↑ **Proliferation** through activation of NF-κB1, p38α & mTOR ↑**mineralisation** Hypothesised due to increased calcium and phosphate uptake (concentrations dropped in cell supernatant) -ALP -TGF-β1	Tassinary et al. 2015, 2018 [46, 130]
Murine preosteoblast cell line MC3T3-E1	Custom device (Smile Sonica, Edmonton, Canada) 1.5 MHz, 200µs, 1 kHz ISATA = 30 mW/cm2 10 or 20 minutes	⭐ Ⓢ Ⓣ Ⓜ Ⓒ Direct coupling. Single transducer coupled to bottom of each well of 6-well plate via coupling gel.	↑ROS; ↑**viability** ↑runx2; ↑ocn; ↑opn. ↑ERK 1/2 activation MAPK activation via ROS generation.	Kaur et al. 2017 [131]
Murine preosteoblast cell line MC3T3-E1	Custom system with 6xtransducers, AER 3.88 cm^2 similar to Exogen bone healing system. 1.5 MHz, 1 kHz, 200µs, ISATA 30 mW/cm^2 20 minutes daily for 10 days	⭐⭐ Ⓢ Ⓣ Ⓜ Ⓒ Direct coupling method, Six transducers coupled to base of 6-well plate. Transducers driven simultaneously. Paper claims no interference between wells – no details given of methods used to determine this. Volume of medium controlled so depth of well was not a multiple of a wavelength to make standing wave less likely to occur. Temperature of medium monitored but results not reported	↑**mineralisation** ↑alp, ↑mmp-13 mRNA Conclusion: enhances endochondral ossification – replacement of soft callus with hard mineralised callus.	Unsworth et al. 2006 [47]

Cell model	US device / exposure	US exposure method	Results	Ref
Murine preosteoblast cell line MC3T3-E1	SAFHS 4000J (Teijin Pharma. Ltd, Japan) ISATA 30 mW/cm2; 1.5 MHz; 200µs; 1 kHz 1x 20 minutes	(★) (S) (T) (M) (C) Direct coupling of single transducer to single culture dish via coupling gel. Temperature not monitored.	-**Proliferation** -ALP ↑bglap (ocn) High-density Oligonucleotide microarray and computational gene expression analysis findings: ↑genes associated with skeletal/muscular development, cellular movement, connective tissues, embryonic development. E.g.: ↑mmp-13, ↑fibrillin, ↑igf-2) ↓genes associated with cell cycle, gene expression, cellular development, growth and proliferation. E.g.: ↓tgf-β1	Tabuchi et al. 2013 [132]
Murine preosteoblast cell line MC3T3-E1	Duoson (SRA Developments, UK). 45 kHz: CW, ISATA = 25 mW/cm² 1 MHz: 3.2 ms, 63 Hz, ISATA = 250 mW/cm² 1: 5mins every 2 days	(★) (S) (T) (M) (C) Tank dip method. Device dipped in 6-well plate sitting in an absorbent silicone rubber chamber filled with water at 37°C.	↑**migration** (At both frequencies, but more so at 1 MHz)	Man et al. 2012 [45]
SAOS-2 cells	SAFHS (Smith & Nephew, US) 1.5 MHz, 200µs, 1 kHz, ISATA 30 mW/cm² 1 x 20 minutes	(★) (S) (T) (M) (C) Direct coupling method. Six transducers coupled to bases of six well plate with coupling gel.	cDNA microarray analysis of 7488 genes at 4h and 24h after exposure ↑Integrins & cytoskeletal genes ↑tgf-β1 & 2, ↑igf 2, ↑mapk ↑Apoptosis-related genes	Lu et al. 2008 [133]

Cell model	US device / exposure	US exposure method	Results	Ref
Primary mouse calvarial osteoblasts	Osteotron D2 (Ito Ltd, Japan). 3 MHz, 30 mW/cm^2 (pulse characteristics not reported) 15 minutes. LIPUS compared with samples placed in 42°C incubator for 20 mins and untreated controls.	★ Ⓢ Ⓣ Ⓜ Ⓒ Direct coupling. Transducer coupled to 35 mm culture dishes via ultrasound gel. Temperature not monitored despite testing specifically for heat shock protein.	LIPUS & Heat shock: ↑HSP90 ↑Phosphorylation of Smad1/5 **↑Mineralisation** ↓HSP27 Mineralised nodule formation enhanced (apparently more so by LIPUS) by both stimuli even under BMP2 signal blockage with Noggin.	Miyasaka et al. 2015 [61]
primary murine periosteum-derived cells	SAFHS-like system, manufactured by National Engineering Research Centre of Ultrasound Research, Chongqing Medical University, China) 1.5 MHz; I_{SATA} = 10, 30, 60 & 90 mW/cm^2; 200µs; prr 1 kHz 30 mins to 2 hours /day for 2 days	★ Ⓢ Ⓣ Ⓜ Ⓒ Direct coupling method. 6-well plate. Ultrasonic field not clearly defined in this publication. References previous paper [157] that used similar system.	2 hours exposure: ↓Inflammation by inhibition of IL-6 and IL-8 via NF-κB pathway. 30 mins exposure: **↑Mineralisation** ↑runx2; ↑osx; ↑opn; ↑ocn	Liu et al. 2019 [134]
primary murine periosteum-derived cells	Osteotron D2 (Ito Co. Ltd, Japan) 3 MHz; I_{SATA} = 30 mW/cm^2; prr 1 kHz 20 minutes daily up to 21 days.	★ Ⓢ Ⓣ Ⓜ Ⓒ Direct coupling method. Single transducer Ø 3.5cm coupled to petri dish with ultrasound gel.	**-Proliferation** ↑ALP (day 7) ↑alp; ↑ocn; In osteogenic media: ↑bmp-2; ↑osx ↑BMP-2; ↑phosphor-SMAD 1/5/9 **↑Mineralisation** (21 days)	Maung et al. 2020 [135]

Cell model	US device / exposure	US exposure method	Results	Ref
Rat osteosarcoma cell line	2 transducers – one for 6-well plate (12mm diameter) and one for 96 well plate (3 mm diameter). (Asahi Irika Co Ltd, Japan) 1.5 MHz, 30 mW/cm^2 20 mins daily for 14 days	(★) (S) (T) (M) (C̶) Benchtop dip. Transducer dipped in well 3-4 mm from cell layer	**↑mineralisation** ↑ mRNA Runx2, Msx2, Dlx5, osterix, BSP, BMP-2 ↑ ALP	Suzuki et al. 2009 [56]
Primary osteoblasts, rat	Sonopuls 490 (Delft, NL) 1 MHz pulse, 2ms, 100Hz ISATP up to 750 mW/cm^2 15 minutes	(★★) (S) (T) (M) (C̶) Absorption tube method. Device in far field (240 mm) intensity at the distance and through single culture dish measured. Temperature of culture medium measured (temperature of cell layer not assessed). Cavitation not assessed.	↑ PGE2 ↑ cell density 1hr post-exposure Optimal Intensity = 600 mW/cm^2	Li et al. 2002 [136]
Primary human mandibular osteoblasts	5 minutes with two US devices: (1) Therasonic 1032 (EMS, Oxfordshire UK): AER 2 cm^2; 1 MHz, pw 2ms prr 100 Hz ISAPA 0.1 – 1 W/cm2. (2) Phys-assist (Orthosonics, UK): AER 12.8 cm^2 (curved face); 45 kHz, CW, 5 – 50 mW/cm2 (ISATA).	(★) (S) (T) (M) (C̶) Tank dip method in multiwell plate. Tank lined with absorber and filled with deionised, distilled water held at 37 °C.	↑PGE2 (via COX-2) ↑NO	Reher et al. 2002 [40]
Mouse Dental Papilla cell-23 (MDPC-23) odontoblast-like cell line	Duoson (SRA Developments, UK). 45 kHz: CW, ISATA = 25 mW/cm^2	(★) (S) (T̶) (M) (C̶) Tank dip method. Device dipped in 6-well plate sitting in an absorbent silicone rubber chamber filled with water at 37°C.	**-viability** **↑ proliferation** **↑differentiation** **↑mineralisation** ↑col1, ↑alp, ↑omd, ↑nes	Man et al. 2012 [6]

Cell model	US device / exposure	US exposure method	Results	Ref
Primary human mandibular fracture haematoma- derived cells (MHCs)	LIPUS exposure device (Teijin Pharma Ltd. Japan) similar to SAFHS 1.5 MHz, 200µs, 1 kHz, 30 mW/cm².	★ Ⓢ Ⓣ Ⓜ Ⓒ Direct coupling. 6 transducers coupled to base of 6 well plate with ultrasound gel.	- **Proliferation** ↑ **Mineralisation** ↑ ALP, OCN, Runx2, OSX, OPN, PTH-R1 mRNA	Imai et al. 2014 [137]
Primary human mandibular fracture haematoma cells (MHCs)	LIPUS exposure device (Teijin Pharma Ltd, Japan) similar to SAFHS 1.5 MHz, 200 µs, 1 kHz, I_{SATA} = 30 mW/cm² 20 minutes daily for up to 20 days	★ Ⓢ Ⓣ Ⓜ Ⓒ Direct coupling method. SAFHS-like system designed specifically for culture vessels. Unclear how the system is characterised. 6-well plate coupled directly to transducers via thin water layer.	↑**Mineralisation** ↑BMP2/4/7 (Significantly different on different days after LIPUS exposure)	Huang et al. 2015 [138]
MG63 osteoblasts	Custom transducers (PZT 26, Ferroperm, Denmark), diameter 25 mm driven with sig gen and amplifiers 1.035 MHz PRF 1 kHz, 200 µs. ISATA 41, 82, 163, 326, 407 mW/cm² 10 min exposure	★★ Ⓢ Ⓣ Ⓜ Ⓒ Inverted tank dip method. Transducers 7.7mm from 24-well plate base. Temperature monitored: temperatures up to 48°C found at highest intensity exposure. Water in tank heated to similar levels and same cellular responses observed. Power levels verfied by Radiation force balance, ISATA estimated by dividing power by transducer front face area	↑wnt/β-catenin pathway (via PI3K/Akt & mTOR cascades (induced by temperature rise)	Olkku et al. 2010 [69]
MG63 human osteoblast-like cell line Human periodontal ligament (PDL) cells	Custom transducer (∅ 22 mm) and drive system 3 MHz CW, ISATA = 140 – 990 mW/cm² Calibrated in same setup as exposures; spatial measurements as well as maxima reported.	★★ Ⓢ Ⓣ Ⓜ Ⓒ Custom tank method. Cells grown and exposed in standard cell culture flask but in situ measurements of acoustic amplitude, temperature and check on cavitation carried out. Temperature rises increased from +0.1°C to +0.5°C over range of intensities. 2005 study showed evidence of cavitation and significant temperature rises at intensities > 500 mW/cm² but not below. Did find fluid flow at all intensities (measured with Doppler technique)	-**proliferation** MG63 osteoblasts: ↑FN (at 140 mW/cm² only); ↓ON; ↓OPN; ↓BSP; -COL1 ↑tgf-β1; ↑tgf-β3 PDL: ↓FN; ↑ON (140 mW/cm² only); ↑OPN (990 mW/cm² only); ↓COL1; ↑rankl, ↓opg	Harle et al. 2001 & 2005 [139, 140]

Cell model	US device / exposure	US exposure method	Results	Ref
Human adipose-derived MSCs (Ad-HMSCs) Human fetal osteoblasts (Hfobs)	Sonicator 740 (Mettler electronics, US) $\varnothing$ 35 mm, 1 MHz, 200μs, 100Hz, 30 mW/cm^2 20 mins daily for 1 day (PCR) up to 12 days (collagen / mineralisation study)	(★) (S) (T) (M) (C) Novel method. Cells grown in Opticell cell culture systems (Nunc, US) and incubated in simulated microgravity. LIPUS exposure involved floating the Opticell in a small tank filled with 3-5mm depth degassed water. The transducer was coupled to the base of the tank (means unknown). Cavitation not assessed – low pressure of simulated microgravity would make cavitation more likely	Both cell types: ↑runx2, ↑osx, Ad-HMSC: ↑ALP (G & μG) ↑rankl/opg ratio Hfobs: ↑collagen ↑mineralisation All effects more significant in μG	Uddin and Qin 2013 [221]
All stages and mature bone: osteocytes as regulators of bone tissue growth and remodelling				
Murine preosteoblast cell line MC3T3-E1, matured for up to 4 weeks in osteogenic media	Custom 6 x $\varnothing$25 mm PZT-4 transducers 1.5 MHz, 200μs, 1 kHz, 30mW/cm^2 ISATA 1 x 20 minutes 4 weeks	(★★) (S) (T) (M) (C) Absorption tube method. Six transducers held in tank 130 mm below six-well plate with silicon absorption chamber on top to eliminate reflections (verified by in situ measurement reported in previous paper [222]).	-col1a1, -alp, -ocn, -runx2, -opg ↑rankl/opg ratio (Encourages osteoclastogenesis)	Bandow et al. 2007 [71]
Osteocyte cell line MLO-Y4 exposed to LIPUS then media used to culture preosteoblast cell line MC3T3-E1	Custom setup with 6 Exogen 4000+ transducers (Smith & Nephew, US) calibrated to deliver 1.5 MHz, 30 mW/cm^2, 200μs, 1 kHz at 3 different separations 0mm, 60 mm and 130 mm from base of culture dish	(★★) (S) (T) (M) (C) Direct coupling method. Single petri dishes on array of six transducers (unsure of coupling / crosstalk between transducers). Separation from transducers to base of culture dishes controlled via rubber cylinders. Acoustic parameters fully assessed except for assessment of effects of dish. Temperature not monitored.	Osteocytes: ↑ β-catenin (Wnt-β-catenin mechanotransduction pathway) at 60 mm and 130 mm. MC3T3-E1 in osteocyte media: ↑**migration** (max 130 mm) ↑**mineralisation** (max 130 mm) ↓**proliferation** (min 130 mm)	Fung et al. 2014 [39]

Table A.2: Summary of in vitro studies, grouped by stage of secondary fracture healing and cell type.
*Device and LIPUS parameters are described and LIPUS exposure setups summarised with symbols from Table A.1. Macro cellular responses are given in bold (e.g., ↓**proliferation**). Protein markers are upper case, e.g., ↑COX-2, and RNA markers in lowercase (e.g., ↑runx2).*

APPENDIX B
PROGRAMS AND MACROS

This appendix provides example programs and macros written and used in the study. The thesis text describes the full purpose of each, and a brief description is provided at the beginning of each program section. A table of contents is provided below, with appendix page number and the thesis page in which the routine is referenced.

B.1 MATLAB Programs

B.1.1 Analyse_XY_Scan_SACellArea.m

This Matlab routine post-processes two-dimensional RASTER scan data from the scanning tank and computes spatial average pressures and intensities across a pre-defined area (in this example, the cell growth area of the biocell).

```matlab
%% Analyse_XY_Scan_SACellArea.m, v2.0
% v1.0 Created by Jill Savva, 31-Jul-2018
% Modified and updated to v2.0 09-May-2019
% Reads in delimited data files from scanning tank
% And converts to usable format for further analysis
% Includes calculation of spatial average parameters across cell-holder
% area (a circle of radius 35mm)
%
%% First clear variables then set up some constants
% Set up density (rho) and speed of sound (c) in water at temp T
% rho values from Preston, c from Lubber & Graaf eqn
clearvars;

T = 30 %degs C
c = 1405.03 + 4.624 * T - 0.0383 * T^2   %m/s
rho = (0.9978 + 0.9973) / 2 * 1000  %kg/m^3
rho_c = rho * c;

freq = 45000;
DC_Offset = 0.60e-3   %average measured with no o/p from sig gen
nSamples = 1000;

%Hydrophone sensitivities
%0.5mm hydrophone (1 MHz) s/n 2714
%Hydrophone sensitivity
%Mh = 297;                  %mV/MPa
%2mm hydrophone s/n 2716 at 45 kHz (interpolated from 40 & 50 kHz M)
Mh = 1639;                 %mV/MPa

%Booster amp gain at 1 MHz
%Booster_Amp_Gain_dB = 30.2;
%Booster_Amp_Gain = 10^(Booster_Amp_Gain_dB/20);         %Linear gain

%Calculate conversion factor - Volts to Pascals
%V2Pa = 1e9/Booster_Amp_Gain/Mh
V2Pa = 1e9/Mh;

% LIPUS pulse repetition rate (prr) and pulse width (pw) for ISATA calcs
prr = 1000;        %Hz
pw = 200e-6;       %seconds

%% Define input file

DataPath = 'C:\Users\jills\OneDrive - University of Glasgow\Transducers\Xuans
Transducers\ShortCosine\ScanData\28-Aug-2019\MI020\';

DataFileStart = '45kHz_6mm_MI020_XY_'
DataFileExt = '_AVG.txt';
delimiter = '\t';
startRow = 2;

%% Format for each line of text:
%   double (%f) for 5 + nSamples
% For more information, see the TEXTSCAN documentation.
F = '%f';
NF = 4 + nSamples;
formatF = F;
for n = 1:NF
    formatF = [formatF, F];
end
formatSpec = [formatF, '%[^\n\r]'];
```

```matlab
%% Scan details
%All distances (span, step, start and end) in um (1e-6 m)
XSpan = 80000;
XStep = 2000;
if (XSpan > 0)
    Xn = round(XSpan/XStep) + 1;
    XEnd = round(XSpan / 2);
    XStart = -XEnd;
else
    Xn = 1;
    XStart = 0;
    XEnd = 0;
end

YSpan = 80000;
YStep = 2000;
if (YSpan > 0)
    Yn = round(YSpan/YStep) + 1;
    YEnd = round(YSpan / 2);
    YStart = -YEnd;
else
    Yn = 1;
    YStart = 0;
    YEnd = 0;
end

ZSpan = 0;
ZStep = 1000;
if (ZSpan > 0)
    Zn = round(ZSpan/ZStep) + 1;
else
    Zn = 1;
end

%% Loop to construct filenames and append data to result array
filecount = 0;
for iz = 0:ZStep:ZSpan

    for iy = YStart:YStep:YEnd
        PosnString = sprintf('Y%dZ%d',iy,iz);
        %Now construct the next data filename
        filename = [DataPath, DataFileStart,PosnString,DataFileExt];

        % Open the data file
        fileID = fopen(filename,'r');

        % Read data into dataArray
        dataArray = textscan(fileID, formatSpec, 'Delimiter', delimiter, 'TextType',
'string', 'EmptyValue', NaN, 'HeaderLines' ,startRow-1, 'ReturnOnError', false,
'EndOfLine', '\r\n');

        % Now close the file
        fclose(fileID);

        %Now either append this to existing data array or create one
        if iz==0 && iy==YStart
            Scan = [dataArray{1:end-1}];
        else
            Scan = [Scan; dataArray{1:end-1}];
        end %if iz,iy
        filecount = filecount + 1;
    end %iy
end %iz

%%Check the DC offset
dataStart = 6;
dataEnd = nSamples + dataStart - 1;
ScanData = Scan(:,dataStart:dataEnd);
AverageRows = mean(ScanData,2);
DC_Offset_Check = mean(AverageRows)
clearvars ScanData AverageRows;

%% Now sort the data array to order the X values
size_Scan = size(Scan);
RowSize = size_Scan(2);
```

```matlab
%Initialise the sorted array
Scan_Sorted = Scan;

for n=0:(filecount-1)
    if mod(n,2) == 1
        rowStart = Xn * n + 1;
        rowEnd = Xn * (n+1);
        %X is in reverse order so correct the order in the sorted array
        Scan_Sorted(rowStart:rowEnd, 1:RowSize) = Scan(rowEnd:-1:rowStart, 1:RowSize);
    end
end

%% Now correct data for dc offset
%Now create data array with DC offset applied
Scan_Sorted_Corrected = Scan_Sorted;

for i = 1:Zn
    for j = 1:Yn
        for k = 1:Xn
            row = Xn * Yn* (i-1) + Xn * (j-1) + k;
            Scan_Sorted_Corrected(row,dataStart:dataEnd) =
Scan_Sorted(row,dataStart:dataEnd) - DC_Offset;
        end %for k
    end %for j
end %for i

%% Find pmax, pmin, prms and pms
%Also calculating spatial average sums
%Set up distances in grids (in mm)
%Z0 = 105000; %Start distance of scan
GridX = [XStart:XStep:XEnd]/1000;
GridY = [YStart:YStep:YEnd]/1000;
%GridZ = [Z0:ZStep:Z0+ZSpan]/1000;

%Now create Vmax, Vmin, Vrms & Vms
Vmax = zeros(Xn,Yn);
Vmin = zeros(Xn,Yn);
Vrms = zeros(Xn,Yn);
Vms = zeros(Xn,Yn);

%Now create pmax, pmin, prms, pms and ptp (temporal peak pressure)
pmax = zeros(Xn,Yn);
pmin = zeros(Xn,Yn);
prms = zeros(Xn,Yn);
pms = zeros(Xn,Yn);
ptp = zeros(Xn,Yn);

% Radius of circle (mm) for spatial average sums
SA_radius1 = 2;
SA_radius2 = 35;

%Set summation values to zero (SA_N = number of points summed)
SA1_N = 0;
SA1_PNP_sum = 0;
SA1_PMS_sum = 0;

SA2_N = 0;
SA2_PNP_sum = 0;
SA2_PMS_sum = 0;

for j = 1:Yn
    for k = 1:Xn
        row = Xn * (j-1) + k;
        %NOTE each y value is a row and x data is in cols in array.
        %So order when indexing array is y,x
        Vmax(j,k) = max(Scan_Sorted_Corrected(row,dataStart:dataEnd));
        Vmin(j,k) = min(Scan_Sorted_Corrected(row,dataStart:dataEnd));
        Vrms(j,k) = rms(Scan_Sorted_Corrected(row,dataStart:dataEnd));
        Vms(j,k) = Vrms(j,k)^2;

        %Now convert to pressures
        pmax(j,k) = Vmax(j,k)*V2Pa;
        pmin(j,k) = -Vmin(j,k)*V2Pa;
        prms(j,k) = Vrms(j,k)*V2Pa;
        pms(j,k) = prms(j,k)^2;
        MI(j,k) = pmin(j,k)/1e6/(freq/1e6)^0.5;
```

```
                %and find the temporal peak acoustic pressure
                %this is the maximum rarefactional or compressional
                %pressure and is used to calculate ISAPA
                ptp(j,k) = max(pmax(j,k), pmin(j,k));

                %Now if distance from centre is <= SA1/2_radius, add to sums
                distance = (GridX(k)^2 + GridY(j)^2)^0.5;
                if (distance <= SA_radius2)
                    SA2_N = SA2_N + 1;
                    SA2_PNP_sum = SA2_PNP_sum + pmin(j,k);
                    SA2_PMS_sum = SA2_PMS_sum + pms(j,k);
                    if (distance <= SA_radius1)
                        SA1_N = SA1_N + 1;
                        SA1_PNP_sum = SA1_PNP_sum + pmin(j,k);
                        SA1_PMS_sum = SA1_PMS_sum + pms(j,k);
                    end %if (distance <= SA1_radius)
                end %if (distance <= SA2_radius)
    end %for k
end %for j

%Pressure parameters
SA1_PNP_kPa = SA1_PNP_sum / SA1_N / 1000;
SA1_MI = SA1_PNP_kPa / 1000;
SATA1_PNP_kPa = SA1_PNP_kPa * pw * prr;
SATA1_MI = SA1_MI * pw * prr;

SA1_PMS = SA1_PMS_sum / SA1_N;
ISAPA_SA1 = SA1_PMS / rho_c / 10;            %mW/cm^2
ISATA_SA1 = ISAPA_SA1 * prr * pw;

SA2_PNP_kPa = SA2_PNP_sum / SA2_N / 1000;
SA2_MI = SA2_PNP_kPa / 1000;
SATA2_PNP_kPa = SA2_PNP_kPa * pw * prr;
SATA2_MI = SA2_MI * pw * prr;

SA2_PMS = SA2_PMS_sum / SA2_N;
ISAPA_SA2 = SA2_PMS / rho_c / 10;            %mW/cm^2
ISATA_SA2 = ISAPA_SA2 * prr * pw;

%% Plot data on colourscale charts
%Y rows, X cols
figure(1); imagesc(GridX, GridY, prms / 1000); axis xy; colorbar;
c1 = colorbar; c1.Label.String = 'kPa';
title('RMS Pressure'); xlabel('X (mm)'); ylabel('Y (mm)');

figure(2); imagesc(GridX, GridY, pmin / 1000); axis xy; colorbar;
c3 = colorbar; c3.Label.String = 'kPa';
title('Peak Negative Pressure'); xlabel('X (mm)'); ylabel('Y (mm)');

figure(3); imagesc(GridX, GridY, MI); axis xy; colorbar;
c3 = colorbar; c3.Label.String = 'MI';
title('Mechanical Index'); xlabel('X (mm)'); ylabel('Y (mm)');

%% Analysis - X and Y line scans
% This will enable beam widths to be found
%Find columns where X=0 (X0)
X0 = round(Xn/2);
%And rows where Y=0 (Y0)
Y0 = round(Yn/2);

%Now find the prms line scans (in kPa)
X_LineScan_rms = prms(Y0,:) / 1000;
Y_LineScan_rms = transpose(prms(:,X0)) / 1000;

%Now plot the line scans
figure(4); plot(GridX,X_LineScan_rms);
title('X Line Scan: RMS Pressure');
xlabel('X (mm)'); ylabel('kPa');

figure(5); plot(GridY,Y_LineScan_rms);
title('Y Line Scan: RMS Pressure');
xlabel('Y (mm)'); ylabel('kPa');
%And now display & store pnp line scans(in kPa)
X_LineScan_pnp = pmin(Y0,:) / 1000;
Y_LineScan_pnp = transpose(pmin(:,X0)) / 1000;

figure(6); plot(GridX,X_LineScan_pnp);
```

```matlab
title('X Line Scan: Peak-negative Pressure');
xlabel('X (mm)'); ylabel('kPa');

figure(7); plot(GridY,Y_LineScan_pnp);
title('Y Line Scan: Peak-negative Pressure');
xlabel('Y (mm)'); ylabel('kPa');

%And now display MI line scans
X_LineScan_MI = MI(Y0,:);
Y_LineScan_MI = transpose(MI(:,X0));

figure(8); plot(GridX,X_LineScan_MI);
title('X Line Scan: Mechanical Index');
xlabel('X (mm)'); ylabel('MI');

figure(9); plot(GridY,Y_LineScan_MI);
title('Y Line Scan: Mechanical Index');
xlabel('Y (mm)'); ylabel('MI');

%Nice surface plot!
figure(10);
surf(GridX,GridY,MI); colorbar;
title('Mechanical Index'); xlabel('X (mm)'); ylabel('Y (mm)');

%% Next find beam parameters
%Convert pms matrix into array
pms_array = zeros(Xn*Yn,1);
ptp_array = zeros(Xn*Yn,1);
pmax_array = zeros(Xn*Yn,1);
pmin_array = zeros(Xn*Yn,1);
for j = 1:Yn
    for k = 1:Xn
        row = Xn*(j-1) + k;
        pms_array(row,1) = pms(j,k);
        ptp_array(row,1) = ptp(j,k);
        pmin_array(row,1) = pmin(j,k);
        pmax_array(row,1) = pmax(j,k);
    end %for k
end %for j

%First find pmst (i.e. total mean square pressure) and ptpt
%(total peak positive acoustic pressure)
% transpose results in scalar sum
pmst = sum(pms_array);
ptpt = sum(ptp_array);

%now sort the arrays into descending order
pms_array_descending = sort(pms_array,'descend');
ptp_array_descending = sort(ptp_array,'descend');
pmin_array_descending = sort(pmin_array,'descend');
pmax_array_descending = sort(pmax_array,'descend');

%Now sum until you get to 0.75pmst (or 0.75ptpt)
BCS_pmst = 0.75*pmst(1);
BCS_ptpt = 0.75*ptpt(1);

sum_n = 0;
sum_n1 = pms_array_descending(1);
i=1;
while sum_n1 <= BCS_pmst
    sum_n = sum_n + pms_array_descending(i);
    sum_n1 = sum_n1 + pms_array_descending(i+1);
    i = i+1;
end % while sum_n1

%Compute area covered by one scan point, in cm^2
A0 = (YStep/10000) * (XStep/10000)
%Compute Beam Cross Sectional Area
npms = i-1
ABCS_pms = A0*npms
%Compute AER. Note this AER figure may be in error if Z is not equal to 0.3cm
AER_pms = 1.333 * ABCS_pms
sum_n = 0;
sum_n1 = ptp_array_descending(1,1);

i=1;
while sum_n1 <= BCS_ptpt
```

```matlab
    sum_n = sum_n + ptp_array_descending(i);
    sum_n1 = sum_n1 + ptp_array_descending(i+1);
    i = i+1;
end % while sum_pmst

%Compute ABCS, in cm^2
nptp = i-1
ABCS_ptp = A0*nptp

%Compute AER
%Note this AER figure may be in error if Z is not equal to 0.3cm
AER_ptp = 1.333 * ABCS_ptp

%% Now calculate output parameters
%Now we can compute intensity parameters for ABCS
ISPTA = ptp_array_descending(1)^2/rho_c / 10
%Note unless ISATA is calculated from AER at 0.3cm, it is an approximation.
ISAPA_61689 = A0 * pmst(1)/rho_c/AER_pms / 10;  %mW/cm^2
ISATA_61689 = ISAPA_61689 * prr * pw;           %mW/cm^2

%Other parameters of interest
pmin_max = pmin_array_descending(1)
p_pos = pmax_array_descending(1)
ptp = max (pmin_max, p_pos)

%Now the max mechanical index (unattenuated) - this is
%pmin_max*f^0.5/1MPaMHz^-0.5
f = 0.045 %MHz
MI_max = pmin_max / 1e6 / f^0.5

%And what is the pmin and MI at centre (X=0, Y=0)?
pmin0 = pmin(Y0,X0)
MI_zero = pmin0 / 1e6 / f^0.5

pms0 = pms(Y0,X0)
I0 = pms0/rho_c

%% Now for more traditional Beam area and ISAPA calcs - using pms
maxpms = pms_array_descending(1);

%Start off looking at all the possibilities!
maxpms3dB = maxpms * 10^(-3/10);
maxpms6dB = maxpms * 10^(-6/10);
maxpms10dB = maxpms * 10^(-10/10);
%maxpms20dB = maxpms * 10^(-20/10);

%set up variables for area count
n3=0; n6=0; n10=0;
%and for sum of pms values
sum3=0; sum6=0; sum10=0;

%use pms_array_descending to find all the necessary points
i=1;

while pms_array_descending(i) >= maxpms10dB
    n10 = n10 + 1;
    sum10 = sum10 + pms_array_descending(i);

    if pms_array_descending(i) >= maxpms6dB
        n6 = n6 + 1;
        sum6 = sum6 + pms_array_descending(i);
    end %if maxpms6

    if pms_array_descending(i) >= maxpms3dB
        n3 = n3 + 1;
        sum3 = sum3 + pms_array_descending(i);
    end %if maxpms3

    i = i + 1;
end %while pms_array_descending >= maxpms10dB

%Now compute the ISAPAs (A0s cancel out, but divide by 1e4 to get mW/cm^2 - 1e3/1e4 = /10)
A_3dB = n3*A0;
ISAPA_3dB = sum3 / n3 / rho_c / 10;     %mW/cm^2
ISATA_3dB = ISAPA_3dB * prr * pw;       %mW/cm^2

A_6dB = n6*A0;
```

```
ISAPA_6dB = sum6 / n6 / rho_c / 10;      %mW/cm^2
ISATA_6dB = ISAPA_6dB * prr * pw;        %mW/cm^2


A_10dB = n10*A0;
ISAPA_10dB = sum10 / n10 / rho_c / 10; %mW/cm^2
ISATA_10dB = ISAPA_10dB * prr * pw;      %mW/cm^2

%% Collate parameters into a suitable format for copying to Excel
pmin0_kPa = pmin0/1000;
pmin_max_kPa = pmin_max/1000;
OutputTable = table({DataFileStart;'SA1(mm)'; 'SA2(mm)'; 'ISAPA_SA1'; 'ISAPA_SA2';
'ISATA_SA1'; 'ISATA_SA2'; 'ISAPA_3dB';'ISAPA_6dB';'ISAPA_10dB';'ISAPA_61689'; 'ISATA_3dB';
'ISATA_6dB'; 'ISATA_10dB'; 'ISATA_61689'; 'pmin0_kPa'; 'pmin_max_kPa'; 'SA1_PNP_kPa';
'SA2_PNP_kPa'; 'MI_zero'; 'MI_max'; 'SA1_MI'; 'SA2_MI'; 'SATA1_PNP_kPa'; 'SATA2_PNP_kPa';
'SATA1_MI'; 'SATA2_MI'}, [0; SA_radius1; SA_radius2; ISAPA_SA1; ISAPA_SA2; ISATA_SA1;
ISATA_SA2; ISAPA_3dB; ISAPA_6dB; ISAPA_10dB; ISAPA_61689; ISATA_3dB; ISATA_6dB; ISATA_10dB;
ISATA_61689; pmin0_kPa; pmin_max_kPa; SA1_PNP_kPa; SA2_PNP_kPa; MI_zero; MI_max; SA1_MI;
SA2_MI; SATA1_PNP_kPa; SATA1_PNP_kPa; SATA1_MI; SATA2_MI])
```

B.1.2 Process_XY20_XY80.m

This Matlab routine combines two sets of XY RASTER scans, with 20 mm span in 0.5 mm
steps and 80 mm span in 2 mm steps. The code was written specifically for scans
conducted on the 1 MHz / V303 transducer to compute accurate spatial average parameters
across a pre-defined area. In this case, the pre-defined area is the cell growth area of a
biocell.

```
%% Process_XY20_XY80.m
% takes the two V303 raster scans with 80mm span (2mm steps)
% and 20 mm span (0.5 mm steps) and combines them, computing more
% accurate spatial-averages

%% Clear variables and set up constants
clearvars;

T = 30 %degs C
c = 1405.03 + 4.624 * T - 0.0383 * T^2   %m/s
rho = 0.9957 * 1000   %kg/m^3
rho_c = rho * c;

freq = 1000000;
prr = 1000;
pw = 200e-6;

%Radius in mm of circle for computing spatial average parameters
Radius = 25;

%% Read in csv files
Path = 'C:\Users\jills\OneDrive - University of Glasgow\Transducers\Olympus V303\Scans\30-
Aug-2019\MI020\';
csv_Filename = [Path, '1MHz_60mm_MI020_XY20__XY_prms.csv'];
XY20_prms_csv = csvread(csv_Filename);
csv_Filename = [Path, '1MHz_60mm_MI020_XY20__XY_pnp.csv'];
XY20_pnp_csv = csvread(csv_Filename);

csv_Filename = [Path, '1MHz_60mm_MI020_XY__XY_prms.csv'];
XY80_prms_csv = csvread(csv_Filename);
csv_Filename = [Path, '1MHz_60mm_MI020_XY__XY_pnp.csv'];
XY80_pnp_csv = csvread(csv_Filename);

%% Convert csv data to pms/pnp with no coordinates
XY20_prms = XY20_prms_csv(2:end,:);
XY20_pms = XY20_prms.^2;
XY20_pnp = XY20_pnp_csv(2:end,:);

XY80_prms = XY80_prms_csv(2:end,:);
XY80_pms = XY80_prms.^2;
```

```matlab
XY80_pnp = XY80_pnp_csv(2:end,:);

A_XY20 = (0.5/10)^2; %area of each raster scan element in cm^2
XY20_pms_xA = XY20_pms .* A_XY20;
XY20_pnp_xA = XY20_pnp .* A_XY20;

%Now sum all the pms x area. This will be the contribution of XY20 to the
%spatial-average intensities
sum_XY20_pms_1 = sum(XY20_pms_xA);
sum_XY20_pms = sum(sum_XY20_pms_1);

%Then do the same for PNP:
sum_XY20_pnp_1 = sum(XY20_pnp_xA);
sum_XY20_pnp = sum(sum_XY20_pnp_1);

%Now clear some vars
clearvars sum_XY20_pms_1 sum_XY20_pnp_1;

%Now sum the elements of XY80_pms and pnp within Radius (mm) of the centre
A_XY80 = (0.2)^2 %in cm^2

%set sums to the XY20 totals (as these will be included in calcs)
sum_pms = sum_XY20_pms;
sum_pnp = sum_XY20_pnp;

%Now loop through the XY80 points. Exclude those covered by XY20, and
% those outside the Radius (mm) radius circle.
for i = 1:41
    i_mm = -40 + (i-1) * 2;
    for j = 1:41
        j_mm = -40 + (j-1) * 2;
        if not((i_mm >= -10) && (i_mm <= 10) && (j_mm >= -10) && (j_mm <= 10))

            distance = (i_mm^2 + j_mm^2)^0.5;
            if distance <= Radius
                sum_pms = sum_pms + XY80_pms(i,j)*A_XY80;
                sum_pnp = sum_pnp + XY80_pnp(i,j)*A_XY80;

            end %if distance
        end % if i etc
    end %for j
end %for i

%% Now compute the spatial average parameters for the cell area
A_cells = pi * (Radius/10)^2; %cm^2
Max_pnp = max(max(XY20_pnp));
SA_PNP_kPa = sum_pnp / A_cells / 1000
SA_MI = SA_PNP_kPa / 1000;

SA_PMS = sum_pms / A_cells
ISAPA_SA = SA_PMS / rho_c / 10            %mW/cm^2
ISATA_SA = ISAPA_SA * prr * pw

%% Now output to a table for easy copying to Excel

OutputTable = table({'Radius (mm)';'Max_pnp'; 'ISAPA_SA'; 'ISATA_SA'; 'SA_PNP_kPa'; ...
    'SA_MI'},[Radius; Max_pnp; ISAPA_SA; ISATA_SA; SA_PNP_kPa; SA_MI])

%table_filename = [Temp_Data_Path, DataFileStart, 'Table.csv'];
%writetable(OutputTable,table_filename);
```

B.1.3 Process_Temperatures.m

This Matlab routine was written to process, analyse and present the results of the in-situ temperature data measured with a fibre-optic hydrophone (see Section 4.2.3).

```matlab
%% Process_Temperatures.m
% Created 25/04/2021 by Jill Savva
% 1) Reads in tab-delimited text files of temperature data from FOH
```

```matlab
% 2) Displays raw results
% 3) Calculates trend (gradients) when US is ON and US is OFF
% 4) Plots the raw data and trend lines

%% Clean up
clear;

%% Initialize variables.
filename = 'C:\Users\jills\Documents\MATLAB\Pressure-temperature\1MHz-MI020-temp.txt';
delimiter = '\t';
startRow = 3;

%% Read in data from tab delimited text file
%   column1: double (%f)
%   column3: double (%f)
% For more information, see the TEXTSCAN documentation.
formatSpec = '%f%*q%f%*s%[^\n\r]';

% Open the text file.
fileID = fopen(filename,'r');

% Read columns of data according to the format.
% This call is based on the structure of the file used to generate this
% code. If an error occurs for a different file, try regenerating the code
% from the Import Tool.
textscan(fileID, '%[^\n\r]', startRow-1, 'WhiteSpace', '', 'ReturnOnError', false,
'EndOfLine', '\r\n');
dataArray = textscan(fileID, formatSpec, 'Delimiter', delimiter, 'TextType', 'string',
'EmptyValue', NaN, 'ReturnOnError', false);

% Close the text file.
fclose(fileID);
RawData = [dataArray{1:end-1}];
RawDataSize = size(RawData);

%Convert time to minutes (./60)
RawData(:,1) = RawData(:,1)./60;

%% Now separate out US ON and US OFF portions to compare temperature gradients
switch_on_time = 1;
switch_off_time = 21;

%first find extent of inital OFF period in array
OFF1_index = 1;
while RawData(OFF1_index,1) < switch_on_time
    OFF1_index = OFF1_index + 1;
end

%Then extent of ON period
ON_index = OFF1_index;
while RawData(ON_index,1) < switch_off_time
    ON_index = ON_index + 1;
end

%Now populate three arrays
OFF1 = RawData(1:OFF1_index,:);
ON = RawData((OFF1_index+1):ON_index,:);
OFF2 = RawData((ON_index + 1):end,:);

%check total size of new arrays are equal to the original data size
OFF1_size = size(OFF1);
ON_size = size(ON);
OFF2_size = size(OFF2);

Total_size = OFF1_size(1) + ON_size(1) + OFF2_size(1)
RawDataSize(1)

%% Perform linear regressions on OFF1, ON and OFF2 data
[OFF1_mc,OFF1_Err] = polyfit(OFF1(:,1),OFF1(:,2),1);
OFF1_m = OFF1_mc(1);
OFF1_c = OFF1_mc(2);
OFF1_Lin = polyval(OFF1_mc, OFF1(:,1), OFF1_Err);
OFF1_Lin_legend= strcat('OFF1 best fit ( ',num2str(OFF1_m,2),'*T ',num2str(OFF1_c,2),' )');

[ON_mc,ON_Err] = polyfit(ON(:,1),ON(:,2),1);
ON_m = ON_mc(1);
ON_c = ON_mc(2);
```

```matlab
ON_Lin = polyval(ON_mc, ON(:,1), ON_Err);
ON_Lin_legend = strcat('ON best fit  ( ', num2str(ON_m,2), '*T ', num2str(ON_c,2),' )');

[OFF2_mc,OFF2_Err] = polyfit(OFF2(:,1),OFF2(:,2),1);
OFF2_m = OFF2_mc(1);
OFF2_c = OFF2_mc(2);
OFF2_Lin = polyval(OFF2_mc, OFF2(:,1), OFF2_Err);
OFF2_Lin_legend = strcat('OFF2 best fit  ( ', num2str(OFF2_m,2), '*T ', num2str(OFF2_c,2),'
)');

%And now do best fit of all data:
[RawData_mc,RawData_Err] = polyfit(RawData(:,1),RawData(:,2),1);
RawData_m = RawData_mc(1);
RawData_c = RawData_mc(2);
RawData_Lin = polyval(RawData_mc, RawData(:,1), RawData_Err);
RawData_Lin_legend = strcat('All data best fit  ( ', num2str(RawData_m,2), '*T ',
num2str(RawData_c,2),' )')

%% Now plot the raw data with the linear regression lines

figure();
p2 = plot(OFF1(:,1), OFF1(:,2), ON(:,1), ON(:,2), OFF2(:,1), OFF2(:,2), ...
    OFF1(:,1), OFF1_Lin,ON(:,1), ON_Lin,OFF2(:,1),OFF2_Lin);
axis([0 23 -1.0 1.0]);
grid on; grid minor; xlabel('Time (minutes)', 'FontSize', 14);
title('Temperature Data 1 MHz', 'FontSize', 16);
ylabel('Temperature change, \circ C', 'FontSize', 14);

%set up colors and styles of lines
p2(1).Color = 'c';
p2(3).Color = 'g';
p2(4).Color = 'b'; p2(4).LineWidth = 1.5; %p2(4).LineStyle = '--';
p2(5).Color = 'k'; p2(5).LineWidth = 1.5; p2(5).LineStyle = '--';
p2(6).Color = 'k'; p2(6).LineWidth = 1.5; %p2(6).LineStyle = '--';

legend('OFF1', 'ON', 'OFF2', OFF1_Lin_legend, ON_Lin_legend, OFF2_Lin_legend);
```

B.1.4 Modulation_Drive_Calcs.m

Matlab routine written to perform and display the results of a Fast Fourier Transform (FFT) on the drive waveforms with fast and slow rise times, used in the rise time study (Section 4.5.1).

```matlab
%% Modulation_Drive_Calcs.m
%  Created by Jill Savva 29/01/2020
%  To calculate effect of amplitude modulation
%  on IPA (aim to maintain IPA and p- by elongating the pulse width)

%% Constants
% Density (rho) and speed of sound (c) in water at temp T
% rho values from Preston, c from Lubber & Graaf eqn

T = 35 %degs C
c = 1405.03 + 4.624 * T - 0.0383 * T^2   %m/s
rho = (0.9978 + 0.9973) / 2 * 1000   %kg/m^3
rho_c = rho * c

freq = 1e6; %Hz
prr = 1000; %Hz
pw = 200e-6; %s

Ts = 1e-8; %sample period
Fs = 1/Ts;

% Set up sine wave to modulate - over one duty cycle.
A = 100;    %amplitude of sine wave (100kPa?)
t = [0:Ts:1/prr-Ts];
wt = 2*pi*freq*t;
sinwt = A*sin(wt);
```

```matlab
%Plot a few cycles of the sine wave
x = t(1:1000).*1e6;
y = sinwt(1:1000);

figno = 1;
figure(figno);
plot(x,y);
axis([0 10 -150 150]);
xlabel('Time, us','FontSize',14); ylabel('Pressure, kPa','FontSize',14);
grid on; grid minor;

%Create normal pw burst
n_pw = pw/Ts %Number of samples in burst
t_size = size(t);
n_total = t_size(2);

%Create array and populate with zeros
NormalBurst = zeros(1,n_total);
%Now put in non-zero values from sine wave:
NormalBurst(1:n_pw) = sinwt(1:n_pw);
%Now plot the burst (including some zero points at end)
nplot = 30000;
xBurst = t(1:nplot) .* 1e6;
yBurst = NormalBurst(1:nplot);
figno = figno+1;
figure(figno);
plot(xBurst,yBurst, 'Color', [220/255 102/255 0]);
axis([0 nplot*Ts*1e6 -150 150]);
title('Fast rise time (rectangular window)','Fontsize',20);
xlabel('Time, us','FontSize',18); ylabel('Pressure, kPa','FontSize',18);
grid on; grid minor;


%% Modulation function setup
% Modulation is just a linear ramp up and ramp down with a period of x1 in
% centre (flat top)

ramp_duration = 50e-6;
flat_top_duration = 166.67e-6;
n_flat_top = flat_top_duration / Ts
T_Mod = 2 * ramp_duration + flat_top_duration;
n_Mod = round(T_Mod / Ts, 0)

rampStep = Ts / ramp_duration
rampup = [0:rampStep:1];
rampdown = [1:-rampStep:0];
ramp_size = size(rampup)

%Now create the modulation array and populate with zeros
Modulation = zeros(1,n_total);
Modulation(1:ramp_size(2)) = rampup;
Modulation(ramp_size(2):ramp_size(2)+n_flat_top - 1) = 1;
Modulation(ramp_size(2) + n_flat_top : 2*ramp_size(2) + n_flat_top - 1) = rampdown;

%plot the modulation function
xMod = t(1:nplot) .* 1e6;
yMod = Modulation(1:nplot);
figno = figno+1;
figure(figno);
plot(xMod,yMod);
axis([0 nplot*Ts*1e6 -0.5 1.5]);
xlabel('Time, us','FontSize',14); ylabel('Modulation multiplier','FontSize',14);
grid on; grid minor;

%Now apply modulation to sin wt
Mod_sinwt = Modulation .* sinwt;
%Now plot modulated sine wave and burst
yMod_sinwt = Mod_sinwt(1:nplot);
figno = figno+1;
figure(figno);
plot(xMod, yMod_sinwt, 'Color', [0 102/255 220/255]);
axis([0 nplot*Ts*1e6 -150 150]);
title('Slow rise time (trapezoidal window)','Fontsize',20);
xlabel('Time, us','FontSize',18); ylabel('Pressure, kPa','FontSize',18);
grid on; grid minor;

%Now calculate pulse-pressure squared integral p2 and pulse Intensity Ip
```

```matlab
Square_NormalBurst = (NormalBurst .* 1000) .^ 2; %*1000 to convert to Pa
p2_NormalBurst = sum(Square_NormalBurst);
%Now find the Pulse average intensity, IPA & Temporal Average, ITA
IPA_NormalBurst = p2_NormalBurst / rho_c / n_pw / 10 %/10 to get mW/cm^2
ITA_NormalBurst = IPA_NormalBurst * pw * prr

Square_Mod_sinwt = (Mod_sinwt .* 1000) .^2;
p2_Mod_sinwt = sum(Square_Mod_sinwt);
%Now find the Pulse average intensity, IPA & Temporal Average, ITA
IPA_Mod_sinwt = p2_Mod_sinwt / rho_c / n_Mod / 10 %/10 converts to mW/cm^2
ITA_Mod_sinwt = IPA_Mod_sinwt * T_Mod * prr

n_FFT = n_total;
%Now compute and display ffts
FFT_sinwt = fft(sinwt(1:n_FFT));
P2 = abs(FFT_sinwt / n_FFT);
P1_sinwt = P2(1 : round(n_FFT / 2 + 1,0));
P1_sinwt(2:end-1) = 2*P1_sinwt(2:end-1);

FFT_NormalBurst = fft(NormalBurst(1:n_FFT));
P2 = abs(FFT_NormalBurst / n_FFT);
P1_NormalBurst = P2(1 : round(n_FFT / 2 + 1,0));
P1_NormalBurst(2:end-1) = 2*P1_NormalBurst(2:end-1);

FFT_Mod_sinwt = fft(Mod_sinwt(1:n_FFT));
P2 = abs(FFT_Mod_sinwt / n_FFT);
P1_Mod_sinwt = P2(1 : round(n_FFT / 2 + 1,0));
P1_Mod_sinwt(2:end-1) = 2*P1_Mod_sinwt(2:end-1);

%Now plot the ffts on the same plot
%Set up frequency (MHz) for x axis
f = Fs*(0:round(n_FFT/2,0))/n_FFT / 1e6;
figno = figno+1;
figure(figno);
%plot(f(750:1250),P1_sinwt(750:1250), f(750:1250), P1_NormalBurst(750:1250), f(750:1250),
P1_Mod_sinwt(750:1250));
%legend('1 MHz sine','1 MHz burst','Modulated 1 MHz burst');

fftLin = plot(f(750:1250), P1_NormalBurst(750:1250), f(750:1250), P1_Mod_sinwt(750:1250));
set(fftLin(1), 'color', [220/255 102/255 0]);
set(fftLin(2), 'color', [0 102/255 220/255]);
%plot(f, P1_NormalBurst, f, P1_Mod_sinwt);
legend({'1 MHz burst','Modulated 1 MHz burst'},'FontSize',14);
xlabel('Frequency, MHz','FontSize',14); ylabel('|FFT|','FontSize',14);
grid on; grid minor;

%log FFT re max
max_FFT = max(max(P1_NormalBurst), max(P1_Mod_sinwt));
figno = figno+1;
figure(figno);
fftLog = plot(f(750:1250), 20*log10(P1_NormalBurst(750:1250) ./ max_FFT),f(750:1250),
20*log10(P1_Mod_sinwt(750:1250) ./ max_FFT));
set(fftLog(1), 'color', [220/255 102/255 0]);
set(fftLog(2), 'color', [0 102/255 220/255]);

%plot(f, 20*log10(P1_NormalBurst), f, 20*log10(P1_Mod_sinwt));
%legend({'1 MHz burst','Modulated 1 MHz burst'},'FontSize',14);
legend({'Fast rise time','Slow rise time'},'FontSize',12, 'Location', 'northeast');
title('FFT','Fontsize',14);
xlabel('Frequency, MHz','FontSize',14); ylabel('20 log_{10} (|FFT| /
|FFT|_{max})','FontSize',14);
axis([0.75 1.25 -50 0]);
grid on; grid minor;
```

B.1.5 Pressure_Mask_from_XY_Scan.m

This Matlab routine reads in an XY RASTER scan (in this case, the combined scan of the
V303, 1 MHz transducer) and sorts the data into bins of pre-determined peak-negative
pressure ranges. As well as displaying contour maps of the bin extents, the routine outputs
a series of 'mask' files to apply to microscope scans covering a 40mm x 40 mm area.

```matlab
%% Pressure_Mask_from_XY_Scan.m
%  Created by Jill Savva, 19-Feb-2020
%  Reads in delimited data files from scanning tank
%  and sorts into pressure bins, creating masks for 40mm x 40mm microscope scans
%% First clear variables then set up some constants
% Set up density (rho) and speed of sound (c) in water at temp T
% rho values from Preston, c from Lubber & Graaf eqn
clearvars;

FigNo = 0;

T = 25.5 %degs C
c = 1405.03 + 4.624 * T - 0.0383 * T^2   %m/s
rho = (0.9978 + 0.9973) / 2 * 1000  %kg/m^3
rho_c = rho * c;

freq = 1000000;
DC_Offset = 0.1e-3  %average measured with no o/p from sig gen
nSamples = 2000;

%Hydrophone sensitivity
%0.5mm hydrophone (1 MHz) s/n 2714
%Hydrophone sensitivity
Mh = 297;                    %mV/MPa

%Calculate conversion factor - Volts to Pascals
V2Pa = 1e9/Mh;

% LIPUS pulse repetition rate (prr) and pulse width (pw) for ISATA calcs
prr = 1000;       %Hz
pw = 200e-6;      %seconds

%% Define input file
DataPath = 'C:\Users\jills\OneDrive - University of Glasgow\Transducers\Olympus
V303\Scans\13-Feb-2020\';

DataFileStart = 'V303_Rigol_60mm_100kPa_XYscan_'
DataFileExt = '_AVG.txt';
delimiter = '\t';
startRow = 2;

%% Format for each line of text:
%   double (%f) for 5 + nSamples
% For more information, see the TEXTSCAN documentation.
F = '%f';
NF = 4 + nSamples;
formatF = F;
for n = 1:NF
    formatF = [formatF, F];
end
formatSpec = [formatF, '%[^\n\r]'];

%% Scan details
%All distances (span, step, start and end) in um (1e-6 m)
XSpan = 45000;
XStep = 500;
if (XSpan > 0)
    Xn = round(XSpan/XStep) + 1;
    XEnd = round(XSpan / 2);
    XStart = -XEnd;
else
    Xn = 1;
    XStart = 0;
    XEnd = 0;
end

YSpan = 45000;
YStep = 500;
if (YSpan > 0)
    Yn = round(YSpan/YStep) + 1;
    YEnd = round(YSpan / 2);
    YStart = -YEnd;
else
    Yn = 1;
    YStart = 0;
    YEnd = 0;
end
```

```matlab
ZSpan = 0;
ZStep = 1000;
if (ZSpan > 0)
    Zn = round(ZSpan/ZStep) + 1;
else
    Zn = 1;
end

%% Loop to construct filenames and append data to result array
filecount = 0;
for iz = 0:ZStep:ZSpan
    for iy = YStart:YStep:YEnd
        PosnString = sprintf('Y%dZ%d',iy,iz);
        %Now construct the next data filename
        filename = [DataPath, DataFileStart,PosnString,DataFileExt];

        % Open the data file
        fileID = fopen(filename,'r');

        % Read data into dataArray
        dataArray = textscan(fileID, formatSpec, 'Delimiter', delimiter, 'TextType',
'string', 'EmptyValue', NaN, 'HeaderLines' ,startRow-1, 'ReturnOnError', false,
'EndOfLine', '\r\n');

        % Now close the file
        fclose(fileID);

        %Now either append this to existing data array or create one
        if iz==0 && iy==YStart
            Scan = [dataArray{1:end-1}];
        else
            Scan = [Scan; dataArray{1:end-1}];
        end %if iz,iy
        filecount = filecount + 1;
    end %iy
end %iz

%%Check the DC offset
dataStart = 6;
dataEnd = nSamples + dataStart - 1;
ScanData = Scan(:,dataStart:dataEnd);
AverageRows = mean(ScanData,2);
DC_Offset_Check = mean(AverageRows)

%% Now sort the data array to order the X values
size_Scan = size(Scan);
RowSize = size_Scan(2);

%Initialise the sorted array
Scan_Sorted = Scan;

for n=0:(filecount-1)

    if mod(n,2) == 1
        rowStart = Xn * n + 1;
        rowEnd = Xn * (n+1);
        %X is in reverse order so correct the order in the sorted array
        Scan_Sorted(rowStart:rowEnd, 1:RowSize) = Scan(rowEnd:-1:rowStart, 1:RowSize);
    end
end

%% Now correct data for dc offset

%Now create data array with DC offset applied
Scan_Sorted_Corrected = Scan_Sorted;

for i = 1:Zn
    for j = 1:Yn
        for k = 1:Xn
            row = Xn * Yn* (i-1) + Xn * (j-1) + k;
            Scan_Sorted_Corrected(row,dataStart:dataEnd) =
Scan_Sorted(row,dataStart:dataEnd) - DC_Offset;
        end %for k
    end %for j
end %for i
```

```matlab
%% Find pmax, pmin, prms and pms
%Also calculating spatial average sums

%Set up distances in grids (in mm)
%Z0 = 105000; %Start distance of scan
GridX = [XStart:XStep:XEnd]/1000;
GridY = [YStart:YStep:YEnd]/1000;
%GridZ = [Z0:ZStep:Z0+ZSpan]/1000;

%Now create Vmax, Vmin, Vrms & Vms
Vmax = zeros(Xn,Yn);
Vmin = zeros(Xn,Yn);
Vrms = zeros(Xn,Yn);
Vms = zeros(Xn,Yn);

%Now create pmax, pmin, prms, pms and ptp (temporal peak pressure)
pmax = zeros(Xn,Yn);
pmin = zeros(Xn,Yn);
prms = zeros(Xn,Yn);
pms = zeros(Xn,Yn);
ptp = zeros(Xn,Yn);

for j = 1:Yn
    for k = 1:Xn
                row = Xn * (j-1) + k;
                %NOTE each y value is a row and x data is in cols in array.
                %So order when indexing array is y,x
                Vmax(j,k) = max(Scan_Sorted_Corrected(row,dataStart:dataEnd));
                Vmin(j,k) = min(Scan_Sorted_Corrected(row,dataStart:dataEnd));
                Vrms(j,k) = rms(Scan_Sorted_Corrected(row,dataStart:dataEnd));
                Vms(j,k) = Vrms(j,k)^2;

                %Now convert to pressures
                pmax(j,k) = Vmax(j,k)*V2Pa;
                pmin(j,k) = -Vmin(j,k)*V2Pa;
                prms(j,k) = Vrms(j,k)*V2Pa;
                pms(j,k) = prms(j,k)^2;
                MI(j,k) = pmin(j,k)/1e6/(freq/1e6)^0.5;
    end %for k
end %for j

%% Plot data on colourscale charts
%Y rows, X cols
FigNo = FigNo + 1;
figure(FigNo); imagesc(GridX, GridY, prms / 1000); axis xy; colorbar;
c1 = colorbar; c1.Label.String = 'kPa';
title('RMS Pressure'); xlabel('X (mm)'); ylabel('Y (mm)');

FigNo = FigNo + 1;
figure(FigNo); imagesc(GridX, GridY, pmin / 1000); axis xy; colorbar;
c3 = colorbar; c3.Label.String = 'kPa';
title('Peak Negative Pressure'); xlabel('X (mm)'); ylabel('Y (mm)');

FigNo = FigNo + 1;
figure(FigNo); imagesc(GridX, GridY, MI); axis xy; colorbar;
c3 = colorbar; c3.Label.String = 'MI';
title('Mechanical Index'); xlabel('X (mm)'); ylabel('Y (mm)');

%Now look at max pmin and define bins
%MAXPmin = max(max(pmin))
MAXPmin = 100e3;
%Create Bins - logarithmic?
Bins = [MAXPmin*0; MAXPmin*0.1; MAXPmin*0.25; MAXPmin*0.5; MAXPmin*0.75; MAXPmin];
MI_CF = (freq/1e6)^(-0.5)/1e6; %Conversion factor for MI
MIBins = Bins .* MI_CF;
nBins = size(Bins,1) - 1;
Masks = zeros(nBins,Xn,Yn);
AreaCount = zeros(nBins,1);

%Try contour plot of p-
FigNo = FigNo + 1; figure(FigNo);
[C,h] = contour(GridX, GridY, pmin/1000,'ShowText','on');
h.LevelList = round( Bins(2:nBins) ./ 1000,1);
axis xy;
title('Contour Plot of Peak Negative Pressure (kPa)'); xlabel('X (mm)'); ylabel('Y (mm)');

for b = 1:nBins
```

```matlab
    for j = 1:Yn
        for k = 1:Xn
            if ((pmin(j,k) > Bins(b)) && (pmin(j,k) <= Bins(b+1)))
                Masks(b,j,k) = 1;
                AreaCount(b) = AreaCount(b) + 1;
            else
                Masks(b,j,k) = 0;
            end %if...
        end %k
    end %j
end %b

%Plot and save the Masks one by one
%Get filename for saving masks
%NB!! The mask files transform the scan coord system to the biocell image
%coord system. Scan coord is top left X = -XSpan/2, Y= +YSpan/2.  Biocell
%images are top left is X=0, Y=0.  AND biocell images are mirrored because
%left on scan is right on the biocell. So need to

Path = uigetdir('Choose a directory to store mask files');

Area = zeros(nBins,1);
%Find start and end rows / cols for +/-20mm: assumes XSpan = YSpan
% & XStep = YStep
for i=1:Xn
    if GridX(i) == -20
        minus20 = i;
    elseif GridX(i) == 20
        plus20 = i;
    end %if
end %for i
MaskSize = plus20 - minus20 + 1
MaskPlot = zeros(MaskSize,MaskSize);

GridY_transpose = transpose(GridY(minus20:plus20))
%And reverse order so that top will be negative (will fit image coords)
GridY_tr = sort(GridY_transpose,'descend')
%And add a row so it has the same number of rows for appending..
GridY_trplus1 = [-100; GridY_tr];

%And need to mirror in X, as biocell image left is scan right...!
GridX_reverse = sort(GridX(minus20:plus20),'descend');

for m = 1:nBins
    %Now need to do some sorting of the data to fit the coordinate system
    %of the biocell images. First get -20 to +20mm data:
    MaskPlot(:,:) = Masks(m,minus20:plus20,minus20:plus20);

    %Then mirror in X. Append the reverse order GridX to top:
    MaskforXSort = [GridX_reverse; MaskPlot];
    %Transpose then sort rows to reverse X order:
    XSort_transpose = transpose(MaskforXSort);
    XSort_transpose_sorted = sortrows(XSort_transpose,'ascend');
    %Now transpose back to have X in cols again
    Mask_XSorted = transpose(XSort_transpose_sorted);

    %Now append GridY to first col:
    MaskPlotGridY = [GridY_trplus1, Mask_XSorted];
    MaskforOPFile = sortrows(MaskPlotGridY,'ascend');

    MaskFilename = [Path,'\V303_mask', num2str(m,'%i') ,'.csv']
    csvwrite(MaskFilename, MaskforOPFile);

    Area(m) = AreaCount(m) * (XStep / 1e3)^2; %Compute area of mask in mm^2

    FigNo = FigNo + 1;
    figure(FigNo); imagesc(GridX, GridY, MaskPlot); axis xy; colorbar;
    c3 = colorbar;
    title0 = ['Mask ', num2str(m,'%i')];
    title1 = [num2str(Bins(m)/1000,'%.1f'),' kPa < P- <= ' num2str(Bins(m+1)/1000,'%.1f'),'
kPa'];
%    title2 = [num2str(MIBins(m),'%.3f'),' < MI <= ' num2str(MIBins(m+1),'%.3f')];
    title3 = ['Area = ', num2str(Area(m),'%.0f'),' mm^2'];
    title({title0, title1, title3});
    xlabel('X (mm)'); ylabel('Y (mm)');
end %m
```

```matlab
%Plot centre mask to check coords are right...
    FigNo = FigNo + 1;figure(FigNo);
    imagesc(MaskforOPFile(1,2:MaskSize+1), MaskforOPFile(2:MaskSize+1,1), ...
        MaskforOPFile(2:MaskSize+1,2:MaskSize+1));
    axis xy; colorbar; c3 = colorbar;
    title0 = ['Mask file', num2str(m,'%i')];
    title(title0);
    xlabel('X (mm)'); ylabel('Y (mm)');

%clearvars;
```

B.1.6 Apply_Masking_DAPI.m

This Matlab routine was written to apply the masking to scanned microscope images, in order to count cells in areas experiencing similar peak-negative pressures within a single pressure bin. The masks are read in from the files produced by the previous program *Pressure_Mask_from_XY_Scan.m.* The routine allows the user to select the 40 mm x 40 mm scan area from the marked area of the biocell using a graphical interface showing the bright field image. The same area of the fluorescent filter image (in this case the DAPI image) is then processed within the area selected. Outputs are a series of microscope image files with the areas outside the pressure bin of interest blacked out.

```matlab
%% Apply_masking_DAPI
% Applies pressure contour masking to Evos microscope images
% user selects analysis rectangle using bright field image
% then areas are masked according to V303 pressure bins in csv files

clearvars;
%Zero figure number
FigNo = 0;

%Pull in the masks - V303 100kPa
Maskdir = 'C:\Users\jills\OneDrive - University of Glasgow\Osteoblast
Trials\FinalTrials2020\Pics\Microscope\Evos\';
Mask1 = csvread([Maskdir, 'V303_mask1.csv'],1,1);
Mask2 = csvread([Maskdir, 'V303_mask2.csv'],1,1);
Mask3 = csvread([Maskdir, 'V303_mask3.csv'],1,1);
Mask4 = csvread([Maskdir, 'V303_mask4.csv'],1,1);
Mask5 = csvread([Maskdir, 'V303_mask5.csv'],1,1);

%Y is in ROWS from -20mm(top) to +20mm(bottom).  X in COLS from -20mm
%(left) to +20mm (right)

%Now read in the GridX coords and calc step size
MaskFileAll = csvread([Maskdir, 'V303_mask1.csv'],0,0);
Grid = MaskFileAll(1,2:end);
GridSize = size(Grid);
Step = Grid(2) - Grid(1);

clearvars MaskFileAll;

%Now for each mask, find extent of mask so you can crop the masked images..
Xmin = [GridSize(2) GridSize(2) GridSize(2) GridSize(2) GridSize(2) GridSize(2)];
Xmax = zeros(1,5);
Ymin = [GridSize(2) GridSize(2) GridSize(2) GridSize(2) GridSize(2) GridSize(2)];
Ymax = zeros(1,5);

for i = 1:GridSize(2)

    for j = 1:GridSize(2)
        if Mask1(j,i) == 1
            if j < Ymin(1)
```

```matlab
                Ymin(1) = j;
            end
            if i < Xmin(1)
                Xmin(1) = i;
            end
            if j > Ymax(1)
                Ymax(1) = j;
            end
            if i > Xmax(1)
                Xmax(1) = i;
            end
        end
        if Mask2(j,i) == 1
            if j < Ymin(2)
                Ymin(2) = j;
            end
            if i < Xmin(2)
                Xmin(2) = i;
            end
            if j > Ymax(2)
                Ymax(2) = j;
            end
            if i > Xmax(2)
                Xmax(2) = i;
            end
        end

        if Mask3(j,i) == 1
            if j < Ymin(3)
                Ymin(3) = j;
            end
            if i < Xmin(3)
                Xmin(3) = i;
            end
            if j > Ymax(3)
                Ymax(3) = j;
            end
            if i > Xmax(3)
                Xmax(3) = i;
            end
        end

        if Mask4(j,i) == 1
            if j < Ymin(4)
                Ymin(4) = j;
            end
            if i < Xmin(4)
                Xmin(4) = i;
            end
            if j > Ymax(4)
                Ymax(4) = j;
            end
            if i > Xmax(4)
                Xmax(4) = i;
            end
        end

         if Mask5(j,i) == 1
            if j < Ymin(5)
                Ymin(5) = j;
            end
            if i < Xmin(5)
                Xmin(5) = i;
            end
            if j > Ymax(5)
                Ymax(5) = j;
            end
            if i > Xmax(5)
                Xmax(5) = i;
            end
        end
    end % for j
end %for i

%% Now for the image - get the .tif filename

[FileName, PathName] = uigetfile('*d4.tif','Select the bright field TIF file');
```

```matlab
BFFilename = [PathName, FileName];
image_BF = imread(BFFilename);

cd(PathName);

%Rotate the image 90 degrees clockwise (assuming top is left on scan)
image_BF_rotated = imrotate(image_BF,-90);
%Convert to 8bit and adjust range of values to improve contrast...
%Max_intensity = max(max(image_BF))
%image_BF_rotated_8bit = uint8(image_BF_rotated/Max_intensity*100+150);

clearvars image_BF; %image_BF_rotated;

FigNo = FigNo + 1;
figure(FigNo);
%h2 = imshow(image_BF_rotated_8bit);
h2 = imshow(image_BF_rotated);
imcontrast(h2);

%m = msgbox({'Draw a rectangle to indicate scan area.' 'Double-click to confirm.'});
rect = imrect
finished = wait(rect);
% get rectangle position - pos_rect is a 1-by-4 array [xmin ymin width height]
pos_rect = getPosition(rect)

Image_BF_cropped = imcrop(image_BF_rotated,pos_rect);

figure(FigNo);
h2 = imshow(Image_BF_cropped);

%Get average scale per mm and round
scale = round( (pos_rect(3) + pos_rect(4)) / 80 )

%get coords of centre point
pos0 = [round(pos_rect(3) / 2), round(pos_rect(4) / 2)];

%Displays the estimated centre point from the scan rectangle.
%Wait for adjustments
%Explain in dialog
figure(FigNo);
p = impoint(gca, pos0(1), pos0(2));
setColor(p, 'c');
%finished = wait(p);
%don't wait - just use the centre position and mark for visual check
pos0 = getPosition(p)

%Now get the DAPI file to process:
[FileName,PathName] = uigetfile('*d0.tif','Select the DAPI TIF file');
DAPIFilename = [PathName, FileName];
image_DAPI = imread(DAPIFilename);

%Pull out biocell ref (assumes filename starts with REF_)
ref=1;
while FileName(ref) ~= '_'
    ref = ref + 1;
end
Biocell_Ref = FileName(1:ref);

%Rotate the image 90 degrees clockwise (assuming top is left on scan)
image_DAPI_rot = imrotate(image_DAPI,-90);
%Now crop the image to include only the scan area.
image_DAPI_rot_crop = imcrop(image_DAPI_rot,pos_rect);

%Clear some memory...
clearvars image_BF_rotated image_DAPI image_DAPI_rot;

%Now apply masking...
%Loop through each pixel, determine position. Then apply mask
%Can use the fact that the mask and images are in the same orientation,
%just different scales.
%Set up new images to hold the image values
DAPI_global = image_DAPI_rot_crop;
DAPI_m1 = image_DAPI_rot_crop;
DAPI_m2 = image_DAPI_rot_crop;
DAPI_m3 = image_DAPI_rot_crop;
DAPI_m4 = image_DAPI_rot_crop;
DAPI_m5 = image_DAPI_rot_crop;
```

```matlab
%Set first index values and positions for masking
MaskX=1;
MaskY=1;

for i = 1:pos_rect(3)-1
    if (i - pos0(1)) ~= 0
            posnX = (i - pos0(1))/scale;
        else
            posnX = 0;
    end %if else i
    X = round((posnX - Grid(1))/Step) + 1;

    for j = 1:pos_rect(4)-1
        posnY = (j - pos0(2))/scale;
        Y = round((posnY - Grid(1))/Step) + 1;

        DAPI_m1(j,i) = Mask1(Y,X) * image_DAPI_rot_crop(j,i);
        DAPI_m2(j,i) = Mask2(Y,X) * image_DAPI_rot_crop(j,i);
        DAPI_m3(j,i) = Mask3(Y,X) * image_DAPI_rot_crop(j,i);
        DAPI_m4(j,i) = Mask4(Y,X) * image_DAPI_rot_crop(j,i);
        DAPI_m5(j,i) = Mask5(Y,X) * image_DAPI_rot_crop(j,i);

    end  %for j
end %for i

%Now crop the images: use the min and max values found previously

%Now convert the max and min values to rectangle arrays for cropping images
%with some additional blank space - 100 pixels?
% NB Checks the bounds on the x=0, y=0 axes but not the max axes
crop_rect = [max( round((Grid(Xmin(2))- Grid(1)-Step)*scale),0), max(round((Grid(Ymin(2)) -
Grid(1)-Step)*scale),0), ...
                round((Grid(Xmax(2)) - Grid(Xmin(2))+Step*2)*scale), round((Grid(Ymax(2))
- Grid(Ymin(2))+Step*2)*scale) ];
DAPI_m2_crop = imcrop(DAPI_m2,crop_rect);
clearvars DAPI_m2;

crop_rect = [max( round((Grid(Xmin(3))- Grid(1)-Step)*scale),0), max(round((Grid(Ymin(3)) -
Grid(1)-Step)*scale),0), ...
                round((Grid(Xmax(3)) - Grid(Xmin(3))+Step*2)*scale), round((Grid(Ymax(3))
- Grid(Ymin(3))+ Step*2)*scale)];
DAPI_m3_crop = imcrop(DAPI_m3,crop_rect);
clearvars DAPI_m3;

crop_rect = [max( round((Grid(Xmin(4))- Grid(1)-Step)*scale),0), max(round((Grid(Ymin(4)) -
Grid(1)-Step)*scale),0), ...
                round((Grid(Xmax(4)) - Grid(Xmin(4))+Step*2)*scale), round((Grid(Ymax(4))
- Grid(Ymin(4))+Step*2)*scale) ];
DAPI_m4_crop = imcrop(DAPI_m4,crop_rect);
clearvars DAPI_m4;

crop_rect = [max( round((Grid(Xmin(5))- Grid(1)-Step)*scale),0), max(round((Grid(Ymin(5)) -
Grid(1)-Step)*scale),0), round((Grid(Xmax(5)) - Grid(Xmin(5))+Step*2)*scale),
round((Grid(Ymax(5)) - Grid(Ymin(5))+Step*2)*scale)];
DAPI_m5_crop = imcrop(DAPI_m5,crop_rect);
clearvars DAPI_m5;

%Now create TIF files from the cropped images.
imwrite(DAPI_global,[PathName, Biocell_Ref, '_DAPI_global.tif']);
imwrite(DAPI_m1,[PathName, Biocell_Ref, '_DAPI_m1.tif']);
imwrite(DAPI_m2_crop,[PathName, Biocell_Ref, '_DAPI_m2.tif']);
imwrite(DAPI_m3_crop,[PathName, Biocell_Ref, '_DAPI_m3.tif']);
imwrite(DAPI_m4_crop,[PathName, Biocell_Ref, '_DAPI_m4.tif']);
imwrite(DAPI_m5_crop,[PathName, Biocell_Ref, '_DAPI_m5.tif']);
```

B.2 ImageJ Macros

B.2.1 Count_all_FUNA.ijm

This ImageJ macro routine was used in the cell adhesion study (Section 4.1.3.2) to automatically count cells before and after washing, by calling pre-determined ImageJ commands to run an automated cell count.

```
// Count_all_FUNA.ijm
// by Jill Savva
// May 2021

//Counts cells in all FUNA files in a given directory including subdirectories recursively
  dir = getDirectory("Choose a directory containing microscope files");
  count = 1;

//Specify start of filename
StartFilename = "10u_20k_FUNA_"

//Create results file and add headers
ResultsFilename = dir + StartFilename + "counts.txt";
ResultsFile = File.open(ResultsFilename);
print(ResultsFile, "FUNA File, #Cells");
File.close(ResultsFile);

PosnArray = newArray("C.jpg", "U.jpg", "D.jpg", "L.jpg", "R.jpg");

for (i=0; i < 5; i++)
{
     ImageFilename = StartFilename + PosnArray[i];
       Filename = dir + ImageFilename;
     print((count++) + ": " + Filename);

     Biocell = ImageFilename;

     BaseFilename = substring(ImageFilename,0, lengthOf(ImageFilename) - 4);
     open(Filename);

     run("8-bit");
       wait(2000);
     run("Enhance Contrast...", "saturated=0.3 normalize");
     wait(2000);

     //save the enhanced version
     GrayFilename = dir + BaseFilename + "_gray.tif";
     saveAs("TIFF", GrayFilename);

       run("Threshold...");
       setThreshold(70, 255);
       setOption("BlackBackground", false);
     wait(2000);

     run("Make Binary");
       wait(2000);
       run("Convert to Mask");
       wait(2000);
     run("Fill Holes");
     wait(2000);
     run("Watershed");
       wait(2000);

     run("Analyze Particles...", "size=20-Infinity circularity=0.30-1.00 show=[Bare
Outlines] display exclude");
       wait(2000);

     //now append the results file with the new cell count
     ResultString = Biocell + "," + nResults;
     File.append(ResultString, ResultsFilename);
```

```
    //now close all windows (plus the results)
    run("Close All");
    selectWindow("Results") ;
    run ("Close") ;
} //for
```

B.2.2 Count_DAPI.ijm

This ImageJ macro routine was used in the Frequency Study to count all cell nuclei (live or

dead) imaged in the DAPI filter (see Section 4.4.2). The routine calls a series of pre-

determined ImageJ functions to automate the cell counts. It was used in conjunction with

Count_RHOD.ijm to produce a viable cell count before and after LIPUS exposure.

```
// Count_DAPI.ijm
// by Jill Savva
// Sept 2019
// Loops through files with standard file names and counts cells using pre-defined settings

//Get directory and file list
FileDir = getDirectory("Choose a directory containing DAPI files");
FileList = getFileList(FileDir);

//Create results file and add headers
ResultsFilename = FileDir + "DAPI_results.txt";
ResultsFile = File.open(ResultsFilename);
print(ResultsFile, "Filename, Count");
File.close(ResultsFile);

for (i=0; i<FileList.length; i++) {

    ImageFilename = FileList[i];
    Filename = FileDir + ImageFilename;
    print(Filename);
    FileExt = substring(ImageFilename,lengthOf(ImageFilename) - 3,
lengthOf(ImageFilename));

    if (FileExt == "tif") {

        BaseFilename = substring(ImageFilename,0, lengthOf(ImageFilename) - 4);
        print(BaseFilename);

        open(Filename);
            run("8-bit");

        run("Enhance Contrast", "saturated=0.35");
        run("Apply LUT");
            run("Subtract Background...", "rolling=50");

        GrayFilename = FileDir + BaseFilename + "_gray.tif";

        saveAs("TIFF", GrayFilename);
            setAutoThreshold("Default dark");

            run("Threshold...");
            setThreshold(40, 255);
            setOption("BlackBackground", false);
            run("Make Binary");
            run("Convert to Mask");
            run("Fill Holes");
            run("Watershed");

            BWFilename = FileDir + BaseFilename + "_bw.tif";
            saveAs("TIFF", BWFilename);

            run("Analyze Particles...", "size=20-Infinity circularity=0.30-1.00
            show=Outlines display exclude clear");

            CountFilename = FileDir + BaseFilename + "_count.tif";
            saveAs("TIFF", CountFilename);
```

```
            CountFilename = FileDir + BaseFilename + "_count.csv";
            saveAs("Results", CountFilename);
        wait(2000);

        //now append the results file with the new cell count
        ResultString = ImageFilename + "," + nResults;
        File.append(ResultString, ResultsFilename);

        //now close all windows (plus the results)
        run("Close All");
        selectWindow("Results");
        run ("Close");

            } else {
            print(ImageFilename + " is not a TIFF file");
    }
}
```

B.2.3 Count_RHOD.ijm

This ImageJ macro routine was used in the Frequency Study to count dead cell nuclei
imaged in the RHOD microscope filter (see Section 4.4.2). The routine allows the user to
either choose to count the dead cells manually (where the dead cell count is low) or to calls
a series of pre-determined ImageJ functions to automate the cell counts. It was used in
conjunction with *Count_DAPI.ijm* to produce a viable cell count before and after LIPUS
exposure.

```
// Count_RHOD.ijm
// by Jill Savva
// Sept 2019
// Loops through RHOD image files in a directory and counts cells

//Get directory and file list
FileDir = getDirectory("Choose a directory containing RHOD files");
FileList = getFileList(FileDir);

//Create results file and add headers
ResultsFilename = FileDir + "RHOD_results.txt";
ResultsFile = File.open(ResultsFilename);
print(ResultsFile, "Filename, Count");
File.close(ResultsFile);

for (i=0; i<FileList.length; i++) {

    ImageFilename = FileList[i];
    Filename = FileDir + ImageFilename;
    print(Filename);
    FileExt = substring(ImageFilename,lengthOf(ImageFilename) - 3,
lengthOf(ImageFilename));

    if (FileExt == "tif") {

        BaseFilename = substring(ImageFilename,0, lengthOf(ImageFilename) - 4);
        print(BaseFilename);

        open(Filename);
            run("8-bit");
            run("Enhance Contrast", "saturated=0.35");
        run("Apply LUT");
            run("Subtract Background...", "rolling=50");

        GrayFilename = FileDir + BaseFilename + "_gray.tif";
        saveAs("TIFF", GrayFilename);

        //Ask user to select to analyse the file automatically or manually
        Dialog.create("Continue Analysis");
```

```
        Dialog.addCheckbox("Continue analysis?", true);
        Dialog.show();

        YesNo = Dialog.getCheckbox();

        if (YesNo){

            setAutoThreshold("Default dark");
            run("Threshold...");
            setThreshold(40, 255);
            setOption("BlackBackground", false);
            run("Convert to Mask");
            run("Make Binary");
            run("Convert to Mask");
            run("Fill Holes");
            run("Watershed");

            BWFilename = FileDir + BaseFilename + "_bw.tif";
            saveAs("TIFF", BWFilename);

                run("Analyze Particles...", "size=20-Infinity circularity=0.30-1.00
show=Outlines display exclude clear");

            CountFilename = FileDir + BaseFilename + "_count.tif";
            saveAs("TIFF", CountFilename);

                CountFilename = FileDir + BaseFilename + "_count.csv";
            saveAs("Results", CountFilename);
          wait(2000);

          //now append the results file with the new cell count
          ResultString = ImageFilename + "," + nResults;
          File.append(ResultString, ResultsFilename);

          //now close all windows (plus the results)
          selectWindow("Results") ;
          run ("Close") ;
          run("Close All");

        } else {
          //Create dialog to allow user to perform manual count if necessary
          Dialog.create("Manual count...");
          Dialog.addNumber("Enter the manual count result: ",0);
          Dialog.show();

          ManualCount = Dialog.getNumber();

          //now append the results file with the new cell count
          ResultString = ImageFilename + "," + d2s(ManualCount,0);
          File.append(ResultString, ResultsFilename);

          //close all windows
          run("Close All");
        }
          } else {
            print(ImageFilename + " is not a TIFF file");
          }
      }
}
```

B.2.4 Count_DAPI_m5_recursive.ijm

This ImageJ routine performs a DAPI count (live + dead cells) on a masked microscope image (in this case, 'm5'). The routine was written to cycle through all sub-directories recursively and search for similar masked files to process. The cell counts are stored in an output text file to allow further analysis.

```
// Count_DAPI_m5_recursive.ijm
```

```
// by Jill Savva
// Nov 2020

//Takes all DAPI global files in a folder and counts cells
//Processing:
//subtract background (50 pixels)
//enhance contrast (0.19%)
//convert to 8-bit - %age proportionate to area so threshold should still be valid
//adjust threshold (50)
//watershed

//Counts cells in all DAPI m5 files in a given directory including subdirectories
recursively

dir = getDirectory("Choose a directory containing microscope files");
count = 1;

//Create results file and add headers
ResultsFilename = dir + "DAPI_m5_SBG_EC_th_50_12Nov2020.txt";
ResultsFile = File.open(ResultsFilename);
print(ResultsFile, "Biocell, #Cells");
File.close(ResultsFile);

listFiles(dir);

function listFiles(dir) {
    list = getFileList(dir);
    for (i=0; i<list.length; i++)
    {
     if (endsWith(list[i], "/")) {
          listFiles(""+dir+list[i]);
     }
        else {

        ImageFilename = list[i];
           Filename = dir + ImageFilename;
        print((count++) + ": " + Filename);

        if (endsWith(ImageFilename, "DAPI_m5.tif"))
        {

            Biocell = substring(ImageFilename,0,lengthOf(ImageFilename) - 13);
            BaseFilename = substring(ImageFilename,0, lengthOf(ImageFilename) - 4);
            open(Filename);
               run("Subtract Background...", "rolling=50");
             wait(2000);
                   run("Enhance Contrast...", "saturated=0.19");
            wait(2000);

            run("8-bit");
               wait(2000);

            //save the enhanced version
            GrayFilename = dir + BaseFilename + "_gray.tif";
            saveAs("TIFF", GrayFilename);

            run("Threshold...");
              setThreshold(50, 255);
              setOption("BlackBackground", false);
                  wait(2000);

                  run("Make Binary");
             wait(2000);

               run("Convert to Mask");
             wait(2000);

               run("Watershed");
             wait(2000);

               run("Analyze Particles...", "size=10-500 pixel circularity=0.30-1.00
show=[Bare Outlines] display exclude");
              wait(2000);

            //now append the results file with the new cell count
            ResultString = Biocell + "," + nResults;
            File.append(ResultString, ResultsFilename);
```

```
                //now close all windows (plus the results)
                run("Close All");
                selectWindow("Results") ;
                run ("Close") ;

            } //if
        } //else
    } //for
} //function
```

B.2.5 Count_CY5_m5_recursive.ijm

This ImageJ routine performs a CY5 count (dead cells) on a masked microscope image (in
this case, 'm5'). The routine was written to cycle through all sub-directories recursively
and search for similar masked files to process. The cell counts are stored in an output text
file to allow further analysis.

```
// Count_CY5_m5_recursive.ijm
// by Jill Savva
// Nov 2020

//Counts cells in all CY5 m5 files in a given directory including subdirectories
recursively
  dir = getDirectory("Choose a directory containing microscope files");
  count = 1;

//Create results file and add headers
ResultsFilename = dir + "CY5_m5_07Nov2020.txt";
ResultsFile = File.open(ResultsFilename);
print(ResultsFile, "Biocell, #Cells");
File.close(ResultsFile);

listFiles(dir);

function listFiles(dir) {
      list = getFileList(dir);
      for (i=0; i<list.length; i++) {
         if (endsWith(list[i], "/")) {
              listFiles(""+dir+list[i]);
         }
         else {
            ImageFilename = list[i];
            Filename = dir + ImageFilename;
            print((count++) + ": " + Filename);

            if (endsWith(ImageFilename, "CY5_m5.tif"))  {

                Biocell = substring(ImageFilename,0,lengthOf(ImageFilename) - 11);

                BaseFilename = substring(ImageFilename,0, lengthOf(ImageFilename) - 4);

                open(Filename);
                        //run("Enhance Contrast...", "saturated=0.3 normalize");
                //wait(2000);

                //run("8-bit");
                    //wait(2000);

                //run("Apply LUT");
                    run("Subtract Background...", "rolling=50");
                    wait(2000);

                //save the enhanced version
                //GrayFilename = dir + BaseFilename + "_gray.tif";
                //saveAs("TIFF", GrayFilename);

                  run("Threshold...");
```

```
                        setThreshold(6, 65535);
                        setOption("BlackBackground", false);
                           wait(2000);

                               run("Make Binary");
                           wait(2000);

                           run("Convert to Mask");
                           wait(2000);

                               //run("Watershed");
                        // wait(2000);

                               run("Analyze Particles...", "size=10-500 pixel circularity=0.30-
1.00 show=[Bare Outlines] display exclude");
                           wait(2000);

                //save the outlines drawing
                //CountFilename = dir + BaseFilename + "_count.tif";
                //saveAs("TIFF", CountFilename);

                //now append the results file with the new cell count
                ResultString = Biocell + "," + nResults;
                File.append(ResultString, ResultsFilename);

                //now close all windows (plus the results)
                run("Close All");
                selectWindow("Results") ;
                run ("Close") ;

            } //if
         } //else
      } //for
} //function
```

B.3 Finite Element (FE) PZFlex Code

B.3.1 2D_Single_Element_1M25Hz_PZ27_D25mm_ML50_back5.flxinp

This PZFlex code was used to design and predict the response of the custom-built LIPUS
transducer, described in Appendix C.

```
C ************************************************************************************************
c                                      FLEX INPUT FILE
c ************************************************************************************************
c
c DESIGNER          : Jill Savva
c MODEL DESCRIPTION  : Flex input file originally generated from the 2D Modeller interface
c DATE CREATED       : 29 Sep 2017
c VERSION            : 1.0
c
c Used to design and assess performance of the custom LIPUS transducer
c ************************************************************************************************

mp omp 1                        /* Number of CPUs to be used

titl model2d Model generated from 2D modeller

c ************************************************************************************************
c                                   DEFINE USER VARIABLES AND MESH SIZE
c ************************************************************************************************
c
c     Set variable for approximate element size for model
c     Must be sufficient to represent wavelengths of interest
c     Recommended that at least 15 elements per wavelength are used
c
c ************************************************************************************************

symb freqint = 1000000.0            /* Frequency of interest (Hz)
```

```
symb wavevel = 1500.                    /* Longitudinal Wave velocity in Material (m/s)
symb nmesh = 15                         /* Defines number of mesh elements in wavelength
symb freqdamp = 1.25e6                  /* Centre frequency for damping function extrapolation
symb wavelgth = $wavevel / $freqint     /* Wavelength of Sound in Material (m)
symb xynumelem = $nmesh                 /* X-Y Plane mesh
symb xybox = $wavelgth / $xynumelem
symb zbox = $xybox

symb water = $wavelgth * 1.5            /* Add a wavelength and half of water if requested

symb DiskOD = 25e-3                              /* Ceramic Disk outer diameter
symb DiskThk = 1.6e-3                            /* Ceramic Disk thickness (1.6 mm measured)
symb ThkML = 0.5e-3                              /* Thickness of matching layer
symb OLML = 0.75e-3                              /* Matching layer overlap (at side of disc)
symb CasingOD = 32e-3                            /* stainless steel casing outer diameter
symb CasingThk = 1.5e-3                          /* stainless steel casing thickness
symb CasingID = $CasingOD - 2 * $CasingThk

c ***********************************************************************************
c                               GEOMETRY LOCATIONS XYZ
c ***********************************************************************************

symb x1 = 0.0000              /* zero (back of Tx)
symb x2 = 0.0030              /* width of water behind Tx (3 mm)
symb x3 = 0.0230              /* add 20 mm backing
symb x4 = $x3 + $DiskThk      /* add ceramic thickness
symb x5 = $x4 + $ThkML        /* add matching layer
symb x6 = 0.0600              /* add 60 mm water on front

symb xlast = $x6              /* max value of x (extent of model)

c Define Reference points for extrapolation
symb iTxBottom = 2           /* Tx (transducer) bottom at x2
symb iCerBottom = 3          /* Bottom of ceramic (pzt27) at x3
symb iCerTop = 4             /* Top of ceramic at x4
symb iTxTop = 5                      /* Top of transducer at x5

symb y1 = 0.00000            /* zero (centre of Tx)
symb y2 = $DiskOD / 2        /* half width of ceramic disc
symb y3 = $y2 + $OLML        /* matching layer epoxy / insulating layer
symb y4 = $CasingID / 2      /* add backing / filler
symb y5 = $CasingOD / 2      /* add casing
symb y6 = 0.03000            /* add water

symb ylast = $y6             /* max value of y (extent of model)

c Define Reference points for extrapolation
symb jCerSide = 2            /* outer side of ceramic at y2
symb jTxSide = 5             /* outer side of Tx at y5

c ***********************************************************************************
c                               INDICES LOCATIONS IJK
c ***********************************************************************************

c ties indices i and j to x and y coords
symb #keyindx i 1 6 1 $xybox 1
symb indgrd = $i6

symb #keyindx j 1 6 1 $xybox 1
symb jndgrd = $j6

c ***********************************************************************************
c                               GRID & GEOMETRY ALLOCATION
c ***********************************************************************************

c now generate the transducer model

grid $indgrd $jndgrd axix

symb numElems = $indgrd  * $jndgrd

geom
     keypnt 6 6
     end

c ***********************************************************************************
```

```
c                                   DRIVING CONDITIONS
c **************************************************************************************
c
c      A number of predefined waveform functions can be accessed in PZFlex.
c      The SINE wave option is used below, other examples include wavelets, gaussians,
c      and step functions. The manual details the function entries
c
c **************************************************************************************

c func wvlt $freqint 1                   /* wavelet used for transmit sensitivity predictions
func sine $freqint 0.5 0 20              /* sine wave used for impedance predictions


c **************************************************************************************
c                                   CREATE AXIS FOR POLING
c **************************************************************************************

axis                        /* Special instance of axis required to pole the ceramic
     form vctr
     end


c **************************************************************************************
c                                   READ IN MATERIALS
c **************************************************************************************

c read in material properties from prepared file
symb #read 'C:\Users\XXXXXXX\Documents\PZFlex\Tutorials\2D Model\2D
Model\2D_Single_Element_1M25Hz_PZ27_OD25mm_ML50_back5.prjmat'


c **************************************************************************************
c                                   BINARY MESHED MODEL FILE
c **************************************************************************************

site
     regn watr                    /* surrounds transducer with water

c     Casing                      /* stainless steel casing
c     ----------------------------
     regn stst $i2 $i5 $j4 $j5

c     Backing                     /* backing material 5% tungsten loaded epoxy
c     ----------------------------
     regn back5 $i2 $i5 $j1 $j4

c     Epoxy matching layer        /* alumina-loaded epoxy (4.6 MRayls)
c     ----------------------------
     regn hardalm2 $i3 $i5 $j1 $j3

c     PZT Disc                    /* piezoelectric disc Ferroperm PZT27
c     ----------------------------
     regn fpz27 $i3 $i4 $j1 $j2

     end

grph                        /* displays a cross-section of the transducer with materials
     line off
     mirr y on               /* mirrors about y to check axisymmetry
     plot matr
     end

term


c **************************************************************************************
c                                   BOUNDARY CONDITIONS
c **************************************************************************************
c      How the model interacts with the 'rest of the world'
c      Commonly used for symmetry (SYMM) and infinite absorbing boundaries (ABSR)
c      If conditions are not specified, FREE (unconstrained) is assumed
c **************************************************************************************

boun
     side 1 absr
     side 2 absr
     side 3 symm
     side 4 absr
     end


c **************************************************************************************
```

```
c                                        CALCULATED PROPERTIES
c ********************************************************************************
c define the properties to calculate

calc
        pres acoustic          /* calculate acoustic pressure (average of stresses in solid)
        max aprs pmin pmax     /* calculate MAX and MIN acoustic pressure
        end

c ********************************************************************************
c                                      ELECTRICAL FIELD APPLICATION
c ********************************************************************************
c
c      Must specify region within which piezoelectric effect occurs (electric window)
c      i.e. all piezoelectric elements and electrodes must be in the window
c      electric window elements more 'expensive' than regular elements - minimise size
c      all materials inside electric window must have dielectric constant specified
c
c      REMEMBER: Use ascale to scale the model if symmetry is being used
c
c ********************************************************************************

piez
        wndo $i$iCerBottom $i$iCerTop $j$j1 $j$jCerSide     /* ELectrical window piezo

        defn tx_actv
        node $i$iCerBottom $i$iCerBottom $j$j1 $j$jCerSide  /* Live electrode node

        defn tx_gnd
        node $i$iCerTop $i$iCerTop $j$j1 $j$jCerSide        /* Ground electrode

        bc tx_actv volt func          /* apply voltage boundary condition to 'top'.
        bc tx_gnd grnd                /* make bottom electrode ground
        slvr dcgd * cont              /* Use fast piezo solver
        end

c ********************************************************************************
c                                      CALCULATED SHAPE PROPERTIES
c ********************************************************************************
c
c      This section adds frequencies where PZFlex will store mode shape data
c      Other properties (e.g. displacements, stresses, strains, pressure),
c      must be requested by the OUT command
c ********************************************************************************

calc
        pres acoustic
        disp
        avrg dtop ydsp * regn $i$iCerTop $i$iCerTop $j$j1 $j$jCerSide
        avrg ptop aprs * regn $i$iCerTop-1 $i$iCerTop $j$j1 $j$jCerSide

shap
        freq 1e6
        freq 1.25e6
        freq 1.5e6
        data xdsp
        data ydsp
        end

c ********************************************************************************
c                                      DEFINE EXTRAPOLATION
c ********************************************************************************
c      This section sets up the extrapolation boundaries for the model
c ********************************************************************************

symb jexstop = $j$jTxSide + 3                    /* Outside of device for extr
symb iexstrt = $i$iTxBottom - 3                  /* Bottom of device for extr
symb iexstop = $i$iTxTop + 3                     /* Outside of device for extr
extr
        driv func                                /* define the driving function
        ref in $x$iCerBottom $y1      /* internal ref point for pressure gradient calc
        defn kirc                                /* kirchoff extrapolation
        node $iexstop $iexstop $j1 $jexstop      /* define node surface
        node $iexstrt $iexstrt $j1 $jexstop      /* define node surface
        node $iexstrt $iexstop $jexstop $jexstop /* define node surface
        end
```

```
c  ********************************************************************************
c                            CHOOSE TIME HISTORIES TO STORE
c  ********************************************************************************
c
c      Save field (such as displacement or pressure) from a node or element for all time
c      steps with POUT command
c  ********************************************************************************

pout
       hist func                              /* Drive function (Universal - always stored)
       histname electrode vq tx_actv          /* Store voltage and charge on electrode
       histname electrode v tx_gnd
       histname avrg a dtop
       histname avrg a ptop
       end


c  ********************************************************************************
c                                  PROCESS MODEL
c  ********************************************************************************
c
c      Issue process (PRCS) command
c      Checks model integrity, and calculates stable time step
c      NOTE: Process command must always be issued
c
c  ********************************************************************************

symb #msg 1
Checking Model Integrity......
prcs                                       /* run process step

grph
       line off
       nvew 3 1
       set sttl 1 'Material Model'
       pset sttl 2 'Acoustic Pressure propagation'
       pset sttl 3 'Charge on electrode'
       mirr y on
       set imag avi
       end


c  ********************************************************************************
c                                   RUN THE MODEL
c  ********************************************************************************
c
c      Specify number of time steps to be run
c      Can be set to auto, by using ringdown
c
c  ********************************************************************************

symb #get { step } timestep
symb i_display = nint ( ( ( 1 / $freqint ) * 3 ) / $step / 10 )
proc showstate save

grph
       arrow pole
       plot matr

       line off
       colr tabl data 6
       plot aprs
       imag
       plot 3
       end
end$ proc

proc showstate rate $i_display

symb #msg 1
Model Running....

exec ringdown electrode q tx_actv 100000 500 0.001

symb ttime = ( $xlast - $x1 ) / $wavevel
symb nexec = $ttime / $step

symb #get { nsteps_now } itimstep
symb nsteps_stat = 0 if noexist
```

```
symb n_extra = nint ( ( $nsteps_now - $nsteps_stat ) / 10 )

symb #msg 1
Simulation is 90% complete

exec $n_extra

c *********************************************************************************
c                                   DATA OUTPUTS SECTION
c *********************************************************************************
c
c      This section stores the pressure data output of the model for later use
c
c *********************************************************************************

symb #get { labl } jobname            /* find name of run

data
       file out '$labl.flxdato'
       out modl
       out shap/all
       out aprs
       out pmin
       out pmax
       end

c *********************************************************************************
c                           Save symbol variables to file for later use
c *********************************************************************************

symb #save '$labl.symb'            /* save in symb file
stop                               /* return to command prompt
```

APPENDIX C
DESIGN AND CONSTRUCTION OF A CUSTOM LIPUS TRANSDUCER

This Appendix details the design and manufacture of the custom LIPUS transducer introduced in Chapter 3.

C.1 Design and Construction

A transducer was designed and built to provide a LIPUS field, with dimensions based on the transducer of the Exogen System (Bioventus, US). The manufacturer's data (Table 1.1) indicates the transducer has a diameter of 22 mm and an operating frequency of 1.5 MHz. The active element of the custom LIPUS transducer was a 25 mm diameter, 1.57 mm thick discs of piezoelectric material PZT27, purchased from Ferroperm (DK). This disc diameter was the closest available to that of the Exogen transducer. the disc thickness results in a thickness resonance of 1.25 MHz. The PZT27 material had a relatively low mechanical Q (80), which enabled the device to be driven in the frequency range 1.0 MHz to 1.5 MHz, the most common LIPUS frequencies.

A 2D axisymmetric model of the disc transducer, illustrated in Figure C.1, was created in the FE modelling package PZFlex (2017, Weidlinger Associates Inc., US). A quarter-wavelength matching layer extended the bandwidth to include 1 MHz and 1.5 MHz. An absorbent backing material was chosen to reduce internal reflections and a stainless steel casing with inner diameter 29 mm and wall thickness 1.5 mm. PZFlex 2D axisymmetric models break up the geometry into 4-sided quadrilaterals. This was done automatically by PZFlex using the 'grid' function. The mesh size chosen was 0.1 mm, corresponding to $1/15^{th}$ of the wavelength in water at the lowest frequency of interest of 1 MHz (allowing for reasonable representation of the wave shape within the analysis at the shortest possible wavelength). The transducer model was surrounded by pure water: a 3 mm layer at the back, 30 mm at the sides and 60 mm at the front. The extra water area at the front (with a length corresponding to 40 wavelengths at 1 MHz) allowed PZFlex to display the propagation of the acoustic field through the water.
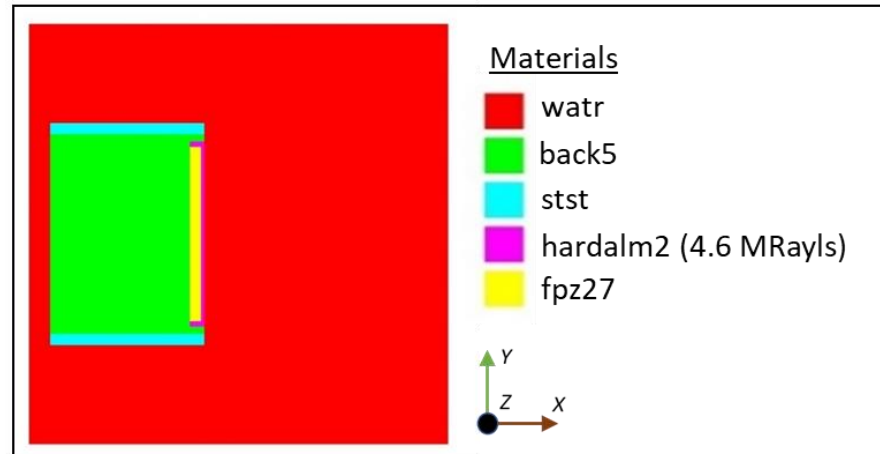
Figure C.1: Cross-section of 2D Axisymmetric FE model of custom LIPUS transducer. Appearing from left to right (back of device to front): the surrounding water (watr), the stainless steel casing (stst), 5% v.f. tungsten-loaded backing (back5), the Ferroperm PZT27 piezoelectric disc (fpz27) and the 4.6 MRayls matching layer (hardalm2).

Propagation through the backing could also be observed, to determine if it was providing enough absorption of internal reflections. PZFlex models this by defining the damping properties of each material at a user-defined frequency (set to the centre frequency of 1.25 MHz in this analysis). PZFlex then extrapolates the damping properties for other frequencies of interest. The materials chosen for the model were all standard PZFlex materials and were not explicitly defined. However, the materials were chosen carefully to have properties as close as possible to the final construction materials of the transducer, with particular attention paid to the specific acoustic impedance. PZFlex has an accurate database of piezoelectric materials, including the Ferroperm PZT27 material chosen as the active element of the custom LIPUS transducer.

The boundary conditions at the outer edges of the water layers were set to infinitely absorbing to simulate free field conditions. PZFlex allows the simulation of piezoelectric materials in response to an applied voltage by defining an electric window around the piezoelectric material. The area within the electric window was solved with an implicit FEA solver, which considers the effects of each node on all others. The model area outside the electric window was solved with the faster explicit solver, where each node is effectively decoupled from other nodes. This solver was recommended by the PZFlex developers for mechanical wave propagation and was therefore considered the most appropriate for acoustic wave propagation in water. The resulting output is a transient analysis and allows parameters such as electrical impedance of the ceramic, acoustic

pressure and acoustic field propagation to be derived in post processing within the PZFlex tool. The PZFlex code used to run the model is provided in Section B.3.1 of Appendix B.

A study of matching layer acoustic impedance (Figure C.2) found the optimum was 4.6 MRayls, achieved in PZFlex with the material hardalm2, which was 50 % volume-fraction (v.f.) alumina loaded epoxy. The matching layer thickness was set to 0.5 mm, corresponding to a quarter wavelength at 1.25 MHz. A backing of 5% v.f. tungsten-loaded epoxy provided attenuation of internal reflections, while optimising the bandwidth and transmit sensitivity. Figure C.2 compares the predicted sensitivity in the form of the Transmit Voltage Ratio (TVR) for a range of matching layers and backings. The TVR was derived within the PZFlex post processing tool, and is the predicted pressure output from the transducer when a voltage is applied to the piezoelectric material, in dB relative to 1µPa/V and at 1 m distance from the transducer front face.
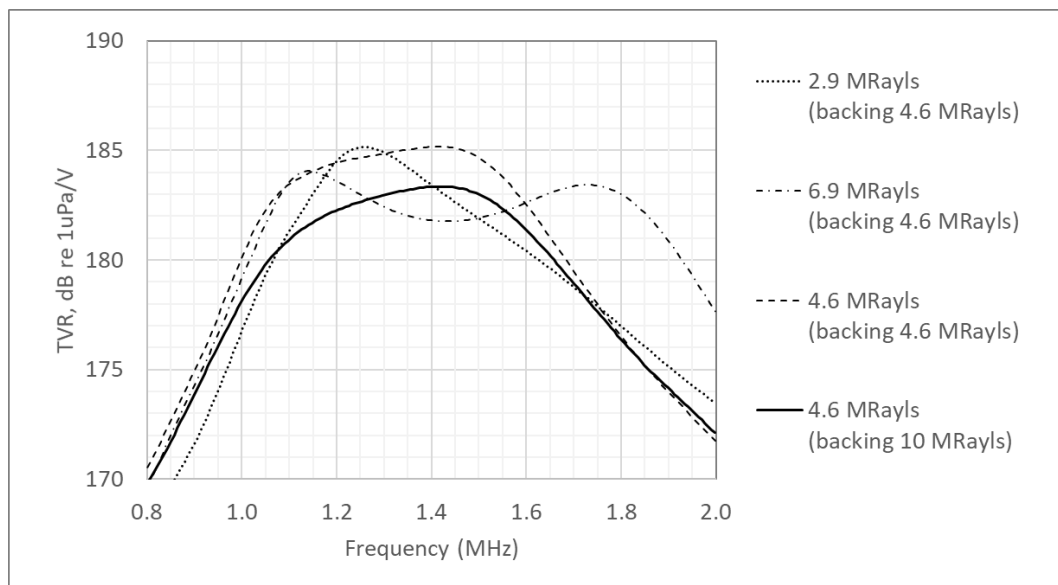
Figure C.2: Effects of varying matching layer specific acoustic impedances on bandwidth. Matching materials in PZFlex with specific acoustic impedance in brackets: epoxy (2.9 MRayls); epoxy + 70 % alumina (6.9 MRayls); epoxy + 50 % alumina (4.6 MRayls). Backing materials were: 4.6 MRayls: epoxy + 5 % tungsten ; 10 MRayls: epoxy + 25 % tungsten. The combination of 4.6 MRayls for both matching layer and backing was chosen to optimise bandwidth and transmit sensitivity of the device.

To achieve the required specific acoustic impedance for the matching layer, reference was made to a comprehensive study of epoxy loaded with alumina particles by Webster [223]. A value of 4.6 MRayls was achieved using Epofix epoxy (Struers, UK) loaded with 1 µm alumina particles at the volume fraction 25 %. A brief description of the transducer

construction process follows. First a bead of silver epoxy was fixed to the front electrode of the PZT27 disc and a mould created with plastic tubing (Figure C.3A). The alumina-loaded epoxy matching layer was mixed, degassed in a vacuum chamber and poured slowly into the mould (Figure C.3B). Once the matching layer was cured the mould was removed and the matching layer lapped to the required thickness of 0.5 mm ± 5 µm (Figure C.3 C & D). The disc and matching layer were potted into a stainless steel casing of inner diameter 29 mm, length 20 mm (Figure C.3E). A track of silver epoxy was painted on the inside edge of the casing and wired to the screen of a 1.5 m coaxial cable (RG174 A/U, 50Ω) with silver epoxy. The inner live cable connection was wired to the back electrode of the PZT27 disc with silver epoxy. These were electrically insulated with a layer of quick-drying epoxy. The casing was then filled with degassed backing material and allowed to cure. The front electrode was connected to ground with silver epoxy paint and a strain relief boot fitted to protect the cable from mechanical strain. A BNC plug was then wired to the end of the coaxial cable (Figure C.3F).
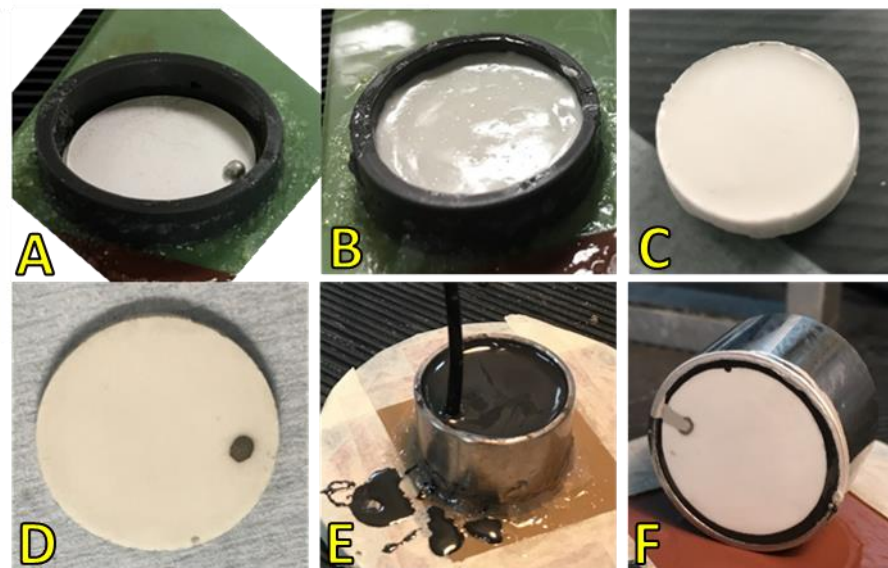
Figure C.3: Construction of the LIPUS transducer.
A: A bead of silver epoxy was fixed to the front electrode of the PZT27 disc and a mould created with plastic tubing. B: The 25 % v.f. alumina-loaded epoxy matching layer was mixed, degassed and poured into the mould. C: Once matching layer was cured the mould was removed. D: The matching layer was lapped to a thickness of 0.5 mm ± 5µm. E: The disc, matching layer and cables were potted in a stainless steel casing. F: The transducer.

The electrical impedance of the device was measured throughout the construction process with impedance analysers (Agilent 424294A or 42194A) and compared with FE-modelled impedances to monitor the process. Initial testing of the final transducer indicated an

internal reflection arriving at the hydrophone 23 µs after the direct sound, indicating the reflection was off the back of the device. A layer of Epofix epoxy with acoustic impedance between that of the backing layer and water was added to the back to mitigate. This reduced the reflection voltage to 1/27th or 29 dB below the direct signal (Figure C.4).
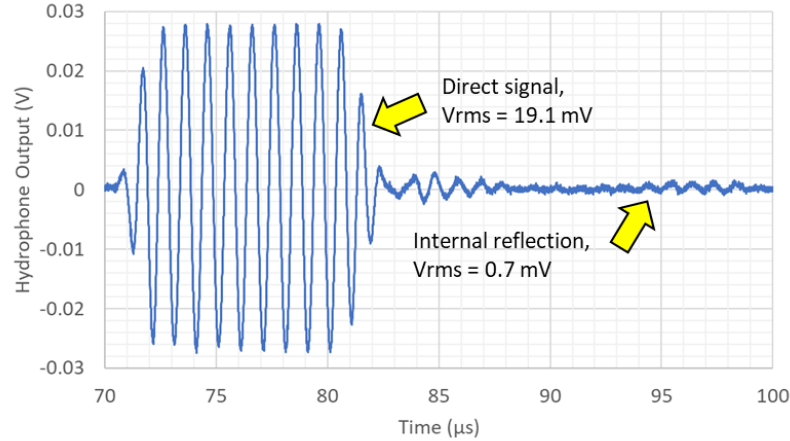
Figure C.4: Evaluation of the LIPUS transducer internal reflection.
The reflection begins at approximately 23 µs after onset of the initial pulse. This delay correlated with the expected delay for a reflection off the back of the backing layer.

An impedance matching circuit matched the transducer impedance to the 50 Ω output of the drive system (Figure C.5).
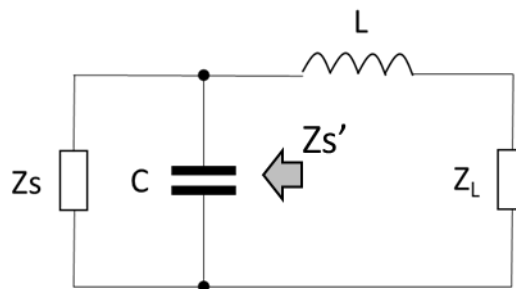
Figure C.5: LIPUS transducer impedance matching circuit

A shunt capacitor transformed the source resistance to equal the load resistance of the LIPUS transducer by:

$$C = \sqrt{\left(\frac{R_S}{R_L} - 1\right)\left(\frac{1}{\omega R_S}\right)^2} \tag{C.1}$$

where C is the shunt capacitance (Farads), R_S the source resistance (50 Ω), R_L the load resistance of the transducer, and ω the radial frequency ($2\pi f_M$ radians). The effective source reactance, X_S' was then found by:

$$Xs' = \frac{-\omega C R_S^2}{\omega^2 C^2 + 1} \tag{C.2}$$

The load reactance was then transformed to equal the effective source reactance X_L using a series inductance, L, calculated by:

$$L = -\frac{1}{\omega}(X_S' + X_L) \tag{C.3}$$

The matching frequency was 1.25 MHz, the centre of the bandwidth, with resulting component values of C = 2.53 nF and L = 10 µH, and matched impedance magnitude of 53 Ω and 8.9° phase at 1.25 MHz (38 Ω / 20° at 1 MHz and 82 Ω / -29° at 1.5 MHz). Initial measurements comparing performance against the FE model were carried out with this matching.

The operating frequency was set to 1 MHz for the LIPUS *in vitro* exposure Pressure Amplitude study detailed in Chapter 4. For this study a new matching circuit with matching frequency 1 MHz was designed (C = 5.1 nF and L = 19 µH). The practical circuit achieved the impedance magnitude 41 Ω and phase -16.7°. The matching was as close to 50 Ω as could be achieved with available components.

C.2 Custom LIPUS Transducer Performance

An initial investigation of the LIPUS transducer was conducted on the HF scanning system to compare its performance with the FE model at 1 MHz and 1.5 MHz. The transducer was held in a clamp with the track of silver paint on the front face pointed upwards, allowing repeat measurements at the same orientation (Figure C.6). The tank temperature was 22.5 ± 0.5 °C
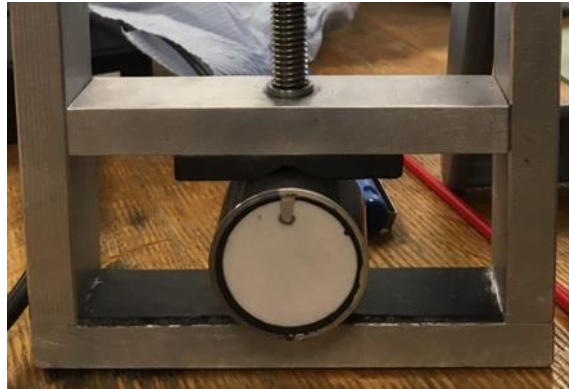
Figure C.6: LIPUS Transducer orientation during tank measurements.

The LIPUS transducer and matching circuit were driven with a signal generator (Agilent 33250A) with 20-cycle bursts every 10 ms and drive voltage of 1 Vpp at 1 MHz and 3 Vpp at 1.5 MHz. 1000 samples were captured at 200 MS/s. In post-processing 1000 samples were analysed at 1 MHz (5 cycles) and 933 samples at 1.5MHz (7 cycles). An axial scan in Z was conducted to find the onset of the far field (the last axial maximum, Z_0). The rms voltage output of the hydrophone was normalised to the rms voltage measured at the last axial maximum so the plots could be compared. Figure C.7 compares axial scan measurements with those predicted by the FE model.
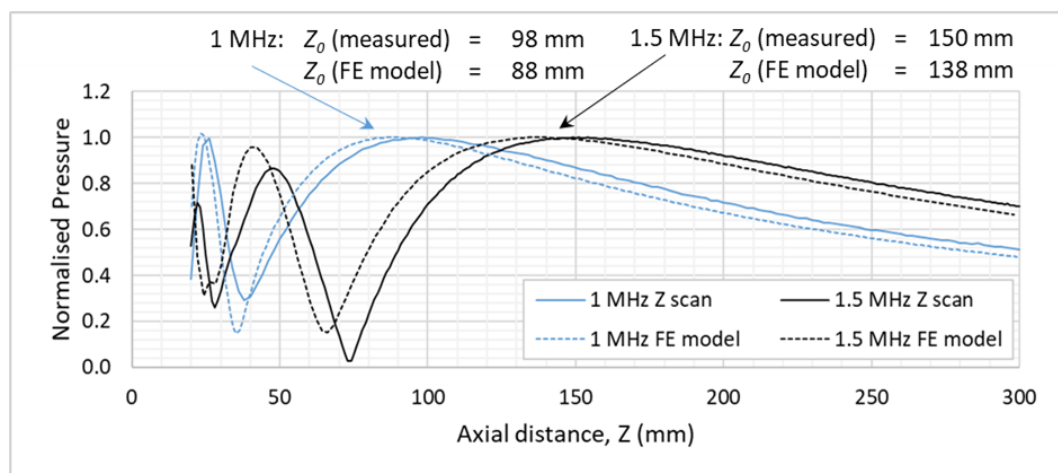
Figure C.7: Axial scans of LIPUS transducer at 1 MHz and 1.5 MHz compared with FE model. The last axial maxima, Z_0, indicate the onset of the far field. Good agreement was achieved in the overall shape of near field and far field profiles, though peaks appeared at greater distance than modelled.

The measured axial scans show good agreement to those generated by the FE model in terms of general shape, but the predicted Z_0 was 8 - 10 % less than the measured Z_0. The Z_0 of a piston of radius r can be approximated by [224]:

$$Z_0 \approx \frac{r^2}{\lambda}, \quad where \ \lambda \ll r \tag{C.4}$$

The measured result suggests the PZT disc is slightly smaller in diameter than modelled. A diameter of 24.4 mm would produce the measured Z_0 at both frequencies, whereas the model assumes a diameter of 25 mm. This illustrates that a small difference in the diameter could have resulted in the higher Z_0 values.

Line scans in X and Y were conducted at Z_0 to determine far field beam shape (Figure C.8). The line scan results were compared with the beam shapes predicted by the FE model and an acoustic aperture field model created in the MATLAB toolbox Field II [189, 190].

Figure C.8: Beam profiles in dB re maximum rms pressure of X & Y line scans, PZFlex model and Field II model at the last axial maxima. A: 1 MHz; B: 1.5 MHz.

Field II splits the acoustic aperture of a transducer into small parts, computes the spatial impulse response of each, then combines the responses to model the acoustic field. Finally, XY raster scans were conducted at both frequencies to obtain an impression of the overall beam shape. The 1 MHz scan covered ±40 mm either side of the beam axis in 1 mm steps. The 1.5 MHz scan was conducted over ±30 mm in 1 mm steps.
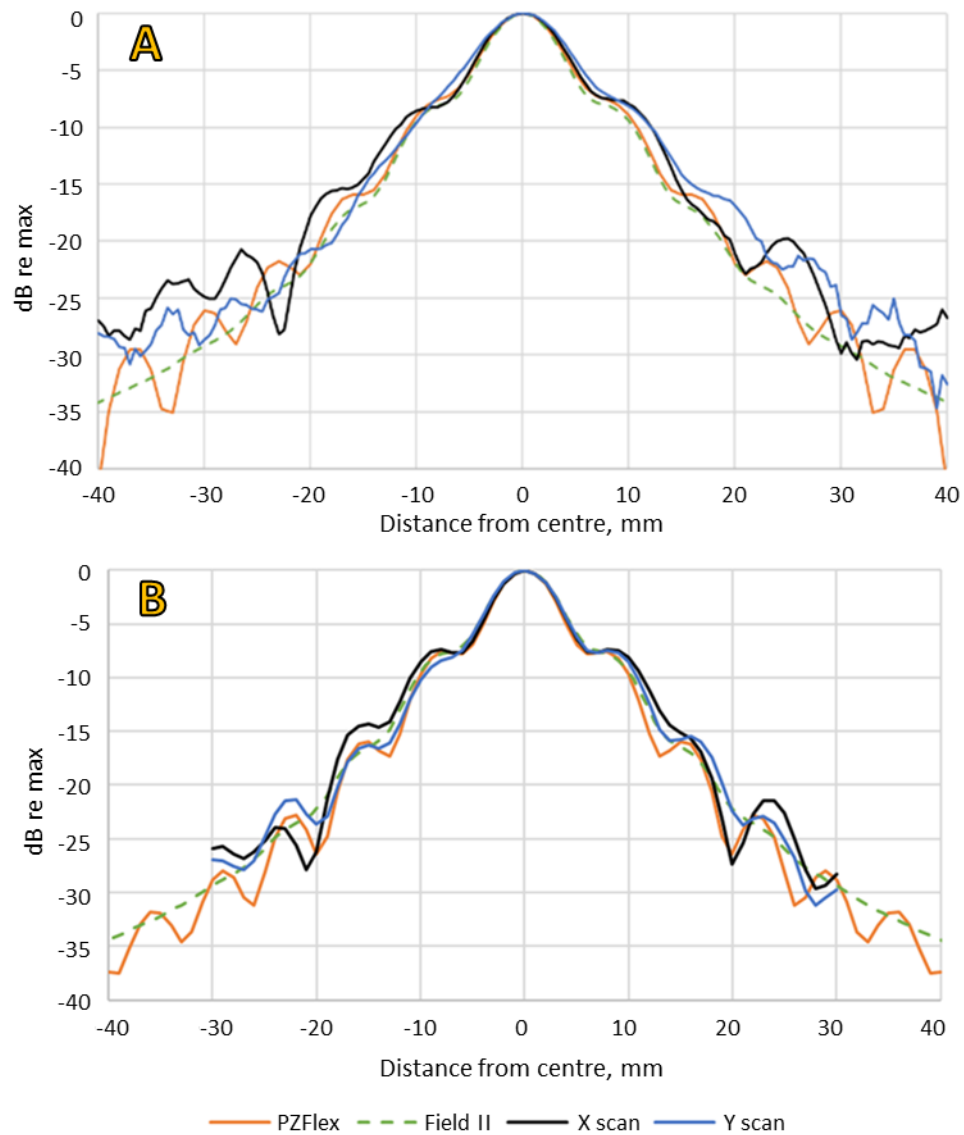
The shape of the beam is similar in all measured and modelled data, especially at 1.5 MHz and around the main beam. The main beam at 1.5 MHz is narrower than that at 1 MHz, due to the shorter wavelength. Comparing the X- and Y-planes, the device is not quite axisymmetric. The main lobe is wider in the Y-plane, where the -6 dB (or half-pressure) beam widths are up to 1.7 mm greater than in X. The X beam shape then widens outside the main beam, resulting in -10 dB beam widths 1.4 to 1.6 mm greater than in Y. The PZFlex FE model underestimates the beam widths but remains within 8 % of the measured values. The Field II model predicts the 1.5 MHz beam width within ± 4 %, but underestimates the beam width at 1 MHz by up to 16%. Overall, the results show that the device performance is close to that expected from the models.

Figure C.9 shows the XY raster scan results in the form of colourmaps of rms pressure. The 1.5 MHz pressure is higher than the 1 MHz pressure due to using a higher drive voltage (three times that of the 1 MHz drive).
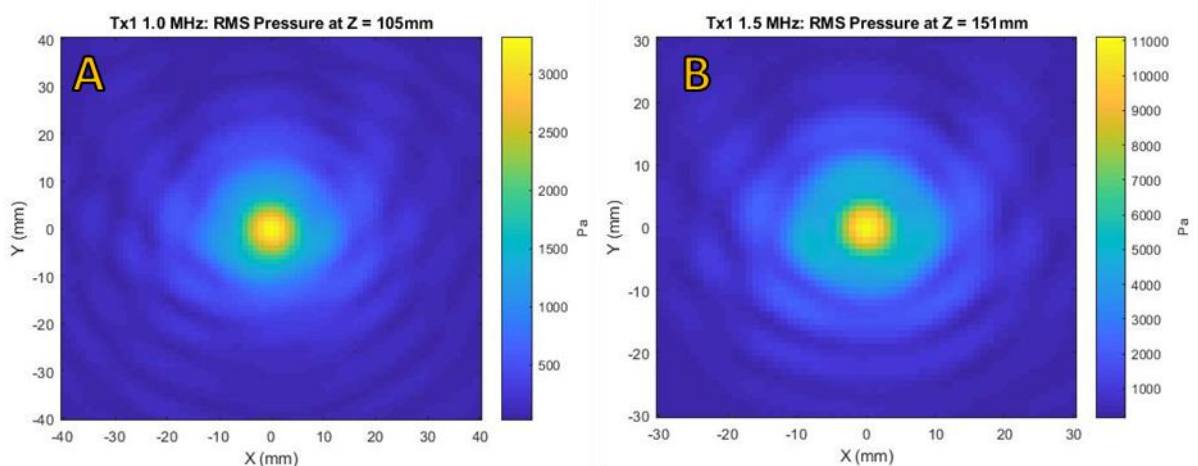
Figure C.9: Colourmaps of LIPUS transducer rms pressure
at A: 1 MHz over ± 40 mm in X and Y and B: 1.5 MHz over ± 30 mm in X and Y. The main lobe of the beam appears axisymmetric but the sidelobes exhibit asymmetry in Y.

The beam shapes are similar, and the beam width is narrower at 1.5 MHz as would be expected for a higher frequency (noting the difference in scan distances) with a flattening-

off in the negative Y direction. Evidence of an interference pattern in the side lobes suggest the internal reflection is having an effect on beam shape. This pattern is not evident in the negative Y direction. It is possible that this flattening of the shape and the lack of interference in the negative Y direction are both due to a thicker layer of backing material between the active element and the outer casing in this area (see Figure C.6). The transducer performance is discussed further in Section 3.2.3.

References

1. *Sonic Accelerated Fracture Healing System (SAFHS) Model 2000, Exogen 2000*, in *PMA P900009*, F.a.D. Administration, Editor. 1994: FDA Pre-market approval database.
2. Pilla, A.A., et al., *Non-Invasive Low-Intensity Pulsed Ultrasound Accelerates Bone Healing in the Rabbit.* Journal of Orthopaedic Trauma, 1990. **4**(3): p. 246-253.
3. Heckman, J.D., et al., *Acceleration of Tibial Fracture-Healing by Non-Invasive, Low-Intensity Pulsed Ultrasound.* The Journal of Bone and Joint Surgery, 1994. **76-A**(1): p. 26 - 34.
4. *MTG12: EXOGEN ultrasound bone healing system for long bone fractures with non-union or delayed healing*, M.T. Guidance, Editor. 2013, National Institute for Health and Care Excellence (NICE).
5. ter Haar, G., *Therapeutic applications of ultrasound.* Progress in Biophysics and Molecular Biology, 2007. **93**(1–3): p. 111-129.
6. Man, J., et al., *Low-intensity Low-frequency Ultrasound Promotes Proliferation and Differentiation of Odontoblast-like Cells.* Journal of Endodontics, 2012. **38**(5): p. 608-613.
7. Gopalan, A., et al., *Evaluation of Efficacy of Low Intensity Pulsed Ultrasound in Facilitating Mandibular Fracture Healing—A Blinded Randomized Controlled Clinical Trial.* Journal of Oral and Maxillofacial Surgery, 2020. **78**(6): p. 997.e1-997.e7.
8. Juyong, W., et al., *Low-intensity pulsed ultrasound prompts tissue-engineered bone formation after implantation surgery.* Chinese medical journal, 2014. **127**(4): p. 669-674.
9. Aliabouzar, M., et al., *Effects of scaffold microstructure and low intensity pulsed ultrasound on chondrogenic differentiation of human mesenchymal stem cells.* Biotechnology and bioengineering, 2018. **115**(2): p. 495-506.
10. Xu, P., et al., *Low-intensity pulsed ultrasound-mediated stimulation of hematopoietic stem/progenitor cell viability, proliferation and differentiation in vitro.* Biotechnology Letters, 2012. **34**(10): p. 1965-1973.
11. Busse, J.W., et al., *Re-evaluation of low intensity pulsed ultrasound in treatment of tibial fractures (TRUST): randomized clinical trial.* BMJ, 2016. **355**.
12. Poolman, R.W., et al., *Low intensity pulsed ultrasound (LIPUS) for bone healing: a clinical practice guideline.* BMJ, 2017. **356**.
13. Commission, I.E., *Medical electrical equipment - Part 2-5: Particular requirements for the basic safety and essential performance of ultrasonic physiotherapy equipment (IEC 60601-2-5:2009).* 2009.
14. Institute, B.S., *BS EN 61689:2013 Ultrasonics - Physiotherapy systems - Field specifications and methods of measurement in the frequency range 0,5 MHz to 5 MHz.* 2013, BSI Standards: UK.
15. Padilla, F., et al., *Stimulation of Bone Repair with Ultrasound*, in *Therapeutic Ultrasound*, J.-M. Escoffre and A. Bouakaz, Editors. 2016, Springer International Publishing: Cham. p. 385-427.
16. *EXOGEN User Guide.* 2014, Bioventus LLC. Image reproduced with permission from the manufacturer.
17. *EMS Therasonic 1032 Manual.* 1992, EMS Physio Ltd. Image reproduced with permission from the manufacturer.
18. *EMS Physio Ltd Primo Therasonic 360 and 460 Product information.* 2016 [11 February 2023]; Product information. Available from:

https://www.emsphysio.co.uk/wp-content/uploads/2016/02/EMS-Physio-Ltd-Primo-Therasonic-360-and-460-Product-information.pdf. Image reproduced with permission from the manufacturer.

19. Reher, P., et al., *Therapeutic ultrasound for osteoradionecrosis: an in vitro comparison between 1 MHz and 45 kHz machines.* European Journal of Cancer, 1998. **34**(12): p. 1962-1968. Image reproduced with permission from the manufacturer.

20. *4-Series Instructions for Use*. 2022, Enraf Nonius. Image reproduced with permission from the manufacturer.

21. *Ito Physiotherapy & Rehabilitation General Catalogue*. Ito Co. Ltd. Image reproduced with permission from the manufacturer.

22. *A.D.A.M. Medical Encyclopedia [Internet]. Johns Creek (GA): Ebix, Inc., A.D.A.M.; c1997-2023. Long bones; [reviewed 19 Jul 2021; cited 4 Feb 2023];. Available from: https://medlineplus.gov/ency/imagepages/9582.htm.*

23. Buckwalter, J.A., et al., *Bone biology. I: Structure, blood supply, cells, matrix, and mineralization.* Instructional course lectures, 1996. **45**: p. 371.

24. Amirazad, H., M. Dadashpour, and N. Zarghami, *Application of decellularized bone matrix as a bioscaffold in bone tissue engineering.* Journal of Biological Engineering, 2022. **16**(1): p. 1. Image of long bone structure from Fig. 1, licensed under Creative Commons Attribution 4.0 (http://creativecommons.org/licenses/by/4.0/). Cropped to highlight cells in structure and figure letters (A,B,C&D) added.

25. Rosa, N., et al., *From mechanical stimulus to bone formation: A review.* Medical Engineering & Physics, 2015. **37**(8): p. 719-728. DOI: https://doi.org/10.1016/j.medengphy.2015.05.015. Adapted excerpt of Fig. 1 reproduced with permission from Springer Nature (license 5482500580936).

26. Loi, F., et al., *Inflammation, fracture and bone repair.* Bone, 2016. **86**: p. 119-130.

27. Salhotra, A., et al., *Mechanisms of bone development and repair.* Nature Reviews Molecular Cell Biology, 2020. **21**(11): p. 696-711.

28. Dallas, S.L., M. Prideaux, and L.F. Bonewald, *The Osteocyte: An Endocrine Cell ... and More.* Endocrine Reviews, 2013. **34**(5): p. 658-690.

29. Bahney, C.S., et al., *Cellular biology of fracture healing.* Journal of Orthopaedic Research, 2019. **37**(1): p. 35-50.

30. Yang, L., et al., *Hypertrophic chondrocytes can become osteoblasts and osteocytes in endochondral bone formation.* Proceedings of the National Academy of Sciences of the United States of America, 2014. **111**(33): p. 12097-12102.

31. Einhorn, T.A. and L.C. Gerstenfeld, *Fracture healing: mechanisms and interventions.* Nature Reviews Rheumatology, 2015. **11**(1): p. 45-54.

32. Marsell, R. and T.A. Einhorn, *The biology of fracture healing.* Injury, 2011. **42**(6): p. 551-555.

33. Hall, J.E., *Guyton and Hall textbook of medical physiology*. 13th ed. 2016, Philadelphia, PA: Elsevier.

34. Morgan, E.F., G.U. Unnikrisnan, and A.I. Hussein, *Bone Mechanical Properties in Healthy and Diseased States.* Annual Review of Biomedical Engineering, 2018. **20**(1): p. 119-143.

35. Jagodzinski, M. and C. Krettek, *Effect of mechanical stability on fracture healing — an update.* Injury, 2007. **38**(1, Supplement): p. S3-S10.

36. Rutkovskiy, A., K.-O. Stensløkken, and I.J. Vaage, *Osteoblast Differentiation at a Glance.* Medical science monitor basic research, 2016. **22**: p. 95-106.

37. Behrens, A., et al., *Impact of genomic damage and ageing on stem cell function.* Nature Cell Biology, 2014. **16**(3): p. 201-207.

38.   Doan, N., et al., *In vitro effects of therapeutic ultrasound on cell proliferation, protein synthesis, and cytokine production by human fibroblasts, osteoblasts, and monocytes.* Journal of Oral and Maxillofacial Surgery, 1999. **57**(4): p. 409-419.

39.   Fung, C.-H., et al., *Osteocytes exposed to far field of therapeutic ultrasound promotes osteogenic cellular activities in pre-osteoblasts through soluble factors.* Ultrasonics, 2014. **54**(5): p. 1358-1365.

40.   Reher, P., et al., *Ultrasound stimulates nitric oxide and prostaglandin e2 production by human osteoblasts.* Bone, 2002. **31**(1): p. 236-241.

41.   Tang, C.-H., et al., *Ultrasound Stimulates Cyclooxygenase-2 Expression and Increases Bone Formation through Integrin, Focal Adhesion Kinase, Phosphatidylinositol 3-Kinase, and Akt Pathway in Osteoblasts.* Molecular Pharmacology, 2006. **69**(6): p. 2047-2057.

42.   Prockop, D.J., *Concise Review: Two negative feedback loops place mesenchymal stem/stromal cells at the center of early regulators of inflammation.* STEM CELLS, 2013. **31**(10): p. 2042-2046.

43.   Arikawa, T., K. Omura, and I. Morita, *Regulation of bone morphogenetic protein-2 expression by endogenous prostaglandin E2 in human mesenchymal stem cells.* Journal of Cellular Physiology, 2004. **200**(3): p. 400-406.

44.   Lai, C.-H., et al., *Effects of Low-Intensity Pulsed Ultrasound, Dexamethasone/TGF-β1 and/or BMP-2 on the Transcriptional Expression of Genes in Human Mesenchymal Stem Cells: Chondrogenic vs. Osteogenic Differentiation.* Ultrasound in Medicine & Biology, 2010. **36**(6): p. 1022-1033.

45.   Man, J., et al., *Low Intensity Ultrasound stimulates osteoblast migration at different frequencies.* The Japanese Society for Bone and Mineral Research and Springer, 2012. **2012**(30): p. 602-607.

46.   Tassinary, J.A.F., et al., *Therapeutic ultrasound stimulates MC3T3-E1 cell proliferation through the activation of NF-κB1, p38α, and mTOR.* Lasers in Surgery and Medicine, 2015. **47**(9): p. 765-772.

47.   Unsworth, J., et al., *Pulsed Low Intensity Ultrasound Enhances Mineralisation in Preosteoblast Cells.* Ultrasound in Medicine & Biology, 2007. **33**(9): p. 1468-1474.

48.   Knippenberg, M., et al., *Prostaglandins Differentially Affect Osteogenic Differentiation of Human Adipose Tissue–Derived Mesenchymal Stem Cells.* Tissue Engineering, 2007. **13**(10): p. 2495-2503.

49.   Stewart, S., et al., *Mechanotransduction in osteogenesis.* Bone & Joint Research, 2020. **9**(1): p. 1-14. Reproduction of Fig.3. Licensed under Creative Commons Attribution Non-Commercial No Derivatives (CC BY-NC-ND 4.0) licence. See https://creativecommons.org/licenses/by-nc-nd/4.0/.

50.   Young, S.R.L., et al., *Focal Adhesion Kinase Is Important for Fluid Shear Stress-Induced Mechanotransduction in Osteoblasts.* Journal of bone and mineral research, 2009. **24**(3): p. 411-424.

51.   ter Haar, G., et al., *Guidance on Reporting Ultrasound Exposure Conditions for Bio-Effects Studies.* Ultrasound in Medicine & Biology, 2011. **37**(2): p. 177-183.

52.   Shui, C. and A. Scutt, *Mild Heat Shock Induces Proliferation, Alkaline Phosphatase Activity, and Mineralization in Human Bone Marrow Stromal Cells and Mg-63 Cells In Vitro.* Journal of Bone and Mineral Research, 2001. **16**(4): p. 731-741.

53.   Richards, V. and R. Stofer, *The stimulation of bone growth by internal heating.* Surgery, 1959. **46**(1): p. 84.

54.   Doyle, J.R. and B.W. Smart, *Stimulation of bone growth by short-wave diathermy.* Journal of Bone and Joint Surgery-American Volume, 1963. **45**(1): p. 15-24.

55. Whitney, N.P., et al., *Integrin-Mediated Mechanotransduction Pathway of Low-Intensity Continuous Ultrasound in Human Chondrocytes.* Ultrasound in Medicine & Biology, 2012. **38**(10): p. 1734-1743.

56. Suzuki, A., et al., *Daily low-intensity pulsed ultrasound-mediated osteogenic differentiation in rat osteoblasts.* Acta Biochimica et Biophysica Sinica, 2009. **41**(2): p. 108-115.

57. Kinsler, L.E., et al., *Fundamentals of Acoustics.* 3rd ed. 1982: John Wiley & Sons Inc.

58. Leskinen, J.J. and K. Hynynen, *Study of Factors Affecting the Magnitude and Nature of Ultrasound Exposure with In Vitro Set-Ups.* Ultrasound in Medicine & Biology, 2012. **38**(5): p. 777-794. DOI: https://doi.org/10.1016/j.ultrasmedbio.2012.01.019. Adapted excerpt in Fig 1.12 adapted from Fig. 9 of the original under licence from Springer Nature (license 5487121481603).

59. Cochran, S., *1 - Piezoelectricity and basic configurations for piezoelectric ultrasonic transducers A2 - Nakamura, K*, in *Ultrasonic Transducers.* 2012, Woodhead Publishing. p. 3-35.

60. Selfridge, A.R., *Approximate Material Properties in Isotropic Materials.* IEEE Transactions on Sonics and Ultrasonics, 1985. **32**(3): p. 381-394.

61. Miyasaka, M., et al., *Low-Intensity Pulsed Ultrasound Stimulation Enhances Heat-Shock Protein 90 and Mineralized Nodule Formation in Mouse Calvaria-Derived Osteoblasts.* Tissue engineering. Part A, 2015. **21**(23-24): p. 2829-2839.

62. Chen, E., et al., *Extracellular heat shock protein 70 promotes osteogenesis of human mesenchymal stem cells through activation of the ERK signaling pathway.* FEBS Letters, 2015. **589**(24PartB): p. 4088-4096.

63. Lubbers, J. and R. Graaff, *A simple and accurate formula for the sound velocity in water.* Ultrasound in medicine & biology, 1998. **24**(7): p. 1065-1068.

64. Azhari, H., *Basics of biomedical ultrasound for engineers.* 2010, Hoboken, N.J: Wiley.

65. Xie, S., et al., *Low-intensity pulsed ultrasound promotes the proliferation of human bone mesenchymal stem cells by activating PI3K/AKt signaling pathways.* Journal of cellular biochemistry, 2019. **120**(9): p. 15823-15833.

66. Zhou, X., et al., *Improved Human Bone Marrow Mesenchymal Stem Cell Osteogenesis in 3D Bioprinted Tissue Scaffolds with Low Intensity Pulsed Ultrasound Stimulation.* Scientific reports, 2016. **6**(1): p. 32876-32876.

67. Secomski, W., et al., *In vitro ultrasound experiments: Standing wave and multiple reflections influence on the outcome.* Ultrasonics, 2017. **77**: p. 203-213.

68. Brekhovskikh, L., *Waves in layered media.* Vol. 16. 2012: Elsevier.

69. Olkku, A., et al., *Ultrasound-induced activation of Wnt signaling in human MG-63 osteoblastic cells.* Bone (New York, N.Y.), 2010. **47**(2): p. 320-330.

70. Zhang, Z., et al., *Low-intensity pulsed ultrasound stimulation facilitates in vitro osteogenic differentiation of human adipose-derived stem cells via up-regulation of heat shock protein (HSP)70, HSP90, and bone morphogenetic protein (BMP) signaling pathway.* Biosci Rep, 2018. **38**(3): p. 1-15.

71. Bandow, K., et al., *Low-intensity pulsed ultrasound (LIPUS) induces RANKL, MCP-1, and MIP-1β expression in osteoblasts through the angiotensin II type 1 receptor.* Journal of Cellular Physiology, 2007. **211**(2): p. 392-398.

72. Webster, D.F., et al., *The role of cavitation in the in vitro stimulation of protein synthesis in human fibroblasts by ultrasound.* Ultrasound in Medicine & Biology, 1978. **4**(4): p. 343-351.

73. Buchtala, V., *Present state of ultrasound therapy.* El Día médico, 1950. **22**(70): p. 2944.

74. Maintz, G., *Animal experiments in the study of the effect of ultrasonic waves on bone regeneration.* Strahlentherapie, 1950. **82**(4): p. 631-638.

75. De Nunno, R., *Effect of ultrasonics on ossification; experimental studies.* Annali italiani di chirurgia, 1952. **29**(4): p. 211.

76. Murolo, C. and F. Claudio, *Effect of ultrasonics on repair of fractures.* Giornale italiano di chirurgia, 1952. **8**(11): p. 897.

77. Corradi, C. and A. Cozzolino, *Effect of ultrasonics on the development of osseous callus in fractures.* Archivio di ortopedia, 1953. **66**(1): p. 77.

78. Bender, L.F., J.M. Janes, and J.F. Herrick, *Histologic studies following exposure of bone to ultrasound.* Archives of physical medicine and rehabilitation, 1954. **35**(9): p. 555.

79. Ardan, N.I., J.M. Janes, and J.F. Herrick, *Ultrasonic Energy and Surgically Produced Defects in Bone.* The Journal of Bone & Joint Surgery, 1957. **39**(2): p. 394-402.

80. Dyson, M., et al., *The stimulation of tissue regeneration by means of ultrasound.* Clinical science, 1968. **35**(2): p. 273.

81. Young, S.R. and M. Dyson, *The effect of therapeutic ultrasound on angiogenesis.* Ultrasound in Medicine & Biology, 1990. **16**(3): p. 261-269.

82. Duarte, L.R., *The stimulation of bone growth by ultrasound.* Archives of Orthopaedic and Traumatic Surgery, 1983. **101**(3): p. 153-159.

83. Klug, W., W.-G. Franke, and H.-G. Knoch, *Scintigraphic control of bone-fracture healing under ultrasonic stimulation: An animal experimental study.* European Journal of Nuclear Medicine, 1986. **11**(12): p. 494-497.

84. Xavier, C.M. and L.R. Duarte, *Ultrasonic stimulation of the bone callus. Clinical application.* Revista brasileira de ortopedia (Impresso), 1983. **18**: p. 73 - 80.

85. Duarte, L.R., *Method for healing bone fractures with ultrasound*, U.P. Office, Editor. 1985: United States.

86. Azuma, Y., et al., *Low-Intensity Pulsed Ultrasound Accelerates Rat Femoral Fracture Healing by Acting on the Various Cellular Reactions in the Fracture Callus.* Journal of Bone and Mineral Research, 2001. **16**(4): p. 671-680.

87. Greenleaf, J.F., R. Kinnick, and M. Bolander, *Ultrasonically induced motion in tissue during fracture treatment?* Ultrasound in Medicine & Biology, 2003. **29**(5, Supplement): p. S157-S158.

88. Hsu, S.-K., et al., *Effects of Near-Field Ultrasound Stimulation on New Bone Formation and Osseointegration of Dental Titanium Implants In Vitro and In Vivo.* Ultrasound in Medicine & Biology, 2011. **37**(3): p. 403-416.

89. Kumagai, K., et al., *Circulating cells with osteogenic potential are physiologically mobilized into the fracture healing site in the parabiotic mice model.* Journal of orthopaedic research, 2008. **26**(2): p. 165-175.

90. Kumagai, K., et al., *Low-intensity pulsed ultrasound accelerates fracture healing by stimulation of recruitment of both local and circulating osteogenic progenitors.* Journal of Orthopaedic Research, 2012. **30**(9): p. 1516-1521.

91. Kitaori, T., et al., *Stromal cell-derived factor 1/CXCR4 signaling is critical for the recruitment of mesenchymal stem cells to the fracture site during skeletal repair in a mouse model.* Arthritis and rheumatism, 2009. **60**(3): p. 813-823.

92. Gibon, E., et al., *MC3T3-E1 Osteoprogenitor Cells Systemically Migrate to a Bone Defect and Enhance Bone Healing.* Tissue Engineering. Part A, 2012. **18**(9-10): p. 968-973.

93.   Fung, C.-H., et al., *Effects of Different Therapeutic Ultrasound Intensities on Fracture Healing in Rats.* Ultrasound in Medicine & Biology, 2012. **38**(5): p. 745-752.

94.   Bronoosh, P., et al., *Effects of low-intensity pulsed ultrasound on healing of mandibular bone defects: an experimental study in rabbits.* International Journal of Oral and Maxillofacial Surgery, 2015. **44**(2): p. 277-284.

95.   Jung, Y.J., et al., *Focused Low-Intensity Pulsed Ultrasound Enhances Bone Regeneration in Rat Calvarial Bone Defect through Enhancement of Cell Proliferation.* Ultrasound in Medicine & Biology, 2015. **41**(4): p. 999-1007.

96.   Fung, C.-H., et al., *Investigation of rat bone fracture healing using pulsed 1.5MHz, 30mW/cm2 burst ultrasound – Axial distance dependency.* Ultrasonics, 2014. **54**(3): p. 850-859.

97.   Heckman, J.D. and J. Sarasohn-Kahn, *The economics of treating tibia fractures. The cost of delayed unions.* Bulletin (Hospital for Joint Diseases (New York, N.Y.)), 1997. **56**(1): p. 63.

98.   Kristiansen, T.K., et al., *Accelerated Healing of Distal Radial Fractures with the Use of Specific, Low-Intensity Ultrasound. A Multicenter, Prospective, Randomized, Double-Blind, Placebo-Controlled Study*.* The Journal of Bone & Joint Surgery, 1997. **79**(7): p. 961-73.

99.   Nolte, P.A., et al., *Low-Intensity Pulsed Ultrasound in the Treatment of Nonunions.* The Journal of Trauma: Injury, Infection, and Critical Care, 2001. **51**(4): p. 693-703.

100.   Cook, S., et al., *Acceleration of Tibia and Distal Radius Fracture Healing in Patients who Smoke.* Clinical Orthopaedics and Related Research, 1997. **337**: p. 198-207.

101.   Romano, C., J. Messina, and E. Meani, *Ultrasuoni pulsati a bassa intensità per il trattamento delle pseudoartrosi settiche.* Quaderni di Infezioni Osteoarticolari, 1999: p. 83–93.

102.   Gebauer, D., et al., *Low-intensity pulsed ultrasound: Effects on nonunions.* Ultrasound in Medicine & Biology, 2005. **31**(10): p. 1391-1402.

103.   Romano, C.L., D. Romano, and N. Logoluso, *Low-Intensity Pulsed Ultrasound for the Treatment of Bone Delayed Union or Nonunion: A Review.* Ultrasound in Medicine & Biology, 2009. **35**(4): p. 529-536.

104.   *Low-Intensity pulse ultrasound to promote fracture healing.* Interventional Procedures Guidance [IPG374] 2010 3 May 2017; Available from: https://www.nice.org.uk/guidance/ipg374.

105.   Rue, J.P.H., et al., *The effect of pulsed ultrasound in the treatment of tibial stress fractures.* ORTHOPEDICS, 2004. **27**(11): p. 1192-1195.

106.   Schandelmaier, S., et al., *Low intensity pulsed ultrasound for bone healing: systematic review of randomized controlled trials.* BMJ, 2017. **356**: p. j656.

107.   Webster, D.F., et al., *The role of ultrasound-induced cavitation in the 'in vitro' stimulation of collagen synthesis in human fibroblasts.* Ultrasonics, 1980. **18**(1): p. 33-37.

108.   ter Haar, G., *Ultrasound bioeffects and safety.* Proceedings of the Institution of Mechanical Engineers, Part H: Journal of Engineering in Medicine, 2010. **224**(2): p. 363-373.

109.   Baker, K.G., V.J. Robertson, and F.A. Duck, *A Review of Therapeutic Ultrasound: Biophysical Effects*, in *Physical Therapy*. 2001. p. 1351.

110.   Zhou, S., et al., *Molecular Mechanisms of Low Intensity Pulsed Ultrasound in Human Skin Fibroblasts.* Journal of Biological Chemistry, 2004. **279**(52): p. 54463-54469.

111. Iwanabe, Y., et al., *The effect of low-intensity pulsed ultrasound on wound healing using scratch assay in epithelial cells.* Journal of Prosthodontic Research, 2016. **60**(4): p. 308-314.

112. Su, Z., et al., *Low-intensity pulsed ultrasound promotes apoptosis and inhibits angiogenesis via p38 signaling-mediated endoplasmic reticulum stress in human endothelial cells.* Mol Med Rep, 2019. **19**(6): p. 4645-4654.

113. Sena, K., et al., *Early gene response to low-intensity pulsed ultrasound in rat osteoblastic cells.* Ultrasound in Medicine & Biology, 2005. **31**(5): p. 703-708.

114. Angle, S.R., et al., *Osteogenic differentiation of rat bone marrow stromal cells by various intensities of low-intensity pulsed ultrasound.* Ultrasonics, 2011. **51**(3): p. 281-288.

115. Marvel, S., et al., *The development and validation of a lipus system with preliminary observations of ultrasonic effects on human adult stem cells.* IEEE Transactions on Ultrasonics, Ferroelectrics, and Frequency Control, 2010. **57**(9): p. 1977-1984.

116. Engler, A.J., et al., *Matrix Elasticity Directs Stem Cell Lineage Specification.* Cell, 2006. **126**(4): p. 677-689.

117. Liu, L., et al., *Calcium Channel Opening Rather than the Release of ATP Causes the Apoptosis of Osteoblasts Induced by Overloaded Mechanical Stimulation.* Cellular Physiology and Biochemistry, 2017. **42**(2): p. 441-454.

118. Lim, K., et al., *In vitro effects of low-intensity pulsed ultrasound stimulation on the osteogenic differentiation of human alveolar bone-derived mesenchymal stem cells for tooth tissue engineering.* BioMed research international, 2013. **2013**: p. 269724-269724.

119. Gao, Q., et al., *Role of Piezo Channels in Ultrasound-stimulated Dental Stem Cells.* Journal of endodontics, 2017. **43**(7): p. 1130-1136.

120. Argadine, H.M., et al. *1 kHz low power sound stimulates ATDC5 chondrocytes.* in *IEEE Ultrasonics Symposium, 2005.* **2**: p. 996-998.

121. Nikukar, H., et al., *Osteogenesis of Mesenchymal Stem Cells by Nanoscale Mechanotransduction.* ACS nano, 2013. **7**(3): p. 2758-2767.

122. Tsimbouri, P.M., et al., *Stimulation of 3D osteogenesis by mesenchymal stem cells using a nanovibrational bioreactor.* Nature Biomedical Engineering, 2017. **1**(9): p. 758-770.

123. Xia, P., et al., *Low-Intensity Pulsed Ultrasound Affects Chondrocyte Extracellular Matrix Production via an Integrin-Mediated p38 MAPK Signaling Pathway.* Ultrasound in Medicine & Biology, 2015. **41**(6): p. 1690-1700.

124. Mukai, S., et al., *Transforming growth factor-β1 mediates the effects of low-intensity pulsed ultrasound in chondrocytes.* Ultrasound in Medicine & Biology, 2005. **31**(12): p. 1713-1721.

125. Javad, P., et al., *Calcium signaling is required for ultrasound-stimulated aggrecan synthesis by rat chondrocytes.* Journal of Orthopaedic Research, 2002. **20**(1): p. 51-57.

126. Parvizi, J., et al., *Low-intensity ultrasound stimulates proteoglycan synthesis in rat chondrocytes by increasing aggrecan gene expression.* Journal of orthopaedic research, 1999. **17**(4): p. 488.

127. Quarles, L.D., et al., *Distinct proliferative and differentiated stages of murine MC3T3-E1 cells in culture: An in vitro model of osteoblast development.* Journal of Bone and Mineral Research, 1992. **7**(6): p. 683-692.

128. Kokubu, T., et al., *Low Intensity Pulsed Ultrasound Exposure Increases Prostaglandin E2Production via the Induction of Cyclooxygenase-2 mRNA in*

Mouse Osteoblasts. Biochemical and Biophysical Research Communications, 1999. **256**(2): p. 284-287.

129. Katiyar, A., R.L. Duncan, and K. Sarkar, *Ultrasound stimulation increases proliferation of MC3T3-E1 preosteoblast-like cells.* Journal of Therapeutic Ultrasound, 2014. **2**(1): p. 1-10.

130. Tassinary, J.A.F., et al., *Low-intensity pulsed ultrasound (LIPUS) stimulates mineralization of MC3T3-E1 cells through calcium and phosphate uptake.* Ultrasonics, 2018. **84**: p. 290-295.

131. Kaur, H., et al., *Role of Reactive Oxygen Species during Low-Intensity Pulsed Ultrasound Application in MC-3 T3 E1 Pre-osteoblast Cell Culture.* Ultrasound in Medicine & Biology, 2017. **43**(11): p. 2699-2712.

132. Tabuchi, Y., et al., *Genes Responsive to Low-Intensity Pulsed Ultrasound in MC3T3-E1 Preosteoblast Cells.* International Journal of Molecular Sciences, 2013. **14**(11): p. 22721-22740.

133. Lu, H., et al., *Identification of genes responsive to low-intensity pulsed ultrasound stimulations.* Biochemical and biophysical research communications, 2009. **378**(3): p. 569-573.

134. Liu, S., et al., *LIPUS inhibited the expression of inflammatory factors and promoted the osteogenic differentiation capacity of hPDLCs by inhibiting the NF-κB signaling pathway.* Journal of periodontal research, 2019. **55**(1): p. 125-140.

135. Maung, W.M., et al., *Low-Intensity Pulsed Ultrasound Stimulates Osteogenic Differentiation of Periosteal Cells In Vitro.* Tissue engineering. Part A, 2020: p. 1-11.

136. Guan-Rong Li, J., et al., *Optimum intensities of ultrasound for pge2 secretion and growth of osteoblasts.* Ultrasound in Medicine and Biology, 2002. **28**(5): p. 683 - 690.

137. Imai, Y., et al., *The osteogenic activity of human mandibular fracture haematoma-derived cells is stimulated by low-intensity pulsed ultrasound in vitro.* International Journal of Oral and Maxillofacial Surgery, 2014. **43**(3): p. 367-372.

138. Huang, W., et al., *Low-intensity pulsed ultrasound enhances bone morphogenetic protein expression of human mandibular fracture haematoma-derived cells.* International Journal of Oral and Maxillofacial Surgery, 2015. **44**(7): p. 929-935.

139. Harle, J., et al., *Effects of ultrasound on transforming growth factor-beta genes in bone cells.* European cells & materials, 2005. **10**: p. 70-6; discussion 76.

140. Harle, J., et al., *Effects of ultrasound on the growth and function of bone and periodontal ligament cells in vitro.* Ultrasound in Medicine & Biology, 2001. **27**(4): p. 579-586.

141. Dyson, M., et al., *Stimulation of Tissue Regeneration by Pulsed Plane-Wave Ultrasound.* IEEE Transactions on Sonics and Ultrasonics, 1970. **17**(3): p. 133-139.

142. Fukada, E. and I. Yasuda, *On the Piezoelectric Effect of Bone.* Journal of the Physical Society of Japan, 1957. **12**(10): p. 1158-1162.

143. Behari, J. and S. Singh, *Ultrasound propagation in 'in vivo' bone.* Ultrasonics, 1981. **19**(2): p. 87-90.

144. Okino, M., et al., *Electrical potentials in bone induced by ultrasound irradiation in the megahertz range.* Applied physics letters, 2013. **103**(10): p. 103701.

145. Jones, S.W., *Overview of Voltage-Dependent Calcium Channels.* Journal of bioenergetics and biomembranes, 1998. **30**(4): p. 299-312.

146. Louw, T.M., et al., *Mechanotransduction of Ultrasound is Frequency Dependent Below the Cavitation Threshold.* Ultrasound in Medicine & Biology, 2013. **39**(7): p. 1303-1319.

147. Culmann, K., *Die graphische statik.* Vol. 1. 1875: Meyer & Zeller (A. Reimann).

148. Pauwels, F., *Biomechanics of the Locomotor Apparatus*. 1980, Germany: Springer, Berlin, Heidelberg.

149. Duncan, R.L. and C.H. Turner, *Mechanotransduction and the functional response of bone to mechanical strain*. Calcified Tissue International, 1995. **57**(5): p. 344-358. DOI: 10.1007/BF00302070. Adapted excerpt of Fig. 2.2 reproduced with permission from Springer Nature (license 5482510750283).

150. Burr, D.B., et al., *In vivo measurement of human tibial strains during vigorous activity*. Bone, 1996. **18**(5): p. 405-410.

151. Wang, L., J. Dong, and C.J. Xian, *Strain amplification analysis of an osteocyte under static and cyclic loading: a finite element study*. BioMed research international, 2015. **2015**: p. 376474-376474.

152. Baron, C., et al., *Interaction of ultrasound waves with bone remodelling: a multiscale computational study*. Biomechanics and Modeling in Mechanobiology, 2020. **19**(5): p. 1755-1764.

153. Weinbaum, S., S.C. Cowin, and Y. Zeng, *A model for the excitation of osteocytes by mechanical loading-induced bone fluid shear stresses*. Journal of Biomechanics, 1994. **27**(3): p. 339-360.

154. Kamel, M.A., et al., *Activation of β-catenin signaling in MLO-Y4 osteocytic cells versus 2T3 osteoblastic cells by fluid flow shear stress and PGE2: Implications for the study of mechanosensation in bone*. Bone, 2010. **47**(5): p. 872-881.

155. Blackwell, K.A., L.G. Raisz, and C.C. Pilbeam, *Prostaglandins in bone: bad cop, good cop?* Trends in Endocrinology & Metabolism, 2010. **21**(5): p. 294-301.

156. Nefussi, J.-R. and R. Baron, *PGE2 stimulates both resorption and formation of bone in vitro: Differential responses of the periosteum and the endosteum in fetal rat long bone cultures*. The Anatomical Record, 1985. **211**(1): p. 9-16.

157. Hu, B., et al., *Low-Intensity Pulsed Ultrasound Stimulation Facilitates Osteogenic Differentiation of Human Periodontal Ligament Cells*. PloS one, 2014. **9**(4): p. e95168.

158. Yavropoulou, M.P. and J.G. Yovos, *The molecular basis of bone mechanotransduction*. Journal of musculoskeletal & neuronal interactions, 2016. **16**(3): p. 221-236. Reproduction of Fig.5. Licensed under Creative Commons Attribution Non-Commercial Sharealike 4.0 International license (CC BY-NC-SA 4.0). See https://creativecommons.org/licenses/by-nc-sa/4.0/.

159. El Haj, A.J., et al., *Mechanotransduction pathways in bone: calcium fluxes and the role of voltage-operated calcium channels*. Medical & biological engineering & computing, 1999. **37**(3): p. 403-409.

160. Noriega, S., et al., *Intermittent Applications of Continuous Ultrasound on the Viability, Proliferation, Morphology, and Matrix Production of Chondrocytes in 3D Matrices*. Tissue Engineering, 2007. **13**(3): p. 611-618.

161. Veronick, J., et al., *Mechanically Loading Cell/Hydrogel Constructs with Low-Intensity Pulsed Ultrasound for Bone Repair*. Tissue Engineering Part A, 2018. **24**(3-4): p. 254-263.

162. Veronick, J., et al., *The effect of acoustic radiation force on osteoblasts in cell/hydrogel constructs for bone repair*. Experimental biology and medicine (Maywood, N.J.), 2016. **241**(10): p. 1149-1156.

163. Vazquez, M., et al., *A New Method to Investigate How Mechanical Loading of Osteocytes Controls Osteoblasts*. Frontiers in Endocrinology, 2014. **5**(208): p. 1-18.

164. Curry, A.S., et al., *Taking cues from the extracellular matrix to design bone-mimetic regenerative scaffolds*. Matrix Biology, 2016. **52-54**: p. 397-412.

165. Kim, H., et al., *Irisin Mediates Effects on Bone and Fat via αV Integrin Receptors.* Cell, 2018. **175**(7): p. 1756-1768.e17.

166. Blair, H.C., et al., *Osteoblast Differentiation and Bone Matrix Formation In Vivo and In Vitro.* Tissue Engineering Part B: Reviews, 2016. **23**(3): p. 268-280.

167. Veronick, J.A., et al., *Mechanically Loading Cell/Hydrogel Constructs with Low-Intensity Pulsed Ultrasound for Bone Repair.* Tissue Engineering Part A, 2018. **24**(3-4): p. 254-263.

168. ATCC, *ATCC Product Sheet, MC3T3-E1 Subclone 4 (ATCC ® CRL-2593^{TM}).* 2018, American Type Culture Collection.

169. Czekanska, E.M., et al., *In Search of an Osteoblastic Cell Model for in vitro research*, in *European Cells and Materials*. 2012. p. 1-17.

170. Langenbach, F. and J. Handschel, *Effects of dexamethasone, ascorbic acid and β-glycerophosphate on the osteogenic differentiation of stem cells in vitro.* Stem Cell Research & Therapy, 2013. **4**(5): p. 117.

171. D'Aniello, C., et al., *Vitamin C in Stem Cell Biology: Impact on Extracellular Matrix Homeostasis and Epigenetics.* Stem Cells International, 2017. **2017**: p. 8936156.

172. Franceschi, R.T. and B.S. Iyer, *Relationship between collagen synthesis and expression of the osteoblast phenotype in MC3T3-E1 cells.* Journal of Bone and Mineral Research, 1992. **7**(2): p. 235-246.

173. Wang, D., et al., *Isolation and Characterization of MC3T3-E1 Preosteoblast Subclones with Distinct In Vitro and In Vivo Differentiation/Mineralization Potential.* Journal of Bone and Mineral Research, 1999. **14**(6): p. 893-903.

174. Cutiongco, M.F.A., et al., *Predicting gene expression using morphological cell responses to nanotopography.* Nature communications, 2020. **11**(1): p. 1-13.

175. Yan, X.Z., et al., *Effects of Continuous Passaging on Mineralization of MC3T3-E1 Cells with Improved Osteogenic Culture Protocol.* Tissue Engineering Part C-Methods, 2014. **20**(3): p. 198-204.

176. Stein, G.S., et al., *Runx2 control of organization, assembly and activity of the regulatory machinery for skeletal gene expression.* Oncogene, 2004. **23**(24): p. 4315-4329.

177. Padilla, F., et al., *Stimulation of bone repair with ultrasound: A review of the possible mechanic effects.* Ultrasonics, 2014. **54**(5): p. 1125-1145.

178. Rasband, W.S., *ImageJ.* 1997-2018, US National Institutes of Health: Bethesda, Maryland, USA.

179. Schneider, C.A., W.S. Rasband, and K.W. Eliceiri, *NIH Image to ImageJ: 25 years of image analysis.* Nature methods, 2012. **9**(7): p. 671.

180. *ab133021 - Prostaglandin E2 ELISA Kit: Instructions for Use*. 2015, Abcam.

181. Pfaffl, M.W., et al., *Determination of stable housekeeping genes, differentially regulated target genes and sample integrity: BestKeeper – Excel-based tool using pair-wise correlations.* Biotechnology letters, 2004. **26**(6): p. 509-515.

182. Piehler, A.P., et al., *Gene expression results in lipopolysaccharide-stimulated monocytes depend significantly on the choice of reference genes.* BMC immunology, 2010. **11**(1): p. 21-21.

183. Chen, G., et al., *Validation of reliable reference genes for real-time PCR in human umbilical vein endothelial cells on substrates with different stiffness.* PloS one, 2013. **8**(6): p. e67360-e67360.

184. Institute, B.S., *BS EN 62127-1:2007+A1:2013 Ultrasonics. Hydrophones. Measurement and Characterization of Medical Ultrasonic Fields up to 40 MHz.* 2008, BSi.

185. Ahmadi, F., et al., *Bio-effects and safety of low-intensity, low-frequency ultrasonic exposure.* Progress in Biophysics and Molecular Biology, 2012. **108**(3): p. 119-138.

186. Gupta, D., et al., *Traditional Multiwell Plates and Petri Dishes Limit the Evaluation of the Effects of Ultrasound on Cells In Vitro.* Ultrasound in Medicine & Biology, 2022. **48**(9): p. 1745-1761.

187. *Duo Son User Handbook for Europe.* 2008, SRA Developments Ltd.

188. Man, J., *Biological Effects of Low Frequency Ultrasound on Bone and Tooth Cells*, in *Faculty of Medicine and Dentistry.* 2011, University of Birmingham: University of Birmingham Research Archive e-theses repository. p. 214.

189. Jensen, J.A. and N.B. Svendsen, *Calculation of pressure fields from arbitrarily shaped, apodized, and excited ultrasound transducers.* IEEE Transactions on Ultrasonics, Ferroelectrics, and Frequency Control, 1992. **39**(2): p. 262-267.

190. Jensen, J.A., *Field: A program for simulating ultrasound systems.* Medical & Biological Engineering & Computing, pp. 351-353, Volume 34, Supplement 1, Part 1, 1996.

191. Li, X., et al., *Limits and Opportunities for Miniaturizing Ultrasonic Surgical Devices Based on a Langevin Transducer.* IEEE Transactions on Ultrasonics, Ferroelectrics, and Frequency Control, 2021. **68**(7): p. 2543-2553.

192. Yudina, A., M. Lepetit-Coiffé, and C.T.W. Moonen, *Evaluation of the Temporal Window for Drug Delivery Following Ultrasound-Mediated Membrane Permeability Enhancement.* Molecular imaging and biology, 2011. **13**(2): p. 239-249.

193. Keller, S., M. Bruce, and M.A. Averkiou, *Ultrasound Imaging of Microbubble Activity during Sonoporation Pulse Sequences.* Ultrasound in Medicine & Biology, 2019. **45**(3): p. 833-845.

194. Beekers, I., et al., *Acoustic Characterization of the CLINIcell for Ultrasound Contrast Agent Studies.* IEEE Transactions on Ultrasonics, Ferroelectrics, and Frequency Control, 2018: p. 1-4.

195. McKeen, L.W., *Film properties of plastics and elastomers.* Fourth ed. 2017, Oxford: William Andrew, imprint of Elsevier.

196. Lerman, M.J., et al., *The Evolution of Polystyrene as a Cell Culture Material.* Tissue Engineering Part B: Reviews, 2018. **24**(5): p. 359-372.

197. Anamelechi, C.C., G.A. Truskey, and W.M. Reichert, *Mylar™ and Teflon-AF™ as cell culture substrates for studying endothelial cell adhesion.* Biomaterials, 2005. **26**(34): p. 6887-6896.

198. Geissler, U., et al., *Collagen Type I-coating of Ti6Al4V promotes adhesion of osteoblasts.* Vol. 51. 2000. 752-760.

199. Lynch, M.P., et al., *The Influence of Type I Collagen on the Development and Maintenance of the Osteoblast Phenotype in Primary and Passaged Rat Calvarial Osteoblasts: Modification of Expression of Genes Supporting Cell Growth, Adhesion, and Extracellular Matrix Mineralization.* Experimental Cell Research, 1995. **216**(1): p. 35-45.

200. Busschots, S., et al., *Non-invasive and non-destructive measurements of confluence in cultured adherent cell lines.* MethodsX, 2015. **2**: p. 8-13.

201. Wäldchen, S., et al., *Light-induced cell damage in live-cell super-resolution microscopy.* Scientific Reports, 2015. **5**(1): p. 15348.

202. Durand, R.E. and P.L. Olive, *Cytotoxicity, Mutagenicity and DNA damage by Hoechst 33342.* Journal of Histochemistry & Cytochemistry, 1982. **30**(2): p. 111-116.

203. Lewis, A.H., et al., *Transduction of Repetitive Mechanical Stimuli by Piezo1 and Piezo2 Ion Channels.* Cell Reports, 2017. **19**(12): p. 2572-2585.

204. Cardillo, G., *Four parameters logistic regression - There and back again*. 2018: https://it.mathworks.com/matlabcentral/fileexchange/38122.

205. Cheng, Z.A., et al., *Nanoscale Coatings for Ultralow Dose BMP-2-Driven Regeneration of Critical-Sized Bone Defects*. Advanced Science, 2019. **6**(2): p. 1800361.

206. Hart, N.H., et al., *Mechanical basis of bone strength: influence of bone material, bone structure and muscle action*. Journal of musculoskeletal & neuronal interactions, 2017. **17**(3): p. 114-139.

207. Liang, C.-C., A.Y. Park, and J.-L. Guan, *In vitro scratch assay: a convenient and inexpensive method for analysis of cell migration in vitro*. Nat. Protocols, 2007. **2**(2): p. 329-333.

208. Krieger, N.S., et al., *Prostaglandins regulate acid-induced cell-mediated bone resorption*. American Journal of Physiology-Renal Physiology, 2000. **279**(6): p. F1077-F1082.

209. Tomura, H., et al., *Cyclooxygenase-2 Expression and Prostaglandin E2 Production in Response to Acidic pH Through OGR1 in a Human Osteoblastic Cell Line*. Journal of Bone and Mineral Research, 2008. **23**(7): p. 1129-1139.

210. Mullen, C.A., et al., *Osteocyte differentiation is regulated by extracellular matrix stiffness and intercellular separation*. Journal of the mechanical behavior of biomedical materials, 2013. **28**: p. 183-194.

211. Take, I., et al., *Prostaglandin E2 Strongly Inhibits Human Osteoclast Formation*. Endocrinology, 2005. **146**(12): p. 5204-5214.

212. Zeng, Q., et al., *Integrin-β1, not integrin-β5, mediates osteoblastic differentiation and ECM formation promoted by mechanical tensile strain*. Biological research, 2015. **48**(1): p. 25-25.

213. Moriishi, T., et al., *Osteocalcin is necessary for the alignment of apatite crystallites, but not glucose metabolism, testosterone synthesis, or muscle mass*. PLOS Genetics, 2020. **16**(5): p. e1008586.

214. Si, J., et al., *Osteopontin in Bone Metabolism and Bone Diseases*. Medical science monitor : international medical journal of experimental and clinical research, 2020. **26**: p. e919159-e919159.

215. Komori, T., *Regulation of Proliferation, Differentiation and Functions of Osteoblasts by Runx2*. International journal of molecular sciences, 2019. **20**(7): p. 1694. DOI: 10.3390/ijms20071694. Reproduction of Fig.1. Licensed under Creative Commons Attribution 4.0 International license (CC BY 4.0). See http://creativecommons.org/licenses/by/4.0/

216. Tarkkonen, K., et al., *Comparative analysis of osteoblast gene expression profiles and Runx2 genomic occupancy of mouse and human osteoblasts in vitro*. Gene, 2017. **626**: p. 119-131.

217. Latchman, D.S., *Transcription factors: An overview*. The International Journal of Biochemistry & Cell Biology, 1997. **29**(12): p. 1305-1312.

218. Wysokinski, D., E. Pawlowska, and J. Blasiak, *RUNX2: A Master Bone Growth Regulator That May Be Involved in the DNA Damage Response*. DNA and cell biology, 2015. **34**(5): p. 35-315.

219. Yoshioka, H., et al., *Single-Cell RNA-Sequencing Reveals the Breadth of Osteoblast Heterogeneity*. JBMR plus, 2021. **5**(6): p. e10496-n/a.

220. Xiao, L. and J. Guo, *Multiplexed single-cell in situ RNA analysis by reiterative hybridization*. Analytical methods, 2015. **7**(17): p. 7290-7295.

221. Uddin, S.M.Z. and Y.-X. Qin, *Enhancement of osteogenic differentiation and proliferation in human mesenchymal stem cells by a modified low intensity*

ultrasound stimulation under simulated microgravity. PloS one, 2013. **8**(9): p. e73914.

222. Iwabuchi, S., et al., *In vitro evaluation of low-intensity pulsed ultrasound in herniated disc resorption.* Biomaterials, 2005. **26**(34): p. 7104-7114.

223. Webster, R.A., *Passive Materials for High Frequency Piezocomposite Ultrasonic Transducers.* 2009, University of Birmingham: Birmingham. p. 232.

224. Preston, R.C., *Output Measurements for Medical Ultrasound.* 1991: British Library. 180.